

Bangor University

DOCTOR OF PHILOSOPHY

Gas-sensitive resistors for detection of nitroaromatics

Jones, B.J.S.

Award date:
2004

Awarding institution:
University of Wales, Bangor

[Link to publication](#)

General rights

Copyright and moral rights for the publications made accessible in the public portal are retained by the authors and/or other copyright owners and it is a condition of accessing publications that users recognise and abide by the legal requirements associated with these rights.

- Users may download and print one copy of any publication from the public portal for the purpose of private study or research.
- You may not further distribute the material or use it for any profit-making activity or commercial gain
- You may freely distribute the URL identifying the publication in the public portal ?

Take down policy

If you believe that this document breaches copyright please contact us providing details, and we will remove access to the work immediately and investigate your claim.

Download date: 11. Apr. 2024

ACKNOWLEDGEMENTS

I would like to thank my supervisor Dr Maher Kalaji for all his help, encouragement and guidance.

I would also like to acknowledge the useful advice and support of Graeme Nicholson, Mark Kan, and Arfon Jones of AWE.

Thanks to everybody in the chemistry tower who have helped to make this work possible, particularly, John Charles, John Sambrook, Mike Lewis, Denis Williams, and Kevin Spencer for their technical support.

Big thanks go to Duarte, Eric, Chris, Juan, Ben, Andy, Dan, Tania, Alfonso, and Hannah for their friendship, football, judo, marathons, and for making my time in Bangor unforgettable.

Finally, I would like to thank EPSRC and AWE for their financial support.



ABSTRACT

Detection of Nitroaromatic Vapours Using Gas-Sensitive Resistors

This study describes the development of gas-sensitive resistors (chemiresistors) as sensors for the detection of nitroaromatic vapours. 2,4-DNT was chosen as the example of the nitroaromatic, and a vapour generator was designed and built to deliver a vapour stream, in the required low ppm_v concentration range, to a sensor port housing the chemiresistor.

The response of chromium titanium oxide (CTO) chemiresistors towards 2,4-DNT vapours was observed as an increase of the films resistance. The response was found to be reversible and proportional to the square root of 2,4-DNT concentration. When a tungsten oxide (WO₃) chemiresistor was exposed to vapours of 2,4-DNT, the response was also observed as an increase of film resistance. However, this response was found to be independent of 2,4-DNT concentration in the range studied, and it is suggested that a competitive adsorption reaction exists between oxygen and 2,4-DNT. Chemiresistors based on conducting polymers were constructed using platinum microband electrodes. Polyaniline and poly(3-methylthiophene) exhibited a small decrease of film resistance in the presence of 2,4-DNT. These responses were enhanced by the incorporation of heteropolyanions (HPAs) into the film. The data indicated that the HPAs acted as charge transfer agents, transferring charge from the π -conjugated backbone of the polymer to the nitroaromatic.

In the second part of this project, the redox switching characteristics of polyaniline (Pani) films, deposited onto platinum microband electrode arrays, were studied using voltammetry and chronoamperometry. The size of the electrode contact area was found to shift the voltammetric oxidation peak to more positive potentials, and influence the charge associated with the reduction process. The time required for the oxidation process to complete after a potential step was also influenced. Furthermore, reducing the contact area between the electrode and the polymer film resulted in diminishing the number of sites available for oxidation of the polymer at the electrode surface, which in turn modified the percolation threshold. The distance that the conducting-insulating interface was required to propagate was also increased. The position of the working electrode within the array was observed to modify the redox switching characteristics of the Pani film. Electrodes at the centre of the array gave rise to faster switching times and lower oxidation peak potentials than electrodes at the edge of the array. It is suggested that the conducting-insulating interface propagated in two opposing directions, which halved the propagation distance. The propagation rate was examined by potentiometric monitoring of electrodes adjacent to the working electrode, and was found to be 2000 $\mu\text{m s}^{-1}$.

CONTENTS

Chapter 1 – Introduction

1.1	Explosives.....	1
1.2	The history of explosives.....	3
1.3	Nitroaromatics.....	5
1.4	The need to detect explosives.....	7
1.5	Methods for the detection of explosives.....	9
1.5.1	Bench-top methods.....	9
1.5.1.1	Mass spectrometric detection.....	9
1.5.1.2	Gas chromatographic techniques.....	10
1.5.1.3	Optical methods of detection.....	11
1.5.2	Chemical sensors.....	13
1.5.2.1	Optical-based sensors.....	14
1.5.2.2	Electrochemical sensors.....	17
1.5.2.2.1	Voltammetric sensors.....	18
1.5.2.2.2	Amperometric sensors.....	19
1.5.2.2.3	Polymer-based sensors.....	19
1.5.2.2.4	Metal oxide sensors.....	20
1.5.2.3	Mass sensors.....	20
1.5.2.3.1	Quartz-crystal resonators.....	21
1.5.2.3.2	Surface acoustic wave sensors.....	23
1.5.3	Summary of techniques.....	24
1.6	Aims and objectives.....	26
1.7	References.....	27

Chapter 2 – Experimental

2.1	Introduction.....	30
2.2	Experimental techniques and procedures.....	30
2.2.1	Solutions and materials.....	30
2.2.2	Cyclic voltammetry.....	30
2.2.3	Chronoamperometry.....	32
2.2.4	The electrochemical cell.....	32

2.2.5	Experimental preparation.....	33
2.2.6	Chemiresistor preparation.....	34
2.2.7	Optical microscope and SEM images.....	35
2.2.8	Measurement of the chemiresistor response.....	35
2.3	The vapour generator.....	36
2.3.1	Introduction.....	36
2.3.2	Vapour generators.....	37
2.3.2.1	Summary of the vapour generation techniques.....	44
2.3.3	The vapour generator – principle and design.....	46
2.3.3.1	The packed column.....	48
2.3.3.2	The aluminium housing and heater unit.....	49
2.3.3.3	The carrier gas and purification units.....	50
2.3.3.4	The mixing chamber and sensor ports.....	51
2.3.3.5	The silanization process.....	53
2.3.4	Experimental.....	53
2.3.4.1	The heater unit.....	53
2.3.4.2	Time to equilibrium.....	54
2.3.4.3	Temperature of the maximum/minimum limits.....	54
2.3.4.4	Precision tests.....	54
2.3.4.5	Calibration of the heater unit.....	54
2.3.4.6	Calibration of the vapour generator.....	55
2.3.4.7	Vapour traps.....	55
2.3.4.8	Standard Solutions.....	56
2.3.4.9	Gas chromatography.....	56
2.3.5	Results and discussion.....	57
2.3.5.1	Time to equilibrium.....	57
2.3.5.2	Temperature of the maximum/minimum limits.....	59
2.3.5.3	Precision tests.....	60
2.3.5.4	Calibration of the heater unit.....	61
2.3.5.5	Standard solutions.....	63
2.3.5.6	Calibration of the vapour generator.....	63
2.4	Conclusions.....	66
2.5	Future work.....	66
2.6	References.....	67

Chapter 3 – Semiconducting metal oxide chemiresistors

3.1	Introduction.....	68
3.1.1	Semiconducting metal oxide chemiresistors.....	68
3.1.2	Electrical conductivity in semiconductors.....	69
3.1.3	The principles of metal oxides as gas-sensitive resistors.....	72
3.2	Experimental.....	77
3.2.1	Metal oxide chemiresistors.....	77
3.2.2	Sensor response.....	78
3.3	Results and discussion.....	78
3.3.1	Chromium titanium oxide chemiresistors.....	78
3.3.1.1	The baseline response.....	79
3.3.1.2	The effect of relative humidity.....	83
3.3.1.3	The effect of carrier gas variables.....	86
3.3.1.4	The response towards 2,4-DNT.....	88
3.3.2	The tungsten oxide chemiresistor.....	99
3.3.2.1	The baseline response towards nitrogen.....	99
3.3.2.2	The baseline response towards air.....	101
3.3.2.3	The response towards 2,4-DNT.....	103
3.4	Conclusions.....	109
3.5	Future Work.....	110
3.6	References.....	110

Chapter 4 – Conducting polymer chemiresistors

4.1	Introduction.....	113
4.1.1	Conduction in polymers.....	113
4.1.2	Polymer-based chemiresistors.....	115
4.1.3	Heteropolyanions (HPAs).....	117
4.1.4	Aims of the study.....	119
4.2	Experimental.....	119
4.2.1	Polymer deposition.....	120
4.2.2	Characterisation – voltammetry.....	121
4.2.3	Response of the polymer-based chemiresistors.....	121

4.3	Results and discussion.....	122
4.3.1	The Pani-Cl chemiresistor.....	122
4.3.1.1	The baseline response of the Pani chemiresistor.....	124
4.3.1.2	The response of the Pani chemiresistor towards 2,4-DNT.....	125
4.3.2	The Pani-TS chemiresistor.....	126
4.3.2.1	Pani-TS.....	126
4.3.2.2	The baseline response of the Pani-TS chemiresistor.....	130
4.3.2.3	The response of the Pani-TS chemiresistor to 2,4-DNT.....	132
4.3.3	The Pani-PM chemiresistor.....	133
4.3.3.1	The baseline response of the Pani-PM chemiresistor.....	135
4.3.3.2	The response of the Pani-PM chemiresistor to 2,4-DNT.....	135
4.3.4	The Poly(3-methylthiophene) chemiresistor.....	137
4.3.4.1	The response of the P3MT chemiresistor.....	138
4.3.5	The P3MT-TS chemiresistor.....	139
4.3.5.1	P3MT-TS.....	139
4.3.5.2	The effect of film thickness on the HPA incorporation.....	141
4.3.5.3	The baseline response of the P3MT-TS chemiresistor.....	143
4.3.5.4	The response of the P3MT-TS chemiresistor to 2,4-DNT....	144
4.3.6	The P3MT-PT chemiresistor.....	145
4.3.6.1	The baseline response of the P3MT-PT chemiresistor.....	146
4.3.6.2	The response of the P3MT-PT chemiresistor to 2,4-DNT....	147
4.3.7	The P3MT-PM chemiresistor.....	148
4.3.7.1	The baseline response of the P3MT-PM chemiresistor.....	149
4.3.7.2	The response of the P3MT-PM chemiresistor to 2,4-DNT....	150
4.4	Conclusions.....	152
4.5	Future Work.....	152
4.6	References.....	154

Chapter 5 – Redox switching of polyaniline

5.1	Introduction.....	158
5.1.1	Polyaniline (Pani).....	158
5.1.2	Redox switching of polyaniline.....	161
5.2	Experimental.....	163

5.2.1	Electrodes.....	163
5.2.2	Polymer deposition.....	165
5.2.3	Voltammetry.....	165
5.2.4	Chronoamperometry.....	165
5.2.5	Potentiometric monitoring.....	165
5.2.6	Film thickness.....	166
5.3	Results and discussion.....	167
5.3.1	The influence of electrode contact area.....	167
5.3.1.1	Case A.....	167
5.3.1.2	Case B.....	168
5.3.1.3	Voltammetry – Case A.....	169
5.3.1.4	Voltammetry – Case B.....	172
5.3.1.5	Voltammetry – discussion.....	176
5.3.1.6	Chronoamperometry – Case A.....	180
5.3.1.7	Chronoamperometry – Case B.....	185
5.3.1.8	Discussion of chronoamperometric results.....	191
5.3.2	The influence of electrode position within the array.....	192
5.3.2.1	Voltammetry of Pani on the eight-electrode array.....	194
5.3.2.2	Chronoamperometry.....	202
5.3.2.3	Potentiometry.....	205
5.3.2.3.1	Potentiometric measurements - voltammetry.....	207
5.3.2.3.2	Potentiometric measurements - potential step.....	211
5.4	Conclusions.....	217
5.5	Future Work.....	219
5.6	References.....	220

Chapter 6 – General conclusions

.....	222
-------	-----

INTRODUCTION

1.1 Explosives

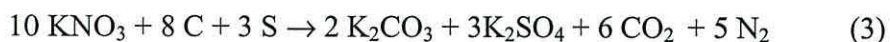
Chemical explosives are best described as compounds or mixtures of compounds that when suitably initiated give rise to a rapid, violent chemical reaction. In order to bring about an explosion, the explosive must satisfy four conditions. Firstly, it must be capable of producing gaseous products; secondly, it must be capable of producing energy; thirdly, the first two conditions must be rapid; and finally, the first three conditions must be self-sustaining, in that they must continue throughout the mass of the explosive when started at any given point within it [1]. These four properties alone constitute those required for a compound to be an explosive. Many other properties may be desirable in an explosive, e.g. the compound only explodes when caused to do so, but they are not essential.

Explosive compounds depend upon chemical reactions that produce energy and gaseous products for their explosive effects. The explosion comes about as a result of the reaction rate being sufficiently high. The reaction rate is dependant upon several conditions including the concentration of reactants at the point of detonation. In practice the majority of explosives depend on two reactions, the oxidation of carbon, and the oxidation of hydrogen, i.e. combustion.



Combustion is a very fast, and highly exothermic reaction. The energy created during the reaction causes the temperature of the un-reacted material to rise, increasing the rate of subsequent reaction. But, for these processes to advance at an explosive rate, a high concentration of oxygen is required, for which air alone is not sufficient. Therefore, two methods are commonly employed to obtain the required amount of oxygen. The first involves preparing a mixture of components, which decompose to produce oxygen.

Gunpowder is the classic example, whereby saltpetre (KNO_3), charcoal, and sulphur are mixed together. The reaction is believed to proceed as follows [2].



The major drawback of these mixture-type explosives is that on the atomic scale the oxidant and fuel are present as relatively large lumps, and considerable mixing has to occur for the reaction to proceed to completion. To overcome this problem the second example has the oxidant and the fuel mixed together in a single compound. Thereby, each molecule of fuel already has associated with it the oxidant required for the compound to react at an explosive rate. A good example of this type of explosive is trinitrotoluene (TNT).

Explosives can be classified by the ease with which they can be ignited and subsequently exploded. Deflagrating explosives are usually easily ignited by a spark or flame. The rate of combustion is subsonic and controlled by the thermal reaction. However, these explosives are able to behave differently, depending on whether or not they are contained. If they are ignited in “the open” they burn with intense heat, but no explosion is likely to occur. However, if they are contained the production of hot gases increases the temperature and pressure of the reactants, increasing the reaction rate sufficiently to cause an explosion. As a result of this behaviour they often tend to be used as propellants.

Detonating explosives burn at a supersonic rate, but are much harder to ignite. Detonation is usually triggered by a supersonic shockwave, caused by another explosion, which propagates through the explosive causing it to explode. The rate of burning is controlled by the high rate of shockwave propagation and hence detonating explosives are used in applications where shattering effects are required, such as blasting operations or in military shells. Detonating explosives are often referred to as high explosives, while deflagrating explosives are classed as low explosives. Another terminology used to classify explosives is that of primary and secondary explosives. Primary explosives are

those that are easily “set off”. These are the relatively unstable explosives such as lead azide, and are used in small quantities in so-called “safe devices”. Secondary explosives are referred to as those that are difficult to “set off”, requiring a suitable shock or the charge of a primary explosive for ignition. Examples of secondary explosives include TNT and RDX and gun propellants [3]. A list of common explosives can be seen in table 1.

1.2 The history of explosives

The first investigation into the explosive properties of gunpowder is accredited to Roger Bacon, during the thirteenth century (1249), although it is reported that the Chinese Taoist monks exploited the explosive properties of saltpetre, sulphur, and charcoal mixtures in 919, and Chinese alchemists as early as 220 BC [2]. The history of high explosives dates back to the mid 19th century, when the limitations of black powder as a blasting explosive became apparent. Mining and tunnelling operations required explosives with more power, and early development work saw the discovery of guncotton (cellulose nitrate) by Schonbein in 1838, quickly followed by nitroglycerin (glyceryl trinitrate) by Sobrero in 1845. The relative instability of nitroglycerin, and a series of devastating accidents, prompted the search for powerful but safe explosives, with the most notable examples being Dynamite and Gelignite, patented by the Nobel family in 1867 and 1875, respectively [2].

Meanwhile, research into explosives was also being carried out for military operations. Turpin found picric acid (trinitrophenol) to be a suitable replacement for black powder in 1885, and it was adopted by the armed forces in 1888. TNT (trinitrotoluene) was first prepared by Wilbrand in 1863, but it was not until 1902 that it replaced picric acid in German munitions. By 1914 TNT was the standard explosive in the munitions of all armies. RDX (cyclotrimethylenetrinitramine) is another common military high explosive. However, RDX was first prepared in 1899 by the German Henning for medicinal use, and was only noted for its explosive value in 1920, by Herz. RDX was used a great deal in the Second World War, but never as the major component in

explosives mixtures, but as an additive to explosives such as TNT to increase the power of the explosion [3].

Name	Chemical formula	Structure	Name	Chemical formula	Structure
Nitro-glycerine	$C_3H_5N_3O_9$		Nitro-guanidine	$CH_4N_4O_2$	
Nitro-cellulose	$C_6H_7O_2-(OH)_x(ONO_2)_y$ where $x + y = 3$		PETN	$C_5H_8N_4O_{12}$	
Picric acid	$C_6H_3N_3O_7$		RDX	$C_3H_6N_6O_6$	
Tetryl	$C_7H_5N_5O_8$		HMX	$C_4H_8N_8O_8$	
TNT	$C_7H_5N_3O_6$		TATB	$C_6H_6N_6O_6$	

Table 1. Structural formulae for some of the more common high explosives including Picric acid (trinitrophenol), TNT (trinitrotoluene), PETN (pentaerythritol tetranitrate), RDX (cyclotrimethylenetrinitramine), HMX (cyclotetramethylenetetranitramine), and TATB (triaminotrinitrobenzene).

Polymer-bonded explosives (PBX) have been developed to reduce the sensitivity of newly synthesised explosive crystals, by embedding the crystals into a rubber-like polymeric matrix. The first PBX composition was developed at the Los Alamos Scientific Laboratories (USA) in 1952. The composition consisted of RDX crystals embedded in plasticised polystyrene. A well-known example of a PBX, based on RDX, is Semtex. More recent research, first introduced by Adkins and Norris in 1978, has seen the introduction of heat resistant explosives such as TATB (1,3,5-triamino-2,4,6-trinitrobenzene). Heat resistant explosives are able to withstand much higher temperatures than their standard counterparts, dramatically reducing accidental explosions [3]. Research and development into explosives that are insensitive towards accidental initiation, still continues.

1.3 Nitroaromatics

Nitroaromatics are compounds containing both an aromatic group such as benzene, and the nitro-functionality, which is attached directly to the aromatic ring. Nitroaromatics are almost always prepared by the action of nitric acid on the aromatic compound, whereby a nitro group replaces a hydrogen atom attached to the aromatic backbone. The most commonly used nitrating agent is a mixture of fuming nitric acid and concentrated sulphuric acid, although sulphuric acid solutions containing metal nitrates can also be used [4]. The sulphuric acid seems to be important in the process for a number of reasons. Firstly, it combines with the water produced during the reaction, preventing the dilution of the nitric acid; secondly, sulphuric acid is capable of dissolving nearly every organic substance; and thirdly, it reduces the oxidising effect of the nitrating agent.

The physical properties of nitroaromatics vary with the degree of nitration and the presence of other functionalities, but generally they are colourless/yellow solids or viscous liquids, with high melting points, and pungent odours (see Table 2). Mono-nitroaromatics are volatile in steam and generally boil without decomposition, while poly-nitroaromatics, if heated at room temperature, will decompose and explode with considerable violence. In almost all cases, the nitro group is firmly bound to the benzene

ring, and in almost no chemical reaction is this bond broken^b. However, in the presence of a proton donor the nitro groups may be reduced to amino groups, where H corresponds to a proton from the proton donor.



Nitro-aromatic	Molecular formula	M _R	T _m / °C	T _b / °C	Vapour pressure	State
nitrobenzene	C ₆ H ₅ NO ₂	123.11	5.7	210.8	0.03 kPa	Pale yellow liquid
1,3-dinitrobenzene	C ₆ H ₄ (NO ₂) ₂	168.11	90.0	291.0	< 0.13 kPa (20°C)	Colourless / yellow rhombic needles
2,4-Dinitroethylbenzene	C ₈ H ₈ (NO ₂) ₂	196.16	-----	117.0	-----	Yellow oily liquid
o-nitrotoluene	C ₇ H ₇ NO ₂	137.14	-10.0	222.0	13.5 kPa	Yellow liquid
2,4-dinitrotoluene	C ₇ H ₆ (NO ₂) ₂	182.14	70.5	300.0*	7.9×10 ⁻⁶ kPa	Yellow monoclinic needles
2,4,6-trinitrotoluene	C ₇ H ₅ (NO ₂) ₃	227.13	80.1	240.0*	0.014 kPa (100°C)	Colourless rhombic needles

Table 2. Physical properties of selected nitroaromatic compounds. Vapour pressures were obtained from either [5] or [6]. * decomposes.

^b The exception to the rule is 2,3-DNT, where it is possible to sever one of the nitrogen atoms from the benzene ring. This makes it possible to replace the -NO₂ group with -ONa, or -NH₂ groups at higher temperatures.

The benzene moiety is very stable towards oxidising agents. When an aromatic compound is treated with an oxidising agent over long periods, any side-chains in the molecule (i.e. alkyl-substituted nitroaromatics) are converted to carboxyl groups, but the benzene ring itself is not oxidised. Toluene for example, when heated with oxidising agents undergoes oxidation of the methyl group to form benzaldehyde, and ultimately benzoic acid, as can be seen in equations 6 and 7, where O corresponds to oxygen from the oxidising agent.



Poly-nitroaromatic compounds will explode with considerable force upon heating, and hence TNT has been adopted as a high explosive, being used extensively in both the mining and blasting industry, as well as in the military. TNT has held favour in these fields right up to the present day, mainly because it possesses many qualities that make it easier and safer to use, as well as possessing a significant explosive force (power index *vs.* picric acid = 115 %). These qualities include cheap raw materials for low manufacturing costs, low sensitivity to friction and impact, good chemical and thermal stability, low volatility and hygroscopicity, and good compatibility with other explosives. TNT also possesses a low melting point (80.8 °C) and can easily be moulded into shells. K10 is a mixture of di- and tri-nitroethylbenzene, and has been investigated as an energetic plasticiser. The K10 is much more stable towards heat and shocks than RDX, but will also explode if suitably initiated. Explosives mixtures containing K10 possess greater stability, while the explosive force per unit mass remains higher than conventional PBXs.

1.4 The need to detect explosives

Explosive compounds have now become an integral part of everyday life, commonly used in civilian applications such as mining, construction, demolition, obstacle elimination, and in the entertainments industry. They also have a wide range of military

applications, commonly used in the construction of mines, artillery projectiles, bursting charges, torpedoes, and grenades. However, the world has also witnessed the many detrimental effects of explosives in warfare, accidents, and terrorism. With the destruction of Pan American Flight 103 in 1988 over Lockerbie, the truck bombings at the World Trade Centre in New York City in 1993, the Murrah Federal Building in Oklahoma City in 1995 [7], and recently the nightclub bombing in Bali, 2002, comes a growing fear from terrorist attacks. Landmines are also a constant problem, being laid during wartime, but causing horrific accidents, maybe years later, when detonated by unsuspecting civilians. This has resulted in a major effort to develop instruments for the detection of explosives and explosive devices, in order that they may be confiscated or deactivated, for the prevention of tragic incidents in the future.

The need to detect, analyse, and quantify explosives, reaches beyond the risk of terrorist attacks and there are major risks to those legitimately handling explosives on a day-to-day basis. Nitroaromatic explosives, although relatively stable, can undergo physical and chemical changes upon aging when stored in sealed vessels. Exudation of dinitrotoluene and trinitrotoluene isomers is one of the major drawbacks of TNT. This often occurs in the storage of projectiles containing TNT, particularly in the higher temperatures experienced in the summer time. The main disadvantage of leaching is the formation of cracks and cavities, which can lead to premature detonation [3]. Migration of these isomers to the screw thread of the fuse can cause the formation of “fire channels”, which can initiate accidental ignition of the charge. If migration of the isomers penetrates to the detonating fuse, malfunctions of the ammunition can occur [3]. Obviously, problems that cause instability in the explosive can render the device hazardous. This can then present huge problems for the storage and movement of explosive devices. Nitroaromatics are also considered to be harmful to human health. The primary routes for exposure are dermal and by ingestion, and despite the low vapour pressures associated with nitroaromatics, inhalation can also be harmful. The government in the U.S. have limited the exposure to di- and tri-nitrotoluenes to 1.5 mg/m^3 [8-10]. Nitroaromatics such as DNT and TNT can cause liver damage, cyanosis, sneezing, coughs, sore throats, peripheral neuritis, muscular pain, kidney damage, cataracts, sensitisation dermatitis,

leukocytosis (large numbers of white cells in blood), leukopenia (low numbers of white cells in blood), and aplitic anaemia [5, 6, 11]. If DNT enters the environment, it is slightly mobile in soil and in water has a tendency to partition to the sediment where it can be degraded by micro-organisms [11].

1.5 Methods for the detection of explosives

Such is the state of global concern over the dangers presented by high explosives that the literature is full of research concerning their analysis and detection. At present, methods for the detection and quantification of nitroaromatic compounds vary considerably, dependent upon required application, and ranges from nuclear techniques involving charged particle accelerators [12, 13], to electrochemical techniques [14, 15], through to optical-based sensors [16, 17]. The choice of technique is obviously determined by the requirements of the application, i.e. the required sensitivity, selectivity, cost, and confinements. This section aims to review some of the progress to date within the requirements of this project, and a more general review can be found in [7].

1.5.1 Bench-top methods

Bench-top methods for explosives analysis offer a good degree of sensitivity, coupled with low limits of detection and high selectivity. Analysis is not necessarily confined to the laboratory, as traditional bench-top instrumentation can now be miniaturised and portable, in some instances. The development of micro and nano-technology has lead to *in situ* detection and monitoring techniques for many different environments.

1.5.1.1 Mass spectrometric detection

Mass spectrometry is one of the best-known gas-analytical techniques for trace analysis. Molecules can be identified by their characteristic fragmentation patterns, and detection limits are constantly decreasing [18]. However, as a tool for the analysis of explosive compounds, mass spectrometry itself shows insufficient selectivity.

Selectivity can be improved in a number of ways. A common method for improving the selectivity of mass spectrometry (ms) is through combination with gas chromatography (GC). GC-ms has been successfully adapted for the separation and detection of explosives mixtures using stationary phases consisting of cross-bonded (100%) dimethylpolysiloxane [19]. The technique was found to be suitable for the unequivocal identification of simple nitroaromatic mixtures and dinitrotoluene isomers. The presence or absence of dinitroethylbenzene could also be detected, and this would allow a degree of batch characterisation for different explosives mixtures. However, the technique was not able to separate complex mixtures sufficiently or reliably enough to exclude the overlap of everyday materials. GC-ms has also been used for the analysis of explosives in the urine of workers from an ammunition dismantling workshop [20].

Gas chromatography allows the different compounds and isomers to be separated using a chromatographic column. However, the detection of multiple nitroaromatics can be achieved with other techniques. By sequentially applying various filtered-noise fields to the end-cap electrodes of a quadrupole ion trap, Asano *et al.* [21] were able to monitor the presence of several target explosives in air, using ion trap mass spectrometry. The capability of this parallel monitoring technique to accumulate and store a wide range of ion masses, coupled with the sequencing of tailored waveforms for ion isolation and collision activation, allowed the direct parallel screening of complex mixtures containing 2,4-dinitrotoluene, 2,4,6-trinitrotoluene, and (2,4,6-trinitrophenyl)methylnitramine.

1.5.1.2 Gas chromatographic techniques

It has been shown above, that gas chromatography can be linked to other detection methods, in order to aid the selectivity of the overall technique. Detection techniques that are commonly linked with GC include electron capture detection, and chemiluminescence detection.

Gas chromatography with electron capture detection (GC-ECD) is a well-known method in trace analysis. Electron capture detection is very sensitive, particularly for the detection of compounds with electronegative functional groups, which makes ECD

extremely suitable for the detection of nitro aromatics. Coupled with gas chromatography, limits of detection in the low picograms region (29, 174, 340 pg for 2,4-DNT, 2,6-DNT, and TNT respectively) were obtained, while the limits of quantification were 88, 527, 1030 pg for 2,4-DNT, 2,6-DNT, and TNT respectively [22].

The combination of gas chromatography with chemiluminescence detection is also very sensitive and shows a high selectivity in the detection of nitro compounds. The separation of the explosives can be achieved using conventional chromatography [23], or electrokinetic chromatography [24-26]. The detection method is based on the formation of nitric oxide during the pyrolysis of nitro compounds. The nitric oxide formed is allowed to react with ozone in a detection chamber to yield electronically excited nitrogen dioxide, which in turn emits photons at 600 nm. These photons can then be detected using a photomultiplier [18].

Other detection techniques have also been employed for nitroaromatics. Burns and Lewis [27] have successfully employed a gas chromatography with flame ionisation detection as a technique for the investigation into the isomer content within the nitro aromatic component in nitroglycerine-based explosives. Flame ionisation yielded high sensitivities (*ca.* 10^{-7} g ml⁻¹) for the nitroaromatic compounds. Meanwhile, Bratin *et al.* have used electrochemical detection methods [15].

The use of gas chromatography as a pre-separation technique, can lead to methods for the detection of nitro aromatic compounds that are fairly selective, and when coupled with a suitable detector, are very sensitive too. However, the biggest drawbacks with these techniques are the cost and the time required for analysis of the samples [18]. Generally, these methods are slow, and analysis of multiple samples can become a long drawn out process.

1.5.1.3 Optical methods of detection

An alternative approach to detecting nitro aromatics is based on the absorption of UV laser radiation in order to photo-dissociate the parent molecule into characteristic

fragments. This technique is known as laser photolysis (LP). If electronically excited during the photolysis, the resulting fragments, including atoms, di- and tri-atomics, may be detected by their prompt emission using laser induced fluorescence (LIF), or by resonance enhanced multiphoton ionisation (REMPI) [28-30]. The nitro group is usually weakly bound to the main skeletal portion of the molecule (40-50 kcal/mol), and is responsible for the weak and structureless absorption feature observed in the UV-Vis region near 230 nm. Nitro aromatic compounds absorb radiation (typically at 226 nm), and photodissociate into fragments. The NO fragment is better suited for detection since it is readily formed by pre-dissociation of NO₂, and its radiative lifetime (~200 ns) is significantly shorter than the NO₂ states excited in the visible region [28]. Ground state NO absorbs a photon to undergo a resonant transition and hence produces fluorescence (LIF) [29], which can be detected with a high degree of sensitivity, giving a limit of detection for DNB in air, of 11 ppb by mass [30], and 40 ppb for TNT [29]. REMPI detection gave rise to a limit of detection of 24 ppb for TNT [28].

As well as fluorescence, spectroscopy in the IR-region has been successful for the detection of explosives [31]. Explosives samples, decomposed on a catalytic bed into characteristic fragments, were analysed by a mid-infrared tuneable diode laser and frequency modulation spectroscopy (FMS). The important fragments were found to be nitrogen containing fragments, such as NO, NO₂, N₂O, and HCN, and the technique demonstrated detection limits of 5 - 10 pg for RDX, but there were a number of engineering and calibration issues, such as 'memory effects', which led to irreproducible results that needed to be addressed before a prototype field instrument could be assembled.

Bench-top techniques for the detection of explosives and other nitrated compounds are very sensitive and selective, but do have several disadvantages. The complex detection systems are invariably expensive, and as a skilled operator is required they can be labour intensive too. Bench-top systems are large, which limits portability of the equipment. This in turn, necessitates sample collection and storage prior to measurement, which can

cause the processes to be time consuming, when it might be simpler if the information about the environment could be obtained *in situ*, in real-time.

1.5.2 Chemical sensors

Modern chemical sensors are able to offer portability, allowing real time measurements to be made, often *in situ*, while not necessarily compromising sensitivity or the required limits of detection. Chemical sensors generally operate through two steps. Firstly, there is the recognition step. This is where the sensor selectively recognises the presence of a particular analyte, through a chemical interaction, and in doing so produces a signal. This signal is usually very weak, and any attempts to directly increase the signal usually results in its distortion and the loss of information. Therefore, the second step is an amplification step. Amplification of the signal is usually achieved through a transducer. The transducer is a physical part of the sensor that amplifies the primary signal to a suitable level.

There are many different types of chemical sensors, which can be characterised by their methods of transduction. Typical transduction methods can be electrochemical, optical, mass sensitive, or a combination of these methods [32].

A typical problem encountered when dealing with individual sensors or sensing elements, is that of selectivity. Selectivity is defined as ‘the ability of the sensing device to measure one chemical component in the presence of others’. A sensor that has a high sensitivity for a component in isolation may not necessarily be good at measuring the component in the field, where it coexists with many similar compounds. Sensor arrays have been developed to counter this problem. Sensor arrays can be described as arrays of partially selective sensing elements formed upon a single substrate for the simultaneous determination of the analyte. Sensing elements in an array give rise to very slightly different, often overlapping responses to a given analyte, which gives rise to a complex signal that can be statistically interpreted in order to obtain a quantifiable measurement. Sensor arrays can also be used for the resolution of gaseous mixtures, where the different sensing elements give rise to a characteristic pattern, which can then be stored in a

databank for future reference. This is known as training the array. When an unknown gaseous mixture is sampled, the pattern obtained is recognised and matched to a pattern stored in the databank. The technique of using arrays of sensing elements, with statistical evaluation and pattern recognition for the detection of gaseous mixtures, is very similar to that of the mammalian olfactory system, and therefore, these devices are often given the working term ‘electronic nose’ [33]. The advantage of using a sensor array is not only limited to the enhanced selectivity and multi-component analysis, fewer sample preparation procedures are involved, which reduces analysis time and helps to eliminate contamination.

1.5.2.1 Optical-based sensors

This is an important category of chemical sensors, where the sensor relies upon an optical transducer for signal measurement. Optical sensors employ the same equipment as the classical spectroscopic instruments, although the arrangement may be slightly different. Bench-top spectrometric techniques often position the sample in the path of a defined beam of light (incident light) and the light passes through the sample (transmitted light) to a detector. However, optical sensors often direct the light beam out of the spectrometer, where it interacts with the sample before being reintroduced into the spectrometer in its primary or secondary form [34]. Most optical sensing processes rely on the absorption of light as the first step, so the depository of spectroscopic knowledge forms the basis for the development of optical sensors. The relationship between the intensity of the incident and transmitted radiation is given through the Beer-Lambert law.

$$A = \epsilon \cdot c \cdot l \quad (8)$$

Where, A is the absorbance – $\log(I/I_0)$, and I_0 and I are the incident and transmitted monochromatic light intensities, respectively. ϵ is the extinction coefficient ($\text{mol}^{-1} \text{cm}^2$). c is the concentration (mol L^{-1}), and l is the cell path length (cm).

Optical fibres can transmit light over large distances with minimal loss of intensity. Therefore, light can be delivered to and from the active sensing area over considerable

distances from the source (km), making this method attractive for applications where the use of electricity might be hazardous. Optical sensors possess a great deal of selectivity, inherent in the transduction process by the choice, for example, of the wavelength or polarisation of the light. However, like other sensors a selective layer can provide the principle source of selectivity by inducing specific reactions with the target analyte. This normally involves a two-phase system in which a reagent is physically confined or chemically immobilised, within a solid substrate such as a membrane, which undergoes a colour change in the presence of the analyte. This type of optical sensor has been given the name ‘optode’. Optodes are usually used in conjunction with optic fibres, and are incredibly versatile. Figure 1 shows various arrangements of optical sensors.

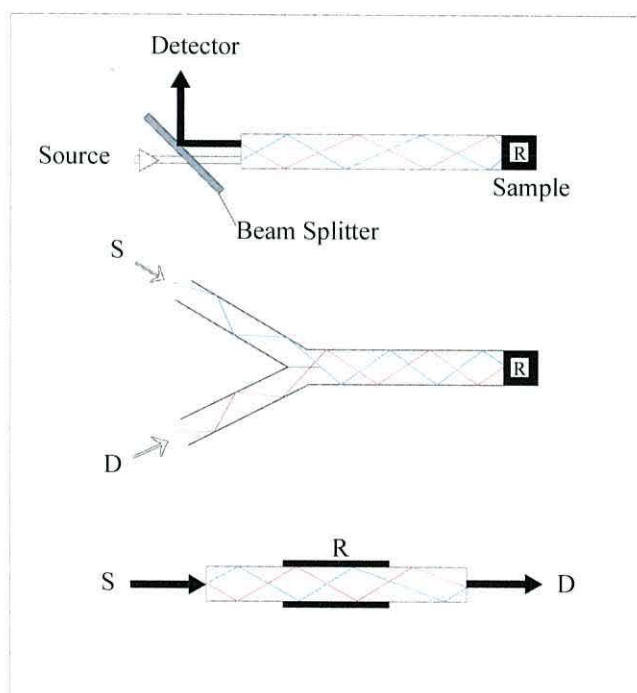


Figure 1. Three of the most common arrangements for optical sensors, where R corresponds to the reagent, S corresponds to the source and D corresponds to the detector [34].

In general, for the detection of nitro-derivatised compounds, the type of optode used is termed ‘intrinsic’. This is where the optode membrane is immobilised onto the distal end window of the fibre, or a chemical reagent is chemically bound to the window. Intrinsic optodes that operate *via* fluorescence modulation when placed in contact with volatile

organic vapours have been developed for the detection of organic vapours [35]. The sensors were constructed from optic fibres, modified at the distal end, by the addition of an analyte-sensitive coating, constructed by incorporating the fluorophore Nile Red into a thin siloxane polymer matrix. When the device was exposed to organic vapours, the vapours were adsorbed into the siloxane rubber, changing the polarity of the microenvironment surrounding the fluorophore. This resulted in a fluorescence enhancement, which was monitored by the optode. Detection limits were quoted to be 1 ppm for xylene. The major disadvantage of this sensor was that it is unable to distinguish between the volatile organic components of mixtures, for detection of specific compounds. This lack of selectivity prompted research into the development of selective optical sensor arrays. Optical sensor arrays have been used in conjunction with pattern recognition techniques, and have paved the way in the development of artificial (optical) olfactory systems, for the characterisation of gaseous mixtures. A cross-reactive optical sensor array, based on the siloxane sensing elements described above, was developed for the characterisation of multi-analyte samples [16]. The array consisted of a 'bundle' of 19 sensing elements each consisting of an optical fibre modified by a different polymer layer containing the fluorophore. Each polymer varied from each other by some degree of polarity, hydrophobicity, pore size, flexibility, or swelling tendency. This created an array with unique sensing regions that gave rise to a series of characteristic fluorescence responses with different organic vapours. The data collected from each fibre was used to train a neural network for vapour responses. One such sensor array was developed with neural networks for the classification and quantification of a mixture containing nine organic vapours [36], and the idea was further developed by Johnson [37], who produced a device capable of identifying and quantifying twenty-analyte vapour sets. The analyte set consisted of 17 pure compounds and three complex mixtures. The device operated through the use of numerical descriptors that encoded the changes in fluorescence data from the optical sensor array. This encoded data was then presented to a learning vector quantisation (LVQ) neural network, which classified each of the presented analytes. Additional LVQ networks could be used to assign a relative concentration to each of the analytes. This data was stored in a data library for future comparison. One of the complex mixtures was a pseudo-explosive of unknown composition.

The idea of mimicking the mammalian olfactory system using high-density optical arrays has achieved remarkable success using bundles of optodes. However, an array can also be created from a single optic fibre [38]. This novel array offered a new approach to sensor array fabrication in that a mixture of different polymer beads were scattered into the microwells on the distal tip of an etched optic fibre, and the identity and specific location of each bead was determined afterwards. The different polymer beads had been modified by coating with fluorescent dye Nile Red. The design of this array, and the distinct intrinsic response characteristics of the different beads, eliminated the need for encoding. Therefore, these sensors were termed self-encoded bead arrays.

Polymers are a useful matrix for the containment of fluorescent dyes, but polymers incorporating the rigid three-dimensional pentyptycene moieties can provide an approach towards stable fluorescent conjugated polymer films that are themselves selective toward nitro aromatic compounds [39, 40]. These rigid three-dimensional pentyptycene moieties prevent π -stacking of the polymer backbones and thereby maintain a high fluorescent quantum yield and good spectroscopic stability. Pentyptycene polymers displayed fast responses to both TNT and DNT, with fluorescence quenching increasing to $50 \pm 5\%$ within 30 s and to $75 \pm 5\%$ over 60 s for TNT, while the response towards DNT was even greater at $91 \pm 2\%$ over 30 s. The greater quenching effect of DNT was assumed to be due to its higher equilibrium vapour pressure. The fluorescence quenching was also found to be dependent on film thickness, rates of diffusion of analytes into the polymer film, and electron transfer from the excited polymer to electron acceptors in the target analytes. Selectivity towards TNT and DNT was obtained through variations in film thickness.

1.5.2.2 Electrochemical sensors

Electrochemical sensors are the largest and oldest group of chemical sensors. The concept that chemical energy could be directly converted to electrical energy by means of an electrochemical process is based on the work Galvani and Volta [34]. Electrochemistry implies the transfer of charge from one phase to another, which can be

solid (i.e. an electrode) or liquid. During this process, chemical changes take place and the charge is carried through the bulk phase. Electrochemical sensors can use these processes and the resultant charge transfer, as a basis for the sensing process. The signal can be measured as a voltage, current, or resistance. Two important factors to note when considering electrochemical sensors are that they require a closed electrical circuit, and that the charge transfer within the transducer and supporting instrumentation of the sensor must always be electronic. There are several types of electrochemical sensors that can be used for gas analysis. This gives rise to diverse range of sensors, such as enzyme electrodes, high-temperature semiconducting metal oxide sensors, fuel cells, and surface conductivity sensors, amongst others. These sensors can be divided into groups according to their mode of transduction. Potentiometric sensors rely on the measurement of voltage, amperometric sensors on the measurement of current, and conductometric sensors on the measurement of conductivity.

1.5.2.2.1 Voltammetric sensors

There has been relatively little attention paid to the electrochemical detection of nitro aromatic explosives, despite their inherent redox activity. This is perhaps a little surprising, considering the reducible nitro group is rare in nature, and most electroactive organic compounds require much higher overpotentials than those required to reduce the nitro- group. Wang *et al.* developed a screen-printed voltammetric sensor for the detection of TNT in aqueous solution [41]. Using square wave voltammetry and single-use carbon-based electrodes, TNT could be detected at a limit of 200 ppb with a wide linear range. This technique was successfully applied to the remote monitoring of natural waters [14]. Voltammetric detection of TNT has also been applied to the vapour phase [42]. In this preliminary study, the sensor employed cyclic voltammetry to study the reduction of TNT at a gold microelectrode. A gold ring acted as the counter and reference electrodes, and these electrodes were covered with a hanging drop of sulphuric acid. When the sensor was held 10 cm over a pure TNT sample the voltammogram of the gold electrode was modified by the addition of a reduction peak at -0.4 V vs. Au , caused by the reduction of TNT.

1.5.2.2.2 Amperometric sensors

A chemical parameter processor (CPS) is a small microprocessor-controlled array of amperometric gas sensors, each of which is adjusted to respond differently to electrochemically active gases and vapours [43]. The device used an array of four different electrochemical sensors, which were operated in four different modes, giving rise to 16 channels of data for each chemical species detected. The data obtained from these sensors was used in conjunction with pattern recognition techniques. The electrochemical responses were used to define the axes of a coordinate system in space. Each compound under investigation was then thought of as a point, whose position in space was defined by the values produced by each sensor. The device was capable of distinguishing between 22 different organic vapours, including nitrobenzene.

1.5.2.2.3 Polymer-based sensors

Polymer-based sensors operate on the principle that conducting polymers will change their electrophysical characteristics during the adsorption or desorption of certain gases. Polymeric phthalocyanine, of the general formula $(XMO)_n$, where X is phthalocyanine, M is a group 4 or 5 element (preferably Si, Ge, or Sn), and O is oxygen, can be produced in films (500 nm thick) by vacuum deposition techniques [44]. The resistance of the silicon and germanium films was found to decrease in the presence of good electron acceptors even at ppm_v levels. Polymeric phthalocyanine (Pc) films were able to detect planar pi-acceptors such as nitroaromatics, aliphatic nitrates, nitrites, and aliphatic nitro compounds. Nitrobenzene could be detected down to a level of 1 ppm_v under optimal conditions. Gas sensors based on $(PcSiO)_n$ or $(PcGeO)_n$ also had the advantage of possessing good thermal stability, which meant that the sensors could be operated at high temperatures (200-250 °C), increasing response and recovery times, without losing sensitivity. Good thermal stability also tends towards longer lifetimes without loss of sensitivity.

Polymer-based sensing elements have also been included in sensor arrays [45]. One such array consisted of 12 different polymer sensors, and was used to monitor a complex

vapour mixture in the headspace above a mixed solvent sample. The sensors were electrochemically grown, with polypyrrole (although some work had also been done with polyaniline), across two electrodes separated by a 10 μm gap. During analysis, the percentage change in resistance, due to polymer/vapour interaction, was used to monitor the composition of the vapours.

1.5.2.2.4 Metal oxide sensors

Semiconducting metal oxide (MOS) gas sensors also detect gases *via* changes in their resistance. At elevated temperatures, charged oxygen adsorbents (O_2^- , O^- , and O^{2-}) cover the surface of the semiconducting metal oxide, and it is thought that these species are important when sensing gases and vapours. The interaction between the metal oxide and the oxygen species results in their chemisorption at the surface. This removes electrons from the oxide surface and increases the film resistance. If the target analyte reacts with these adsorbed oxygen species, resulting in their removal from the surface, the electrons are returned to the oxide, the resistance of which is modified accordingly. Semiconductor metal oxide sensors will respond to almost any inflammable gas and this serves to be their major disadvantage, as it leads to low selectivity. A more detailed explanation of MOS sensors is given in chapter 3.

Le Centre de Recherches et d'Etudes de la logistique de la Police Nationale Française (CREL) conducted a study into the development of a portable hand-held explosives detector, based on an array of MOS sensors coupled with neural networks [46]. The MOS sensor was made from tin oxide deposited onto an alumina tube. The tube was heated to 350 $^{\circ}\text{C}$, and the freely varying resistance of the MOS sensing element was measured. The change in resistance due to adsorption of the target analyte was related to the concentration, but the work was still in progress and no detection limits were quoted.

1.5.2.3 Mass sensors

The measurement of mass is known as gravimetry. Scales and balances are not usually considered as sensors, for they are a standard piece of laboratory equipment. However,

when the masses to be measured are so small that microbalances are required, microgravimetry can be regarded as a sensing process. Most microbalances are based on the piezoelectric effect. Pierre and Jacques Curie first discovered the piezoelectric effect in 1880. When pressure is applied to a crystal that has no centre of symmetry (such as α -quartz), an electric potential is established between the deformed surfaces. By application of electrodes to the surfaces of the crystal, a current will flow through an external circuit. On release of this pressure, a transient current will flow in the opposite direction. Sensors based on this principle are called 'bulk wave sensors'. If an alternating potential is applied, a mechanical oscillation is set up within the crystal at a resonant frequency that is dependant upon the crystal dimensions. By applying a reactive reagent, analytes can be adsorbed the crystal surface, altering the frequency of the mechanical oscillation. This change in frequency can be measured and related to the mass of analyte deposited on the crystal surface, through the Sauerbrey equation.

$$\Delta F = -2.3 \times 10^6 F^2 (M/A) \quad (9)$$

Where ΔF is the change in frequency (Hz), F is the oscillating frequency of the quartz crystal, A is the electrode area of coated onto the film, and M is the mass of deposited analyte. A piezoelectric sensor is ideal for the detection of gases or vapours, as it possesses the requisite low-power consumption and intrinsic sensitivity. However, it does suffer selectivity problems due to difficulties in finding a coating, which is only reactive towards a given target analyte.

1.5.2.3.1 Quartz-crystal resonators

The best-known example of a bulk wave piezoelectric sensor is the quartz crystal microbalance. A coating with an affinity for the analyte is deposited on the surface of the quartz crystal, and depending on the thickness of the layer, the analyte is adsorbed or absorbed at the surface. Coatings can be applied by painting, dipping, or spraying, or by deposition from the vapour state. Finding sensitive materials that are selective towards the analyte of interest is often the main obstacle for analytical chemists, and this has

prompted a great deal of research into the development of analyte-specific coatings [47]. New coatings specific for nitroaromatics tend to include functionalities capable of forming chemical bindings (e.g. hydrogen bonding with $-OH$, $-NH_2$, $-PH_2$, $-SH$ groups), or possess structural features such as cavities for host-guest interactions. Cyclodextrin derivatives have been employed as selective coatings for QCRs, relying on host-guest interactions, with detection limits in the ppb_v range [48]. Antibodies are well known biological molecules that have a tendency to bind to specific compounds. Vali [49] has filed a Patent for an antibody-modified QCR device, for the detection of TNT and DNT. The device employs two QCRs one modified, and the other plain, to eliminate possible interferences from temperature, pressure, and humidity.

Sensors based on poly(dichlorophosphazene)-modified QCRs, responded reversibly towards nitrobenzene, with a limit of detection of 1 ppm [50]. The selectivity of polymer-coated QCRs can be modified through changes in the dielectric constant of the polymer coating. This can be achieved through variation of the attached functional groups. This was demonstrated using poly(ethyl acrylate), poly(octadecylmethacrylate), poly(dichlorophosphazene), and poly{bis(1-trimethoxysilane)propylaminophosphazene} [51]. The authors also suggested that the combination of sensors coated with the four different polymer coatings could be the basis of a sensor array, which, coupled with pattern recognition techniques, could also significantly improve selectivity.

It is sometimes not possible to find a suitable selective coating for the target analyte, due to adverse conditions or the strong responses of contaminants in the sample. Another way of achieving selectivity is to break down the target molecule into more reactive molecules. This technique was employed for the detection of nitroaromatics in landfill gas [52]. The nitroaromatics were thermally decomposed and the NO_2 fragment was detected using a Cu-phthalocyanine modified QCR. The device was successfully calibrated for nitrotoluenes and used to detect a real gas sample with a concentration of 1.82 mg m^{-3} .

1.5.2.3.2 Surface acoustic wave sensors

Surface acoustic wave (SAW) sensors are another example of mass sensors that employ the piezoelectric effect. It was Rayleigh, who in 1885, predicted that surface acoustic waves could propagate along a solid surfaces, when in contact with a medium of low density, such as air. Hence, these waves are sometimes known as Rayleigh waves [34]. SAW sensors consist of two sets of electrodes, a transmitting set, and a receiving set, deposited onto the surface of a piezoelectric solid. The electrodes are separated by what is known as the delay line, which is the area where the chemically sensitive layer is deposited. Each set of electrodes are interleaved, and by the application of an oscillating potential to the transmitter set, an oscillating piezoelectric wave is formed, which propagates from the transmitter to the receiver. Once the wave reaches the receiver electrodes, it is converted back into an electric signal. This is shown in Figure 2.

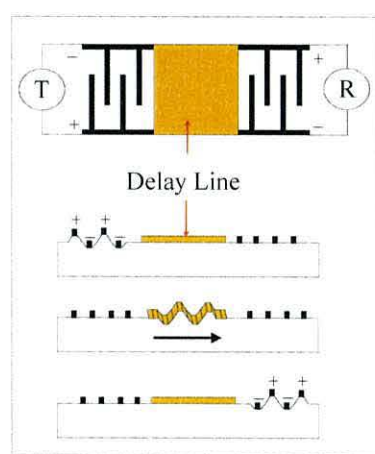


Figure 2. A simple schematic diagram of a SAW sensor, showing the propagation of a SAW between the transmitting (T) and receiving (R) electrodes.

When the target analyte is present at the surface of the delay line, the propagated piezoelectric wave interacts with the analyte causing a change in the frequency of the wave that can be detected at the receiver. It should also be noted that the delay line does not necessarily have to be made of a piezoelectric compound. This gives rise to a great number of possibilities when considering the technique for chemical sensing. An advantage of SAW sensors is their great sensitivity. The closer the electrode spacing, the

higher the frequency of the wave produced. Higher frequency waves are more sensitive to changes of mass at the surface of the chemically sensitive layer. Advances in micro-technology means that SAW sensors have great gas sensing abilities.

As with the bulk wave mass sensors, selectivity is derived from the modified layers deposited onto the delay line. These chemically sensitive layers can be the same as those used for bulk wave mass sensors, and sensitive layers of permethylated beta-cyclodextrin molecules have been shown to detect o-nitrotoluene down to levels as low as 6 ppb [53]. The choice of compound deposited onto the delay line is not a random process, and the properties of the coating can be chosen to complement those of the target analyte. These properties include, polarisability, dipolarity, hydrogen-bond acidity and basicity, and solubility [47]. Nitroaromatics demonstrate hydrogen-bond basicity, and therefore are suited to interact with hydrogen-bond acidic molecules. This theory was applied by McGill [54] who designed a series of functionalised silicone polymers for the detection of nitroaromatics. These polymers were based on siloxanes functionalised with hexafluoroisopropanol groups, and the best examples had detection limits in the ppt concentration range. ATR-FTIR was used to confirm the presence of hydrogen bonding between the polymer and the nitroaromatic analytes [55]. Similar studies have also found (aminopropyl)triethoxysilane (APTES) [56] and 3-glycidoxypyrpyltrimethoxysilane (GOPS) to be equally as suitable.

1.5.3 Summary of techniques

It has been shown that there is considerable need for the detection and characterisation of explosive compounds, ranging from safe storage and the protection of those who handle them, to the prevention of terrorist attacks. The preferred method for the detection of these explosives is largely dependent upon the particular application for which the device will be used, whether it is for airport security or the detection of landmines.

Mass spectrometry, as applied to the detection of nitro aromatics, yields low limits of detection (pg range). The main disadvantage of mass spectrometric detection is selectivity. Alone, mass spectrometry is simply not a selective technique. Attempts to

improve selectivity have generally consisted of coupling mass spectrometry to other separation techniques, such as gas chromatography. Gas chromatography is also used in conjunction with electron-capture-detection (30 pg). Optical methods offer a different approach to the detection of nitro aromatics, based on the study of fluorescence (emission) radiation of excited, laser-induced, photofragmentation products such as NO. These methods are very sensitive and selective, and limits of detection were in the range of ppb for nitro aromatics.

The real problem with the bench-top methods described above, is that they are not portable, and cannot be used for real-time *in situ* monitoring. They also require the acquisition of samples. Sample processing is generally a slow procedure, which becomes labour intensive, as the equipment is complicated and requires a skilled operator. However, gas chromatography on the micro-scale, has a potential application as a pre-separation technique, in order to increase the selectivity of smaller sensing devices.

Sensors offer the possibility of *in situ*, real-time continuous monitoring, without necessarily compromising sensitivity. Sensors, in general, have adequate limits of detection and sensitivity, but suffer due to a lack of selectivity. Sensor arrays effectively resolve this problem through pattern recognition techniques. Optic fibres can transmit light over long distances with minimal loss of intensity, making them ideal for environments where the use of electricity is hazardous, which could be of particular importance when dealing with explosive compounds. Sensors based on fluorescence measurements, as with the bench-top methods, have high signal-to-noise ratios, and low limits of detection. The excitation and emission maxima associated with the fluorophor, varies with the hydrophobicity of the surrounding environment, which is related to the concentration of organic vapours. Sensors based on this principle have the advantage of being incredibly small, giving real-time *in situ* sensitive measurements, and have reasonable limits of detection (1 ppm). Polymers have been shown to be well suited as selective films for use with optical transducers. Pentiptycene polymers offer good spectroscopic stability and high fluorescence quantum yields. They have a fast response towards nitro-aromatic compounds such as DNT and TNT, which act to quench the

fluorophor. Electrochemical sensors based on phthalocyanine polymers have been shown to have reasonable sensitivity, and limits of detection for nitrobenzene are in the region of 1 ppm. Polypyrrole has been used in an array system for organic vapours, and this array could be trained towards nitro-aromatics using neural networks. Mass sensors, based on the piezoelectric effect, possess intrinsic sensitivity. They also operate with extremely low power consumption, making them especially suitable for sensors. However, problems still arise due to their lack of selectivity, and most research with mass sensors concentrates on finding a good selective layer. Poly(dichlorophosphazene), (aminopropyl)triethoxysilane (APTES), and 3-glycidoxypyltrimethoxysilane have lead to detection limits of 1 ppm.

1.6 Aims and objectives

The intention of this research was to produce a sensitive, non-invasive sensing system to monitor levels of alkylated-nitroaromatic compounds in the headspace of a sealed vessel, in order to gain information about the behaviour of the parent materials upon aging of the capsule. Typical nitroaromatic compounds present in the capsule include TNT, DNT, NT, DNEB, DNB, and NB. The majority of these compounds will be present in the ppm_v concentration range, and therefore this set the standard for the devices sensitivity and limit of detection. The atmosphere within the capsule consisted mainly of nitrogen, but also contained low levels of oxygen, carbon dioxide, hydrogen, helium and various methyl-organics. The sensing device was required to be very small to fit within the sealed vessel.

The approach chosen for this project was to develop a series of gas-sensitive resistors that were sensitive towards nitroaromatic vapours. The gas-sensitive resistors were based on commercially available semiconducting metal oxides (chromium titanium oxide and tungsten oxide) and conducting polymers (polyaniline and poly 3-methylthiophene). The conducting polymer gas-sensitive resistors were prepared in-house by depositing a polymer layer over platinum microband electrode arrays. These polymers were also modified by inclusion of heteropolyanions to enhance their response towards nitroaromatic vapours. 2,4-DNT was chosen to represent the nitroaromatic compounds,

as it possessed both multiple nitro groups and an aliphatic side chain, both of which are present in all the nitroaromatics within the capsule. 2,4-DNT was also commercially available, did not require a storage licence, and possessed a significantly higher vapour pressure compared with TNT. A vapour generator was designed, constructed, and calibrated (by gas chromatography) to produce vapours of 2,4-DNT within the specified ppm_v concentration range. The responses of the gas sensitive resistors were monitored through changes in their resistance upon exposure to both pure nitrogen streams, and nitrogen streams containing 2,4-DNT vapours. Variations of the ambient conditions were also studied, where appropriate.

In a further study, polyaniline-based gas sensitive resistors were studied to establish the effects of the contact area and location of the working electrode, on the redox switching characteristics of the film. The films were characterised using cyclic voltammetry, chronoamperometry, and potentiometric measurements of adjacent electrodes within the array.

1.7 References

1. H. J. Yallop and S. S. Kind, *Explosion Investigation*. A Series of Monographs, ed. W. A. Harland. The Forensic Science Society and Scottish Academic Press Ltd., Harrogate, (1980).
2. P. Tooley, *Fuels, Explosives and Dyestuffs*. John Murray Ltd., London, (1971).
3. J. Akhavan, *The chemistry of explosives*. The Royal Society of Chemistry, Cambridge, (1998).
4. J. M. Mellor, S. Mittoo, R. Parkes, and R. W. Millar, *Tetrahedron*. **56** (2000) 8019-8024.
5. Sigma-Aldrich, *Material Safety Data Sheet*, <http://infonew.sigma-aldrich.com> (2003).
6. J. Frank, M. Fleischer, and H. Meixner, *Sensors and Actuators B: Chemical*. **34** (1996) 373-377.
7. J. I. Steinfeld and J. Wormhoudt, *Annual Review of Physical Chemistry*. **49** (1998) 203-232.
8. P.-G. Su, W. Ren-Jang, and N. Fang-Pei, *Talanta*. **59** (2003) 667-672.
9. B. T. Marquis and J. F. Vetelino, *Sensors and Actuators B: Chemical*. **77** (2001) 100-110.
10. C. M. Hockensmith, J. C. Goldsby, and T. Kacik, *Thermochimica Acta*. **340-341** (1999) 315-322.

11. Spectrum Laboratories, *Chemical fact sheet for 2,4-DNT*, <http://www.speclab.com> (2003).
12. K. W. Habiger, J. R. Clifford, R. B. Millar, and W. F. McCullough, *Nuclear Instruments in Physics Research*. **B56-57** (1991) 834-838.
13. T. Gozani, *Nuclear Instruments and Methods in Physical Research B*. **79** (1993) 601-604.
14. J. Wang, R. K. Bhada, J. Lu, and D. MacDonald, *Analytica Chimica Acta*. **361** (1998) 85-91.
15. K. Bratin, P. T. Kissinger, R. C. Briner, and C. S. Bruntlett, *Analytica Chimica Acta*. **130** (1981) 295-311.
16. T. A. Dickinson, J. White, J. S. Kauer, and D. R. Walt, *Nature*. **382** (1996) 697-700.
17. D. Heflinger, T. Arusi-Parpar, Y. Ron, and R. Lavi, *Optical Communications*. **204** (2002) 227-231.
18. P. Kolla, *Angew. Chemistry, International Edition*. **36** (1997) 800-811.
19. D. T. Burns and R. J. Lewis, *Analytica Chimica Acta*. **307** (1995) 89-95.
20. M. Bader, T. Goen, J. Muller, and J. Angerer, *Journal of Chromatography B*. **710** (1998) 91-99.
21. K. G. Asano, D. E. Goeringer, and S. A. McLuckey, *Analytical Chemistry*. **67** (1995) 2739-2742.
22. M. E. Sigman and C.-Y. Ma, *Analytical Chemistry*. **71** (1999) 4119-4124.
23. A. Crowson, R. W. Hiley, T. Ingham, T. McCreedy, A. J. Pilgrim, and A. Townshend, *Analytical Communications*. **34** (1997) 213-216.
24. A. Hilmi and J. H. T. Luong, *Analytical Chemistry*. **72** (2000) 4677-4682.
25. J. Wang, R. Polsky, B. Tian, and M. P. Chatrathi, *Analytical Chemistry*. **72** (2000) 5285-5289.
26. S. R. Wallenborg and C. G. Bailey, *Analytical Chemistry*. **72** (2000) 1872-1878.
27. D. T. Burns and R. J. Lewis, *Analytica Chimica Acta*. **309** (1995) 189-195.
28. G. W. Lemire, J. B. Simeonsson, and R. C. Sausa, *Analytical Chemistry*. **65** (1993) 529-533.
29. D. Wu, J. P. Singh, F. Y. Yueh, and D. L. Monts, *Applied Optics*. **35** (1996) 3998-4003.
30. J. Shu, L. Bar, and S. Rosenwaks, *Applied Optics*. **38** (1999) 4705-4710.
31. H. Riris, C. B. Carlisle, D. F. McMillen, and D. E. Cooper, *Applied Optics*. **35** (1996) 4694-4704.
32. R. W. Catrall, *Chemical sensors*. Oxford University Press, Oxford, (1997).
33. T. Gibson, O. Prosser, and J. Hulbert, *Chemistry and Industry*. (2000) 287-289.
34. J. Janata, *Principles of Chemical Sensors*. Plenum Press, New York, (1989).
35. S. M. Barnard and D. R. Walt, *Environmental Science and Technology*. **25** (1991) 1301-1304.
36. J. M. Sutter and P. C. Jurs, *Analytical Chemistry*. **69** (1997) 856-862.
37. S. R. Johnson, *Analytical Chemistry*. **69** (1997) 4641-4648.
38. T. A. Dickinson, K. L. Michael, J. S. Kauer, and D. R. Walt, *Analytical Chemistry*. **71** (1999) 2192-2198.
39. J.-S. Yang and T. M. Swager, *Journal of the American Chemical Society*. **120** (1998) 5321-5322.

40. J.-S. Yang and T. M. Swager, *Journal of the American Chemical Society*. **120** (1998) 11864-11873.
41. J. Wang, F. Lu, D. MacDonald, J. Lu, M. E. S. Ozsoz, and K. R. Rogers, *Talanta*. **46** (1998) 1405-1412.
42. M. Krausa and K. Schorb, *Journal of Electroanalytical Chemistry*. **461** (1999) 10-13.
43. J. R. Stetter, P. C. Jurs, and S. L. Rose, *Analytical Chemistry*. **58** (1986) 860-866.
44. P. D. Jeffery and P. M. Burr, *World Patent* 9,005,160 (1990).
45. D. Hodgins, *Sensors and Actuators B*. **26-27** (1995) 255-258.
46. V. Grimaldi and J.-L. Politano, *SPIE*. **2937** (1997) 90-99.
47. J. W. Grate and M. H. Abraham, *Sensors and Actuators B*. **3** (1991) 85-111.
48. X. Yang and B. Swanson, *World Patent* 9,822,795 (1996).
49. V. Vali, *European Patent* 0,453,224 A2 (1991).
50. R. Zhou, A. Menon, and F. Josse. *A Chemical Sensor with Improved Selectivity using a Modified-Electrode QCR*. in *IEEE International Frequency Control Symposium*. 1997.
51. A. Menon, M. Haimbodi, R. Zhou, and F. Josse, *Electronics Letters*. **33** (1997) 287-289.
52. T. A. P. Rocha-Santos, M. T. S. R. Gomes, A. C. Duarte, and J. A. B. Pereira Oliveira, *Talanta*. **51** (2000) 1149-1153.
53. X. Yang, X.-X. Du, J. Shi, and B. Swanson, *Talanta*. **54** (2001) 439-445.
54. R. A. McGill, T. E. Mlsna, R. Chung, V. K. Nguyen, and J. Stenowski, *Sensors and Actuators B*. **65** (2000) 5-9.
55. E. J. Houser, T. E. Mlsna, V. K. Nguyen, R. Chung, R. L. Mowery, and R. A. McGill, *Talanta*. **54** (2001) 469-485.
56. W. M. Heckl, F. M. Marassi, K. M. R. Kallury, D. C. Stone, and M. Thompson, *Analytical Chemistry*. **62** (1990) 32-37.

EXPERIMENTAL

2.1 Introduction

The techniques used during the preparation, characterisation and response measurements of the gas-sensitive resistors are discussed in this chapter. These techniques, including cyclic voltammetry, chronoamperometry and scanning electron microscopy are briefly reviewed here, but specific details are referred to in the relevant chapters. The development, construction and calibration of the vapour generator used to deliver the 2,4-DNT vapour stream to the chemiresistors is also described.

2.2 Experimental techniques and procedures

2.2.1 Solutions and materials

All reagents used during this work were of “Analar” grade purity and obtained from Sigma-Aldrich, unless otherwise stated. All aqueous solutions were prepared using ultra pure water from an ELGASTAT UHQII water purifier. All organic electrolyte solutions were prepared using acetonitrile, which had been previously dried over molecular sieve.

2.2.2 Cyclic voltammetry

Potential sweep techniques have become immensely popular tools in electrochemistry, and at the same time the mathematical descriptions of these techniques have been developed sufficiently to enable kinetic parameters to be determined for a wide variety of mechanisms [1]. Cyclic voltammetry is one of the most popular of these techniques, and this is due not only to its simplicity, but also to its great range of applications and the relatively large amount of obtainable information. Voltammetry involves the application of a potential-time waveform to an electrode where the process of interest will occur, the working electrode (WE), while the resultant current that flows in the external circuit between the working electrode and an auxiliary electrode, the counter electrode (CE), is monitored. The potential is measured relative to a stable potential that is supplied by a

reference electrode (RE). In linear sweep voltammetry the potential is swept at a constant sweep rate (v) between two limits, E_1 and E_2 , where the waveform then stops. In cyclic voltammetry, when the potential reaches limit E_2 , the waveform is reversed, and the potential is then swept to a third limit, E_3 . Limit E_3 may or may not be equal to limit E_1 (Figure 1). The sweep rate during the reverse sweep is usually equal to that of the forward sweep, but may be different in such cases as the study of coupled homogeneous reactions [1, 2].

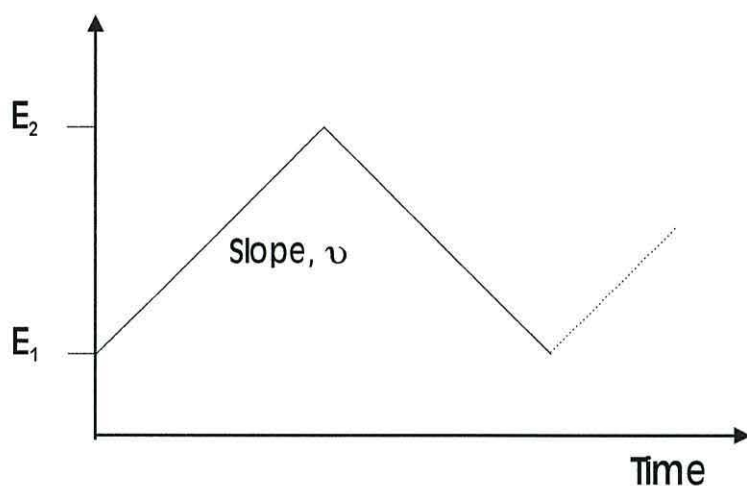


Figure 1. The potential-time profile adopted in cyclic voltammetry.

Voltammetry yields a great deal of information about the nature of the electrochemical reactions occurring in the system under observation. The overall shape of the resultant voltammogram can give rise to information concerning the reversibility of the reactions taking place through the measurement of the separation of peak potentials, ($E_{pa} - E_{pc}$), of a redox couple. The sweep rate dependence of the current maxima (I_p) can also be used to elucidate the reversibility of reaction, but it is also able to identify diffusion limiting characteristics and any coupled homogeneous reactions taking place [3]. Other mechanistic information can be determined by the use of multiple cycles. A more detailed explanation can be found in [1].

2.2.3 Chronoamperometry

Chronoamperometry involves the application of a potential step to the working electrode. The potential step (Figure 2), between two limits E_1 and E_2 , is instantaneous and the resultant current is then monitored as a function of time.

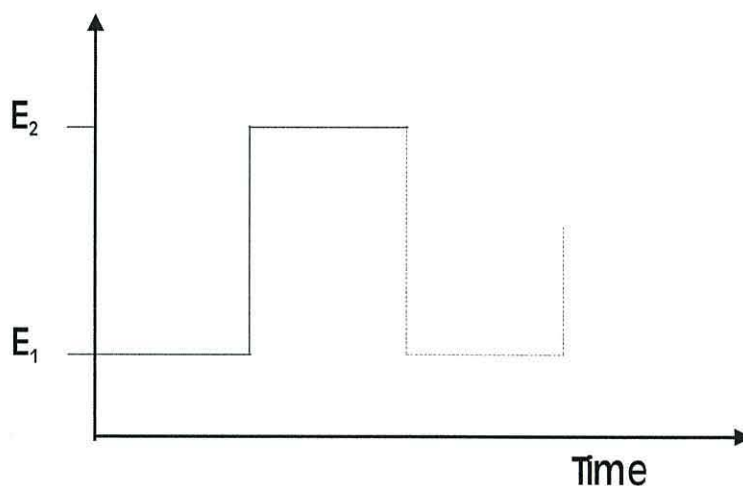


Figure 2. The potential-time profile adopted in chronoamperometry.

The duration of the potential step may be controlled and multiple steps can be employed. The magnitude of the first and subsequent potential steps may be different. As the potential step is instantaneous, from a potential where no reaction occurs to a potential where the reaction occurs, information regarding the thermodynamics of the system may not be obtained. However, information regarding the kinetics of the system can be determined, and this technique is often used to study diffusion-limited currents [2].

2.2.4 The electrochemical cell

All voltammetric and chronoamperometric experiments were performed in a glass cell designed specifically to incorporate a typical three-electrode arrangement. Figure 3 shows a typical glass cell that was used with the platinum microelectrode arrays. The cell consisted of a main compartment, which housed the working and counter electrodes. The

reference electrode was housed in a separate compartment and was kept in close contact to the working electrode through the use of a Luggin-capillary, so to avoid a potential drop caused by the resistance of the electrolyte solution [1]. The working electrodes used in the construction of the chemiresistors were platinum microband electrodes. A glassy carbon electrode, 0.7 cm^2 , was also used during the study of the heteropolyacids (HPAs). A platinum foil counter electrode ($\sim 1\text{ cm}^2$) was used with the microelectrodes, and a platinum mesh counter electrode was used with the glassy carbon (GC) electrode. A Saturated Calomel Electrode (SCE) was used as the reference electrode with the aqueous systems, while in the organic solvents an Ag/Ag^+ (0.01 M AgNO_3) reference electrode was used. The cell also incorporated a bubbler system that was filled with the electrolyte solution. This was used to degas the solutions prior to any measurement. It also prevented air from re-entering the cell, allowing the system to be held under a nitrogen atmosphere. All joints were sealed with PTFE tape.

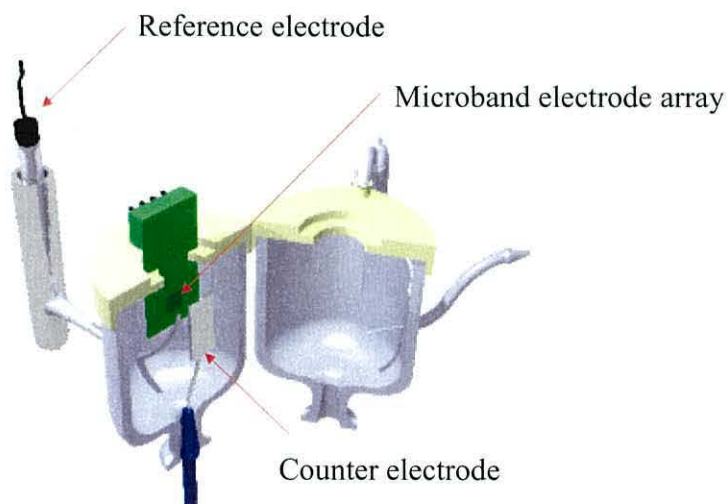


Figure 3. A schematic diagram of the cell and electrodes used for the deposition and characterisation of the conducting polymer chemiresistors.

2.2.5 Experimental preparation

Before each experiment, it was essential to ensure that the glassware and electrodes were cleaned thoroughly. The glassware was cleaned overnight in an acid bath consisting of 1:1 nitric acid/sulphuric acid, rinsed with deionised water, and then steamed for thirty

minutes to remove any traces of acid. Finally, immediately prior to use, the glassware was rinsed with the solvent to be used during the experiment.

The technique employed to clean the platinum microband electrodes involved rinsing with deionised water, followed by cycling the potential of the electrodes in dilute acid until a typical CV of platinum was obtained. Polycrystalline platinum foil and platinum mesh counter electrodes were cleaned by flame annealing in a Bunsen flame until the metal glowed red-hot. Clean glassy carbon surfaces were prepared by polishing with alumina powder (1.0, 0.3, and 0.05 μm), on a polishing cloth. Alumina traces were then removed using an ultrasonic bath for five minutes.

In order to remove oxygen and any other dissolved gaseous species, the electrolyte solutions were degassed with nitrogen for a minimum period of ten minutes prior to use, and then held under a nitrogen atmosphere.

During the initial work, cyclic voltammetry and chronoamperometric experiments were performed using a home-built potentiostat equipped with positive feedback iR compensation, and a HI-TEK PPR1 waveform generator. The resultant voltammograms were plotted using a Lloyd Instruments X-Y recorder. Later experiments, particularly those for the redox-switching chapter, were performed using an Autolab PGSTAT30, with a USB interface to a PC.

Any deviation from the experimental procedure described here will be detailed in the appropriate section.

2.2.6 Chemiresistor preparation

After the microband electrodes had been cleaned, the polymer films were prepared potentiodynamically. Polyaniline was deposited by cycling the potential of the working electrode between -0.2 V and $+0.75\text{ V}$ vs. SCE, at a sweep rate of 100 mVs^{-1} . The monomer solutions were prepared from 1 M aniline (used as purchased), in 1 M HCl. A high monomer concentration was adopted to reduce the time that the electrode arrays

were exposed to the acid. The electrode arrays degraded rapidly in acidic solutions, resulting in disconnection of the contact wires joining the electrodes to the printed circuit board (pcb). Polyaniline films doped with heteropolyacids (Pani-HPAs) were prepared from a 0.1 M monomer solution in a 0.1 M HPA acetonitrile solution. The potential limits were 0 to 1.2 V *vs.* Ag/Ag⁺ (0.01 M), at a sweep rate of 50 mVs⁻¹. Poly-3-methylthiophene films were prepared from a 0.1 M monomer solution in acetonitrile with 0.1 M tetrabutylammonium hexafluorophosphate (TBAPF₆) as the primary electrolyte, between 0 and +1.4 V *vs.* Ag/Ag⁺, at 50 mVs⁻¹. Poly-3-methylthiophene films doped with HPAs (P3MT-HPAs) were prepared from a 0.5 M monomer, 0.1 M HPA solution in acetonitrile. Potential limits were 0 to 1.4 V *vs.* Ag/Ag⁺, at 50 mVs⁻¹. The higher 3-methylthiophene monomer concentration was required for polymerisation to proceed [4, 5].

After the appropriate amount of charge had been passed, films were removed from the monomer solution and rinsed thoroughly with the appropriate solvent. The polymer films were then allowed to dry in air over 48 hours.

2.2.7 Optical microscope and SEM images

The metal oxide and conducting polymer chemiresistors were characterised by microscopy. Optical images were made with a Prior N334 optical microscope fitted with a Panasonic WVCP410/B colour CCTV camera. Prior to SEM imaging the polymer films were coated with a thin layer (~200 nm) of gold to aid conduction. The gold layer was deposited by sputtering in an E5000 sputter coater from Polaron Equipment Limited. SEM images were taken with a Hitachi S-520 SEM microscope.

2.2.8 Measurement of the chemiresistor response to organic vapours

The responses of the chemiresistors towards 2,4-DNT were measured using a vapour stream produced by the vapour generator. The column was prepared before each experiment by packing with freshly coated glass beads. Contaminants were removed from the column by flowing de-humidified N₂ through the column for a period of two

hours. Prior to measurement, the vapour generator was allowed to stabilise at the required temperature for a period of 30 minutes. Relative humidity was introduced into the vapour stream by mixing two vapour streams. The first vapour stream consisted of purified N₂ containing 2,4-DNT vapours, while the second vapour stream consisted of purified N₂ saturated with de-ionised water. The relative level of humidity was governed by the ratio of the flow rates of the two vapour streams (the sum was constant at 50 ml/min), and was confirmed *via* measurement with a hygrometer (Rotonic A1 Hygrometer®). Dilution of the vapour stream was achieved through mixing with a second purified N₂ flow.

The responses of the chemiresistor were determined by exposing the sensors to a N₂ vapour stream containing the analyte. Prior to all measurements, the sensor was inserted into the sensor port and allowed to equilibrate in air (~50 % RH) until the resistance had become stable, typically 20 minutes. The sensor was then connected to the vapour generator and the resistance monitored at 10 second intervals using a Metex® M-3800 digital voltmeter. On completion of the measurement, the sensor was removed from the vapour generator and allowed to recover in air. Recovery times varied, typically with the concentration of the analyte and length of exposure.

2.3 The vapour generator

2.3.1 Introduction

The development of gas sensors requires careful observation of the sensors response upon exposure to known concentrations of the analyte. In this particular case, the analyte in question was a vapour from a nitroaromatic compound such as 2,4-dinitrotoluene. Nitroaromatic compounds usually exist as solids or oily liquids under standard conditions, and all exhibit low vapour pressures (2,4-DNT \approx 1 mm Hg, 20°C). Therefore, the acquisition of nitroaromatic vapours, particularly those of known concentration, requires a vapour generator.

2.3.2 Vapour generators

A vapour generator is a device or system that can produce vapours from materials that would not otherwise exist in that state. Vapour generators have been used in a variety of applications ranging from deodorant spray dispensers [6] to chemical vapour deposition reactors in the coating industry [7]. In his patent titled “vapour generator”, Earnest [8] described a system for use as a heat exchanger with the Rankine cycle heat engine. However, although excellent for their purpose, these generators offer no control over the concentration of vapour stream produced, something that is of paramount importance in the research and development of sensor devices.

Many apparatus have been described for the preparation of vapour streams and vapour mixtures of known composition. Mckelvey and Hoelscher [9] claimed that extremely dilute mixtures of gases could be produced, over a wide range of concentrations, using a Diffusion Cell (Figure 4).

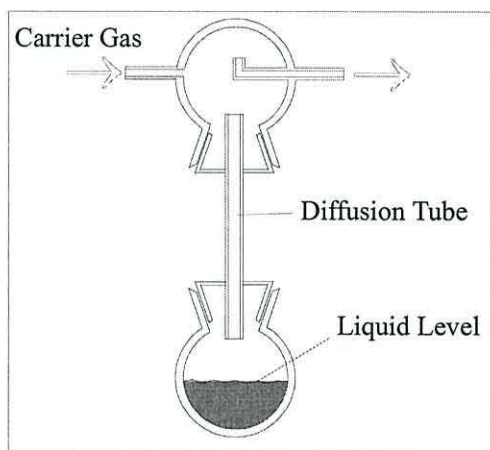


Figure 4. The Diffusion Cell developed by Mckelvey and Hoelscher [9].

The lower flask was partially filled with the reagent and the entire cell submerged into a constant temperature water bath. The space above the liquid became saturated with vapours of the reagent, which diffused through the tube into the upper flask, where they mixed with a gas stream passing through the flask. For a given cell, the diffusion rate was dependent on the total pressure and the vapour pressure of the liquid. If the total

pressure was held constant, then the diffusion rate was a function of temperature, which was subsequently governed by the temperature of the water bath. Therefore, the concentration of the vapour stream was controlled by the temperature of the bath and the flow rate of the gas stream.

Hori and Yanagisawa [10] developed a similar idea, for a multi-component organic vapour generator for the production of vapours of desired composition. Organic solvents were mixed together, at the required ratio, and held in a solvent reservoir. The mixture was then transferred *via* capillary effects to a folded glass microfibre filter known as the “evaporator” (Figure 5).

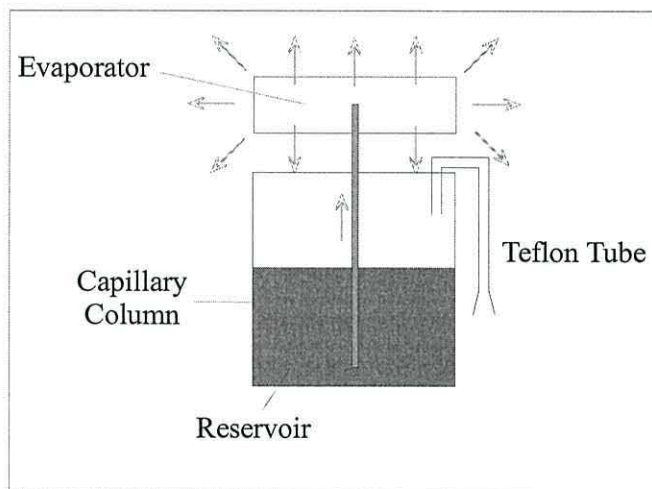


Figure 5. A schematic diagram of the vapour generator developed by Hori and Yanagisawa [10].

The composition of the mixture was unchanged during this procedure and at the evaporator surface the solvent was dispersed into the carrier gas. After an initial change in vapour composition (i.e. the more volatile component vaporises first) the composition of the vapour was found to be identical to that of the liquid. The composition remained constant for long periods because the vaporisation of the components at the evaporator surface was dependant upon the feed from the solvent reservoir, which was of a constant composition. The experimental results indicated that this system worked well for two-three component systems, and the composition of the vapour could be controlled by the

molar fraction of the liquid in the reservoir. The vapour concentration however, varied depending upon the experimental conditions. The flow rate of the gas flowing over the evaporator was found to be inversely proportional to the vapour concentration, while the temperature and evaporator surface area were found to be directly proportional. For quantitative use, the experimental conditions would need to be controlled.

Pella [11] developed a vapour generator to produce known concentrations of explosives such as 2,4,6-TNT, 2,4-DNT, and 2,6-DNT. The vapours were formed by passing an inert carrier gas through a column, held at a given temperature, where the explosive was held on an inert support. The carrier gas became saturated with vapours of the explosive as it flowed through the column, and was then diluted to the correct concentration by gas blending with another stream of carrier gas. The concentration of the vapour could then be calculated using the equation

$$C_O = (C_C F_1) / (F_1 + F_2)$$

Where C_O = concentration (ppb)

C_C = equilibrium vapour concentration

F_1 = flow rate of the vapour gas stream

F_2 = flow rate of the dilution gas

$F_1 / F_1 + F_2$ = the dilution factor.

The vapour generator could be used to produce a 0.2 ppb TNT vapour stream (at 30 °C) [11].

Drinkwine and Cage [12] further developed a vapour generator of this type in their patent titled “method for generating vapour streams” (1998). This generator (Figure 6) used a column packed with glass beads, onto which the nitroaromatic had been immobilised. A carrier gas was then flowed over the glass beads in the same manner as in Pella’s design.

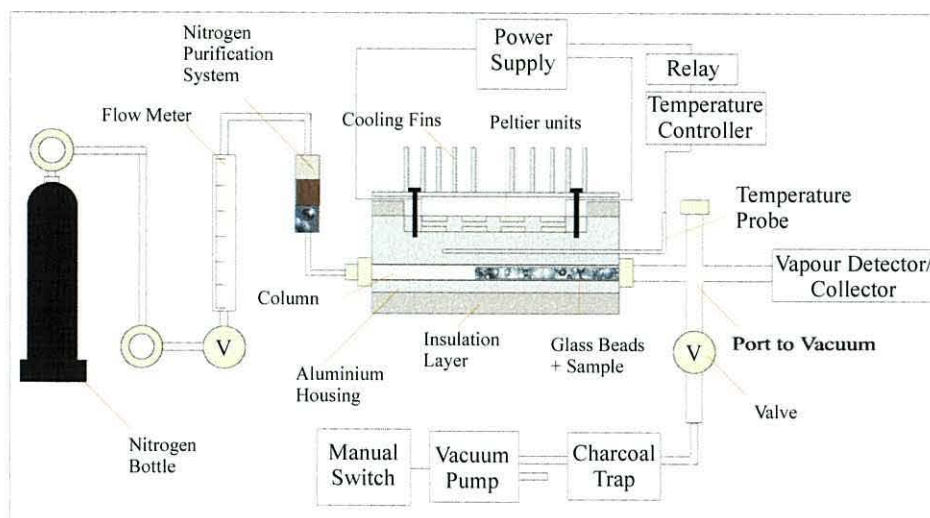


Figure 6. The vapour generator designed by Drinkwine and Cage for the production of nitroaromatic vapours [12].

The design proposed by Drinkwine and Cage possessed several advantages over that of Pella. The length of the column was significantly shorter, reducing the overall size of the generator, and an aluminium block/Peltier heat exchange unit, as opposed to Pella's water bath, was used to control the temperature. The aluminium/Peltier unit combination was found to give better temperature control (± 0.1 °C) than the water bath. The concentration of the vapour in the gas stream was found to be dependent on the flow rate of the nitrogen gas stream, and also the temperature of the glass beads within the column, and the flow rate of the carrier gas was selected (< 100 ml/min) to ensure that vapour saturation was maintained as the gas passed through the column. Saturation of the carrier gas is critical to ensure that vapour concentrations are kept constant. The vapour stream that left the column could undergo dilution by gas blending with another stream of purified carrier gas to achieve lower concentrations.

Gases have been found to permeate through various plastics. This process is highly temperature dependent, but seems to be unaffected by most other conditions, such as fluctuations of atmospheric pressure and composition. Permeation tubes can therefore, be used to dispense very small quantities of a gas at a controlled rates, if held at a constant temperature. O'Keeffe and Ortman [13] used this theory to develop a vapour

generator based on permeation tubes. The tubes predominantly consisted of fluorinated ethylene propylene resin, and the substance contained within permeated through the walls of the tube at a constant rate, which was and readily measured. The tubes were sealed at each end with steel balls 1.5 times the internal diameter of the tube. These steel balls not only gave a satisfactory seal, but also allowed the tubes to be refilled. Before calibration, the tubes were shown to possess varying permeation rates in environments of varying humidity. However, once calibrated the tubes could be used in these environments without humidity effects. Primary calibration consisted of collecting weight data (loses) over a period of days, weeks, or months. Secondary calibration was achieved by enriching an accurately metered stream of air with the permeated gas, and monitoring the resultant gas stream with a sensitive detector such as a flame ionisation analyser. The permeation tubes suffered from disadvantages such as blisters when used with certain compounds. Blisters were caused by nitrogen oxides on the outer surface, penetrating to a few microns depth. The blisters could not be explained by the author, but were observed to affect the permeation rate. Fluorinated compounds caused another problem. The fluorinated ethylene propylene resin swelled noticeably when filled with these compounds and the tube softened. After two to three hours the tubes ruptured, placing a question mark over their suitability for use with or around these compounds. However, the permeation tube approach to vapour generation was found to be most successful for other hydrocarbons, and hence was adopted by Kin-Tek, who have designed a range of products for laboratory calibration of detectors and analysers. The highly temperature dependent permeation rate is controlled by a permeation oven. The permeation tube within the oven emits a small precisely known flow of the compound it contains into the carrier gas flowing through the oven (Figure 7). The output from the oven can then be selectively added to a controlled flow of dilution gas, before it is ready for use (Figure 8). Using this method, concentrations of low ppb to over 1000 ppm can be prepared directly from the pure compounds.

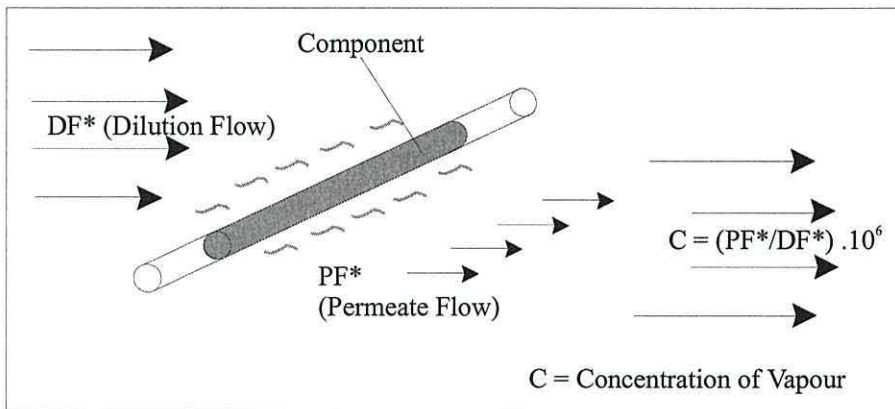


Figure 7. The permeation tube used by Kin-Tek for vapour generation.

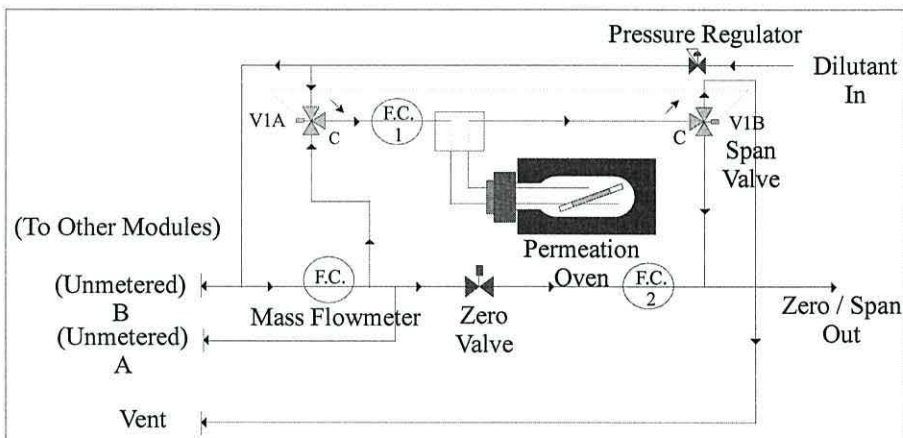


Figure 8. The vapour generator produced by Kin-Tek, employing the Permeation Tube.

The concentration of the vapour can be calculated from the equation

$$C = PF / DF \times 10^6,$$

where C is the concentration of the vapour (ppm), PF is the component emission at a temperature (T) from the permeation tube, and DF is the dilution gas flow.

This system can also be used in order to blend mixtures of gases. Up to six permeation tubes can be used in a single oven to give a mixture of gases entering the carrier or dilution gas flow, and by using a calibration bench, up to thirty ovens can be used at any

one time. Additional features also allow environmental factors such as humidity to be controlled through a gas standard humidification module.

The main disadvantage of the Kin-Tek system is its cost. The basic module costs around £8000, with additional costs for the humidification and expansion modules. The calibration bench costs around £30,000.

Meininghaus, Schauenburg, and Knoppel [14] developed a reliable and flexible generation system for VOCs for indoor air research. The generator was based on a modified droplet ejector working on the principle of a piezoceramic ink-jet printer (Figure 9).

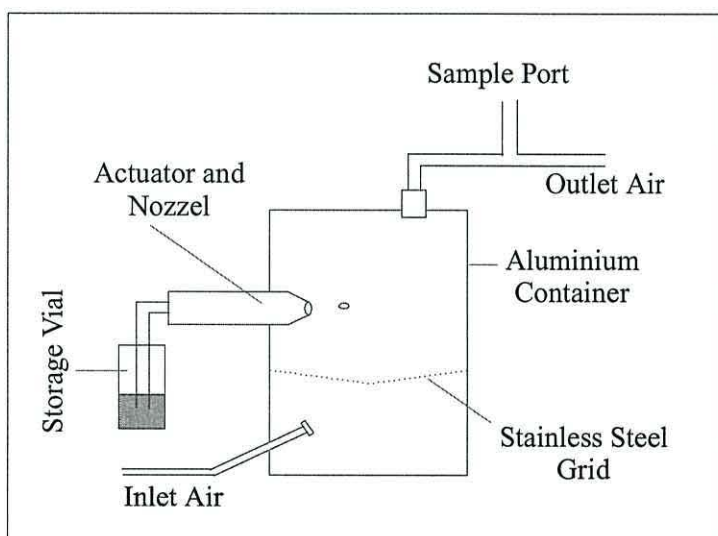


Figure 9. A schematic diagram of the VOC generation system developed by Meininhaus, Schauenburg, and Knoppel [14].

Pre-filtered liquid was transferred from a vial to an actuator/nozzle system through a Teflon capillary. The piezoceramic actuator produced acoustic waves in the capillary system, which caused a droplet to be formed (70 pl) at the nozzle (50 μm diameter). The droplets were then ejected into a container where they fell towards a stainless steel grid, upon which they were broken up into smaller droplets. The container was flushed with a

gas (flow rate = 300 ml/min.) and the smaller droplets were easily evaporated. In order to keep the composition of the vapour constant, environmental parameters such as temperature and humidity were kept constant. This system proved to be successful for creating atmospheres in both small (research type) and large (walk-in type) test chambers, but calibration for each mixture was required for quantitative analysis.

2.3.2.1 Summary of the vapour generation techniques

The examples described above are all capable of generating organic vapours of known concentrations and/or composition. Therefore, the exact requirements of the vapour generation system were required in order to determine which method was the most suitable. The vapour generator was required to give a constant flow of the appropriate nitroaromatic vapour in an inert carrier gas such as nitrogen, at a given constant concentration (ppm) that may be varied at intervals during the experiment. Before and after each experiment it was necessary for the gas stream to be “switched on” and “switched off” so that the sensors could be exchanged. The vapour generator was also required to produce at least two nitroaromatic vapours, which could be mixed before the gas stream reached the sensor, to represent a simple mixture, with some control over the humidity of the vapour stream.

Several of the techniques above will satisfy these requirements. Therefore, the performance of each should be evaluated by examining their respective advantages and disadvantages. The diffusion cell described by McKelvey and Hoelscher [9] was the most basic of the vapour generators described. The cell allowed the generation of vapours from liquids. Not all of the nitroaromatic compounds are liquids and therefore, would have needed to be dissolved in a solvent. This would have resulted in a vapour stream containing a large fraction of the solvent, which would not have been appropriate for this application. The cell would also not allow the humidity of the vapour stream to be controlled, and temperature control would have been *via* a water bath, which would not have allowed control to the required precision. The system developed by Hori and Yanagisawa [10] suffered from similar disadvantages.

Meininghaus, Schauenburg, and Knoppel's vapour generator for indoor air research [14] is a generator for creating artificial atmospheres to study the interaction of vapours with material surfaces, as opposed to a vapour stream for calibration purposes. The system works on the basis of emitting VOC droplets in pulses to create a vapour within a sealed test chamber. This would have had the effect of prohibiting the exchange of sensors, without upsetting the atmosphere. The system also requires the analyte to be in the liquid phase so that droplets could be formed, and there is no humidity control. However, it would allow the possibility of having multiple sensors running simultaneously.

The vapour generation methods based on Permeation Tubes had several advantages and disadvantages. Permeation Tubes were able to deliver a quantitative flow of the compound in question into a stream of carrier gas with great accuracy. The concentration of the vapour stream was easily controlled by modulation of the flow rate and oven temperature, and levels as low as ppb were attainable. However, pre-calibration of the Permeation Tubes in the factory was essential. This could have proved to be time consuming if several nitroaromatics were to be used with the system. Permeation Tubes are also known to suffer disadvantages such as blisters and ruptures [13], which again could have led to inaccurate permeation rates, particularly in the presence of nitro groups. But, the main disadvantage of the permeation method was cost, especially when looking at vapour mixtures with humidity control.

The vapour generator described by Pella [11] used a column, containing the immobilised compound, through which a carrier gas flowed and became saturated with the vapour. This method had the advantage over the permeation tube method, in that the flow of carrier gas travelled through the column, which was directly heated, as opposed to the Kin-Tek system, where the carrier gas flowed over the Permeation Tube within an oven. Pella's generator used a coiled column and the temperature was controlled by a water bath. This is not as accurate as the temperature control system adopted by Drinkwine and Cage [12], who used a straight column encased within an aluminium housing with Peltier heat exchange units maintaining the temperature. The system described by Drinkwine and Cage had many advantages. The gas stream was purified and each column could be

freshly prepared eliminating any contamination effects. There was the option to dilute the vapour stream and a port connected to the vacuum could be used to divert the gas flow away from the sensor port, allowing the simple exchange of sensors. The system also described a gas purification system, which ensured that there was no contamination from the carrier gas in the final vapour stream, although this could also have been applied to other methods. Multiple vapour mixtures could have been achieved by using several of these units together, separated by a layer of insulation. Mixing the vapour stream with a humidified carrier gas could have controlled the humidity of the system. The system could also have been constructed at a price far below that of the permeation method.

2.3.3 The vapour generator - principle and design

The information above suggested that a suitable design for the vapour generation of nitroaromatic compounds would be similar in principle to that described by Drinkwine and Cage [12]. The vapour generator that was to be constructed had to satisfy the following conditions: -

- Deliver a purified carrier gas stream to the column
- Control, and allow adjustment of the carrier gas flow rate
- Control the temperature of the column precisely (to within 0.1 °C)
- Allow the exchange of columns easily
- Allow the vapour and the gas stream to interact so that the gas stream can become saturated with the vapour
- Generate a vapour of a nitroaromatic compound of specified concentration and supply the vapour stream to a sensor
- Generate two vapours of nitroaromatic compounds and blend the vapour streams together
- Allow variation of the vapour concentration without exchanging the column
- Control the humidity of the final mixture
- Divert the gas stream away from the sensor port in order to exchange the sensor
- Allow the sensors to be exchanged easily without affecting the column

A schematic diagram of the vapour generator designed for this project, and a photograph of the actual vapour generator built can be seen in Figure 10 and Figure 11, respectively.

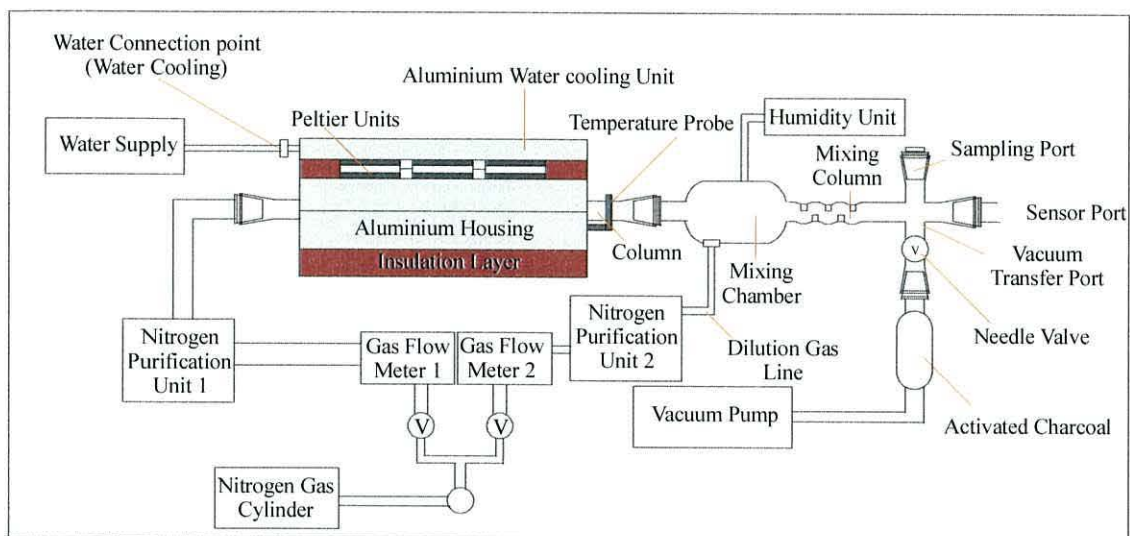


Figure 10. A schematic diagram showing the design of the nitroaromatic vapour generator.

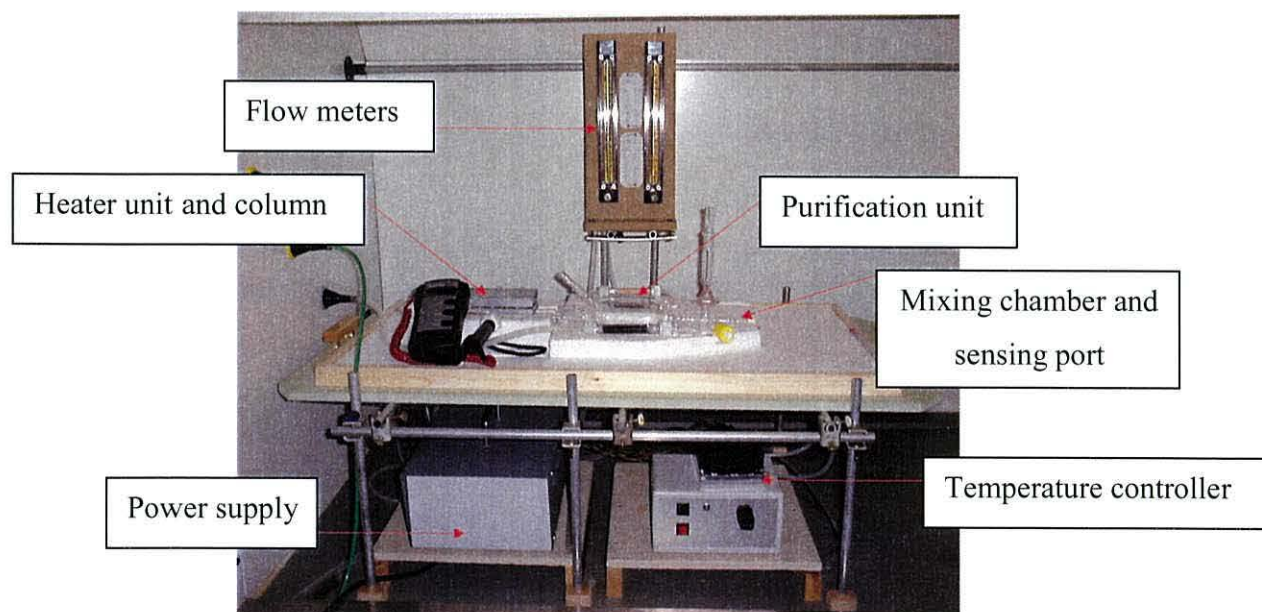


Figure 11. A photograph of the vapour generator built for the generation of nitroaromatic vapours.

The vapour generator was similar in principle to that described by Drinkwine and Cage [12], and consisted of two glass columns lying side-by-side, packed with glass beads onto which the nitroaromatic compound to be vaporised had been immobilized. The columns were encased in an aluminium housing, which maintained a constant temperature. A carrier gas, having been previously purified by a purification unit, passed through the column(s) becoming saturated with vapours of the nitroaromatic compound and a vapour stream was formed of known concentration/composition. The vapour stream was then mixed or diluted (if necessary) in a mixing chamber, before reaching the sensor port.

2.3.3.1 The packed column

The column was constructed from thin walled, silanized glass tubing (internal diameter = 6 mm, external diameter = 8 mm). The walls of the tube were thin (1 mm), so as to increase thermal conduction. The column was packed with glass beads (diameter = 425-600 μm). The surface area of the beads was high to allow a large surface area of the immobilised compound, which in turn allowed a greater percentage of the compound to exist in the vapour phase at equilibrium. This also helped to reduce the error associated with small variations in surface area between different columns. The glass beads were held in the column by silanised glass wool plugs at either end. The nitroaromatic compound was immobilised onto the glass beads by mixing the beads with a “slurry” of the nitroaromatic and dichloromethane, and removing the solvent by evaporation. Approximately, 10 % (by weight) of 2,4-DNT was found to be suitable for immobilization onto the glass beads. 0.5 g of 2,4-dinitrotoluene was dissolved into 20 ml of DCM. 4.5 g of glass beads were then mixed into the mixture until thoroughly coated. The resultant “slurry” was then placed into the oven and heated to 40 °C until nearly all the solvent had been removed. The slurry was then mixed to ensure that the 2,4-DNT was coated onto the glass beads until the coated beads were completely dry. The beads were allowed to cool to room temperature, before 5.0 g of the 2,4-DNT coated glass beads were introduced into the silanized glass column, held between two silanized glass wool plugs.

2.3.3.2 The aluminium housing and heater unit

The column was held within an aluminium housing designed to maintain a constant temperature. The aluminium housing ($150 \times 70 \times 30$ mm) was constructed in two halves, held together by a set of three nylon bolts (Figure 12). The aluminium housing was also encased within a layer of insulation (polystyrene) to limit heat transfer to or from the surroundings.

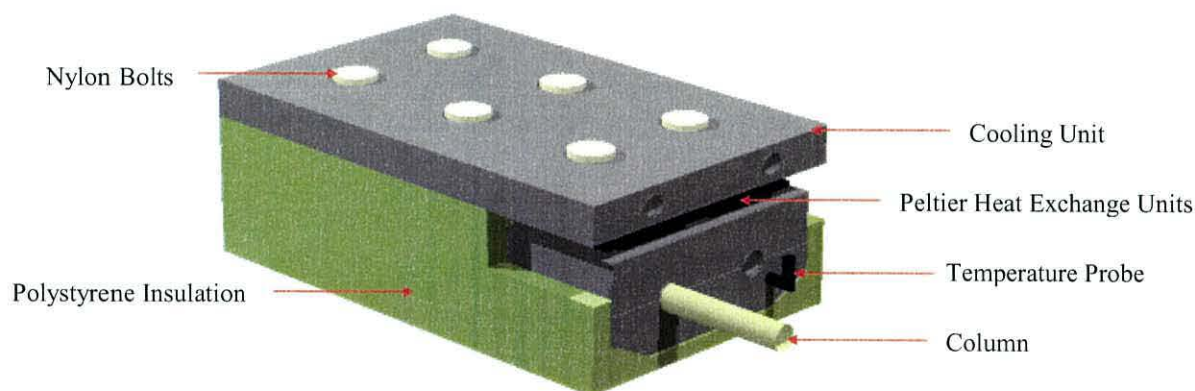


Figure 12. A diagram of the central section of the vapour generator.

The constant temperature within the aluminium housing was governed by a set of three thermoelectric units (39 W SealTEC™ Peltier Effect heat pumps, 30 mm \times 34 mm), which transferred heat to or from the aluminium housing upon the application of a current. A constant current was applied to the units by a 24 V power supply, and the whole system was controlled using an MPT-5000 temperature controller. The temperature controller operated in accordance with a temperature probe (platinum resistance thermometer), which was fixed inside the aluminium housing. The temperature probe acted to relay information from the aluminium housing to the temperature controller, which in turn controlled the activity of the Peltier units. This set-up controlled the temperature of the aluminium housing to ± 0.1 °C. This degree of accuracy was required as the vapour pressure (and hence the vapour concentration) is directly proportional to the temperature of the environment in which the compound is situated. The heat transferred from the Peltier units was removed from the system to a

cooling unit ($150 \times 70 \times 10$ mm). The cooling unit (Figure 13) consisted of an aluminium casing containing a series of channels through which a constant stream of water flowed. Heat was transferred to or from the Peltier units through the thin aluminium case (1 – 2 mm) of the cooling unit to the water, which in turn was constantly replaced with fresh water.

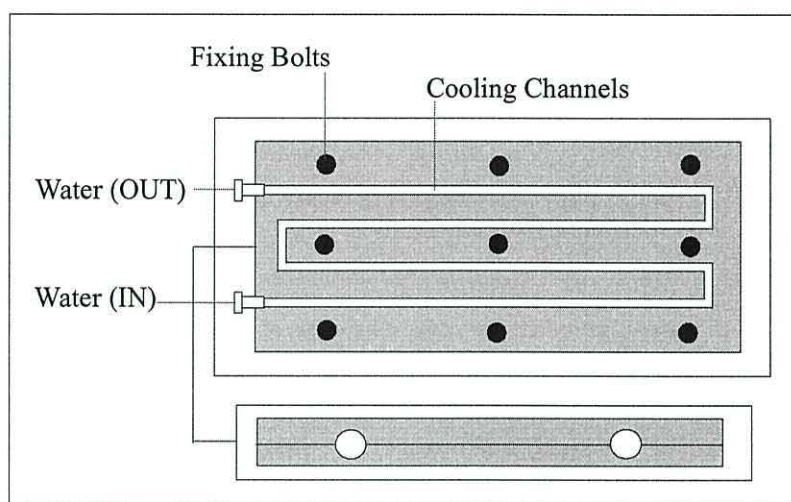


Figure 13. The water-cooling unit (heat sink).

2.3.3.3 The carrier gas and purification units

The carrier gas used in this study was nitrogen. The flow of nitrogen through the system was controlled using a pressure regulator and a flowmeter. The pressure was regulated to 20 psi and the flow rate was measured and controlled using a Supelco 5 - 250 ml/min Rotameter with needle valve. An important factor to be considered for the generation of equilibrium vapour streams of known concentration, is that the nitrogen flow rate through the column must be at a sufficiently low level to permit saturation of the carrier gas with vapours of the compound of interest. Pella [11] found that the vapour concentration was independent for flow rates between 10 and 100 ml/min for 2,4-DNT, and therefore the flow rate was held at 50 ml/min during this study.

It was essential to ensure that the carrier gas was perfectly free from all contamination. Therefore, a purification unit was included, which was situated between the flow meter and the column. A diagram of the purification unit can be seen in Figure 14. The unit consisted of three cells (250 mm × 15 mm), each containing an adsorbent. Each cell had a screw lid to enable it to be re-filled easily. The silica gel cell (silica gel blue, 2 mm) was primarily used to remove water vapour from the gas stream. Activated charcoal (granular) and molecular sieve (UOP Type 4A) were included to remove hydrocarbon contaminants and other gases such as carbon monoxide and water vapour.

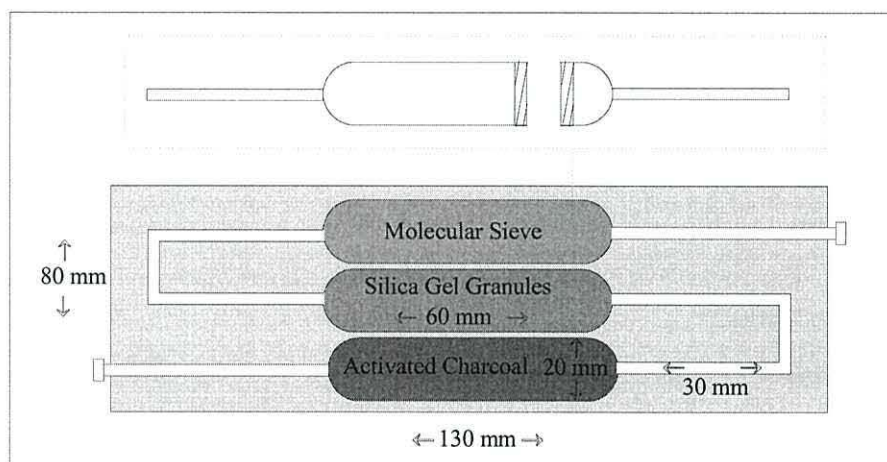


Figure 14. The purification unit.

2.3.3.4 The mixing chamber and sensor ports

As the carrier gas passed through the column, it became saturated with vapours of the nitroaromatic. On exiting the column the carrier gas could be diluted in order to vary the concentration of the vapour stream during experiments or achieve the correct concentration if a dilute vapour stream was required. Dilution could be achieved *via* a dilution line, which supplied a second stream of carrier gas (also purified and of known flow rate) to a mixing chamber. The vapour streams of one or both columns entered the mixing chamber and could be mixed together with the dilution stream (Figure 15). The diluted vapour concentration could then be calculated *via* the following equation.

Diluted Vapour Concentration = Equilibrium Vapour Concentration \times Dilution Factor

Where, Dilution Factor = $F_1 / (F_1 + F_2)$,

F_1 = the gas flow rate (of the vapour + carrier gas) to the mixing chamber

F_2 = the gas flow rate (of the diluting gas) to the mixing chamber

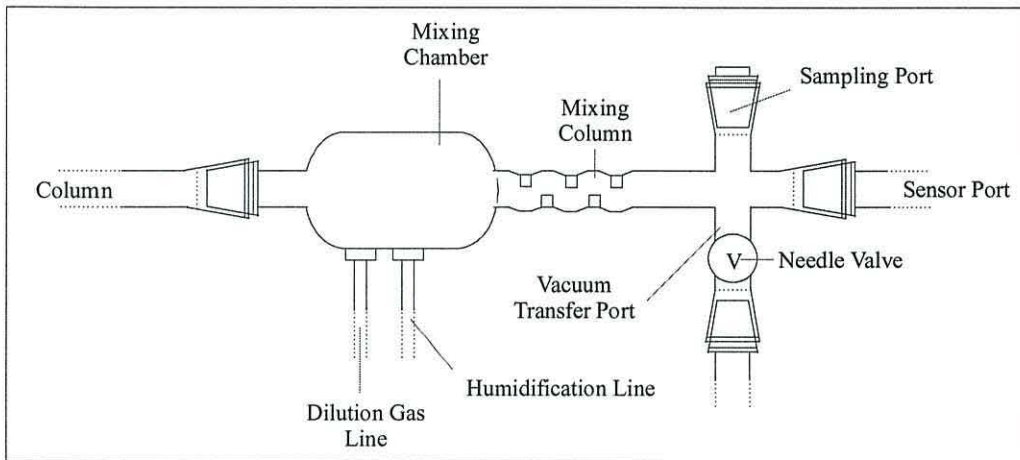


Figure 15. The mixing chamber and ports.

Humidity was controlled through a separate unit consisting of a Dreschel bottle filled with deionised water. The secondary flow of nitrogen became saturated with water as it passed through the Dreschel bottle and the humidity of the final vapour stream was controlled by varying the ratio of carrier gas streams. The humidity of the final vapour stream was tested before the experiment using a hygrometer (Rotronic A1 Hygrometer). The final vapour stream travelled through a section of dimpled pipe, which caused turbulence in the gas stream to ensure thorough mixing before the gas stream reached the sensor port. The entire mixing apparatus had a layer of insulation surrounding it in order to reduce heat loss from the vapour stream that could cause the vapour to condense. A vacuum and a sampling port were included in the apparatus, situated before the sensor port. The vacuum port allowed the vapour stream to be transferred away from the sensor port. This allowed adjustment or exchange of the sensors if required. The vacuum was controlled by a Young tap positioned inline, to ensure that the vapour stream could be diverted from the sensor without upsetting the column. The vapour stream passed

through the vacuum port and through an activated charcoal trap before the gas was released. The activated charcoal trap was included to remove any nitroaromatic vapours from the nitrogen stream, as these vapours are known to be hazardous to health. The sampling port allowed samples of the gas stream to be collected, in order to test the composition of the final vapour stream by GC, as well as allowing the humidity to be tested.

The sensor ports were individually tailored to fit the different types of sensor used. The ports were designed to connect to the generator at a universal junction, which allowed the easy exchange of the sensors.

2.3.3.5 The silanization process

All of the glassware used in the vapour generator was silanized by treatment with dimethyl-dichlorosilane. This helped to reduce adsorption of the nitroaromatic compound onto the walls of the glass tubing. It was essential, when silanizing the glassware, that the surface of the glassware to be treated was completely free of contamination as the silane compound did not adhere to dirty surfaces. Therefore, all the glassware was cleaned using a three-stage process. The first stage involved leaving the glassware submerged in a mixture (50/50) of concentrated nitric/sulphuric acids for a period of six hours. The glassware was removed from the acid bath and rinsed with deionised water before being moved to a steam bath for 30 minutes. Finally the glassware was rinsed with toluene. The clean glassware was submerged in the dimethyl dichlorosilane solution for a period of 60 minutes. The treated glassware was then removed, thoroughly rinsed with toluene, and dried in an oven at 110 °C.

2.3.4 Experimental

2.3.4.1 The heater unit

The heater unit was able to control the temperature of the column in order to generate a known vapour pressure of the nitroaromatic compound. The temperature of the

aluminium housing was controlled by the MPT-5000 temperature control unit *via* a ten-turn dial with a scale of 0-1000. Before the counter was calibrated to the temperature of the aluminium housing, the time to equilibrium, the temperature at max/min limits, and the precision of the temperature controller was ascertained.

2.3.4.2 Time to equilibrium

To determine the time required for the heater unit to reach a steady-state temperature, having been set to a given counter value, the heater was first allowed to stabilise (attain constant temperature) at a counter value of 0. The counter value was then changed to a value of 500, and the temperature of the heater unit was monitored over a period of 60 minutes. This procedure was repeated for changes in the counter value from 500 to 550 and then 550 to 560, while the temperature of the heater unit monitored for 12 minutes.

2.3.4.3 Temperature of the maximum/minimum limits

The temperature of the aluminium housing was recorded at the maximum and minimum limits of the counter, having stabilized over the predetermined stabilization period.

2.3.4.4 Precision tests

The precision with which a temperature could be obtained by setting the counter to a predetermined value was measured using the following method. The counter was set to a specific value and the temperature allowed to stabilize. The temperature was then recorded and the counter value changed to a different value. After a further stabilization period, the counter value was returned to the original value, allowed to stabilize again, and the temperature was re-recorded. This process was repeated until five values had been obtained. The counter values 250, 500, 750, and 900 were chosen for this test.

2.3.4.5 Calibration of the heater unit

The temperature of the aluminium housing was measured for the counter values 0, 100, 200, 300, 400, 500, 600, 700, 800, 900, and 1000. The counter value was set to the

required value and the temperature of the aluminium housing was allowed to stabilize, before the measurement was recorded. The calibration was repeated to ensure the results were consistent.

2.3.4.6 Calibration of the vapour generator

The vapour generator was able to produce a nitroaromatic vapour stream of known concentration, by controlling the temperature of the column and the flow rate of the nitrogen passing through the column. The vapour generator had to be calibrated so that the temperature of the column could be related to the resultant equilibrium vapour concentration in the final gas stream. The vapour generator could then be set up before an experiment, so that a vapour stream containing a predetermined amount of the nitroaromatic could be produced.

2.3.4.7 Vapour traps

The vapour generator was set up to include a vapour trap. The vapour trap was positioned between the column and the exit for the vapour stream, and had the purpose of adsorbing any nitroaromatic present in the stream. The trap was constructed from a transfer pipette, which contained 1.5 g of activated charcoal held between two silanized glass wool plugs (see Figure 16).

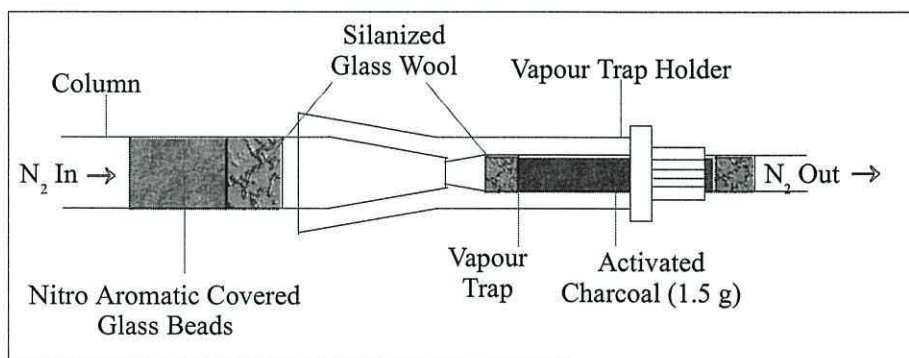


Figure 16. A vapour trap used in the calibration of the vapour generator.

The vapour stream was allowed to flow through the trap for a period of three hours. During this period any nitroaromatic present in the vapour stream became immobilised onto the activated charcoal *via* absorption. The nitroaromatics were then eluted from the charcoal by washing the charcoal with 10 ml of DCM for analysis by GC.

2.3.4.8 Standard solutions

A series of standard solutions were prepared by the dilution of a stock solution containing 1000 ppm of 2,4-DNT. The stock solution was prepared by dissolving 0.731 g of 2,4-DNT into 100 ml of DCM. The standards were prepared by the dilutions shown in Table 1.

2.3.4.9 Gas chromatography

The dinitrotoluene eluted from the vapour traps was analysed by GC, and the concentration of sample determined by comparison of the peak area of the sample with a calibration curve constructed from the peak areas obtained from the standard solutions (Table 1).

Required concentration (ppm _v 2,4-DNT)	Quantity of 2,4-DNT	Final volume (Solvent = DCM)
1000	0.731 g 2,4-DNT	100 ml
500	50 ml of 1000 ppm sol.	100 ml
100	10 ml of 1000 ppm sol.	100 ml
50	25 ml of 500 ppm sol.	50 ml
25	12.5 ml of 50 ppm sol.	25 ml
10	2.5 ml of 100 ppm sol.	25 ml
5	2.5 ml of 50 ppm sol.	25 ml
1	2.5 ml of 10 ppm sol.	25 ml
0.1	2.5 ml of 1 ppm sol.	25 ml

Table 1. The dilution factors for the preparation of the standard solutions for the calibration of the vapour generator.

The GC was set up to run isothermally at 175 °C. The sample was injected directly into the column. The injector temperature was set to 250 °C, as was the temperature of the flame ionisation detector. The mobile phase used was N₂, and the stationary phase was Stabilwax[®]. 2,4-DNT required a time of 3.4 - 3.6 minutes to pass through the column, and as 2,4-DNT was the only component present in the sample a run time of 5 minutes was used.

2.3.5 Results and discussion

2.3.5.1 Time to equilibrium

To show how the temperature of the aluminium heater unit varied with time having been set at a given counter value, the counter value was set at 500, 550, and 560, respectively, and the temperature of the heater unit observed. For the counter setting of 500 (Figure 17), the graph shows that the temperature of the housing increased rapidly to 50 °C and then relaxed back to a constant value of 48.8 °C.

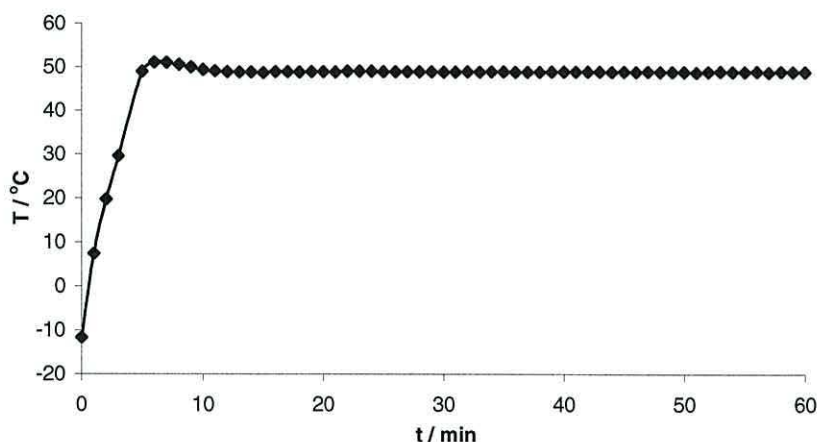


Figure 17. The response of the aluminium heater unit to a 0 - 500 counter unit change.

As the temperature stabilized, there was a slight variation in temperature over a period of 25 minutes, after which the temperature became stable with a maximum deviation of ± 0.2 °C. When the counter setting was changed from 500 to 550 (Figure 18), the

temperature increased at a slower rate, stabilizing after just 8 minutes, with a temperature deviation of ± 0.2 °C from this point.

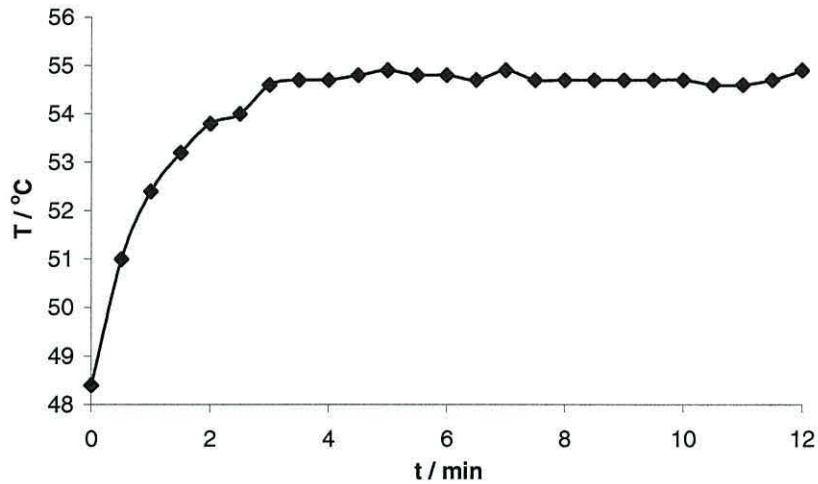


Figure 18. The response of the aluminium heater unit to a 500 - 550 counter unit change.

The small increase from 550 to 560 (Figure 19) showed once more a steady increase of temperature, which stabilized after 5 minutes with a temperature deviation of ± 0.2 °C.

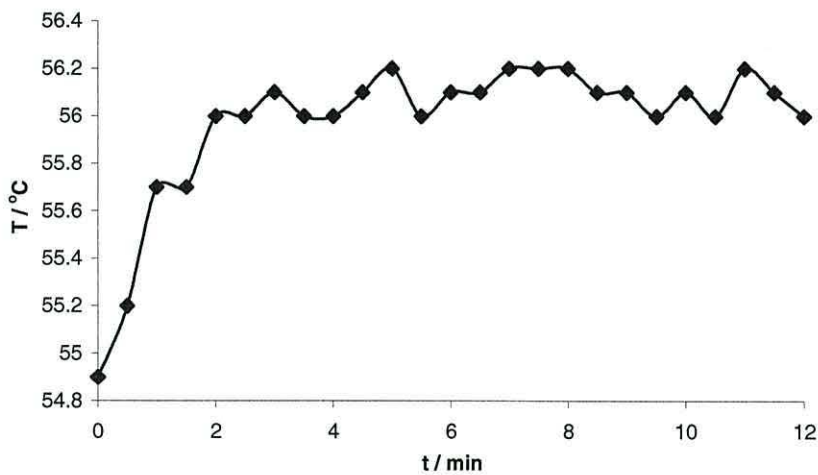


Figure 19. The response of the aluminium heater unit to a 550 - 560 counter unit change.

Therefore, the stabilization period appeared to be dependant upon the magnitude of the temperature change. For the purpose of this work a stabilization period of 30 minutes was chosen to ensure that the temperature and hence the resultant vapour pressure would be stable. The maximum deviation of the temperature, ± 0.2 °C, is ideal for the purpose of this work to ensure consistent results.

2.3.5.2 Temperature of the maximum/minimum limits

The temperature of the aluminium housing, was recorded after a 30-minute stabilization period for the maximum and minimum counter values 0 and 1000, respectively. These results (Table 2) give the range of temperature that the column was able to work within and an approximate idea of the range of vapour pressures that could be produced for the compounds of interest. This information was important for setting the gain of the temperature controller so that the correct range of vapour pressures can be achieved.

Counter value	Temperature (°C)
0	-10.5
1000	+115.5

Table 2. Max/Min temperatures attainable by the heater unit.

The results show that the working temperature range was between the temperatures -10 and $+115$ °C. This was a good working range that was expected to give an approximate range of concentrations between 0.01 and 100 ppm_v 2,4-DNT.

2.3.5.3 Precision tests

The precision of the heater unit can be seen in the tables (3-6) below.

Reading	Temperature (°C)
1	19.1
2	18.9
3	19.0
4	19.0
5	19.1
Average	19.0 ± 0.1

Table 3. The precision test results for a counter value of 250.

Reading	Temperature (°C)
1	48.5
2	48.4
3	48.5
4	48.5
5	48.6
Average	48.5 ± 0.1

Table 4. The precision test results for a counter value of 500.

Reading	Temperature (°C)
1	79.1
2	78.8
3	78.7
4	79.0
5	78.7
Average	78.9 ± 0.2

Table 5. The precision test results for a counter value of 750.

Reading	Temperature (°C)
1	97.5
2	97.3
3	97.2
4	97.5
5	97.3
Average	97.4 ± 0.2

Table 6. The precision test results for a counter value of 900.

The results show that the temperature of the aluminium housing can be controlled very precisely, with a maximum associated error of ± 0.2 °C for the 750 and 900 tests. This error translates to a 0.2% error, which shows that the vapour generator would give a very reproducible temperature, and hence vapour pressure, when set at a specific counter value. This in turn, would help to produce a precisely controlled concentration of vapour in the final vapour stream.

2.3.5.4 Calibration of the heater unit

The tests above suggested that the vapour generator would be able to maintain a given temperature, with precision and stability, over a period of 60 minutes. It was estimated that the vapours of 2,4-DNT would be within the correct concentration range, and therefore the vapour generator was considered ready for calibration. The calibration results (Figure 20) show that the calibration data collected for the aluminium heater unit was linear with an associated error of just 0.0004%. From this graph the equation for the line of best fit was obtained, and was used to calculate a table (Table 7) of temperatures for each counter value. This enabled the required temperature to be translated to a counter value.

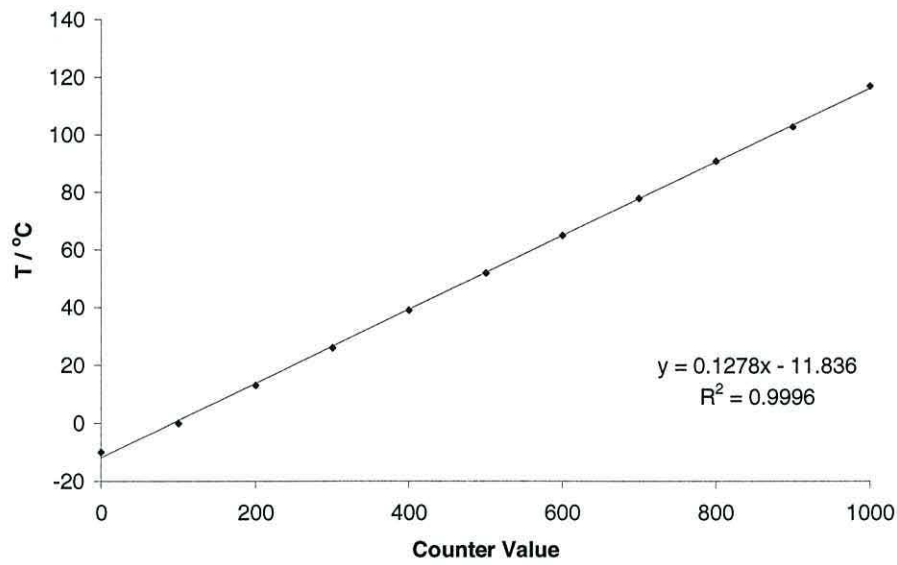


Figure 20. A graph to show the calibration curve obtained for the heater unit.

Counter Reading	Temperature (°C)
0	-9.9
100	0.0
200	13.1
300	26.0
400	39.0
500	51.9
600	64.9
700	77.8
800	90.7
900	102.6
1000	116.8

Table 7. Calibration results for the heater unit.

2.3.5.5 Standard solutions

In order to calibrate the vapour generator, a calibration curve constructed from a series of standard solutions was required. The standard solutions were analysed by gas chromatography and the resultant peak areas (average) are shown in Figure 21. The Calibration curve displays good precision, with a R^2 value of 0.999. The curve was then used to determine the concentration of the samples taken from the vapour generator.

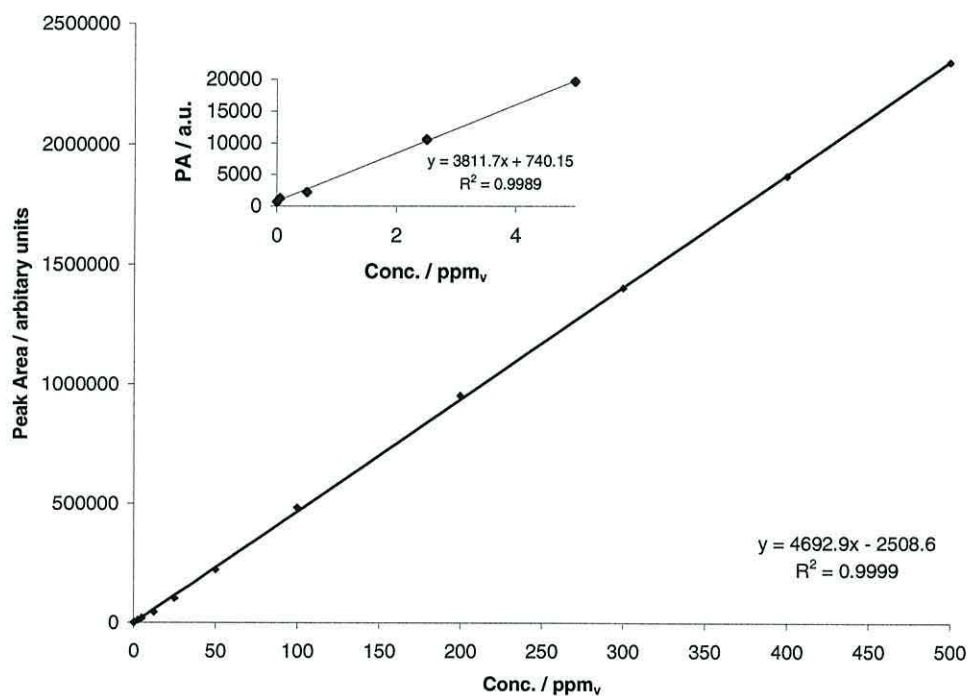


Figure 21. The calibration curve obtained from a series of 2,4-DNT standard solutions.

2.3.5.6 Calibration of the vapour generator

Vapours of 2,4-DNT were collected on the vapour traps and eluted into 10 ml of DCM, ready for analysis by GC. In order to obtain sufficient 2,4-DNT to be analysed by GC, the samples were collected over three-hour periods. Samples were collected at different operating temperatures, -10, 20, 52, 84, and 117 °C. The average peak areas were calculated by taking the mean peak area of three samples, and are recorded in Table 8,

below. The concentration was then calculated from the equation for “the line of best fit” from the calibration curve of the standard solutions.

Counter Reading	Operation Temperature (°C)	Average Peak Area (pA)	Corresponding Concentration (ppm _v)
0	-10	1038	0.47
250	20	1557	0.60
500	52	2206	0.77
750	84	3697	1.16
1000	117	9844	2.78

Table 8. The calibration data obtained from the vapour generator.

The data for the calibration of the vapour generator is plotted as shown in Figure 22, below.

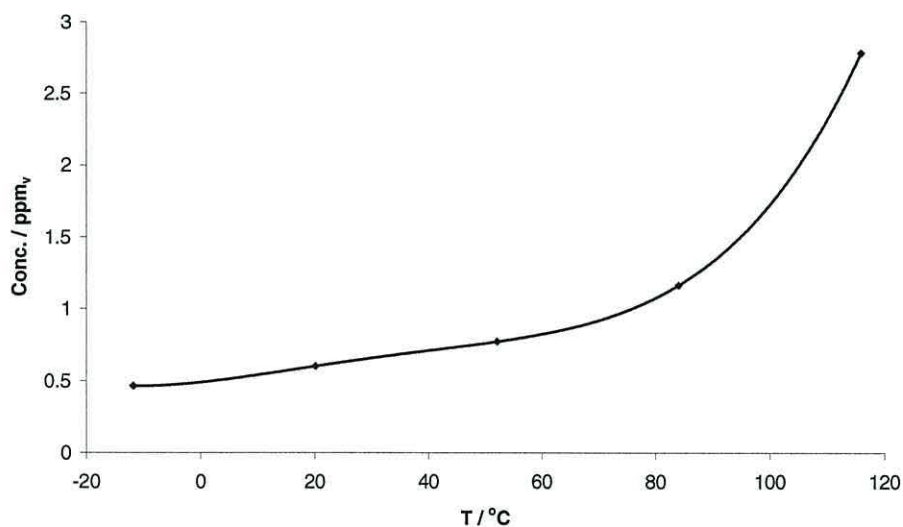


Figure 22. The calibration curve for the vapour generator.

Calibration showed that the vapour generator was able to produce a 2,4-DNT vapour stream within the range of 0.47 – 2.78 ppm_v, which was confirmed by second and third calibrations. The vapour concentration was lower than expected from the results obtained by Pella [11] using a similar system, who reported a vapour concentration range between 0.02 – 55.70 ppm. Pella's column had the dimensions 0.64 cm external diameter by 190cm long, and used Chromosorb G (60/80 mesh) as the solid adsorbent (as opposed to glass beads). It is not thought that the use of glass beads would have reduced the concentration range. In fact, Chromosorb is an adsorbent, and this would be expected to suppress the vapour pressure.

The gas flow through the apparatus was also tested to ensure that the gas passage was not impaired in any way or the system was not leaking, leading to a lack of vapour being carried to the trap. Flow meters were positioned at the start and the exit of the system, to measure the flow rate of the gas entering and exiting the system. The flow rates were found to be identical.

The vapour trap itself was tested to ensure that the vapour was being adsorbed onto the activated charcoal. Initially, the charcoal adsorbent was exchanged with Tenax TA to establish whether the adsorbent was at fault, but the results were similar to those obtained with the charcoal trap.

The eluting procedure was also evaluated, by analysis of the activated charcoal from a used trap, for any trace of 2,4-DNT remaining on the charcoal. But again the analysis showed no significant quantities of 2,4-DNT remaining on the charcoal indicating that all the nitroaromatic had been eluted by the original 10 ml of DCM.

It was later established that the vapours of 2,4-DNT were condensing from the vapour stream onto the glassware as they left the column. The column was heated on the inside of the heater unit, but the glassware outside of the heater unit the column was exposed to room temperatures, several degrees (up to 90°C) lower than in the heater unit when operated at its maximum. The cold walls of the column allowed the vapour to condense.

This fact went unnoticed initially as 2,4-DNT condensed to give a transparent film. But 2,6-DNB condensed to yield a yellow film, which made the observation possible. A secondary heater unit was designed to specifically keep the temperature of the glassware outside the heater unit at a temperature above the heater unit. This would reduce the effects of condensation to a negligible level. However, the secondary heater unit was designed late in the project, after most of the experimental work had been completed, and since the initial calibrations were repeatable, it was not employed in the following experiments. Any future work would benefit from the adoption of the secondary heater unit, and this should give rise to a greater concentration range, somewhere closer to that observed by Peter Pella [11].

2.4 Conclusions

A vapour generator was produced to generate vapours of nitroaromatic compounds. The vapour generator consisted of a packed column with variable temperature control, ranging from -10 to $+115$ °C. A nitrogen carrier gas was used to create and transfer the vapour stream to a sensor port at a flow rate of 50 ml/min. The concentration range obtained for 2,4-DNT was 0.47 to 2.78 ppm_v. The concentration range could be greatly improved by the development of an external heater unit.

2.5 Future work

The initial design of the vapour generator, although adequate for the present study, suffered from several drawbacks. Each of these problems could be addressed to enhance the performance of the vapour generator for future work. It has already been mentioned that the nitroaromatic condensed onto the glassware situated outside of the heater unit. An external heater unit could be employed to heat the glassware to a higher temperature than within the column. This would make it difficult for the nitroaromatic to condense and would improve the concentration range towards that observed by Pella [11]. An external heater unit was developed, similar to that shown in Figure 23, but was not employed during this study. Despite the condensation problem, the vacuum port also proved to be unsuitable. When the port was open, the vacuum was too strong and caused

the contents of both the vapour trap, and on occasion the column, to be sucked through the system. This could easily be resolved by replacing the glass wool with a more suitable plug, such as a porous glass frit.

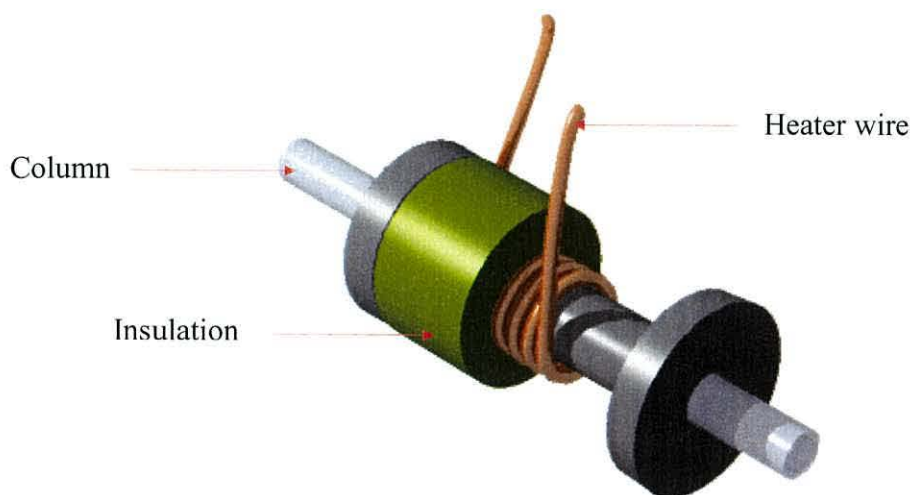


Figure 23. The external heater unit designed to heat the external column of the vapour generator.

2.6 References

1. Southampton Electrochemistry Group, R. Greef, R. Peat, L. M. Peter, D. Pletcher, and J. Robinson, *Instrumental Methods in Electrochemistry*, ed. T. J. Kemp. Ellis Horwood Ltd, Chichester, (1990).
2. C. M. A. Brett and A. M. O. Brett, *Electrochemistry: Principles, Methods, and Applications*. Oxford University Press, Oxford, (1993).
3. G. A. Mabbott, *Journal of Chemical Education*. **60** (1983) 697-702.
4. G. Bidan and M. Lapkowski, *Synthetic Metals*. **28** (1989) C113-C120.
5. M. Lapkowski, G. Bidan, and M. Fournier, *Synthetic Metals*. **41-43** (1991) 407-410.
6. D. A. Dimacopoulos and R. Reach, *US Patent* 4,173,604 (1979).
7. D. Bertone, *US Patent* 5,380,367 (1995).
8. E. R. Earnest, *US Patent* 3,874,345 (1975).
9. J. M. McKelvey and H. E. Hoelscher, *Anal. Chem.* **29** (1957) 123.
10. H. Hori and Y. Yanagisawa, *Environ. Sci. Technol.* . **27** (1993) 2023-2030.
11. P. A. Pella, *Anal. Chem.* **48** (1976) 1632-1637.
12. A. D. Drinkwine and B. R. Cage, *US Patent* 5,789,258 (1998).
13. A. E. O'Keefe and G. C. Ortman, *Anal. Chem.* **38** (1966) 760-763.
14. R. Mieninghaus, H. Schauenburg, and H. Knoppel, *Environ. Sci. Technol.* . **32** (1998) 1861-1863.

SEMICONDUCTING METAL OXIDE CHEMIRESISTORS

3.1 Introduction

Semiconducting metal oxide sensors appear at the low cost end of the sensors spectrum. They have good sensitivity towards a wide range of volatile organics and as a result of this apparent cross-sensitivity, they are commonly used as part of an array [1-4]. Very little research has been conducted concerning the prospective use of metal oxides as sensors for nitroaromatics, and TNT has been tested on only one occasion [5]. Preliminary experiments were performed to establish whether metal oxides could exhibit a significant response towards alkyl-polynitroaromatics, using 2,4-DNT as the example.

3.1.1 Semiconducting metal oxide chemiresistors

It was in 1962 that the electrical properties of semiconducting metal oxides, operated at elevated temperatures, were found to be sensitive to the composition of the surrounding atmosphere. This phenomenon was utilised later that year and thin-film ZnO and porous SnO₂ ceramics were demonstrated as gas sensing devices [6]. These devices were improved by the addition of small amounts of noble metals such as Pt and Pd, which improved their sensing properties. The report given by Sieyama *et al.* [7] gave rise to unprecedented development and commercialisation of a host of semiconducting metal oxides for the detection of a variety of gases [8]. In 1968, after considerable development work the first gas sensors based on the resistance of semiconducting metal oxides reached the market. These sensors were used to monitor the leakage of gas and petroleum [9].

Recent research has expanded the range of practical applications for semiconducting metal oxide sensors. Tin oxide is now widely employed as the basis for these sensors [10] and this has led to the development of a series of sensors capable of monitoring environmentally important gases to sub-ppm levels.

3.1.2 Electrical conductivity in semiconductors

The fundamental difference between conductors and semiconductors lies in their ability to carry charge as a function of temperature. At standard temperature conductors have a low resistance, which increases with temperature. Semiconductors on the other hand, exhibit much higher resistances at standard temperature, which decreases as their temperature increases. This difference arises from their means of conduction, which is best-explained using band theory [11].

When atoms are brought close together, as in the formation of a crystal lattice, their atomic orbitals overlap to form an LCAO-MOs (linear combination of atomic orbitals - molecular orbitals). Two atomic orbitals overlap to give rise to two molecular orbitals, one totally bonding and the other totally antibonding. When a third, fourth, and fifth atomic orbitals are introduced, three, four, and five molecular orbitals are formed, one fully bonding, another fully antibonding, and the others forming intermediate orbitals. Eventually, N atomic orbitals give rise to N molecular orbitals, the energies of which fall into a narrow range with finite width, called a band. s-Orbitals give rise to s-bands and p-orbitals give rise to p-bands. The difference in energy between these bands is known as the band gap

$$E_g = E_c - E_v \quad (1)$$

Where E_g is the energy of the band gap, E_c is the energy of the conductance band and E_v is the energy of the valence band (Figure 1).

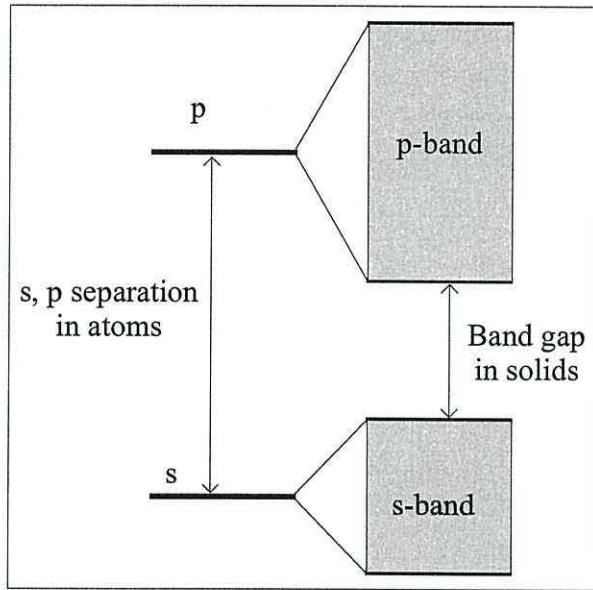


Figure 1. A schematic of the s and p bands that are formed by the overlap of s and p atomic orbitals.

The magnitude of the band gap can be used to classify the solid. At absolute zero, all electrons occupy the lowest energy levels available. If the band is only partially full, or the band gap is so small that the bands effectively overlap, the solid is classed as a conductor. At temperatures above absolute zero the electrons are mobile and free to move between the free orbitals throughout the crystal grain. Conversely, if the band is full and there is a band gap separating the bands, electrons are required to “jump” the gap before they can become mobile. If there is insufficient energy available for the electrons to “jump” this gap (*via* thermal excitation), then the material is classed as an insulator. If the band is full at $T = 0$ K, but the band gap is small (0.1-3.0 eV), then at temperatures greater than zero the electrons are able to “jump” from the valence to the conductance band. In this case the material is termed a semiconductor (see Figure 2). Once an electron moves from the valence band to the conductance band, leaving behind a “positive hole”, it is free to move between the molecular orbitals. Conduction occurs through the movement of both electrons and holes.

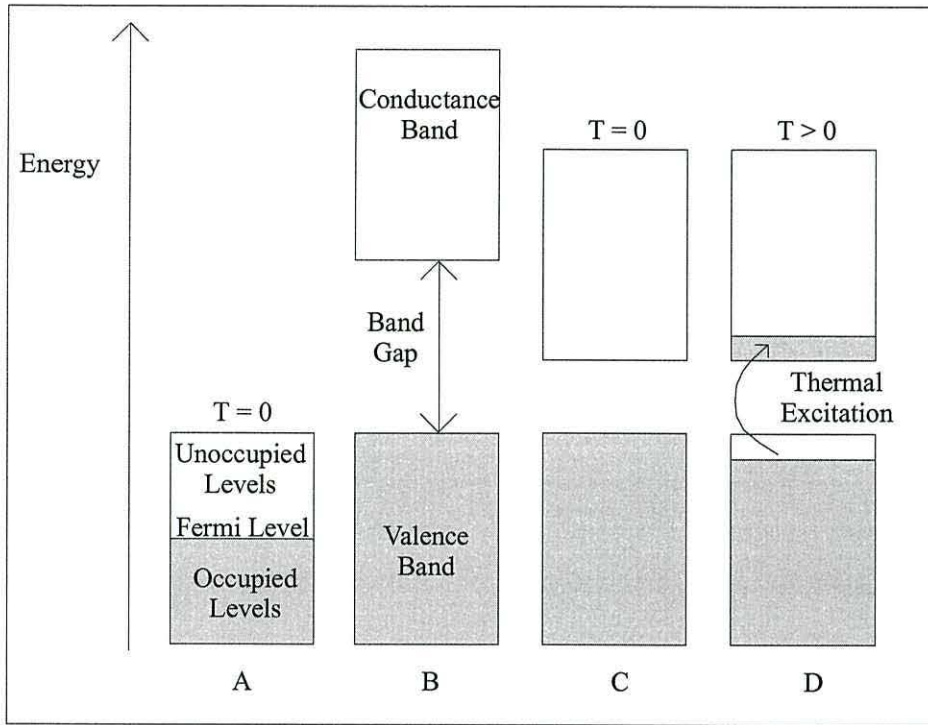


Figure 2. A simple schematic representation of conductors (A), insulators (B) and semiconductors (C and D), according to band theory.

The number of electrons with sufficient energy to “jump” the band gap is a function of temperature. For an intrinsic semiconductor, the concentration of electrons, n , and holes, p , are found to be equal and can be calculated using the equation

$$n = N_c \exp(-E_g / 2k T) = p = N_v \exp(-E_g / 2k T) \quad (2)$$

Where N_c and N_v are the effective density of energy states of conductance and valence bands, respectively. The Fermi level (E_f), which expresses the average energy position of an electron [12], is given by

$$E_f = (E_c + E_v) / 2 + (k T / 2) \ln N_v / N_c \quad (3)$$

The addition of an impurity (a dopant) can be used to manipulate the polarity of the semiconductor, tuning the conductivity. The introduction of an electron acceptor (p-type

doping) or electron donor (n-type doping) into the system effectively shifts the Fermi level towards the valence or conductance band, respectively, by introducing orbitals into the band gap.

The transport of charge through a semiconductor is carried out by both the holes and electrons, and the material conductivity (σ) is defined by

$$\sigma = q \mu_p [p] + q \mu_n [n] \quad (4)$$

where, the mobility of holes (μ_p) and electrons (μ_n) depends on the effective mass (m^*) of the carriers and is given approximately by equation 5.

$$\mu = (m^*)^{-3/2} T^{1/2} \quad (5)$$

3.1.3 The principles of metal oxides as gas-sensitive resistors

The principle behind the operation of the semiconducting gas sensors lies in their surface chemistry at elevated temperatures. When exposed to aerobic environments, oxygen adsorbs to the surface as charged species, O_2^- , O^- , and O^{2-} . At the operating temperature (typically 300-500 °C) O^- is believed to be the prevailing adsorbed species [13]. The absorption of oxygen species at the surface of the oxide removes an electron from the surface. If the films are thin, the coverage of O^- species controls the overall resistance of the sensor [1].

In the case of n-type semiconducting metal oxides, the formation of oxygen adsorbents builds up a space-charge region on the surface of the metal oxide grains (see Figure 3), due to electron transfer from the grain surfaces to the adsorbents as follows.



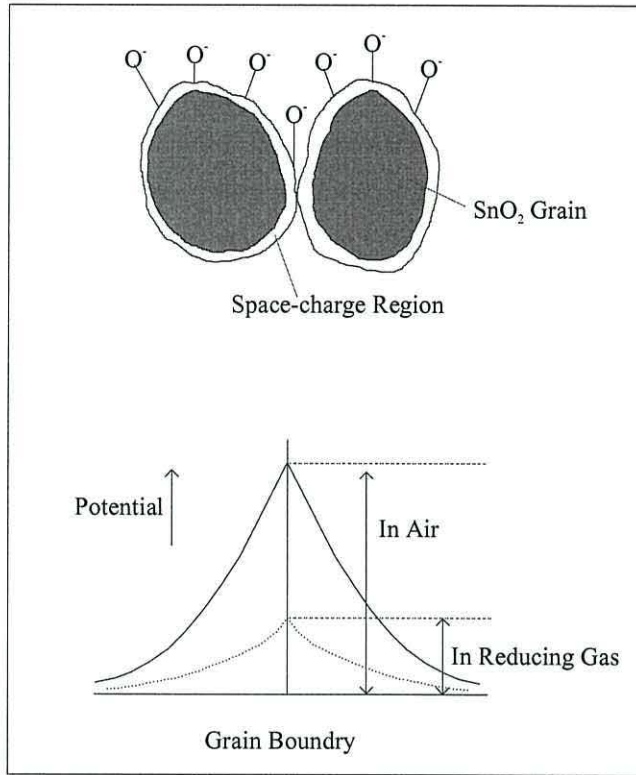


Figure 3. The space-charge region at the surface of n-type metal oxide grains, showing the potential barrier to electronic conduction [6].

The space charge region is a region that is deficient in charge carriers, which sets up a potential barrier to conduction. Because oxygen species remove charge carriers from the surface this barrier is particularly high between two adjacent grains. The depth of the space charge layer is a function of the surface coverage of oxygen adsorbents and the intrinsic electron concentration in the bulk [6]. The resistance of the n-type semiconducting metal oxide gas sensor is therefore high, due to the development of a potential barrier to electronic conduction at each grain boundary. When the sensor is exposed to inflammable gases in the atmosphere, subsequent reactions between the adsorbed oxygen and the gas leads to the removal of some oxygen adsorbents [8], returning electrons back to the metal oxide grain.



This reduces the surface coverage of the adsorbed species, resulting in a reduction of the oxide resistance^a, and this change in resistance is used as the transduction mechanism for the chemiresistor-type sensor. n-Type semiconductor gas sensors react in the opposite way if exposed to an oxidising analyte. The reaction between the metal oxide and the oxidising gas results in the chemisorption of the gas at the surface, which results in an increase of resistance due to the removal of electrons from the surface.

In the case of p-type semiconducting metal oxides, the majority charge carrier is the positive hole. Therefore, interactions at the oxide surface results in an opposite behaviour compared to n-type oxides. The presence of oxygen adsorbents, which withdraw electrons from the surface of the oxide, leads to a low resistance in air as more positive holes are created. The consumption of oxygen adsorbents during an interaction with reducing species decreases the concentration of holes at the grain surface and hence the resistance increases. Conversely, the adsorption of oxidising gases on p-type semiconducting metal oxides results in the decrease of the sensor's resistance.

In general, semiconducting metal oxide sensors can be used for the detection of any combustible gas, including H₂, CO, and hydrocarbons. In fact, this serves to be the single major disadvantage of these sensors; their inherent lack of selectivity. Therefore, much of the recent research has been dedicated to improving the sensitivity and selectivity of MOS chemiresistors towards individual target species.

The first materials studied in detail were ZnO and SnO₂ [6] but many oxides have since been investigated including Cr₂O₃ [14], Ga₂O₃ [15], WO₃ [16], TiO₂ [17], and Fe₂O₃ [18]. The search for new innovative materials has also led to the development of mixed-metal oxides. The intrinsic semiconductor may be doped by substitution of secondary elements into the lattice. This serves to vary the surface density and nature of the gas adsorption sites present at the surface of the material. Such sites are often termed acidic

^a Another oxygen removal process of importance is the dissociation of the lattice, or by the presence of lattice defects. For this, imperfections (e.g. oxygen interstitials or anionic/cationic vacancies) must be mobile at the temperature of operation.

or basic, according to whether they interact with gases such as ammonia and hydrogen sulphide (acidic sites) or carbon dioxide (basic sites). An example of this is the addition of chromium into a SnO_2 lattice, which serves to increase the acidity of the surface sites. Other examples include $(\text{Cr}_2(\text{Ti})\text{O}_3)$ [19], $\text{Ba}_2(\text{Sn})\text{O}_3$ [20, 21], $\text{Zn}(\text{Ga})\text{O}$ [22], $\text{Ga}_2(\text{Sn})\text{O}_3$ [23], $\text{Sn}(\text{Sb})\text{O}_2$ [24], $\text{Sn}(\text{Al})\text{O}_2$ and $\text{Sn}(\text{In})\text{O}_2$ [25], $\text{W}(\text{Ti})\text{O}_3$ and $\text{Sr}(\text{Ti})\text{O}_2$ [26], where the elements in parenthesis are the dopant ions. However, it is worth noting that it still appears unclear how the adsorption sites couple with the charge carriers present in the solid, so as to lead to a change in the conductivity of the oxide upon the adsorption or dissociation of the analyte gas molecules.

The operating temperature of the metal oxide is known to affect its sensitivity towards particular analytes [6]. This is because different gases have different optimum oxidation temperatures. This temperature/sensitivity dependence can also be used to increase the selectivity of the device [27]. By cycling the temperature of the metal-oxide sensing element in the presence of an analyte, a conductance–temperature profile is obtained. This profile can be characteristic to the analyte, which can then be used to identify it [6, 27-29]. In general, the temperature of the gas sensor surface is controlled by varying the voltage applied to the sensor heater [30].

Another method commonly employed for improving the selectivity of MOS sensors is the use of filters. Filters, in the physical sense, can act to prevent interfering gases from reaching the sensing surface through adsorption or absorption, whilst the analyte is able to pass through the filter. Typical examples of physical filters are charcoal and zeolite [31]. Filters can also act in the chemical sense, where they break down any interfering gases into products that will not interact with the sensor nor hinder the detection of the species of interest. An example of a chemical filter is Ga_2O_3 [32], which at the appropriate temperature, actively oxidises interfering gases before they can reach the sensor surface, while allowing methane to pass through unaltered.

Perhaps the most widely used approach to increasing the selectivity of a sensing element is through the addition of dopants to the oxide surface. Catalytic noble metals such as

platinum [33], palladium [34-36], rhodium [37], and gold [38] are known to improve the sensing characteristics of metal oxides towards certain gases. The addition of an appropriate amount of the noble metal can serve to enhance selectivity by increasing the sensitivity of the sensing element towards the analyte and moving the maximum sensitivity to lower temperatures, where interfering gases interact less readily. It is important to note that the choice of metal needs to be carefully matched to the metal oxide material, with respect to the analyte, in order to achieve the required result [6]. The catalytic effect of a noble metal arises from its ability to activate inflammable gases, so to react with the oxygen adsorbents more readily. This type of promoting effect is known as chemical sensitisation [6]. Another important promoting effect is electronic sensitisation, which has been observed for SnO₂ sensors loaded with Pd [39]. Electronic sensitisation is a direct result of an increased space charge layer at the surface of the metal oxide grains. At high temperatures (~500 °C) the dopant metal also becomes covered with oxygen adsorbents, which results in the removal of electrons from the metal surface. If the noble metal has a larger work function than the oxide has electron affinity, it will in turn remove electrons from the semiconductor surface. This results in a diminished charge carrier (electron) concentration at the surface of the oxide, which increases the space-charge-layer and causing greater sensitivity [6].

The behaviour of semiconducting oxide materials can be manipulated by changing the size of the crystallite grain, and the surface area per unit mass of the material exposed to the gas [16, 26, 40-42]. The sensitivity has been shown to increase as the crystallite size (D) decreases, with dramatic changes below $D = 10$ nm approaching a maximum at $D = 5$ nm [43]. The explanation commonly given for this phenomenon is that as the crystallite size (D) decreases, the relative space charge layer (L) increases. The increasing depth of the space charge layer (L) is accompanied by an increase in sensitivity. At sizes approaching $2L$ (~ 6 nm), the space charge layer spreads through the entire crystallite, and a maximum sensitivity is observed.

3.2 Experimental

3.2.1 Metal oxide chemiresistors

The semiconducting metal oxide chemiresistors (MOS) were donated by Capteur Sensors Ltd. The sensors (Figure 4) consisted of an oxide layer deposited on an alumina substrate. The resistance of the chemiresistor was measured across the diagonal with a DVM. The sensors were operated at elevated temperatures (typically 300-500 °C) using a platinum heating-element.

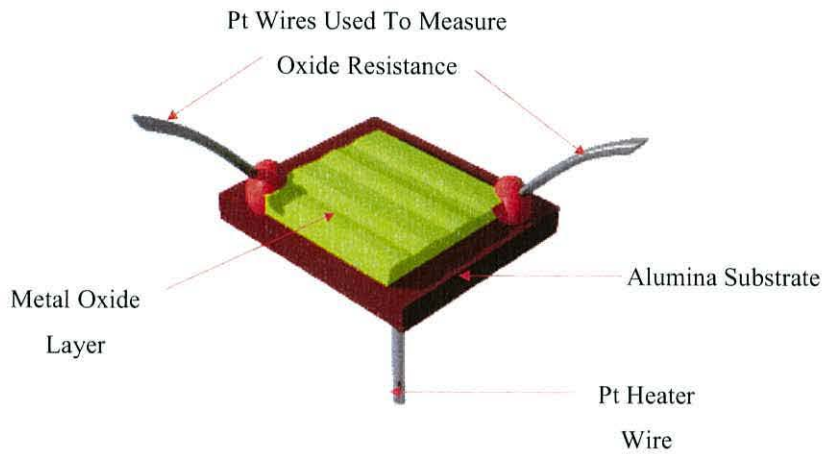


Figure 4. A simple representation of the MOS chemiresistors.

The baseline and gas response of these sensors are known to be a function of their operating temperature, so to ensure the stability of the sensor, it is essential to maintain the operating temperature to within a fraction of a degree. In order to prevent any variation in operating temperature, these sensors require a heater driver. The heater driver formed part of a Wheatstone Bridge with the heater element acting as one of the resistors. The current passing through the heating element is variably controlled so to keep the element at a constant resistance. This in turn, maintains the sensor's temperature regardless of the changes in ambient temperature. The heater driver circuit is shown in Figure 5.

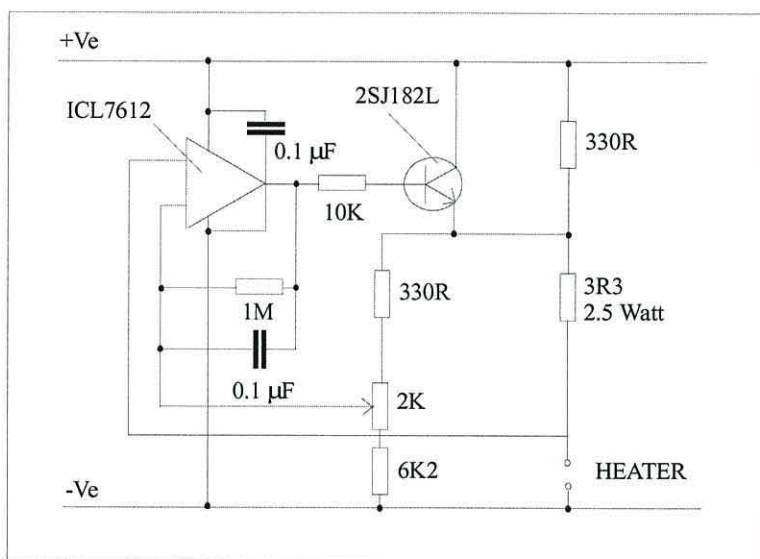


Figure 5. The circuit diagram for the heater driver used in this study.

3.2.2 Sensor response

Prior to all measurements, the sensor was fixed into the sensor port and allowed to equilibrate in air (50 % RH) until the resistance had become stable, typically 20 minutes. The sensor port was then connected to the vapour generator and the resistance of the sensor monitored at 10-second intervals, while being exposed to a N_2 vapour stream containing the analyte. On completion of the measurement, the sensor was removed from the vapour generator and allowed to recover in air. Recovery times typically varied with the concentration of the analyte and length of exposure, between 10 minutes and 24 hours.

3.3 Results and discussion

3.3.1 Chromium titanium oxide chemiresistors

Chromium titanium oxide (CTO) is a p-type semiconductor. Chromium oxide is the intrinsic semiconductor (Cr^{3+}) and titanium (Ti^{4+}) is introduced into the lattice as the dopant. The resultant mixed metal oxide was claimed by the manufacturers to have the

composition $\text{Cr}_{1.8}\text{Ti}_{0.2}\text{O}_3$ and behaved as a p-type semiconductor, undergoing an increase in resistance on exposure to a reducing gas.

The CTO chemiresistor can be seen in Figure 6. The oxide layer can be seen as the green layer with the measuring contacts in the upper diagonal corners. The heater element is the Pt wire running on the under side of the alumina substrate.

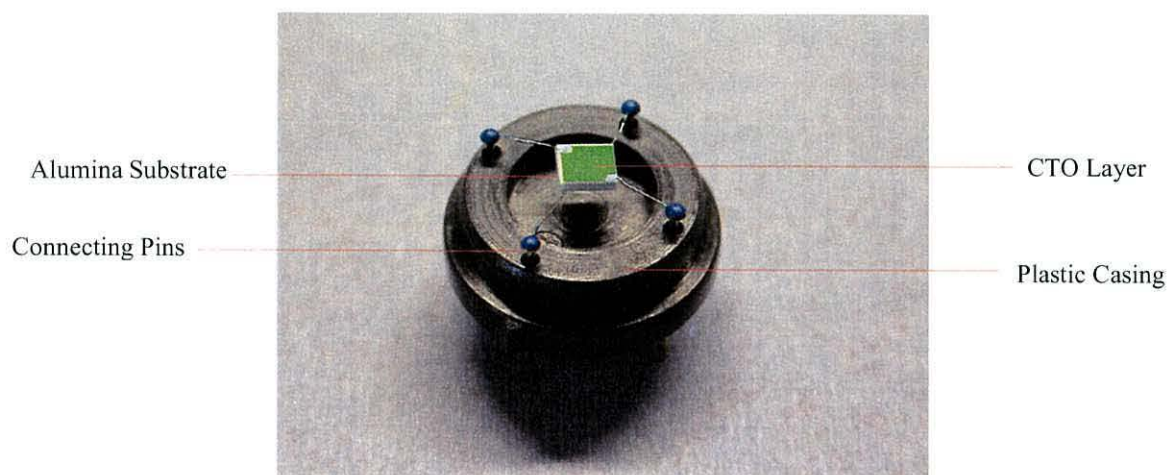


Figure 6. A chromium titanium oxide chemiresistor, as received from Capteur Sensors Ltd.

The CTO was set up to operate at the manufacturers specifications. This related to an operating temperature of $340\text{ }^{\circ}\text{C}$, and a baseline resistance of $80\text{ k}\Omega$ (air, 50 % RH). The relationship between the sensor resistance and analyte concentration was stated to follow a square root law, $R_g = R_o \sqrt{[g]}$ (for toluene, air, 50 % RH), where R_g is the resistance in the presence of the target analyte, R_o is the base resistance in the absence of the target analyte, and $[g]$ is the concentration of the target analyte.

3.3.1.1 The baseline response

The response of the CTO chemiresistor in the following study is given as the percentage resistance difference from the rest value in static air, 50 % RH, taken immediately before the measurement.

$$\text{Response} = [(R_g - R_o) / R_o] \times 100 \quad (8)$$

Where, R_g is the resistance in the presence of the gas stream, and R_o is the resistance in static air (50% RH), prior to measurement.

The baseline response of the CTO was measured in 50 ml/min flow of different carrier gases. The carrier gas is the matrix in which the analyte is transported to the sensor. In Figure 7, it can be seen that the CTO undergoes an increase in resistance upon exposure to argon, nitrogen, and air. As the CTO is a p-type semiconductor, this relates to an increase in the population of electrons in the oxide layer.

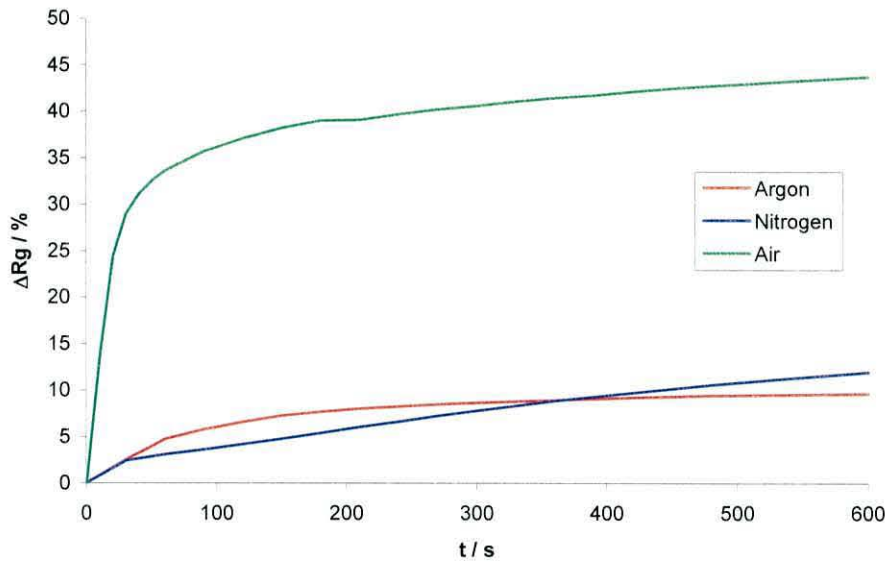


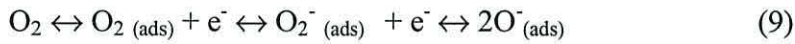
Figure 7. The baseline responses of the CTO chemiresistor in various carrier gases.

The increased electron density in a metal oxide film is usually attributed to the loss of oxygen adsorbents from the surface, or the negative chemisorption (i.e. donation of electrons to the oxide) of an analyte [6, 8, 13, 44, 45]. However, the response in the presence of oxygen is greater than purified N_2 or Ar. The level of RH is also known to have a pronounced effect on the baseline response of metal oxides [13, 44, 46]. In order to understand these observations it is essential to predict all the surface processes that are

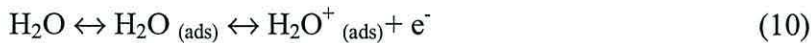
likely to occur during the stabilisation period prior to exposure, and those occurring during exposure of the CTO chemiresistor to the carrier gas, in the presence and absence of oxygen and water vapour.

During the stabilisation period, prior to exposure of the chemiresistor to the carrier gas, the CTO chemiresistor was exposed to laboratory air. The RH of the air in the laboratory was measured and found to lie in a range varying from 40 – 55 % RH. There is also likely to be oxygen, CO₂, and some lower order hydrocarbons present. The hydrocarbon content of the laboratory air was not known, but at the operating temperature, oxygen, and water vapour content were known.

The adsorption of oxygen, at the operating temperature, is thought to proceed through a mechanism shown in equation 9.

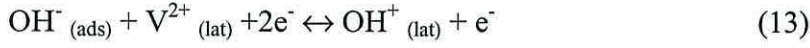


This adsorption requires electrons, which are removed from the oxide, lowering the resistance of the film. It has been demonstrated for SnO₂ that O₂ desorbs at approximately 80 °C, O₂²⁻ at 150 °C, and O⁻ at 500 °C [47]. So at the operating temperature of the CTO chemiresistor, it is likely that O⁻ will be the major adsorbed species. Water vapour is also able to adsorb to the surface as a neutral physisorbed molecule or as a chemisorbed species.



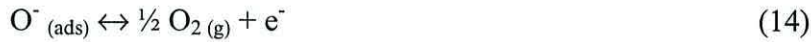
This process gives rise to electron density at the surface, increasing the resistance of the layer. Adsorbed water can also undergo dissociation to form two surface-bound hydroxyl groups, using lattice oxygen [46], which can then either ionise or migrate back into the vacancy created during hydroxyl formation.





Where V^{2+} is an oxygen vacancy in the oxide lattice. All these processes are likely to occur at the CTO surface, and influence the base resistance of the chemiresistor.

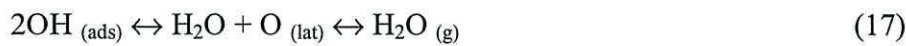
When the CTO chemiresistor is exposed to nitrogen, the composition of the surrounding atmosphere is radically altered. There is no longer oxygen or water vapour present in the atmosphere. Therefore, the potential processes occurring at the oxide surface during exposure to the nitrogen carrier gas are likely to be dehydration due to desorption of molecular water, dehydroxylation, and removal of oxygen. Exposure of the CTO to an anaerobic nitrogen flow may result in the removal of oxygen from the surface of the oxide, which is likely to be a permanent process, while the sensor remains in the nitrogen flow. This would cause a net increase in the films resistance.



Observation (Figure 7) showed that the resistance of the CTO chemiresistor increased upon exposure to the nitrogen carrier gas, which is in agreement with previous observations that a decrease in oxygen partial pressure is accompanied by a resistance decrease for n-type semiconductors and resistance increase for p-type semiconductors [48]. The CTO chemiresistor acts as a surface conductance type sensor, at these operating temperatures. Therefore, the rapid increase in resistance may be attributed to the removal of oxygen from the surface layer with rapid electron diffusion to the bulk, while the much slower increase observed thereafter, may be attributed to the much slower diffusion of vacancies into the bulk of the material [48].

However, if the removal of oxygen from the oxide is the dominant process, then the baseline response of the CTO chemiresistor in a flow of air is somewhat counterintuitive.

The observed baseline response in air (Figure 7) is much greater than that in nitrogen or argon, which would not be expected as it might be assumed that partial pressure of oxygen present in the carrier gas would be similar to that in static air and hence able to replace any oxygen removed. This surely must indicate that it is not just the removal of the oxygen adsorbents that is responsible for the resistance increase, but oxygen must have an effect on any processes occurring at the surface. The presence of oxygen may facilitate desorption of other adsorbed species such as water, hydrogen, hydrocarbons, or CO. Both dehydration (eq.15) and dehydroxylation (eq. 16 and 17) are able to affect the electron density in the oxide, so variation of the film resistance may depend on the ratio of the adsorbed molecular water and hydroxyl species. However, molecular water is known to desorb from SnO₂ at lower temperatures than hydroxyl groups (100 °C, as opposed to 400 °C [47]), and this too may influence the resistance change although this would need to be confirmed through another method such as IR spectroscopy. At 340 °C, if there is no adsorbed molecular water, dehydroxylation may account for the observed resistance increase, although it is still unclear exactly how oxygen influences this process.

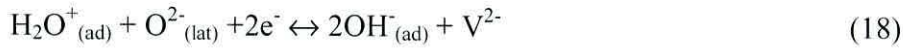


3.3.1.2 The effect of RH on the baseline response

Relative humidity (RH) is known to affect the resistive characteristics of semiconducting metal oxides [13, 44-47]. Figure 8 shows the effect of relative humidity on the baseline response of the CTO when N₂ was used as the carrier gas. The response of the CTO is shown to increase with relative humidity. This has been observed for several metal oxides and is caused by the chemisorption of water to the oxide surface. At higher temperatures water will act as an electron donor [13, 44, 46, 49].



As the CTO is a p-type semiconductor, the additional electron density that results from the adsorption of water vapour causes an increase in the resistance of the oxide film. However, the adsorbed water molecule can further dissociate at the surface to form two hydroxyl-groups consuming lattice-bound oxygen and electrons, generating a negatively charged oxygen vacancy (V^{2-}), and decreasing the resistance of the oxide.



If lattice oxygen is unavailable or is removed by the nitrogen carrier gas, or if this process is slower than the adsorption of molecular water, this process would be unfavourable and water adsorption would be the dominant process, and this may account for the observed increase in resistance.

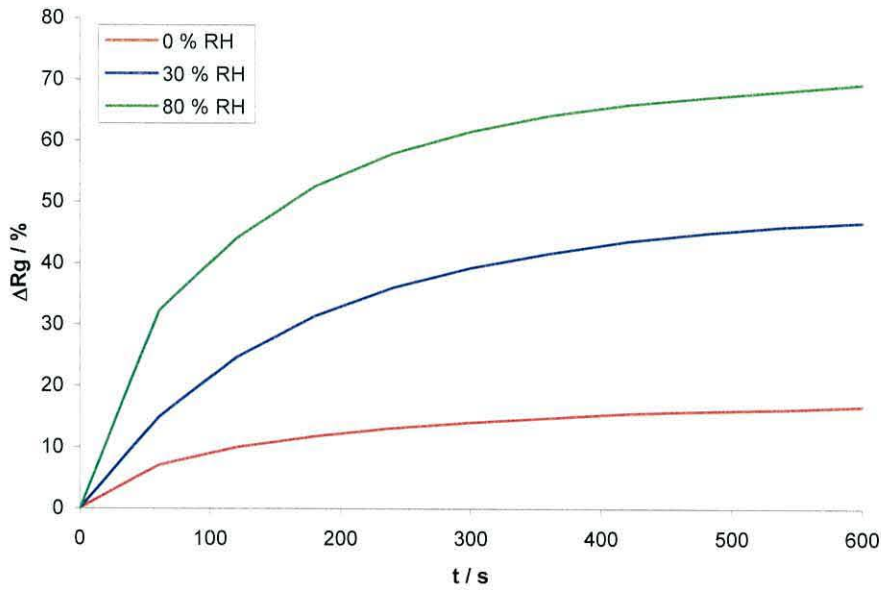


Figure 8. The effect of relative humidity on the baseline response of the CTO chemiresistor (N_2 , 50 ml/min).

The effect of RH when air is used as the carrier gas, Figure 9, displays quite the opposite behaviour to that observed when N_2 is used, which again shows that the level of oxygen in the carrier gas has a dramatic effect on the response characteristics. The response decreases from 51 to 20 % as the level of RH increases from 0 to 75 %. This response may indicate that in an oxygen-containing environment, where lattice oxygen is not removed or is replaced, dissociation of water to form hydroxyl groups is the dominant process (equations 11 and 12) and the loss of electron density during this process accounts for the decrease in film resistance.

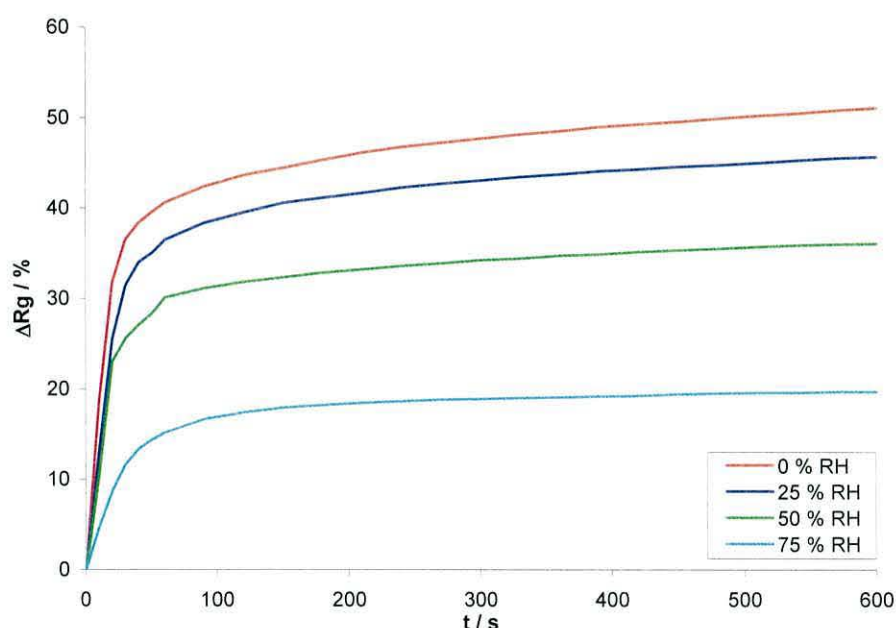


Figure 9. The effect of relative humidity on the baseline response of the CTO chemiresistor (Air, 50 ml/min).

Another possibility arises when the changes of the dominant charge carriers are considered. This type of behaviour has been seen before, for bulk conductance-type $BaFe_{0.67}Ta_{0.33}O_{3-x}$, whose conductance changes from n-type to p-type at an oxygen partial pressure of 10^{-10} atm. Another MOS (TiO_{2-x}), undergoes a transition from n-type to p-type behaviour conductance as the oxygen partial pressure is increased past the transition

point (~ 1 atm) [48]. The CTO may be adopting p-type behaviour in zero or low oxygen concentrations, whilst exhibiting n-type behaviour at higher (~ 20 %) levels. However, this behaviour has not been reported for CTO, and would not be expected for the change of oxygen partial pressure. In this case, during exposure to humidified carrier gases, the processes likely to be responsible for the observed responses are the removal of oxygen and the adsorption of molecular water. During exposure to humidified nitrogen, the CTO chemiresistor would display p-type behaviour, increasing in resistance as oxygen is removed (equation 15) or water adsorbed (equation 14). During exposure to dry air, the CTO chemiresistor would display n-type behaviour. In this instance, the observed response would not be due to the loss of oxygen, as it would be expected that oxygen in air would replace any oxygen removed, but due to the dehydration process. It may be noted that oxygen may adsorb to sites vacated by the dehydration process, which would further remove electrons and increase resistance. This may account for the enhanced response in air. During exposure to humidified air, the adsorption of molecular water would give rise to an increased electron density in the oxide, which would act to decrease the resistance. Here it is assumed that the adsorption/desorption of molecular water is the dominant process, and hydroxylation/dehydroxylation is insignificant. This also agrees with other data that suggests that the adsorption of molecular water is a much faster process than its dissociation and formation of hydroxyl species at lower temperatures [46, 50].

Whatever the reason for this contradictory behaviour, it was necessary to ensure that the RH was controlled during subsequent measurements, and so the carrier gas was always passed through a gas purification system containing silica gel, and RH was introduced and measured just before the vapour stream entered the sensor port.

3.3.1.3 The effect of carrier gas variables on the baseline response

Other variables that may affect the baseline response of the metal oxide chemiresistor are the temperature and the flow rate of the carrier gas. The flow rate and temperature of the carrier gas (N_2) were varied and the responses can be seen in Figure 10 and Figure 11, respectively. It can be seen that neither the flow rate nor the temperature of the carrier

gas significantly affected the baseline response of the CTO within experimental error. Therefore, as the flow rate is controlled precisely, and the temperature of the carrier gas was always held within the range studied, no further emphasis was placed on these variables.

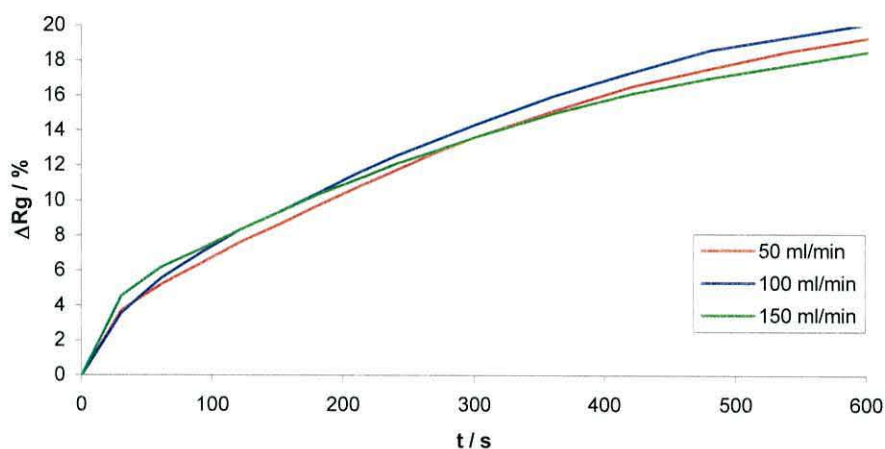


Figure 10. The effect of carrier gas flow rate on the baseline response of a CTO chemiresistor, in N_2 (50 ml/min).

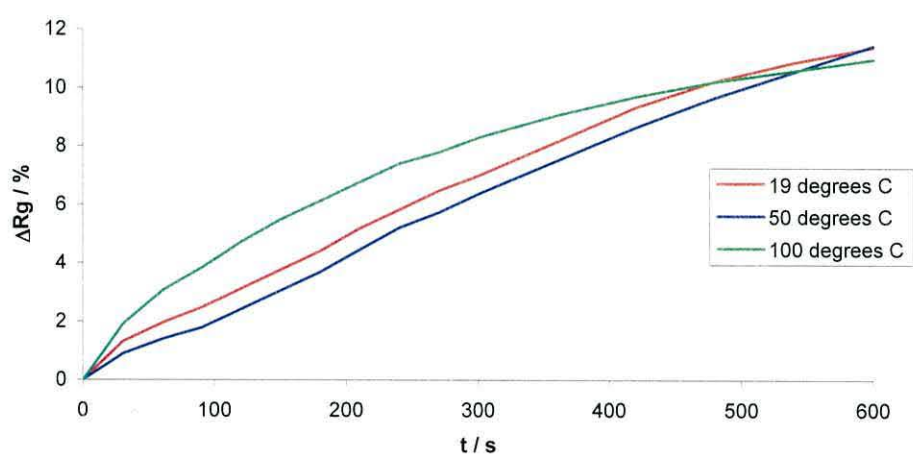


Figure 11. The effect of carrier gas temperature, on the baseline response of the CTO in N_2 (50 ml/min).

3.3.1.4 The response towards 2,4-DNT

It was necessary to establish whether the CTO chemiresistor would exhibit a response towards vapours of 2,4-DNT. The CTO was allowed to stabilise in air (50 % RH) with a resistance of approximately $80\text{ k}\Omega$, before being exposed to a vapour stream of 2.8 ppm 2,4-DNT in N_2 (50 ml/min). Upon exposure to the vapour stream a rapid resistance increase was observed, which stabilised over a period of approximately 600 s at a new resistance of approximately $160\text{ k}\Omega$. The resistance continued to increase very slightly with time. The preliminary response can be seen in Figure 12, and indicates that the CTO was able to respond to DNT vapours, and therefore further tests were performed to establish the nature of the response.

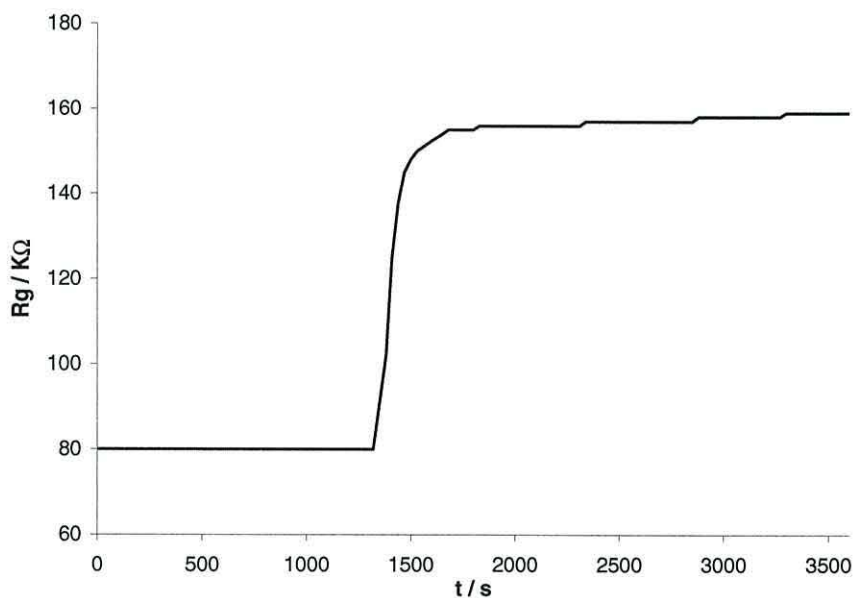


Figure 12. The preliminary response of a CTO chemiresistor towards 2,4-DNT (2.78 ppm_v, 50 ml/min N_2).

The CTO chemiresistor is known to display p-type behaviour [19]. The increase in resistance would therefore indicate that electron density is increasing in the oxide layer. Increased electron density can be caused by the removal of oxygen adsorbents from the grain surface, signifying that the 2,4-DNT may interact directly with the oxygen surface

species, or that the 2,4-DNT interacts directly with the oxide surface undergoing a negative-type chemisorption (i.e. donates charge on adsorption). At the operating temperature of the CTO, 2,4-DNT may also decompose on the surface of the oxide and the response may be a consequence of the interaction of the CTO with the decomposition products. The resistance of the CTO appeared to stabilise after 600 seconds, which may signify saturation of the signal due to the removal of all the oxygen absorbents, or negative-adsorption of 2,4-DNT to all the available surface sites. Alternatively, it may signify a dynamic equilibrium of 2,4-DNT interactions with the surface. Therefore, the CTO chemiresistor was exposed to 2,4-DNT vapours of different concentrations (Figure 13). This would determine whether the signal was saturating, or whether an equilibrium process was in operation.

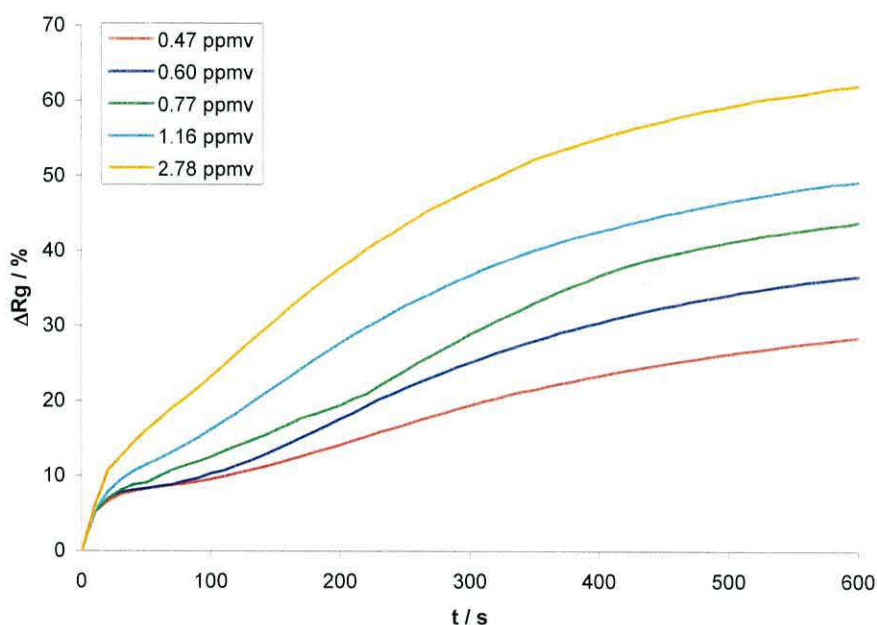


Figure 13. The response of a CTO towards vapour streams containing 2,4-DNT (N_2 , 50 ml/min).

The resistance of the CTO chemiresistor stabilised in all cases after an approximate period of 1000 s, at a resistance that was dependent on the concentration of 2,4-DNT. This would suggest that the sensor signal was not saturating within the time-scale of these

experiments, and that the response was in fact an equilibrium, concentration-dependent value.

Another important aspect of a sensor's performance is that the response is fully reversible. This was demonstrated for the CTO chemiresistor by removing the sensor from the 2,4-DNT vapour stream whilst continuing to monitor the film resistance. The resistance of the CTO chemiresistor was seen to return to its original value upon standing in air (50 % RH). The time required for the resistance to return to its base value was dependent on the concentration of the 2,4-DNT vapour stream it had been exposed to, and was observed to take several hours to complete. The recovery in a nitrogen gas stream also exhibited a decrease in resistance but never returned to the original value, indicating that some oxygen must be removed from the surface during exposure.

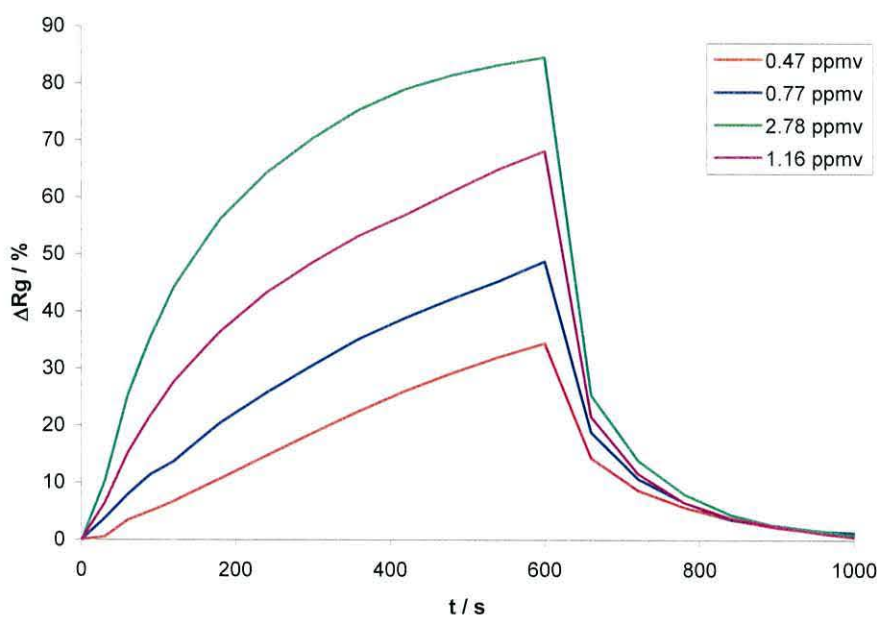


Figure 14. The recovery time of a CTO after exposure to vapour streams containing 2,4-DNT (N_2 , 50 ml/min).

The response of the CTO chemiresistor, after a given time (600 seconds in Figure 13) of exposure to a vapour stream containing different concentrations of 2,4-DNT can be used to ascertain the sensitivity of the sensor. The CTO displayed an approximate (within experimental error) square root dependence on the concentration of 2,4-DNT vapours, as can be seen in Figure 15. From this plot, an equation relating the concentration of the vapour stream to the response of the CTO chemiresistor can be derived.

$$\text{Conc.}_{(\text{ppm 2,4-DNT})} = [(\Delta R_g - 11.735) / 41.267]^2 \quad (12)$$

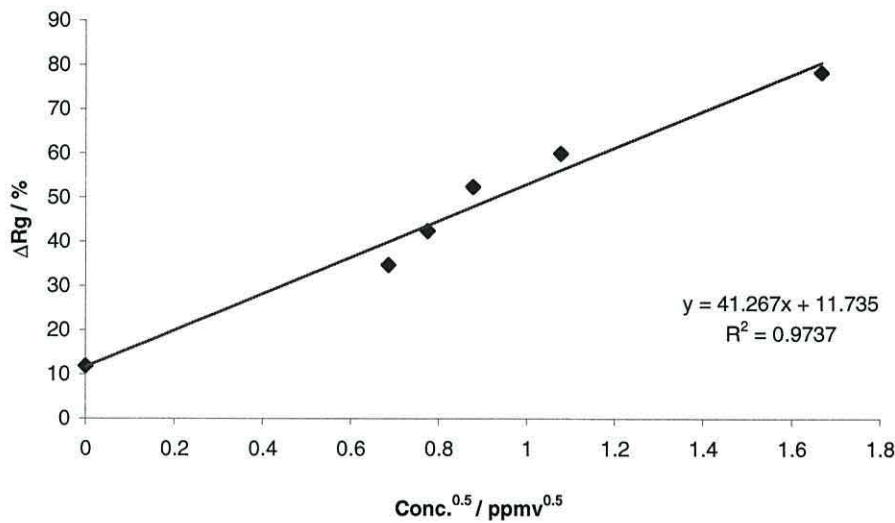


Figure 15. The sensitivity of the CTO towards 2,4-DNT in nitrogen (50 ml/min).

It is important when considering a chemiresistor as a sensor for 2,4-DNT that the response is repeatable. Repeatability refers to the precision of a sensor's response towards identical vapour streams of the analyte. Therefore, a single CTO chemiresistor was repeatedly exposed to a vapour stream containing 2.78 ppm_v 2,4-DNT, and the response recorded. The average response of the CTO chemiresistor can be seen in Figure 16. It can be seen that the error associated with the response is not greater than 3.2 %. This value is less than the difference between the responses towards the different concentrations, and therefore the CTO chemiresistor should have no difficulty in distinguishing between vapour streams varying by 0.2 ppm_v 2,4-DNT.

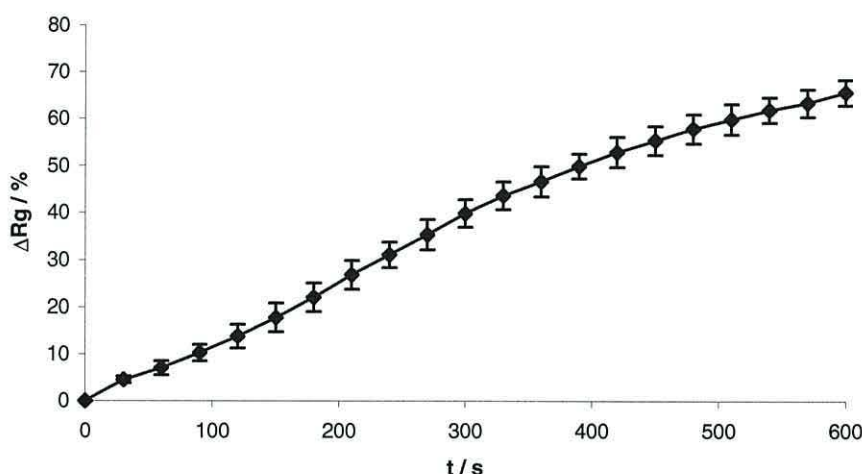


Figure 16. The repeatability of a CTO chemiresistor towards 2.78 ppm_v 2,4-DNT (N₂, 50 ml/min).

As well as the repeatability of a single sensor, reproducibility of a batch of sensors is required. Reproducibility is the ability of similar sensors to yield identical responses towards an identical vapour stream on different occasions. Therefore, four CTO chemiresistors were exposed to a vapour stream containing 1.16 ppm_v 2,4-DNT. Although each sensor gave rise to very repeatable responses, they are not identical (Figure 17), with variations occurring in the magnitude of ΔR_g , and the time required for stabilisation of the response. The most plausible explanation for these variations can be attributed to the fabrication of the sensors. Although the sensors are produced from the same material, deviations are likely to occur in the thickness of the oxide layer, spacing of the electrical contacts, resistance of the heater wire. These differences will affect the operating temperature and resistance of the chemiresistor, which in turn will affect the response characteristics. Therefore, each sensor would need to be calibrated prior to use.

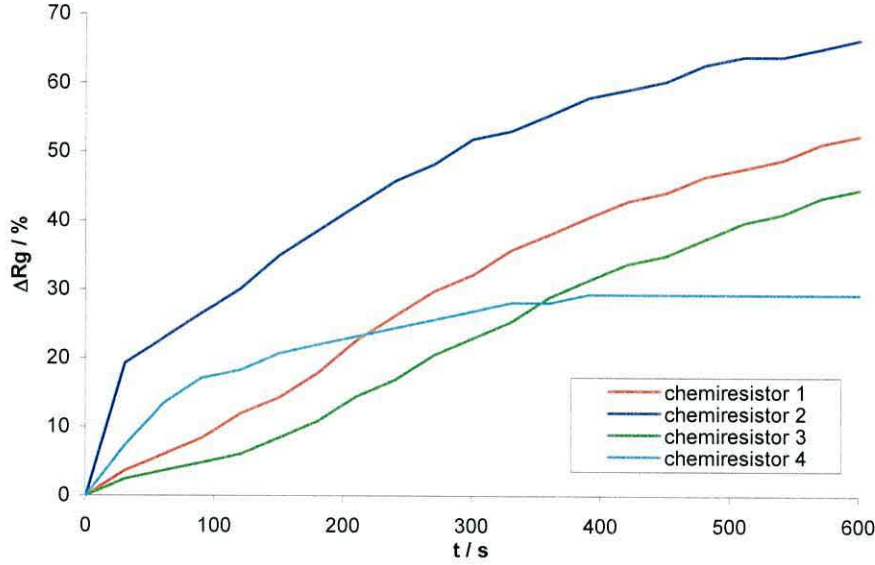


Figure 17. The reproducibility of four different CTO chemiresistors towards 1.16 ppm, 2,4-DNT (N_2 , 50 ml/min).

As stated previously, the operation temperature of the sensor is critical to the characteristics of the response. The operation temperature therefore needs to be controlled precisely, and hence a heater driver is employed. The heater driver maintains a sufficient current through the heating element so that the resistance of the heating element is held constant.

The operating temperature was estimated by treating the heating element as a platinum resistance thermometer [51], as can be seen in equation 9.

$$T = (A/2B) - \sqrt{[(A/2B)^2 - (R_t - R_o/R_oB)]} \quad (9)$$

R_t is the resistance of the platinum wire at operating temperature, R_o is the resistance at room temperature, and A and B are constants of value 3.9083×10^{-3} and -5.7750×10^{-7} , respectively.

The operating temperature was shown to affect the response of the CTO chemiresistor. As the operating temperature increases, the base resistance value of the CTO decreases (Figure 18, top). This observation is not only characteristic of semiconductors, but also of the conductivity control that adsorbed oxygen species are likely to have on a p-type semiconductor. However, when the resistance-time profiles are normalised against the base resistance value for air, 50 % RH, it can be seen that the magnitude of the response does not follow the same trend (Figure 18, middle), i.e. the largest responses are not observed for the highest temperatures. It has already been established that reactions at the surface of the metal oxide have optimum temperatures where maximum sensitivity is observed [6]. When the magnitude of the response is plotted against the operating temperature, there is a clear maximum between 300-330 °C (Figure 18, bottom). Therefore, in order to obtain maximum sensitivity towards 2,4-DNT, the CTO chemiresistor would need to be operated within this region.

The maximum response occurred at a temperature of 300 °C, which coincides with the decomposition temperature of 2,4-DNT. This may provide further evidence that the response of the CTO chemiresistor is due to the adsorption of the decomposition products, and above 330 °C interactions with these products is unfavourable.

Oxygen adsorbents play a critical role in the surface chemistry of metal oxides at elevated temperatures. It is obvious that if the sensor is operated at these temperatures in a nitrogen carrier gas there will be no oxygen available to replace any oxygen adsorbents, or lattice oxygen removed from the oxide surface. With respect to the desired application of this project, there is a limited fraction of oxygen available within the sealed vessels (< 2 %), and so it is pertinent to observe the CTO response towards 2,4-DNT in the presence of oxygen. The baseline response of the chemiresistor, in air, has already been shown to be much greater compared with nitrogen (Figure 7).

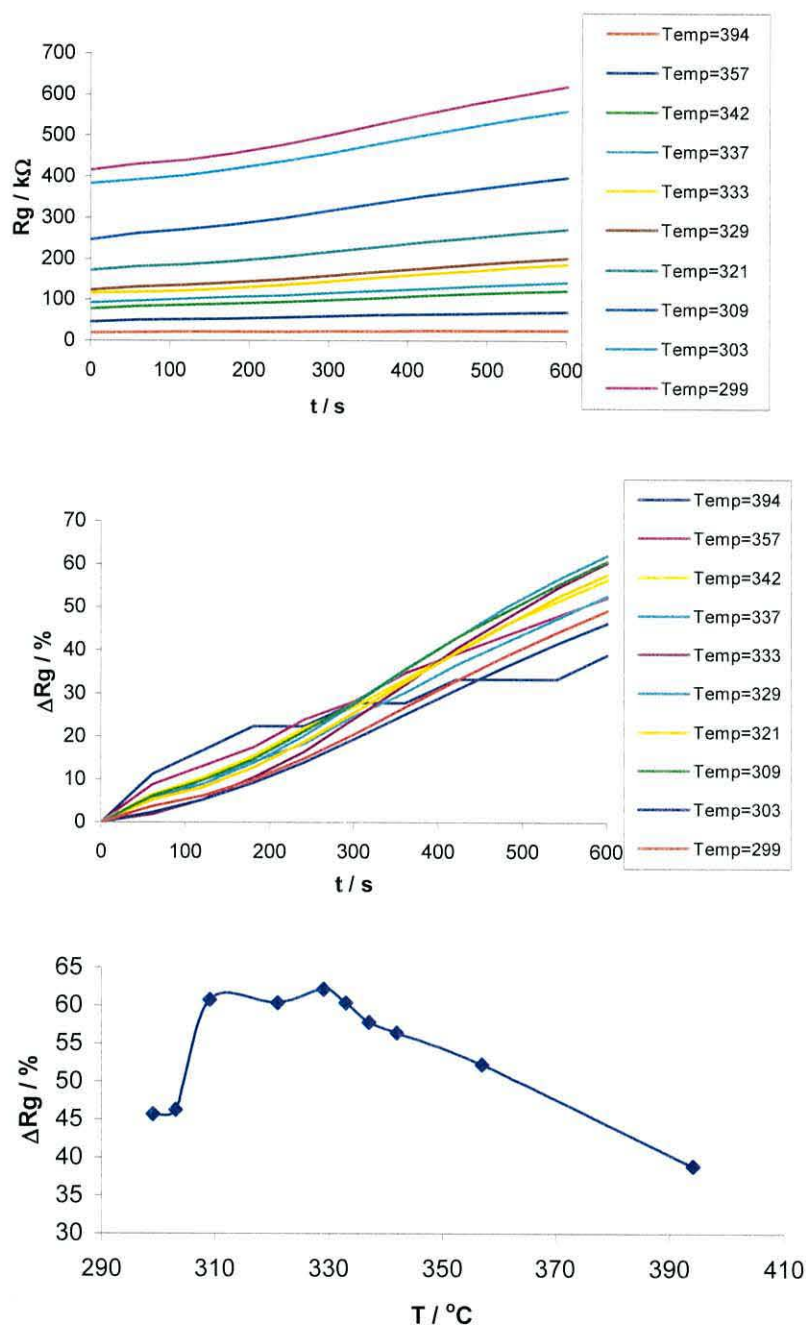


Figure 18. The effect of operating temperature (°C) on the resistance (top), normalised response (middle) of a CTO towards 2.78 ppm_v 2,4-DNT (N₂, 50 ml/min). The optimum operating temperature for maximum sensitivity towards 2,4-DNT is also shown (bottom).

The response of the CTO chemiresistor in air (50 ml/min) towards 2,4-DNT is not dissimilar to the response obtained in nitrogen (Figure 19). The CTO undergoes an increase of resistance and the magnitude of the response increases with increasing 2,4-DNT concentration. However, the range (ΔR_g) of responses is smaller in air than in nitrogen, as the baseline response is greater and the maximum response to 2.78 ppm_v 2,4-DNT appears to be similar. At higher concentrations, oxygen appears not to be the limiting factor as the resistance in nitrogen and air are similar. In order to establish whether 2,4-DNT decomposed at the surface and to help establish the possible reaction mechanism giving rise to the observed response, numerous attempts were made to trap and analyse the products of the interaction between the CTO and 2,4-DNT using a vapour trap and gas chromatography. However, the concentration of these products in the 2,4-DNT vapour stream was so low that they could not be distinguished from background noise. Further evidence is required to compliment this data and elucidate the precise mechanism of the interaction with 2,4-DNT.

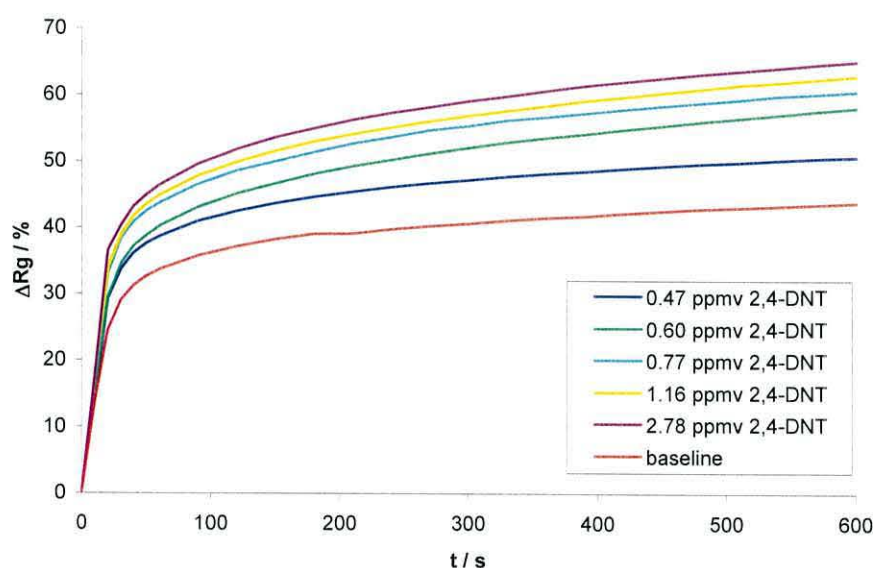


Figure 19. The response of a CTO chemiresistor towards 2,4-DNT (air, 50 ml/min, 50 % RH).

The plot of response versus the square root of 2,4-DNT concentrations (Figure 20) reveals that in air the square root dependence is not followed. The resultant plot is a curve that deviates dramatically from linear. When compared with the plot employing nitrogen as the carrier gas, this shows that the oxygen partial pressure affects the response of the CTO chemiresistor. This result shows that the oxygen partial pressure is an important parameter in the determination of 2,4-DNT in oxygen containing atmospheres, and would need to be known if a quantitative analysis was required.

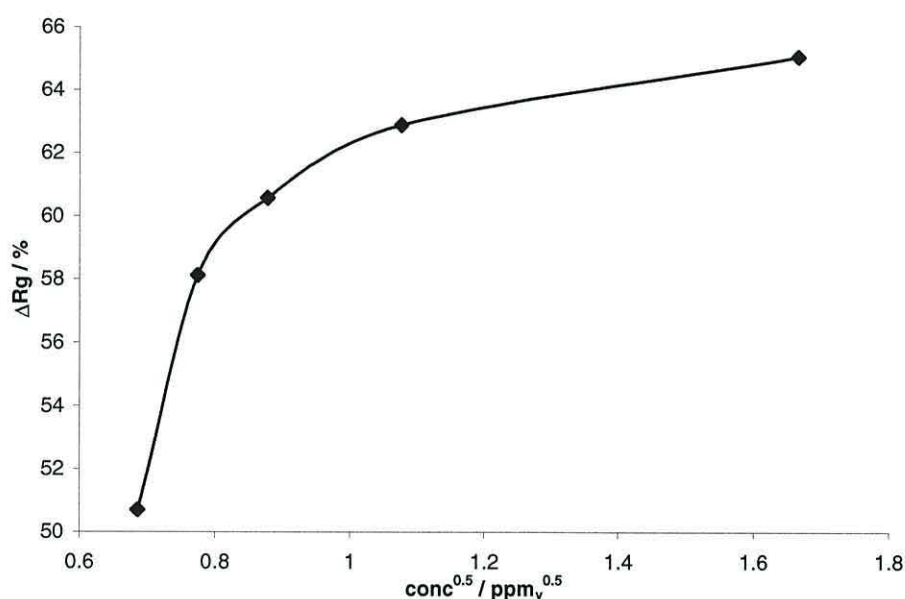


Figure 20. The sensitivity of a CTO chemiresistor exposed to 2,4-DNT in air (0 % RH, 50 ml/min).

The sensor will be required to operate within a sealed vessel and will need to monitor the concentration changes *in situ*. Therefore, an experiment was conducted, whereby the concentration of the 2,4-DNT vapour stream (air, 50 ml/min, 50 % RH) was stepped between 0.47 and 2.78 ppm_v without removing the chemiresistor from the vapour stream. It can be seen in Figure 21 that when the sensor was introduced to the vapour stream, the characteristic response curve was observed. As the concentration was stepped up to 0.60 ppm_v (20 °C), the response of the sensor increased accordingly. The concentration of the vapour stream was further increased to 0.77 ppm_v (60 °C) and a large spike in the

response of the chemiresistor was observed, which settled to a value higher than at the previous lower concentration. A similar spike was observed when the concentration was stepped up to 1.16 ppm_v (80 °C). These spikes occurred as the temperature of the 2,4-DNT in the column of the vapour generator was increased past the melting point of 2,4-DNT (67-70 °C). It is suggested that the rise in temperature caused the 2,4-DNT to melt. At this point the column would become essentially blocked with molten 2,4-DNT as it melted between the beads. This would produce a build up of pressure until the liquid could be pushed through the column leading to an unnaturally high concentration in the vapour stream. As the carrier gas finds a route through the column, the concentration of the vapour stream settles, and this is observed in the sensor response. At 2.78 ppm_v, which corresponds to a temperature of 115 °C, the DNT is completely in the liquid phase, hence no spike is observed, just an increase in the response of the chemiresistor. The fact that the magnitude of ΔR_g after a concentration increase from 0.47 to 2.78 ppm_v, is similar to that observed in Figure 19 further supports this idea.

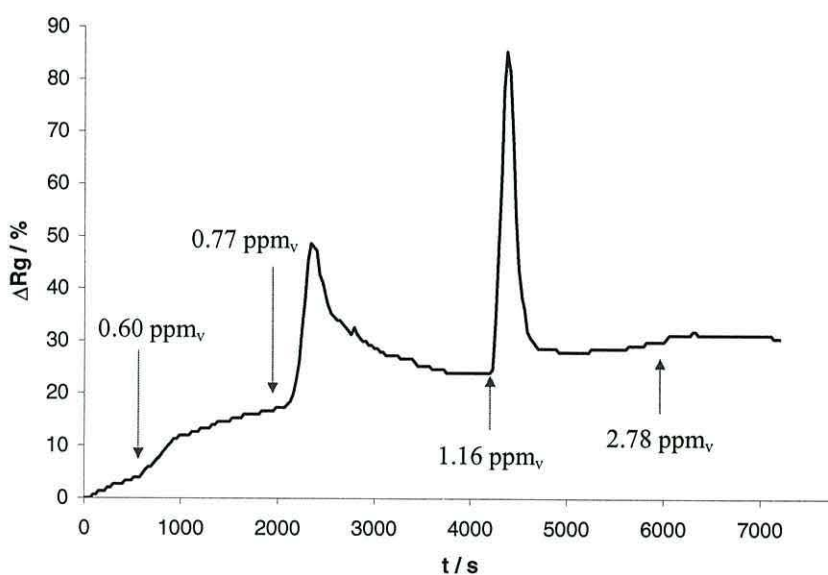


Figure 21. The *in situ* response of the CTO chemiresistor towards 2,4-DNT (air, 50 ml/min), as the concentration was increased from 0.47 ppm_v to 2.78 ppm_v.

3.3.2 The tungsten oxide chemiresistor

Semiconducting tungsten oxide (WO_3) displays n-type behaviour, and undergoes a decrease in resistance upon exposure to a reducing gas [45, 48].

A WO_3 chemiresistor can be seen in Figure 22. It is similar in design to the CTO chemiresistor and the tungsten oxide can be seen as the yellow/green layer. The measuring contacts are situated at the upper diagonal corners, and the heater element is seen as the Pt wire running on the under side of the alumina substrate. The WO_3 chemiresistor was set up to operate at the manufacturers specifications. This corresponds to an operating temperature of 500 °C and a baseline resistance of 1.5 k Ω (air, 50 % RH). The relationship between the sensor resistance and the analyte concentration was stated to follow the square root law, $R_g = R_o \sqrt{[g]}$ (for ozone, air, 50 % RH), where R_g is the resistance in the presence of the target analyte, and R_o is the base resistance.

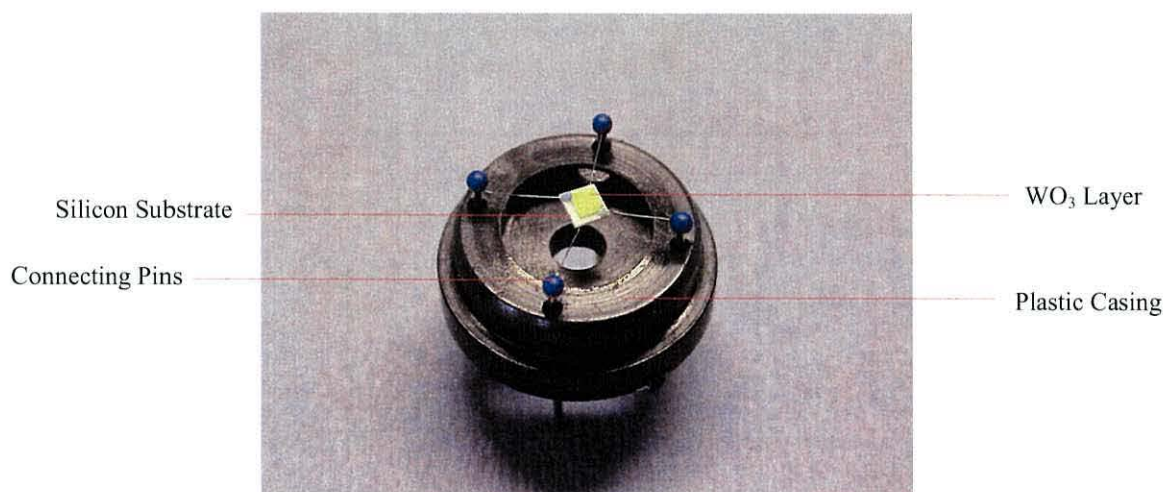


Figure 22. A tungsten oxide (WO_3) chemiresistor.

3.3.2.1 The baseline response towards nitrogen

When the WO_3 chemiresistor is exposed to a nitrogen carrier gas, the composition of the surrounding atmosphere is radically altered. Oxygen and water vapour are removed, and therefore as with CTO, the processes that are likely to occur at the oxide surface are dehydration (equation 15), dehydroxylation (equations 16 and 17), or the removal of

adsorbed or lattice-bound oxygen (equation 14). These processes are likely to contribute to the overall control of the chemiresistor base resistance. The baseline response of the WO₃ chemiresistor in nitrogen was observed as a decrease of the sensors resistance (44 % over 600 s, Figure 23).

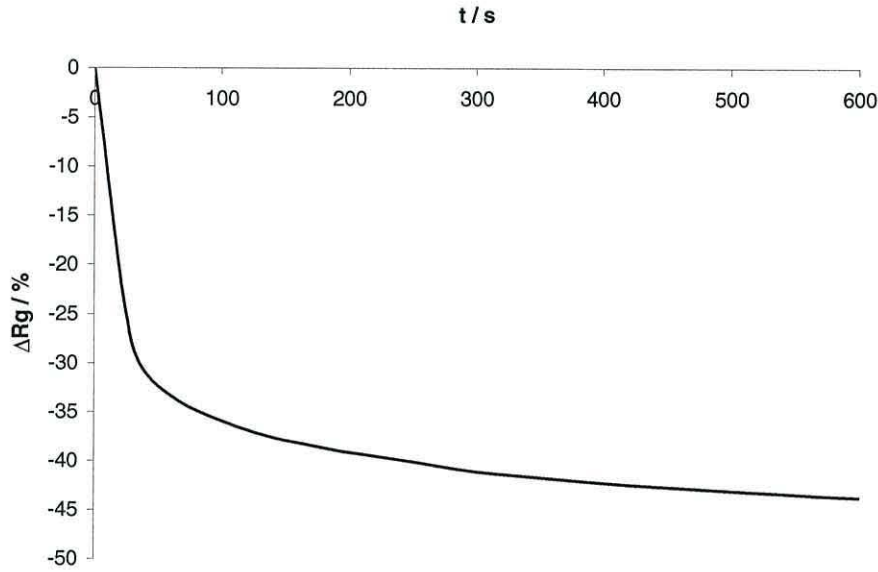


Figure 23. The baseline response of the WO₃ chemiresistor (N₂, 50 ml/min).

This response was opposite in nature to that exhibited by the CTO chemiresistor, which is to be expected since the WO₃ is an n-type semiconductor, but similar to observations in the literature [45, 52] where the resistance was observed to decrease with decreasing oxygen partial pressure. As with the CTO chemiresistor, the fast initial response slowed down and the resistance stabilised, but continued to decrease very slowly with time. This slow decrease of resistance is probably due to the percolation of oxygen vacancies to the oxide bulk, which then become ionised according to equation 20 [48]. However, at these operating temperatures the mobility of the vacancy is very low.



The decrease in film resistance shows that the removal of oxygen species from the surface of the oxide, thus increasing electron density, is likely to be the dominant process, especially since the baseline response of the WO_3 in nitrogen was not significantly affected by the presence of relative humidity, as can be seen in Figure 24. The response of the WO_3 chemiresistor, at different levels of RH, shows little difference in magnitude, follows no particular order, and falls within experimental error of the 0 % RH response.

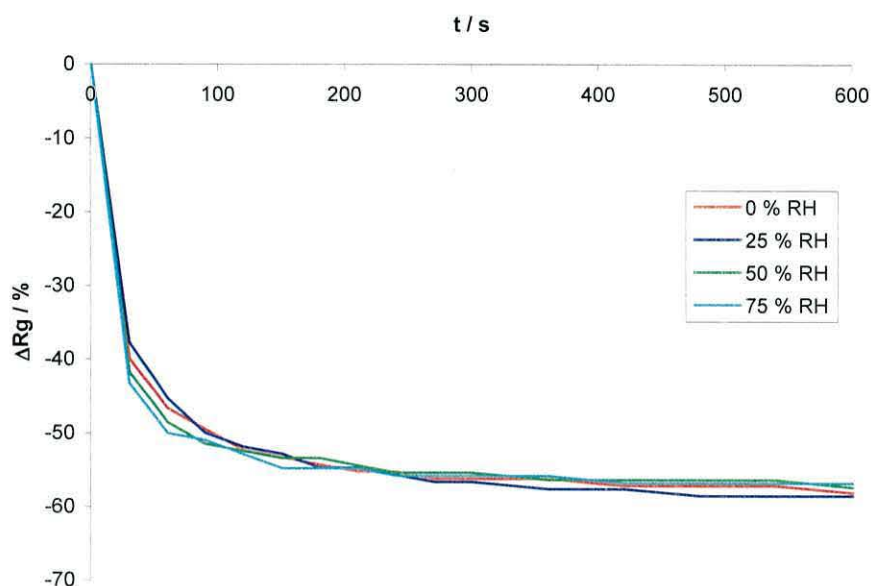


Figure 24. The effect of relative humidity (RH) on the baseline response of a WO_3 chemiresistor (N_2 , 50 ml/min).

3.3.2.2 The baseline response towards air

The assumption that the removal of adsorbed oxygen species and lattice oxygen can be re-enforced by the fact that the negative response is not observed when air is used as the carrier gas (Figure 25). The baseline response of the WO_3 chemiresistor in air was quite different from the response observed in nitrogen. The net response was observed as an increase of the sensors resistance (9.7 % over 600 s).

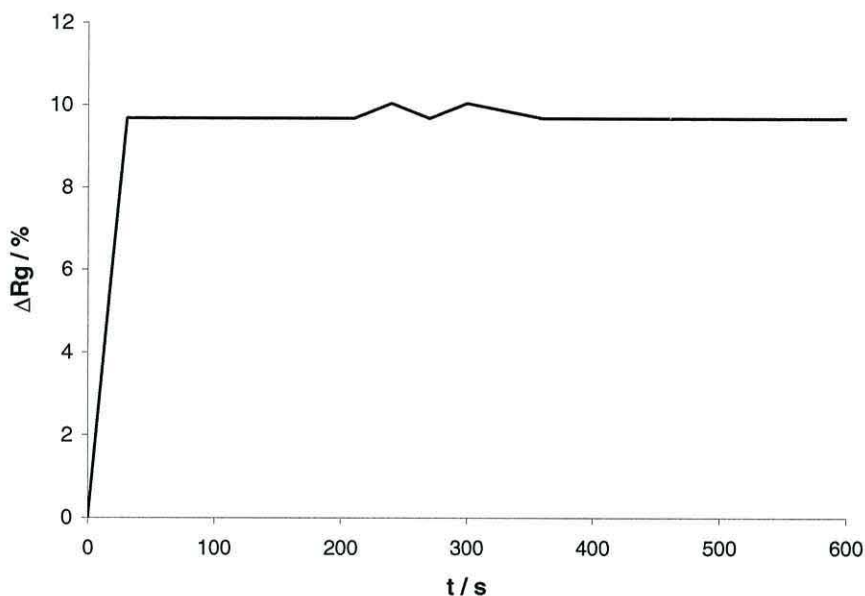


Figure 25. The baseline response of the WO_3 chemiresistor in air (50 ml/min).

As can be seen from Figure 23 and Figure 25, the processes involved during exposure of the chemiresistor towards the carrier gas are clearly influenced by the presence of oxygen, which is most likely able to replace any oxygen species lost from the surface due to the flow of the carrier gas. The slightly positive response is then assumed to be due to the dehydration of the surface, which is supported by the fact that the response decreases as relative humidity is introduced into the air stream (Figure 26). The hydroxylation reaction may be too slow at this temperature to have a significant effect on the response characteristics, at least in the time-scale of this experiment.

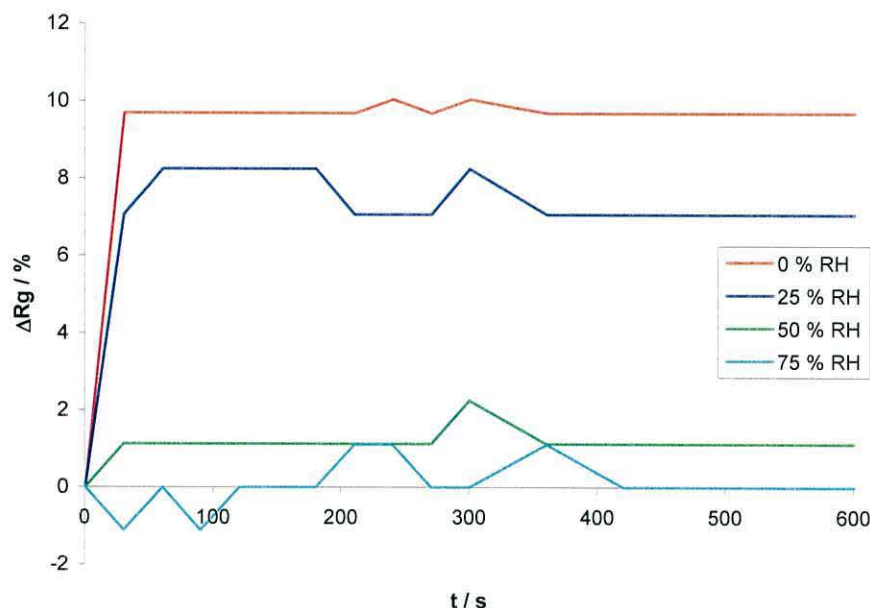


Figure 26. The effect of relative humidity on the baseline response of a WO_3 chemiresistor (air, 50 ml/min).

3.3.2.3 The response towards 2,4-DNT

The response of the WO_3 chemiresistor towards 2,4-DNT in N_2 (50 ml/min) is shown in Figure 27. The resistance of the chemiresistor increased only very slightly, but this response is much greater when compared with the negative baseline response. Therefore, the measurement was repeated by first exposing the chemiresistor to nitrogen, before adding 2,4-DNT into the vapour stream. This separated response, Figure 28, clearly shows the effect of both N_2 and 2,4-DNT on the resistance of the WO_3 layer. Initially, the resistance decreased in the presence of nitrogen, which may be due to the removal of adsorbed oxygen species or lattice oxygen, by the nitrogen carrier gas, as was observed in the baseline response. When 2.78 ppm_v 2,4-DNT was introduced into the vapour stream the resistance of the chemiresistor increased rapidly to a value slightly greater than the base value in static air (50 % RH).

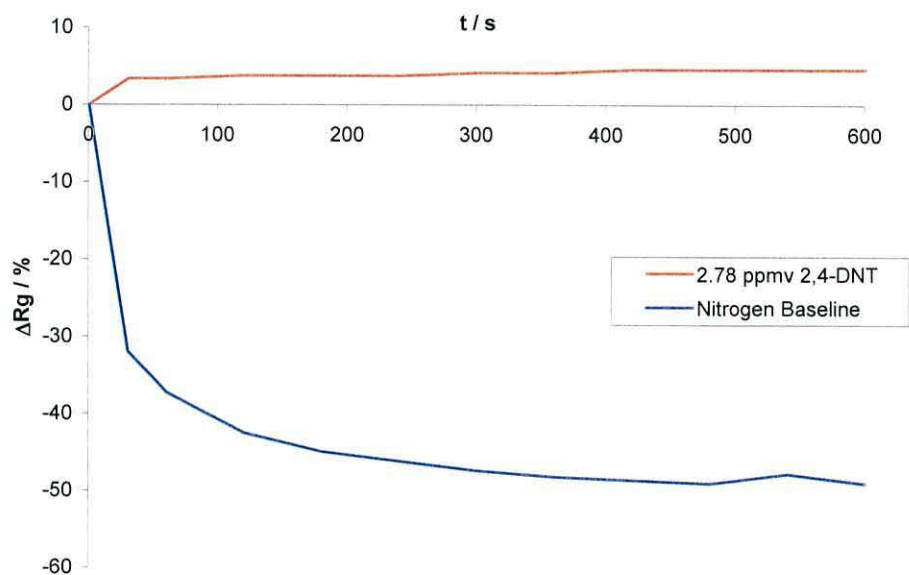


Figure 27. The preliminary response of a WO_3 chemiresistor towards 2.78 ppmv 2,4-DNT (N_2 , 50 ml/min).

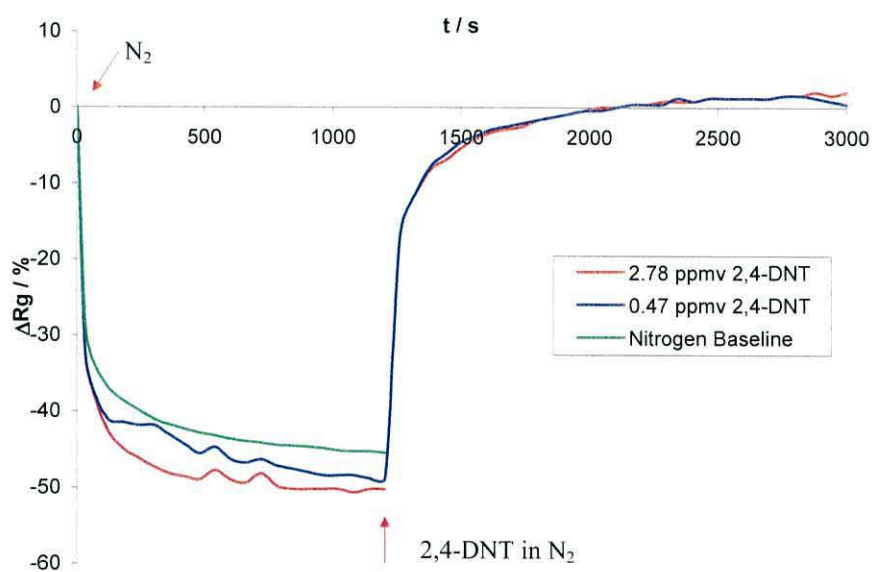


Figure 28. The baseline and subsequent response of a WO_3 chemiresistor towards 2,4-DNT (N_2 , 50 ml/min). 2,4-DNT was introduced into the carrier gas at 1200 s.

These results would favour the suggestion that 2,4-DNT dissociates at the surface of the oxide. This suggestion is perfectly feasible at an operating temperature of 500 °C, as the decomposition temperature for 2,4-DNT is only 300 °C. At this point the NO_x groups may chemisorb to the surface of the WO₃, causing electrons to be removed from the layer, increasing resistance [53]. However, it is known that a decrease in oxygen partial pressure results in the formation of oxygen vacancies, with charge balanced by reduction of W(VI) to W(IV) [52], charge carriers are produced by thermal excitation of electrons from the reduced tungsten into the conductance band [54]. So, it would appear that the nitro groups act to replace the vacant oxygen sites in the lattice, in a similar manner to ozone [52], a point that can be re-enforced by the response of the WO₃ chemiresistor to 2,4-DNT in air.

The response of the WO₃ chemiresistor towards 2,4-DNT in air is very different from that observed in N₂ (Figure 29), showing that the presence of 2,4-DNT acted to very slightly reduce the response of the chemiresistor (~3 %). This decrease in the response was quite low and only just outside experimental error (~2 %). However, it is similar to the response in N₂ after the resistance has increased past the base value. This would certainly suggest that the nitrogen carrier gas resulted in the removal of oxygen adsorbents or lattice oxygen, and the 2,4-DNT filled the oxygen vacancies. If this was the case, it might be assumed that the response of the WO₃ chemiresistor towards 2,4-DNT would be insensitive towards concentration differences in either nitrogen or air, as saturation of the oxide surface would result once the vacancies had been filled. At most, the response might be time dependent at lower concentrations in the nitrogen carrier gas. The lack of concentration dependence was certainly observed in air, as is seen in Figure 28 and Figure 30, respectively.

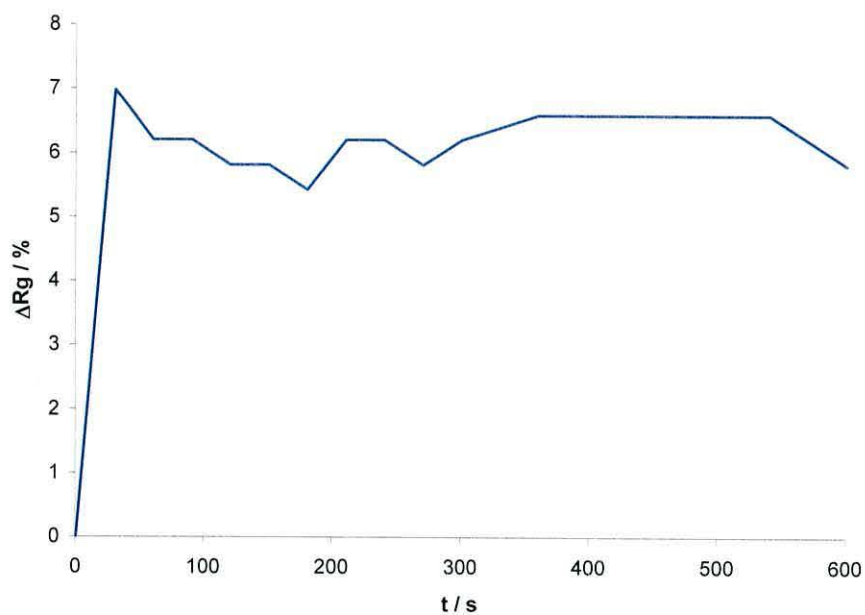


Figure 29. The preliminary response of a WO_3 to 2.78 ppm, 2,4-DNT (air, 50 ml/min).

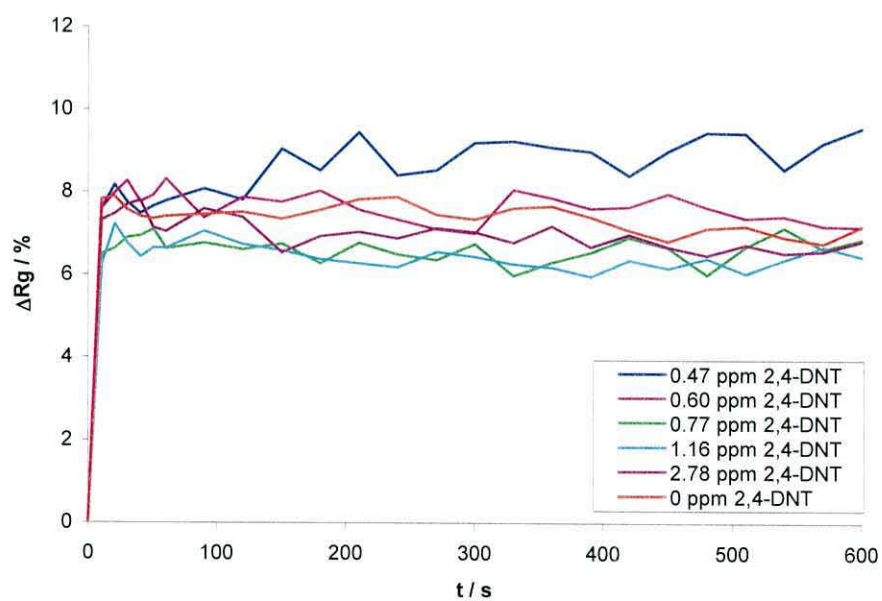


Figure 30. The response of a WO_3 chemiresistor towards 2,4-DNT (air, 50 % RH, 50 ml/min).

The behaviour of the WO_3 chemiresistor, towards 2,4-DNT, was also examined *in situ*. As the temperature of the column was increased, and hence the vapour concentration of 2,4-DNT increased from 0.47 ppm_v to 2.78 ppm_v, there was no significant increase in the resistance of the WO_3 film. Even at the melting point of 2,4-DNT (300 °C), which occurs as the vapour concentration exceeds 0.77 ppm_v 2,4-DNT, no sharp variation in the response is observed. This supports the idea that in the presence of ~20 % oxygen, the WO_3 chemiresistor displays no significant response towards 2,4-DNT vapours. This fact further suggests that there is a competitive adsorption between oxygen and the nitroaromatic to fill oxygen vacancies, and since oxygen is at a much higher concentration, it dominates the adsorption, occupying the available sites.

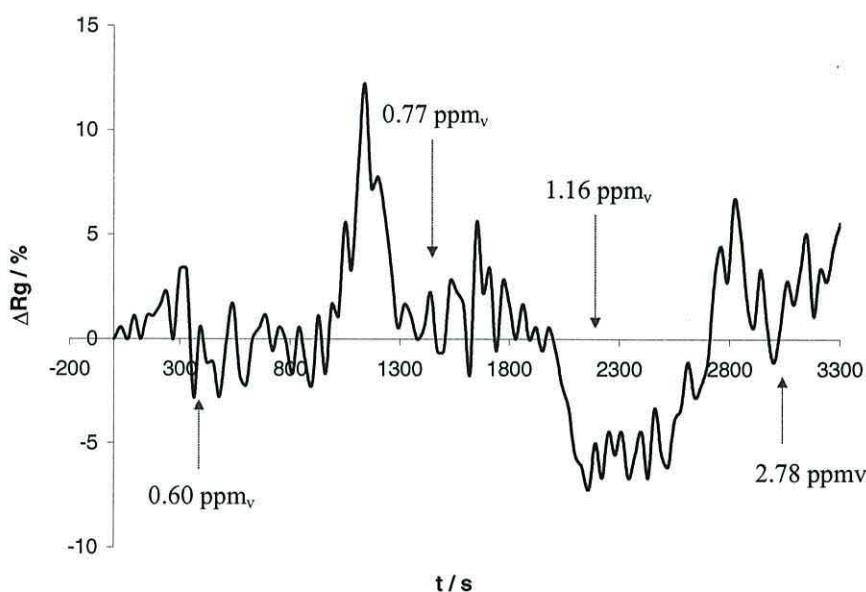


Figure 31. The *in situ* response of a WO_3 chemiresistor towards 2,4-DNT (air, 50 % RH, 50 ml/min), as the concentration was increased from 0.47 ppm_v to 2.78 ppm_v.

For the WO_3 chemiresistor to be suitable as a sensor for nitroaromatics, it appears that a much lower oxygen partial pressure is required. This acts to introduce oxygen vacancies in the WO_3 lattice and decreases the number of adsorbed oxygen species at the surface of the film. 2,4-DNT is likely to decompose at the surface and the decomposition products “fill” the vacancies. It was observed that 0.47 ppm_v 2,4-DNT led to a rapid response,

filling the vacancies, and quickly saturating the sensor. Therefore, the WO_3 chemiresistor would need to be exposed to a greatly diluted 2,4-DNT vapour stream, in order to see whether any separation of responses could be observed for different concentrations. Another means of creating more oxygen vacancies is to increase the operating temperature of the oxide layer. This also results in a more mobile vacancy that can migrate to the bulk; leading to a bulk-type conductance mechanism (equations 4 and 5). It is noted that the increased operating temperature may not be a welcomed change to the system, as nitroaromatics can be explosive.

The effect of operating temperature was examined at 280, 360, 400 °C, and 500 °C. Initially, the resistance of the WO_3 chemiresistor increased with temperature, which is not characteristic of a semiconductor, and the opposite response to that of the CTO. However, this is likely to be due to the effect of oxygen adsorbents. As the temperature increased, the concentration of adsorbents at the surface is also likely to have increased. Oxygen adsorbents remove electron density from the surface, increasing the resistance. Between 400 and 500 °C adsorbed oxygen species (O^-) may be removed as desorption becomes more favourable. This has been observed to occur at 500 °C for O^- on SnO_2 [47]. This would cause the electron density to increase in the oxide, and the fact that the oxide is n-type, would cause the resistance to decrease. This is in agreement with other evidence that suggests that at elevated temperatures, oxygen adsorbents control the resistance of a thin semiconductor layer [1]. The response towards 2,4-DNT at these different temperatures displayed a slight trend. The response became more positive as the temperature increased. This response also suggests that the response of the chemiresistor, towards 2,4-DNT is dependent on the temperature of the oxide film. The response was also dependent on the concentration of oxygen at the surface of the film, and it appears that there is a competitive process of adsorption between oxygen and 2,4-DNT.

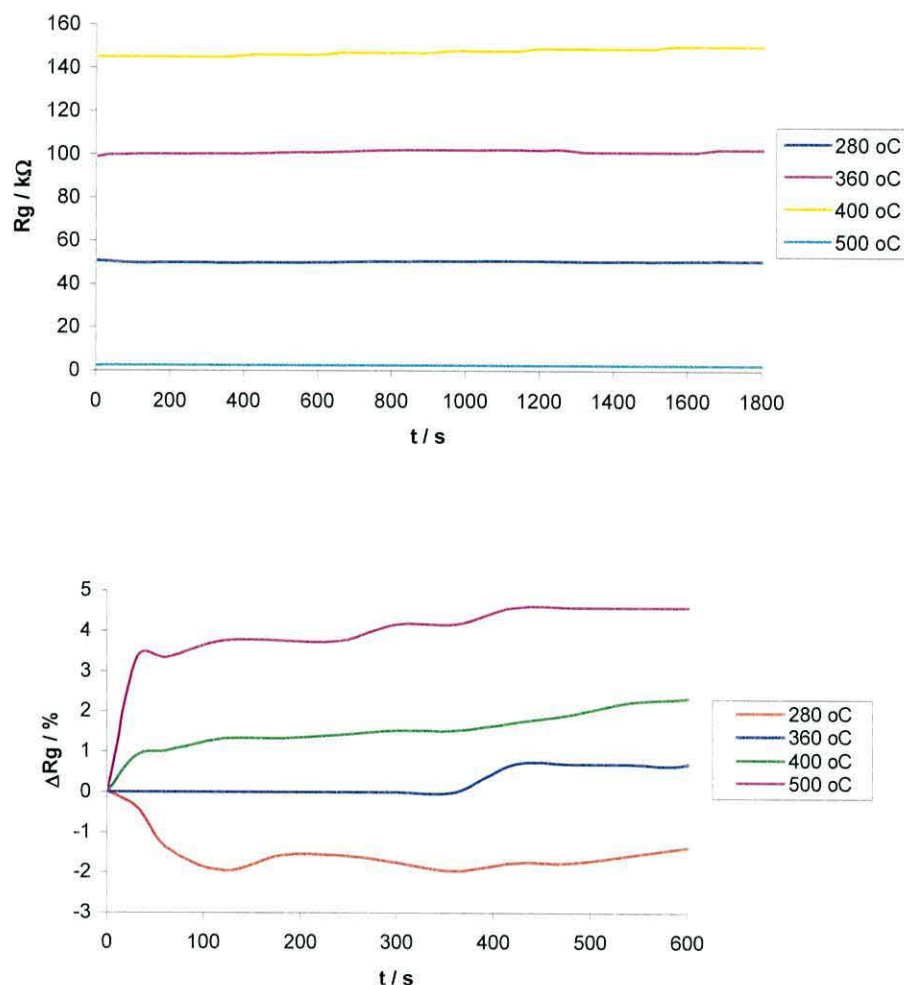


Figure 32. The effect of operating temperature on the resistance (top) and normalised response (bottom) of a WO_3 chemiresistor towards 1.16 ppm, 2,4-DNT (N_2 , 50 ml/min).

3.4 Conclusions

Metal oxide gas-sensitive resistors such as chromium titanium oxide and tungsten oxide were examined as possible sensors for the detection of alkyl-polynitroaromatics. CTO was observed to undergo an increase of resistance upon exposure to a nitrogen carrier gas, which is believed to be due to a combination of the removal of adsorbed oxygen species and dehydration/dehydroxylation processes. The presence of RH gave rise to a greater response, due to the negative-type chemisorption of molecular water. 2,4-DNT also prompted an enhanced response, which was shown to be proportional to $\sqrt{[DNT]}$,

and reversible. The optimum operation temperature for maximum sensitivity towards 2,4-DNT was found to lie between 300 and 330 °C. WO₃ exhibited a decrease in resistance upon exposure to a nitrogen carrier gas, which was found to be due to the removal of adsorbed oxygen species and independent of RH. 2,4-DNT resulted in a positive (i.e. increase of film resistance) response, which was independent of concentration but competitive with oxygen. The response varied with operating temperature, with the optimum being the highest temperature tested, 500 °C. It is proposed that 2,4-DNT decomposes at the oxide surface at the operating temperature and replaces the oxygen vacancies. The presence of oxygen in the carrier gas severely diminished the response.

3.5 Future work

The study discussed above was carried out to establish the possibility of using metal oxide chemiresistors as sensors for nitroaromatics. There is still a great deal of work required in order to establish the precise nature of the interactions of these metal oxides with 2,4-DNT. Experiments are required to determine the desorption-temperatures of adsorbed and lattice oxygen from the oxide, the desorption temperatures of H₂O and OH species from the oxide surface. It would also be very useful to ascertain the nature of water adsorption when the oxide is exposed to relative humidity. It must also be ascertained whether or not 2,4-DNT decomposes at the oxide surfaces, and at what temperature, if any, decomposition occurs. These experiments would require the precise measurement of the sensors operating temperature and also a technique for identifying surface species.

3.6 References

1. K. J. Albert, *Chem. Rev.* **100** (2000) 295-2626.
2. D.-S. Lee, C.-H. Shim, J.-W. Lim, J.-S. Huh, D.-D. Lee, and Y.-T. Kim, *Sens. Actuators, B.* **83** (2002) 250-255.
3. D.-S. Lee, H.-Y. Jung, J.-W. Lim, M. Lee, S.-W. Ban, J.-S. Huh, and D.-D. Lee, *Sens. Actuators, B.* **71** (2000) 90-98.
4. J. R. Stetter, S. Strathmann, C. McEntegart, M. Decastro, and W. R. Penrose, *Sens. Actuators, B.* **69** (2000) 410-419.

5. V. Grimaldi and J.-L. Politano, *SPIE*. **2937** (1997) 90-99.
6. Y. Shimizu and M. Egashira, *MRS Bull.* . **24** (1999) 18-24.
7. T. Seiyama, A. Kato, K. Fujiishi, and N. Nagatami, *Anal. Chem.* **34** (1962) 1502.
8. A. M. Azad, S. A. Akbar, S. G. Mhaisalkar, L. D. Birkfield, and K. S. Goto, *J. Electrochem. Soc.* **139** (1992) 3690-3704.
9. J. Watson and K. Ihokura, *MRS Bull.* . **24** (1999) 14-15.
10. G. Williams and G. S. V. Coles, *MRS Bull.* . **24** (1999) 25-27.
11. P. W. Atkins, *Physical Chemistry*. 5th ed. Oxford University Press, Oxford, (1997).
12. J. Janata, *Principles of Chemical Sensors*. Plenum Press, New York, (1989).
13. D. Kohl, *Sens. Actuators, B.* **18** (1989) 71-113.
14. B. K. Miremadi, R. C. Singh, Z. Chen, S. Roy Morrison, and K. Colbow, *Sens. Actuators, B.* **21** (1994) 1-4.
15. M. Fleischer, H. Meixner, M. Seth, and C.-D. Kohl, *Sens. Actuators, B.* **36** (1996) 290-296.
16. D.-S. Lee, S.-D. Han, J.-S. Huh, and D.-D. Lee, *Sens. Actuators, B.* **60** (1999) 57-63.
17. H.-M. Lin, C.-H. Keng, and C.-Y. Tung, *Nanostruct. Mater.* **9** (1997) 747-750.
18. J. S. Han, T. Bredow, D. E. Davey, A. B. Yu, and D. E. Mulcahy, *Sens. Actuators, B.* **75** (2001) 18-23.
19. D. H. Dawson, G. S. Henshaw, and D. E. Williams, *Sens. Actuators, B.* **26-27** (1995) 76-80.
20. U. Lampe, J. Gerblinger, and H. Meixner, *Sens. Actuators, B.* **25** (1995) 657-660.
21. U. Lampe, J. Gerblinger, and H. Meixner, *Sens. Actuators, B.* **26** (1995) 97-98.
22. S. Matsubara, D. Ikeda, K. Kobayashi, and G. Okada, *Chem. Lett.* (1992) 323-326.
23. J. Frank, M. Fleischer, H. Meixner, and A. Feltz, *Sens. Actuators, B.* **49** (1998) 110-114.
24. V. Dusastre and D. E. Williams, *J. Phys. Chem. B* **102** (1998) 6732-6737.
25. I. Sayago, J. Gutierrez, L. Ares, J. I. Robla, M. C. Horrillo, J. Getino, J. Rino, and J. A. Agapito, *Sens. Actuators, B.* **26-27** (1995) 19-23.
26. J. Shieh, H. M. Feng, M. H. Hon, and H. Y. Juang, *Sens. Actuators, B.* **86** (2002) 75-80.
27. A. Fort, M. Gregorkiewicz, N. Machetti, S. Rocchi, B. Serrano, L. Tondi, N. Ulivieri, V. Vignoli, G. Faglia, and E. Comini, *Thin Solid Films* **418** (2002) 2-8.
28. R. Gutierrez-Osuna, A. Gutierrez-Galvez, and N. Powar, *Sens. Actuators, B.* **93** (2003) 57-66.
29. M. Fleischer and H. Meixner, *Sens. Actuators, B.* **25** (1995) 544-547.
30. A. P. Lee and B. J. Reedy, *Sens. Actuators, B.* **60** (1999) 35-42.
31. R. Muller and E. Lange, *Sens. Actuators.* **9** (1986) 39-48.
32. M. Fleischer, S. Kornely, T. Weh, J. Frank, and H. Meixner, *Sens. Actuators, B.* **69** (2000) 205-210.
33. M. H. Madhusudhana Reddy and A. N. Chandorkar, *Thin Solid Films* **349** (1999) 260-265.
34. M. Eriksson and L.-G. Ekedahl, *Sens. Actuators, B.* **42** (1997) 217-223.
35. J. Mizsei, *Sens. Actuators, B.* **28** (1995) 129-133.

36. K. D. Schierbaum, U. K. Kirner, J. F. Geiger, and W. Gopel, *Sens. Actuators, B.* **4** (1991) 87-94.
37. H. Teterycz, R. Klimkiewicz, and B. W. Licznarski, *Appl. Catal., A* **214** (2001) 243-249.
38. Y. Shimizu, N. Matsunaga, T. Hyodo, and M. Egashira, *Sens. Actuators, B.* **77** (2001) 35-40.
39. J. G. Duh, J. W. Jou, and B. S. Chiou, *J. Electrochem. Soc.* **136** (1989) 2740-2747.
40. M. L. Grilli, E. Di Bartolomeo, and E. Traversa, *J. Electrochem. Soc.* **148** (2001) H98-H102.
41. J. L. Solis, S. Saukko, L. B. Kish, C. G. Granqvist, and V. Lantto, *Sens. Actuators, B.* **77** (2001) 316-321.
42. Y.-K. Chung, M.-H. Kim, W.-S. Um, H.-S. Lee, J.-K. Song, S.-C. Choi, K.-M. Yi, M.-J. Lee, and K.-W. Chung, *Sens. Actuators, B.* **60** (1999) 49-56.
43. C. Xu, J. Tamaki, N. Miura, and N. Yamazoe, *Sens. Actuators, B.* **3** (1991) 147-155.
44. F. Reti, M. Fleischer, J. Gerblinger, U. Lampe, E. B. Varhegyi, I. V. Perczel, H. Meixner, and J. Giber, *Sens. Actuators, B.* **26-27** (1995) 103-107.
45. D. E. Williams, *Sens. Actuators, B.* **57** (1999) 1-16.
46. J. Giber, I. V. Perczel, J. Gerblinger, U. Lampe, and M. Fleischer, *Sens. Actuators, B.* **18-19** (1994) 113-118.
47. G. Martinelli and M. C. Carotta, *Sens. Actuators, B.* **23** (1995) 157-161.
48. P. T. Moseley, *Sens. Actuators, B.* **6** (1992) 149-156.
49. T. Hubert, *MRS Bull.* **24** (1999) 49-54.
50. F. Reti, M. Fleischer, H. Meixner, and J. Giber, *Sens. Actuators, B.* **18-19** (1994) 138-142.
51. , *CRC Handbook of Chemistry and Physics*. 76th ed, ed. D. R. Lide. CRC Press, Inc., London, (1995).
52. D. E. Williams, S. R. Aliwell, K. F. E. Pratt, D. J. Caruana, R. L. Jones, R. A. Cox, G. M. Hansford, and J. Halsall, *Meas. Sci. Technol.* **13** (2002) 923-931.
53. H. Kawasaki, J. Namba, K. Iwatsuji, Y. Suda, K. Wada, K. Ebihara, and T. Ohshima, *Appl. Surf. Sci.* **197-198** (2002) 547-551.
54. S. R. Aliwell, J. Halsall, K. F. E. Pratt, J. O'Sullivan, R. L. Jones, R. A. Cox, S. R. Utembe, G. M. Hansford, and D. E. Williams, *Meas. Sci. Technol.* **12** (2001) 684-690.

CONDUCTING POLYMER CHEMIRESISTORS

4.1 Introduction

Conducting polymers have rapidly become a very important class of materials, particularly in the electronics industry where they are utilised for both their electronic and electrochromic properties. Real interest in conducting polymers was triggered by Heeger, MacDiarmid and Shirakawa in 1977, when they showed that a ten fold increase in the conductivity of polyacetylene could be obtained by doping with iodine [1, 2]. This prompted research into the possible use of polyacetylene in the construction of batteries [3, 4]. The ensuing period gave rise to the discovery of many other conducting polymers, with polyaniline, polypyrrole and polythiophene amongst the most studied.

4.1.1 Conduction in polymers

The precise nature of charge carriers in conducting polymers varies from material to material, and is still a matter of debate [5]. Therefore, electronic conduction in polymers is best-explained using polyacetylene as the simplest example. In polyacetylene, carbon units are linked together by an alternating pattern of single and double bonds, which forms an extended π -system along the carbon chain. This alternating pattern gives rise to a number of possible structures, of which the two *trans* structures are thermodynamically equivalent and stable. This not only gives rise to two degenerate ground states, but also the possibility of defects where the two states meet on a single chain (Figure 1). The defect site, known as a soliton, will have an unpaired electron (although the overall charge will remain zero), which creates a new energy level within the band-gap. This neutral state has spin $\frac{1}{2}$ and is estimated to be delocalised over 15 carbon atoms [5]. However, as the energy gap (band-gap) in the pristine polymer is comparatively large (~ 1.6 eV for polyacetylene), the intrinsic conductivity will be quite low [6]. As the soliton gives rise to a mid-gap energy level it can also accept or release charge, giving rise to charged defects possessing no spin. Two neutral solitons, caused by the defect, might be expected to recombine unless isolated by a topological defect. Two charged solitons are likely to repel each other, leading to isolated defects. However, if a charged defect meets a neutral defect they

will tend to combine forming a polaron [7], which is a radical cation, creating two states in the band-gap.

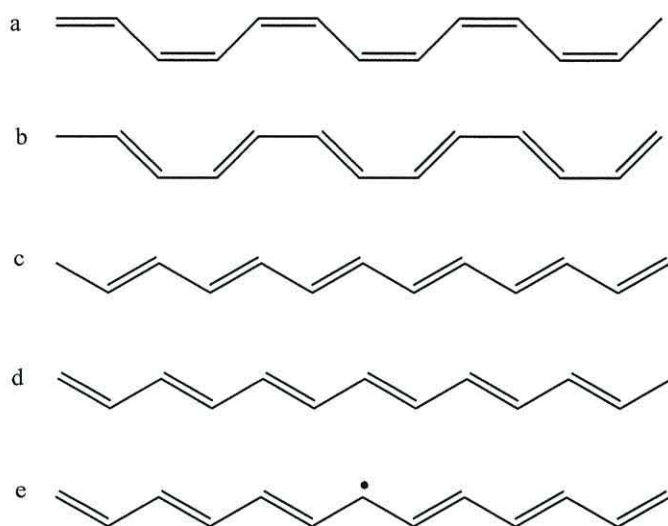


Figure 1. Possible structures for polyacetylene showing two non-degenerate cis structures, two degenerate trans structures (c and d) and a soliton defect at the junction of two degenerate trans phases (e).

Trans-polyacetylene is unique in its ground state degeneracy, and most other conducting polymers possess no degeneracy, which in turn affects the nature of charge carriers that they can support. In such polymers the formation of solitons is energetically unfavourable and the preferred configurations involve paired sites. If a pair of radicals exists on the chain and they are both neutral they will recombine to eliminate the defect, but if one is charged a polaron is formed, which for polyaromatics is delocalised over five rings. However, in contrast to polyacetylene, when both defects are charged, rather than separating along the chain they are predicted to pair up to form a bipolaron [7]. A bipolaron is a doubly charged defect, which is also delocalised over approximately five rings, but has no spin. At high doping levels bipolarons may also form a bipolaron band within the band-gap. A more detailed explanation is given in [8].

Conducting polymers generally exhibit semiconducting to insulating levels of conductivity in their pristine (neutral) state but can approach near metallic conductivity upon adequate doping [9]. It must be emphasised that the term doping is not analogous with that used for semiconductors. In semiconductors, the dopant,

which possesses different electron affinity, replaces an atom in the lattice framework, whereas in conducting polymers doping refers directly to the addition or removal of charge from the π -conjugated backbone of the polymer. During the doping process of conducting polymers anions are incorporated into the film in order to maintain charge neutrality. Table 1 shows the conductivities of the four most common conducting polymers and their counter ions.

Polymer	Counter ion	Conductivity
Polyacetylene	I ₂ chemically	$< 100 \text{ Scm}^{-1}$
Polyaniline	Cl ⁻	$9 \times 10^{-2} \text{ Scm}^{-1}$
Polythiophene (film)	PF ₆ ⁻	10 Scm^{-1}
Polypyrrole (film)	BF ₄ ⁻	$30\text{-}100 \text{ Scm}^{-1}$

Table 1. A table showing conductivities for polyacetylene [1, 2], polyaniline [10], polythiophene [5], and polypyrrole [5, 8].

It should be noted that the conductivity of Polyaniline (Pani) is dependent not only on the oxidation state, but also on the level of protonation. As it is believed that only the imine nitrogen are protonated; protonation reaches a maximum level of 50 %.

4.1.2 Polymer-based chemiresistors

Chemiresistors offer a simple yet effective means of monitoring the presence of an analyte. This is because the semiconducting layer acts not only as the reactive site for interaction with the analyte, but also the transducer. One problem with traditional inorganic solids, such as the metal oxides, is their inherent lack of selectivity. Organic conductors, with receptors attached directly to their backbone offer a viable approach towards increasing selectivity [11]. Hence, conducting polymer-based materials have been utilised as gas-sensitive materials and have found application in the detection of several analytes, including ammonia [12, 13], methanol [14, 15], ethanol [14], nitrogen oxides [13, 16-18], toluene [19], xylene [20], hydrogen chloride [12], hydrogen cyanide [21], and hydrogen sulphide [16].

Polymer-based chemiresistors are typically formed by casting a polymer film over two metal electrodes, typically microelectrodes separated by a gap of several μm .

Deposition of the polymer layer can be achieved through dip coating [12], spin casting [14, 17, 19, 22] or electrochemical means [16, 20, 23, 24]. This renders an electrical connection between the electrodes, which can then be measured with a simple ohmmeter. The principle behind the utilisation of a polymer-based resistor as a chemical sensor relies on changes in the electrophysical properties of the polymer upon interaction with the analyte. The overall dc conductivity (σ) of conducting polymers is affected by three components.

$$\Delta\sigma = (\Delta\sigma_{\text{intra}}^{-1} + \Delta\sigma_{\text{inter}}^{-1} \Delta\sigma_{\text{ionic}}^{-1})^{-1} \quad (1)$$

Where $\Delta\sigma_{\text{intra}}$ is the overall change in the intra-molecular conductivity caused by changes in the doping levels in the polymer. $\Delta\sigma_{\text{inter}}$ is the change in the inter-molecular conductivity caused by modulation of electron hopping across polymer chains due to the presence of the analyte. $\Delta\sigma_{\text{ionic}}$ is the change of ionic conductivity between chains caused by analyte sorption. The value $\Delta\sigma_{\text{ionic}}$ is not only a function of ion migration upon condensation of the analyte, but also a function of proton tunnelling rates if hydrogen-bonding to the polymer backbone is significant [25].

Changes in the electrophysical properties of the polymer can arise from polymer swelling [9, 25], counter ion solvation [24, 25], changes in the pH of the surrounding environment [26], addition or removal of charge carriers from the π -conjugated backbone [9] or interactions with reactive functional groups attached to the polymer backbone [9, 25]. Polymer swelling occurs as the polymer layer absorbs the analyte, causing structural changes or kinks in the π -conjugated backbone that limits the extent of delocalisation, thereby causing the film resistance to increase [15]. The analyte may also be able to interact directly with the conjugated backbone of the polymer. If the analyte is an electron acceptor molecule, charge may be removed from the backbone and vice versa. This may act to increase or decrease the film resistance, depending on the nature of the analyte and the initial doping level of the polymer. Polypyrrole and polythiophene derivatives have been shown to exhibit increased conductivity when exposed to gases such as NO_2 and SO_2 [13, 16, 17]. The analyte is believed to act as a dopant, removing charge from the polymer backbone in a similar manner to the doping of polyacetylene with iodine [1]. Conversely, the exposure of

Pani to ammonia results in a decrease in the film conductivity and it has been suggested that this is due to leaching of the polaronic sites [26].

Polymer-based chemiresistors can be modified to increase their sensitivity towards a particular analyte by the addition of functional groups to the polymer backbone. Examples in the literature include 3-alkyl and 3-carboxy substituted polypyrroles [27] and 3-alkoxy modified polythiophene [22] for the detection of volatile organics. Polymers can also be modified by the entrapment of enzymes or other reactive materials within the bulk of the polymer [9, 20]. A report by MacDiarmid in 1997, following a study concerning the response of dodecylbenzenesulfonate doped polypyrrole towards various organic solvents, stated that the response of a gas sensitive resistor to a given analyte was dependent on the nature of the dopant anion in the polymer [28]. This effect seemed to be useful in promoting selectivity. Non-conducting polymers loaded with conducting graphite or carbon black fillers have also been utilised as gas-sensitive resistors, with large responses observed for both xylene and ethanol [20].

4.1.3 Heteropolyanions (HPAs)

Heteropolyanions are a class of inorganic cluster compounds, usually prepared using molybdenum and tungsten. There are up to 35 heteroatoms that have been used in the production of heteropolyanions, including many non-metals and transition metals, often in more than one oxidation state [29]. There are many different types of HPAs, including Dawson $[X_2M_{18}O_{62}]^{n-}$ and Keggin $[XM_{12}O_{40}]^{n-}$ types, where M is a metal addenda ion (typically W^{VI} or Mo^{VI}), and X is the heteroatom (including Si^{IV} , Ge^{IV} , P^V , and As^V). The Keggin type HPA consists of a heteroatom, X, which adopts tetrahedral co-ordination, cloaked by four trigonal groups of edge-sharing MO_6 octahedra, each sharing corners with neighbouring groups and with the central heteroatom tetrahedron [30]. This structural formation leads to a near spherical polyanion as can be seen in Figure 2.

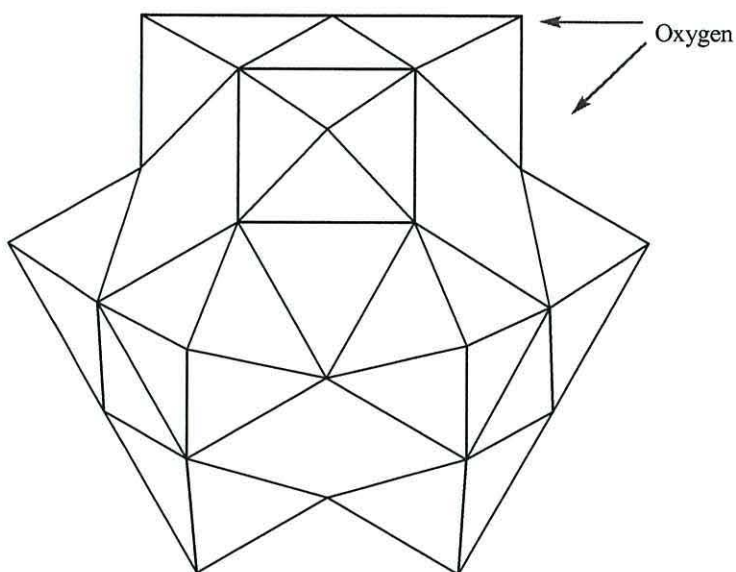


Figure 2. The co-ordination polyhedra representation of the Keggin structure ($\text{XM}_{12}\text{O}_{40}^{n-}$, the fourth set of M_3O_{13} is not shown for clarity) [31].

It is well known that Keggin type HPAs have interesting acid and redox catalytic properties. They are also highly stable in most of their redox states and there is the possibility of tuning the redox potentials by changing the hetero and addenda ion, without affecting their structure [32]. This has inspired a great deal of interest in their use as catalysts and charge transfer agents in a variety of chemical processes, including the reduction of bromate [33], chlorate [34], nitrite [35-39], the carbonylation of nitrobenzene [40], hydrogenation reactions [41], including the hydrogenation of nitro compounds [42], the synthesis of methyl tertbutyl ether [43], peroxide generation at polymer electrodes [44], and the detection of cations [45] and NO [46]. HPAs are multi-electron oxidants (electron acceptors) and the mechanism of reduction of Keggin HPAs involves the transfer of up to six electrons without collapse of the structure [30]. In their reduced form HPAs can also act as reductants (electron donors) [47]. Mixed valence HPAs are characterised by an intense blue colour (heteropolyblue). A more detailed survey of the catalytic properties of HPAs can be found in references [30] and [32].

Heteropolyanions can be used directly in solution or immobilised within different supports, and for the sake of efficiency, the supported method is often preferred [31]. There have been many reports on the immobilisation of HPAs into polymer-based supports using both conducting and non-conducting polymers [47]. Conducting

polymer-HPA composite materials can be produced chemically [48] or electrochemically [33, 34, 37-39, 45-47, 49-53]. Electrochemical deposition can be performed as one-step or two-step processes. The one-step process involves the polymerisation of the monomer in the presence of the HPA. Usually, the heteropoly compound acts as the supporting electrolyte and its anions are incorporated into the film on doping to maintain charge neutrality, where they subsequently become trapped in the polymer matrix [51] as the film thickness increases. The two-step process involves forming an initial polymer layer by conventional techniques, followed by cycling the film in a solution containing only the HPA. The heteropolyanion diffuses into the film over time [47]. In all cases the modified polymer films not only display the redox characteristics of the conducting polymer, but also the redox characteristics of the HPA.

4.1.4 Aims of the study

The aim of this study was to undertake a preliminary investigation into the potential use of unmodified and HPA-modified conducting polymer films for the detection of nitroaromatic vapours. Emphasis was placed on attaining a sufficient response from the polymer films in order that a sensor for nitroaromatics could be produced and tested. Therefore, the preliminary responses of different films were evaluated rather than a complete study of any single film.

4.2 Experimental

The polymer-based chemiresistors consisted of a polymer film deposited onto two platinum microband electrodes. The microband electrodes were approximately $1000 \times 100 \mu\text{m}$, and separated by a gap of $5 \mu\text{m}$ (Figure 3). These electrodes acted as the electrical contacts through which the resistance of the film was measured.

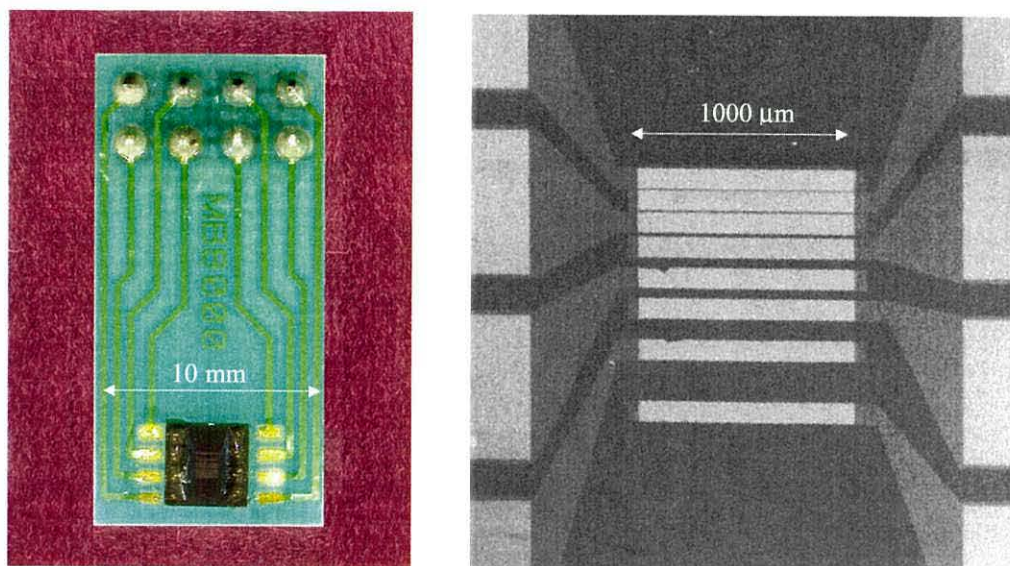


Figure 3. A platinum electrode array. The array consists of eight electrodes with separations varying from 5 – 200 μm . The array is also shown mounted on a pcb connecting board, left.

4.2.1 Polymer deposition

Once the electrodes had been cleaned as described in the experimental section, the polymer films were deposited electrochemically. Details of the deposition conditions are given in Table 2. Pani films were prepared from aqueous HCl solutions using a Pt-foil counter electrode, and all potentials are quoted relative to the saturated calomel electrode (SCE). Poly(3-methylthiophene) and Polymer-HPA films were prepared from acetonitrile solutions using a Pt-foil counter electrode, and all potentials were measured relative to the Ag/Ag^+ (0.01 M) electrode. After the appropriate amount of charge had been passed the films were removed from the monomer solution and rinsed thoroughly with monomer free electrolyte solution.

It should be noted that in order for polymerisation of 3-methylthiophene to proceed in the presence of the HPA, a larger monomer concentration was required compared with the growth of the plain P3MT- PF_6 films. This has also been noted in [50, 51].

Polymer	Electrolyte solution	Monomer concentration	Potential range	Sweep rate
Pani-Cl	1 M HCl _(aq)	1 M	-0.2 – 0.75 V	100 mVs ⁻¹
Pani-HPA	0.1 M HPA, Acetonitrile	0.1 M	-0.2 – 1.0 V	100 mVs ⁻¹
P3MT-PF ₆	0.1 M TBAPF ₆ , Acetonitrile	0.1 M	0 – 1.2 V	50 mVs ⁻¹
P3MT-HPA	0.1 M HPA, Acetonitrile	0.5 M	0 – 1.2 V	50 mVs ⁻¹

Table 2. The polymerisation conditions used during the preparation of the polymer-based chemiresistors.

4.2.2 Characterisation – voltammetry

Prior to characterisation, all polymer films were cycled in monomer-free solutions to ensure the removal of any residual monomer trapped within the polymer layer. The films were then characterised in the solvent that was used during the growth of the films. Therefore, Pani-Cl films were characterised in aqueous solutions containing 1 M HCl, between -0.2 and +0.5 V at 10 mVs⁻¹, while Pani-HPA and all other P3MT films were characterised in acetonitrile solutions containing 0.5 M HClO₄. The potential limits were -0.5 to +0.6 V vs. Ag/Ag⁺ (0.01 M), and the sweep rate was 50 mVs⁻¹, unless otherwise stated.

4.2.3 Response of the polymer-based chemiresistors

Following the characterisation, the oxidation state (doping level) of the polymer film was “set” by holding the polymer at the required potential for a period of 5 minutes. Charge neutrality was maintained through the incorporation of the anion into the film. The polymer-based chemiresistors were then removed from solution and rinsed with the electrolyte solvent and allowed to dry in air over 48 hours.

The responses of the polymer-based chemiresistors were determined by exposing the sensors to a N₂ vapour stream at a flow rate of 50 ml/min, containing 2.78 ppm_v 2,4-DNT vapours. Prior to all measurements, the sensors were inserted into the sensor

port and allowed to equilibrate in the laboratory air (50 % RH) until the resistance had become stable, typically 30 minutes. The sensors were then connected to the vapour generator and the resistance monitored at 10-second intervals over a period of 600 s. On completion of the measurements, the sensors were removed from the vapour generator and allowed to recover in air.

4.3 Results and discussion

4.3.1 The Pani-Cl chemiresistor

The first polymer to be utilised in this study was polyaniline. Pani was chosen due to its ease of deposition and stability in the dried state [54-56]. Pani has also been employed in many other gas-sensing applications [12, 14, 15, 19, 21, 26]. The Pani chemiresistor can be seen in Figure 4. The SEM images show that the polyaniline layer was deposited successfully onto both electrodes and resulted in their connection. The Pani film shown was estimated to be 25 μm thick. Closer examination of the film showed that the morphology of the film was fibular in nature, and clearly porous.

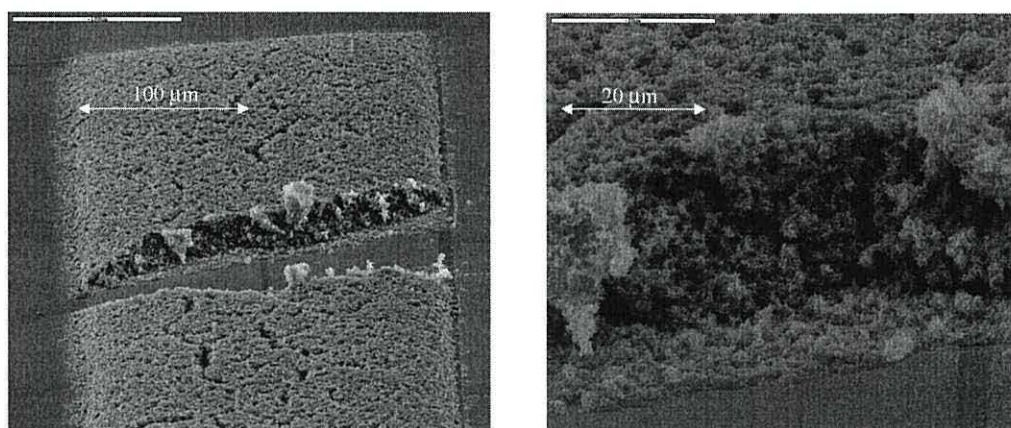


Figure 4. The polyaniline chemiresistor. The Polyaniline layer was deposited onto two platinum microband electrodes and is shown with a pin scratch to highlight the depth and profile.

The SEM image also showed that a dense globular layer existed close to the electrode surface, and this layer was estimated to be 500 nm thick. This observation is in agreement with the literature [5].

Although microscope images of the Pani layer show that the electrodes are physically connected by the polymer, electrical connection must be confirmed by the measurement of the electrical conductivity between the electrodes [57], or through measurement of the charge associated with the voltammetric peaks upon the redox switching of the polymer film [58, 59]. In the latter example the polymer layer would be addressed using, as the working electrode, each of the electrodes in turn and then the electrodes operated together as a pair. If the electrodes were electrically connected, the switching charge would be equal in each case since each electrode configuration should be capable of addressing the entire film. The voltammograms obtained using each electrode and the electrodes operated as a pair can be seen in Figure 5.

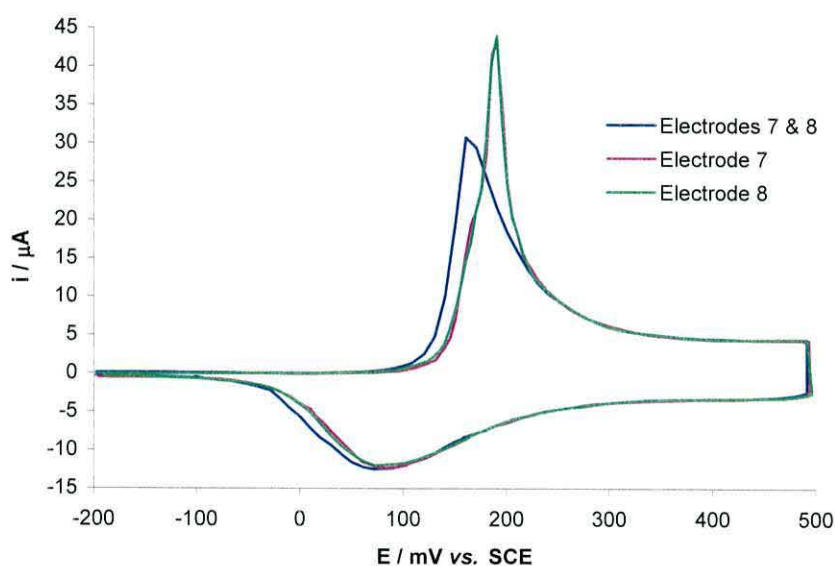


Figure 5. Voltammetric analysis of the Pani layer deposited onto two Pt microband electrodes to form the Pani-Chemiresistor, using each electrode individually and both electrodes operated together as a pair.

The voltammetry of the Pani layer is consistent with previous reports [5, 29, 60] and displays a redox couple attributed to the oxidation/reduction of the conjugated backbone of the polymer, switching between the leucoemeraldine and emeraldine forms. The potential-current plots were integrated and found to possess identical charges, $Q_{ox} = 340 \mu C$. This suggests that each electrode was able to address the entire film and also indicates that the electrodes were electrically connected. It can be

seen that the anodic peak potentials are not identical in each case, but this will be dealt with in the following chapter. The potential of the polymer was set at + 0.4 V *vs.* SCE. The polymer was then removed from solution and dried in air. The conductivity of the polymer was measured and found to be 42 Ω . This conductivity was relatively stable over a period of hours, but drifted over a period of eight weeks to 157 Ω , due to de-doping or deprotonation of the film.

4.3.1.1 The baseline response of the Pani chemiresistor

The baseline response of the Pani chemiresistor, i.e. the response towards the carrier gas, was measured in a flow of dry nitrogen at a flow rate of 50 ml/min. This response can be seen in figure 5. The resistance of the polymer layer increased by 9.6 ± 0.7 % upon exposure to nitrogen over a period of 10 minutes. This response is believed to be due to the drying effect of the nitrogen gas flow, which removes water from the film. The conductivity of Pani is known to be dependent on relative humidity (RH), and this was confirmed by varying the relative humidity of the carrier gas.

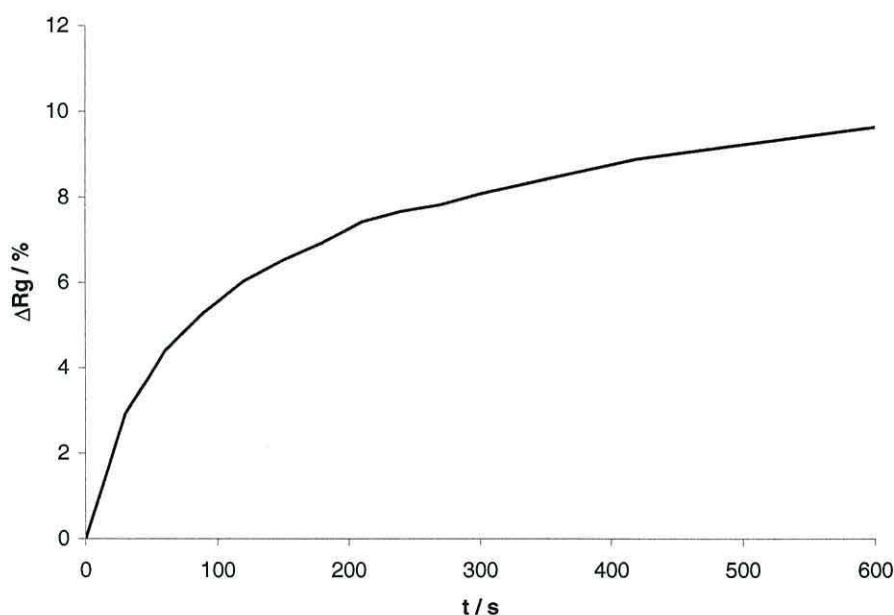


Figure 6. The baseline response of the Pani chemiresistor (+0.4 V *vs.* SCE) towards a gas flow of nitrogen, at a flow rate of 50 ml/min.

4.3.1.2 The response of the Pani chemiresistor towards 2,4-DNT

The effect of 2.78 ppm_v 2,4-DNT on the response of the Pani chemiresistor can be seen in Figure 7.

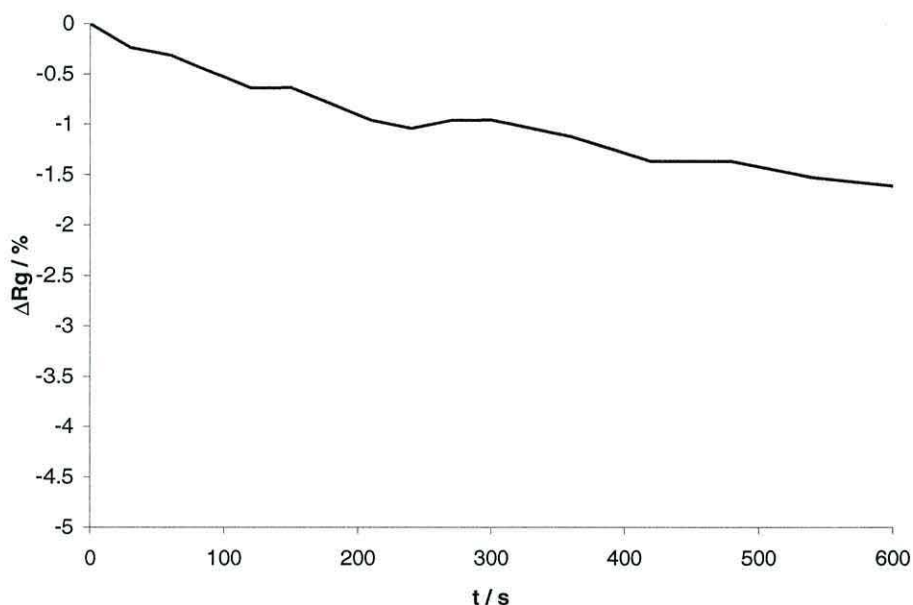


Figure 7. The response of the Pani chemiresistor (+0.4 V vs. SCE) towards 2.78 ppm_v 2,4-DNT, in N₂ at a flow rate of 50 ml/min.

As with the baseline response, the response towards 2,4-DNT was positive (i.e. the film resistance increased). However, this response was not as large as the baseline response, and the plot is shown as a negative response normalised against the baseline response. 2,4-DNT caused an averaged decrease of 1.6 ± 0.3 % in the magnitude of the response. This indicates that 2,4-DNT acted to increase the conductivity of the Pani film, which is not consistent with the theory of polymer swelling. Polymer swelling is thought to disrupt the degree of delocalisation of the polaronic lattice, effectively acting to hinder conduction and increasing the resistance of the film. The increase in the conductivity of the film might suggest that the extent of doping was enhanced or that the degree of delocalisation across the backbone was extended. As the polymer is p-doped, this would involve the removal of charge from the polymer backbone, and since the nitro group of 2,4-DNT is electron deficient it might accept electrons from the polymer. The nitro group is also capable of forming hydrogen

bonds with acidic protons, which may also act to withdraw charge from the polymer backbone.

4.3.2 The Pani-TS chemiresistor

Although there was a clear difference between the average baseline response and the response towards 2,4-DNT, the pure Pani-Cl film displayed insufficient response to qualify it as a suitable material for the detection of nitroaromatics. Therefore, polyaniline required modification to enhance its response towards nitroaromatic compounds. It appeared that polymer swelling was not responsible for the relatively small response of Pani towards 2,4-DNT, so it was decided that the interaction between the analyte and the π -conjugated system should be enhanced. Heteropolyanions are known to act as charge transfer complexes [61], and can easily be immobilised into the polymer film, compensating for the positive charge induced by doping. It was hoped that the HPAs would then be able to catalyse the transfer of electrons from the polymer to the nitroaromatics, enhancing the response of Pani films towards 2,4-DNT.

4.3.2.1 Pani-TS

The first heteropolyanion employed with the Pani chemiresistors was the silicotungstate anion, in the form of tungstosilicic acid ($\text{H}_4\text{SiW}_{12}\text{O}_{40}$). The voltammetry of tungstosilicic acid, in the potential range between 0.2 and -0.5 V vs. Ag/Ag^+ (0.01 M), revealed two redox couples at $E_{1/2} = -0.28$ and -0.41 V vs. Ag/Ag^+ (0.01 M), respectively, as can be seen in Figure 8. These have been ascribed to the reduction of the $[\text{SiW}_{12}\text{O}_{40}]^{4-}$ anion to $[\text{SiW}_{12}\text{O}_{40}]^{6-}$, with the electrons being taken up by the tungsten^(VI) atoms [32].

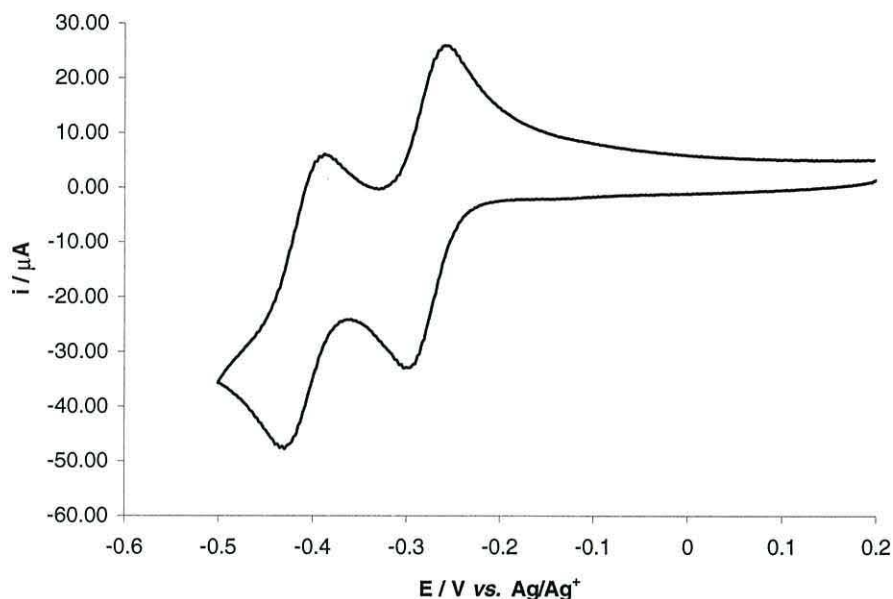


Figure 8. The voltammogram obtained from 1mM $\text{H}_4\text{SiW}_{12}\text{O}_{40}$, and 0.1 M HClO_4 in acetonitrile measured at 50 mV/s with a glassy carbon working electrode.

When polyaniline is grown in the presence of tungstosilicic acid, charge neutrality in the film is maintained through the incorporation of the silicotunstate (TS) anion. Subsequent growth of the Pani effectively traps the anion in the polymer matrix. Voltammetric analysis of such films showed that the HPA retains its redox chemistry [33, 51, 52] and this was confirmed for Pani-TS films used in this study, as can be seen in Figure 10.

To see if the HPA could catalyse the interaction between Pani film and the 2,4-DNT, the voltammetry of the Pani-TS film was studied in the presence of 2,4-DNT. Figure 11 shows that as the concentration of 2,4-DNT increased, the current associated with the redox couples for the reduction of the HPA also increased. These higher currents indicate that the 2,4-DNT is being reduced at the HPA, and it should be noted that the reduction of 2,4-DNT at Pani-Cl electrodes occurred at a significantly higher overpotential. A shift of the polymer oxidation peak potential to more negative potentials was also observed, and the associated charge decreased. These observations are usually associated with the memory effect, but may be an indication that the polymer interacts with the HPA.

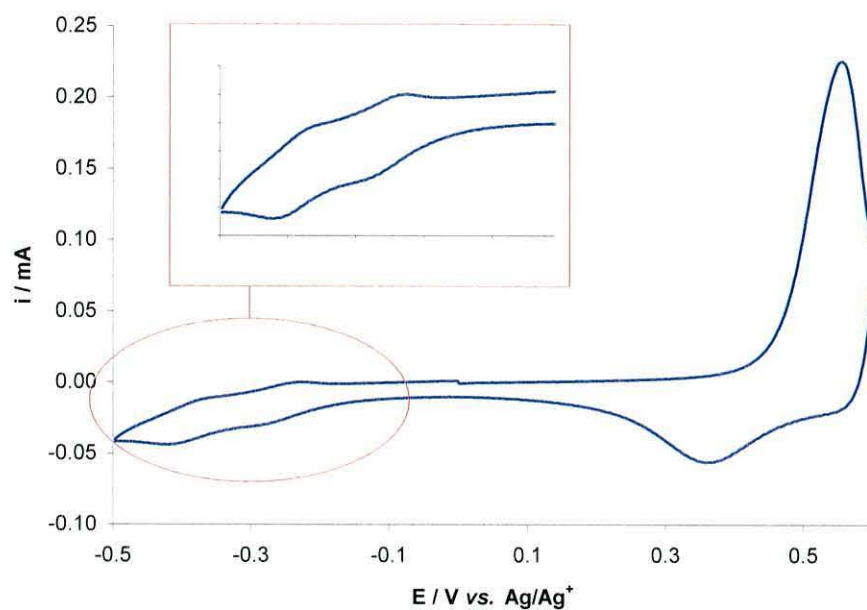


Figure 10. The voltammetric analysis of a Pani-TS layer showing the redox characteristics of both polyaniline and the silicotungstate anion.

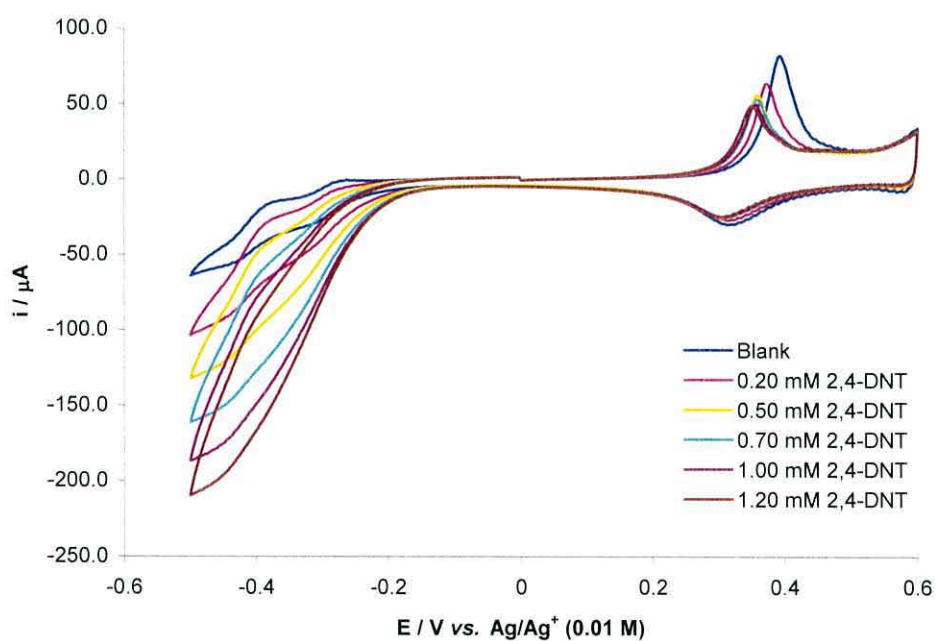


Figure 11. The effect of 2,4-DNT on the voltammetry of a Pani-TS film on a GC electrode in an acetonitrile solution containing 0.1 M HClO_4 .

If the 2,4-DNT is reduced at the HPA, then the HPA is likely to become electron deficient and would counter that by removing electrons from Pani. This would act to

oxidise the polymer, decreasing the amount of polymer that can be oxidised and as the oxidised material is conducting, lowering the oxidation potential. These results are very similar to those observed for the catalytic reduction of oxygen [52] and bromate [33] at polymer-HPA modified electrodes. These observations inspired confidence to study the effects of the HPAs on the response of the polymer-based chemiresistors, however further work is required to establish the precise nature of these observations.

Pani-TS was grown onto two microband electrodes until sufficient polymer had been deposited to join the electrodes together, as revealed by the microscope picture in Figure 12.

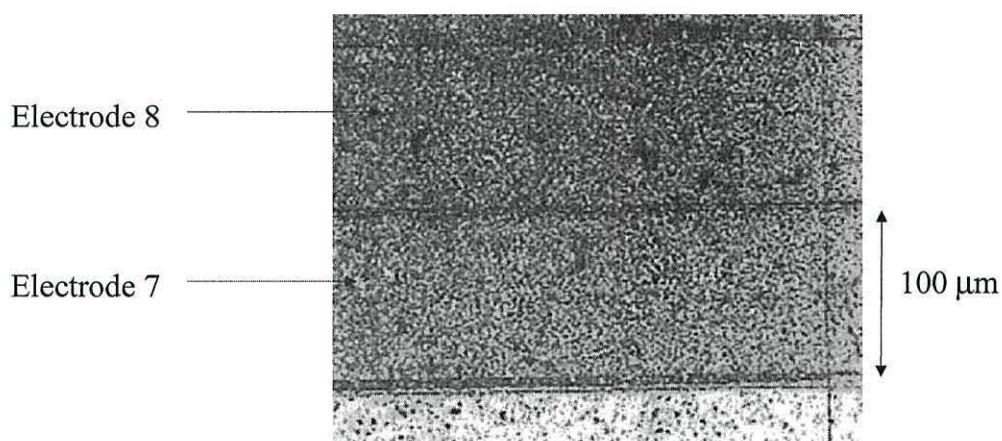


Figure 12. An image of the Pani-TS chemiresistor from an optical microscope.

Thick films of Pani-TS were difficult to obtain by voltammetry, as has been observed previously [52]. Therefore, a long deposition period was required in order to deposit a film thick enough to electrically connect the electrodes (<5 hours). This consequently resulted in the degradation of the electrode array and the breakdown of the electrical contacts between the electrodes and the printed circuit board (pcb) connecting board. Figure 13 shows how the electrolyte attacked the epoxy resin used to cover the electrical contacts between the microband electrodes and the pcb connecting board. The epoxy had swollen and “lifted” the embedded contact wires from the silicon, breaking the connection.

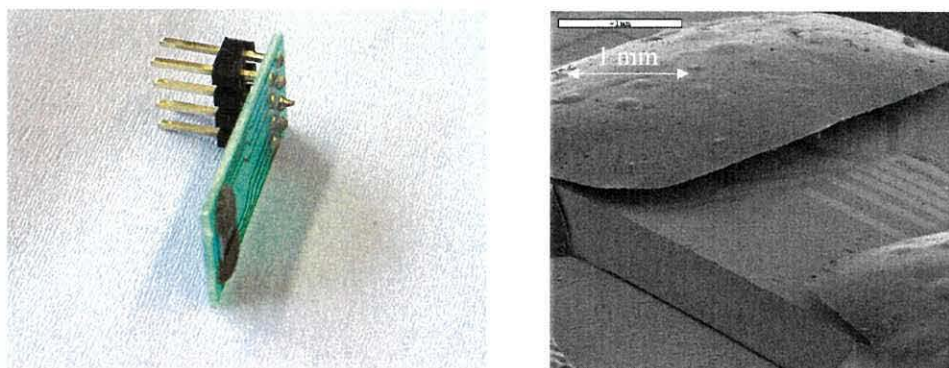


Figure 13. Photographic and SEM Images showing the effect of the acidic electrolytic solution on the epoxy resin of the microband arrays.

Because of the sensitivity of the epoxy resin towards acidic media, the electrical connection of the electrodes for polymer-HPA films was not tested using voltammetry, as this would require the array to be in the acid for longer periods, further degrading the array. Alternatively, the electrical connection of the electrodes was confirmed by drying the films and measuring the resistance between them. The resistance of the film was measured at 3.97 k Ω . This was much higher than that observed for the Pani-Cl chemiresistor, but this was expected since it was considerably more difficult to grow the film, and the film was likely to be much thinner. However, it may also reflect the extent of doping. The polymer films were set at a potential that would render the polymers oxidised, and hence conducting. Therefore, the potential of the Pani-Cl film was set above the oxidation peak potential, which corresponded to + 0.4 V *vs.* SCE. In order to set the potential of the Pani-TS films above the oxidation peak potential, the films were set at + 0.5 V *vs.* Ag/Ag⁺, which corresponds to + 0.8 V *vs.* SCE. At 0.8 V *vs.* SCE it would be expected that the second oxidation of Pani would occur, resulting in the over-oxidation of the film and corresponding increase of the film resistance. However, upon repeated cycling of other Pani-TS films no loss of oxidation charge was observed, so this is unlikely.

4.3.2.2 The baseline response of the Pani-TS chemiresistor

The baseline response of the Pani-TS chemiresistor in nitrogen, at a flow rate of 50 ml/min can be seen in Figure 14.

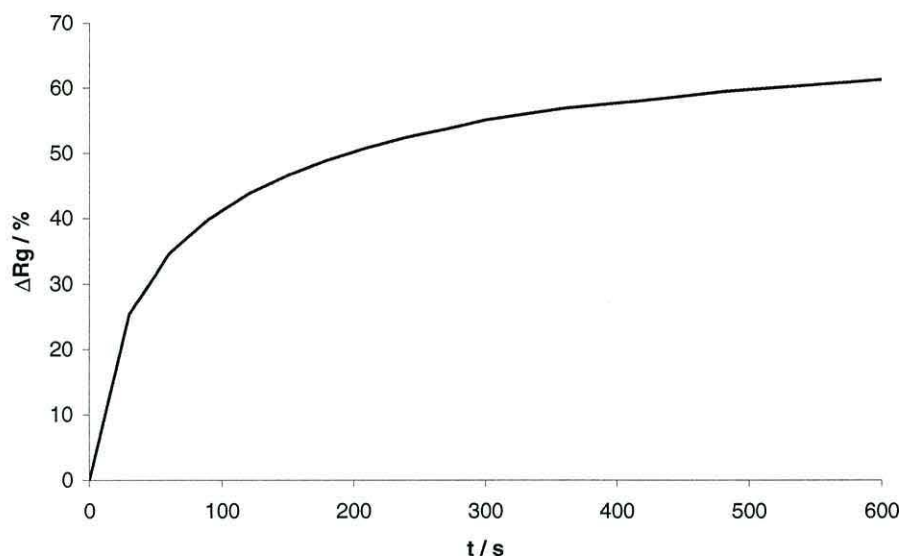


Figure 14. The baseline response of the Pani-TS (+0.5 V vs. Ag/Ag⁺) towards nitrogen, at a flow rate of 50 ml/min.

The response of the Pani-TS chemiresistor, as with the Pani-Cl chemiresistor, was observed as an increase of film resistance. The magnitude of the response is much larger than that observed with the Pani-Cl chemiresistor. This may be due to the fact that the film is much thinner than the Pani-Cl film, but may also reflect the presence of the HPA anion. Again, the response is most likely to be due to the drying effect of the nitrogen flow, and this was confirmed by the effect of RH on the baseline response, as can be seen in Figure 15. Therefore, it appears that the silicotungstate anion enhances the response of the Pani films towards relative humidity.

Figure 15 shows that the response of the chemiresistor decreased as the level of relative humidity increased towards that of the laboratory air, ~ 47 %. The response then increased as the RH increased from 50 to 75 %. It is not certain why the response increased beyond 50 % RH, as this would not be expected for Pani, but may be due to the fact that the HPAs are not mobile.

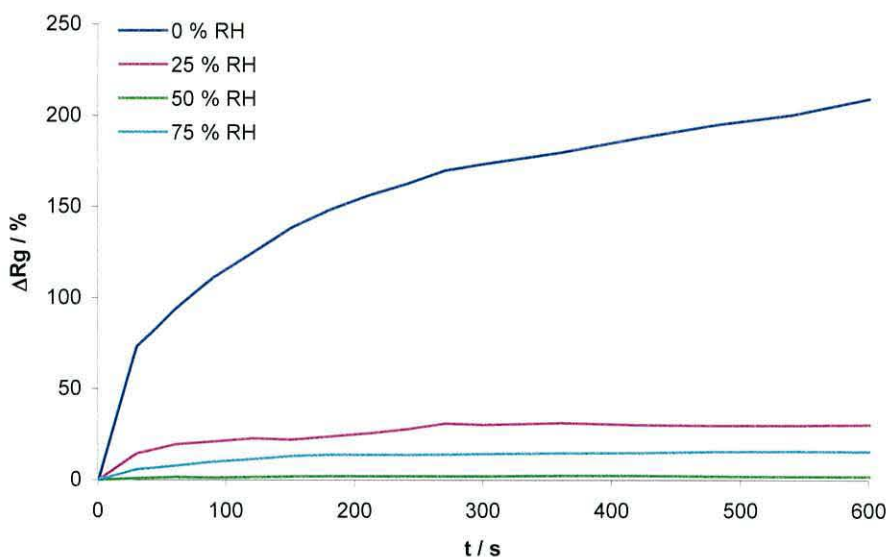


Figure 15. The effect of relative humidity on the baseline response of Pani-TS film (+0.5 V vs. Ag/Ag⁺), in nitrogen at a flow rate of 50 ml/min.

4.3.2.3 The response of the Pani-TS chemiresistor towards 2,4-DNT

The response of the Pani-TS chemiresistor towards 2,4-DNT can be seen in Figure 16. Once again, the response was observed as an increase of film resistance, which was not as great as the response towards pure nitrogen. Therefore, the normalised response is seen to be negative indicating that the Pani-HPA film increased in conductivity upon exposure to 2,4-DNT. The response was much greater than that for Pani-Cl, showing that the presence of the HPA enhanced the charge transfer interaction between the nitroaromatic and the polymer film.

Figure 16 also shows the effect of the oxidation states of the Pani-film and the heteropolyanion on the response of the Chemiresistor towards 2,4-DNT. It should be noted that below 0.2 V the Pani film should be in the reduced leucoemeraldine state, which is insulating in nature. As a result, the resistance of the film should be too high to measure and the chemiresistor rendered useless. However, it was found that the film retained some conductivity even when set at – 0.8 V.

Initially, the electrochemical potential was set at + 0.5 V vs. Ag/Ag⁺ (0.01 M). This would render the Pani film in the doped, partially oxidised, emeraldine state, while the

HPA would be in the oxidised state (W^{VI}). When the film was held at -0.2 V vs. Ag/Ag^+ (0.01 M), the Pani layer would be rendered in the reduced leucoemeraldine state, but the TS anion would still be in the oxidised state (W^{VI}). At -0.8 V vs. Ag/Ag^+ (0.01 M), the Pani film would still be in the reduced leucoemeraldine state and the TS anion would also be in the reduced heteropoly blue state (W^{IV}). From the observed responses, it appears that the best combination, for the detection of 2,4-DNT, was found at -0.8 V vs. Ag/Ag^+ (0.01 M). It is suggested that at this potential 2,4-DNT can interact and remove charge from the TS anion. In turn, the TS anion extracts electron density from the polymer. The polymer is in the un-doped reduced state. Any electron density removed effectively dopes the polymer causing an increase in the conductivity of the film. However, further evidence would be required to confirm these hypotheses.

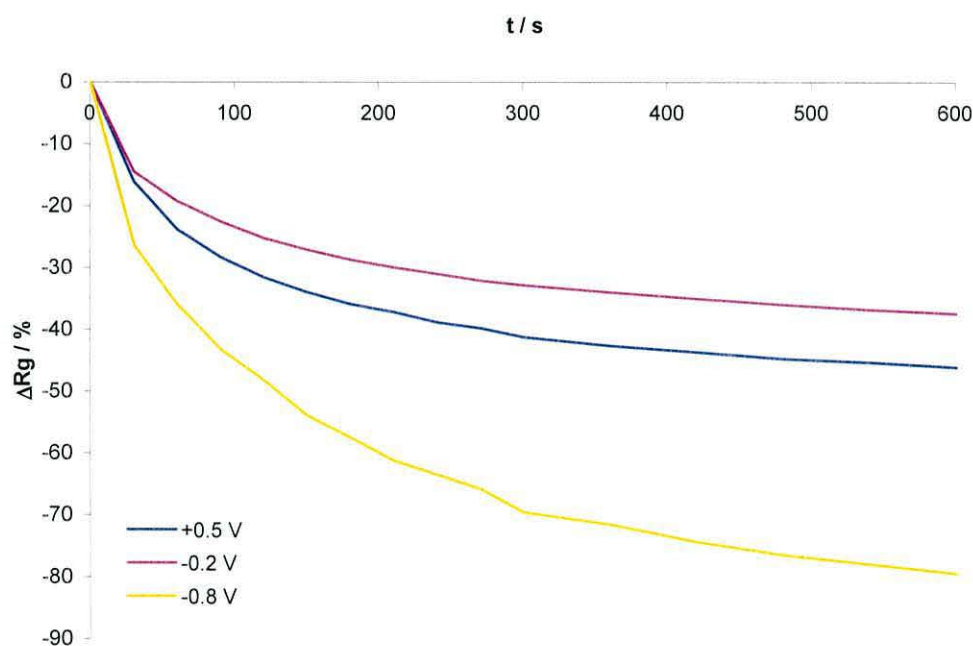


Figure 16. The response of the Pani-TS chemiresistor towards 2.78 ppm, 2,4-DNT (N_2 , 50 ml/min), set at 0.5 V, -0.2 V and -0.8 V vs. Ag/Ag^+ .

4.3.3 The Pani-PM chemiresistor

The molybdophosphate anion was also employed to modify the Pani chemiresistors, in the form of phosphomolybdic acid ($H_3PMo_{12}O_{40}$). The voltammetry of phosphomolybdic acid in acetonitrile, shown in Figure 17, exhibits three redox

couples with $E_{1/2} = 0.17, 0.41,$ and 0.55 V, respectively. These redox couples have potentials that are closer to the switching potential of Pani.

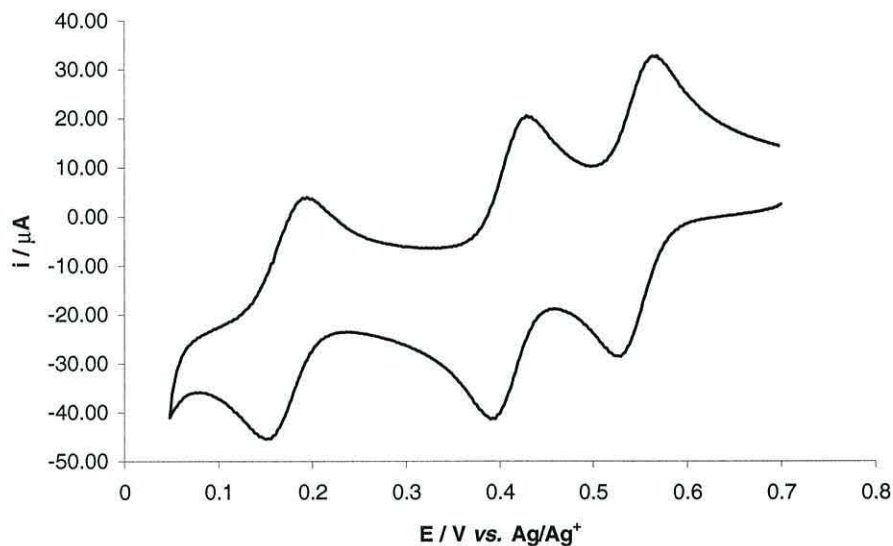


Figure 17. The voltammogram obtained from 1mM $\text{H}_3\text{PMo}_{12}\text{O}_{40}$, in an acetonitrile solution containing 0.1 M HClO_4 . Measurements were taken at 50 mV/s using a glassy carbon working electrode.

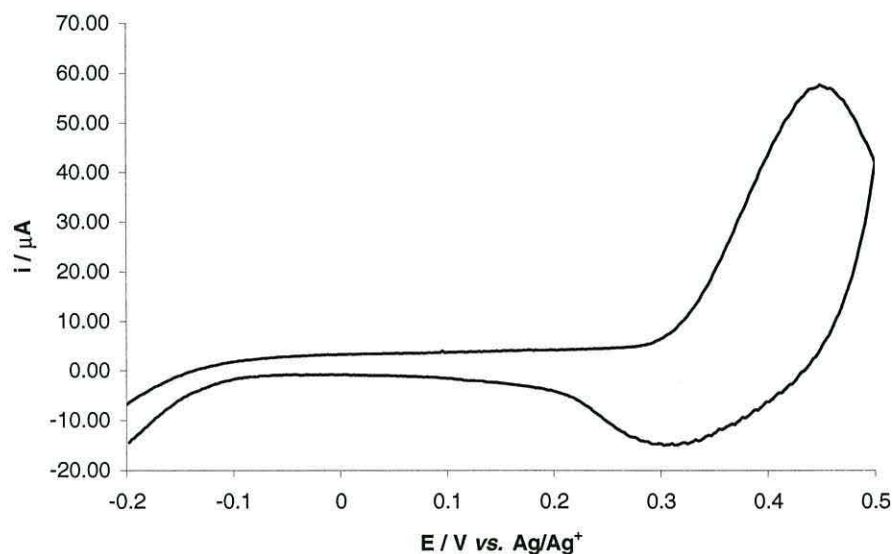


Figure 18. Voltammetric analysis of a Pani-PM layer. Note that the characteristics of polyaniline are present, but not those of the molybdophosphate anion.

When the Pani chemiresistor was grown in the presence of the phosphomolybdate (PM) anion, it was found that it was much more difficult to obtain thick films. In fact, the presence of the PM anions is hardly observable in the voltammetry of the film, as can be seen in Figure 18. This is inconsistent with Pani-PM film reported in the literature, where the three redox couples from the PM anion are observable [33]. However, the present film is likely to be very thick in comparison, and the redox chemistry of the PM anion is likely to be “swamped” by that of the polymer, as will be shown later. However, a film was obtained (Figure 19) that resulted in the electrical connection of the microband electrodes and a resistance of $41.6\text{ k}\Omega$ was observed ($+0.5\text{ V vs. Ag/Ag}^+$).

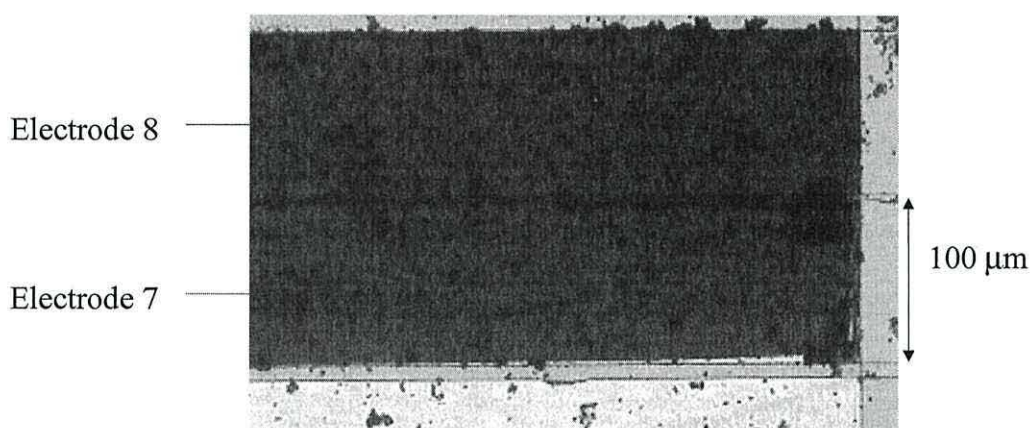


Figure 19. An image of the Pani-PM chemiresistor from an optical microscope.

4.3.3.1 The baseline response of the Pani-PM chemiresistor

The response of the Pani-PM chemiresistor, shown in Figure 20, was comparable to that observed for Pani-TS, and this response was again observed as an increase of the films resistance, $\Delta R_g = 52\%$ after 600 s.

4.3.3.2 The response of the Pani-PM chemiresistor towards 2,4-DNT

The response of the Pani-PM chemiresistor towards 2.78 ppm_v 2,4-DNT was also observed as a decrease of the baseline response, indicating that the conductivity of the film increased when in the presence of the nitroaromatic (Figure 21).

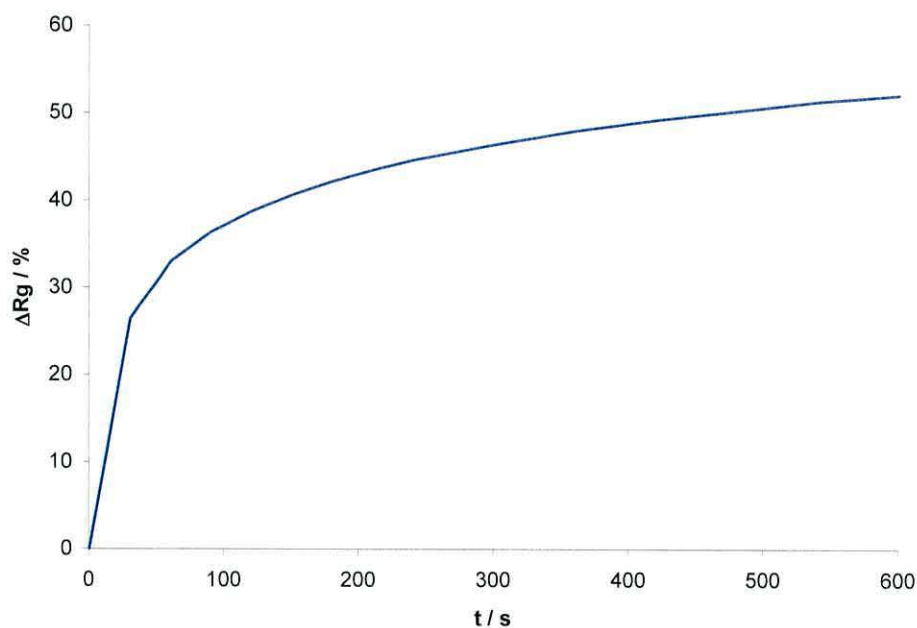


Figure 20. The baseline response of the Pani-PM (+0.5 V vs. Ag/Ag⁺) chemiresistor towards a stream of nitrogen, at a flow rate of 50 ml/min.

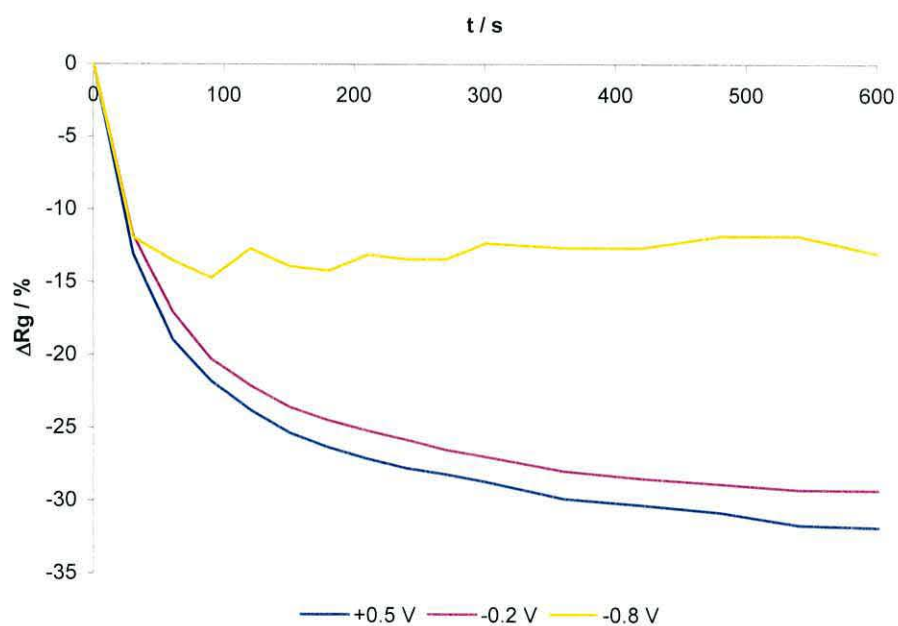


Figure 21. The response of the Pani-PM chemiresistor towards 2.78 ppm, 2,4-DNT (N₂, 50 ml/min), when the film was set at +0.5 V, -0.2 V and -0.8 V vs. Ag/Ag⁺.

The response of the Pani-PM film at + 0.5 V and -0.2 V *vs.* Ag/Ag⁺ (0.01 M), are 32 % and 29 %, respectively, which are comparable to those observed for Pani-TS chemiresistors. However, when the film was held at - 0.8 V *vs.* Ag/Ag⁺ (0.01 M) the response was much less than that observed for Pani-TS, at 13 % after 600 s. This is most likely to be due to the irreversible reduction of the PM anion, which results in the breakdown of the HPA structure, rendering it incapable of acting as a charge transfer agent [32].

4.3.4 The Poly(3-methylthiophene) chemiresistor

Poly(3-methylthiophene) (P3MT) was also tested as a possible material for the detection of nitroaromatics, as P3MT is known to be very stable with a high conductivity [62-64]. Another important factor in the choice of this polymer was the lack of sensitivity towards water vapour. Pani films suffered greatly from humidity effects and in all cases the response to relative humidity was greater than the response to 2,4-DNT.

P3MT-PF₆ was grown electrochemically onto the two microband working electrodes, until sufficient polymer had been deposited to result in their electrical connection. Figure 22 shows an optical image of the P3MT chemiresistor, and the fibular nature the polymer morphology.

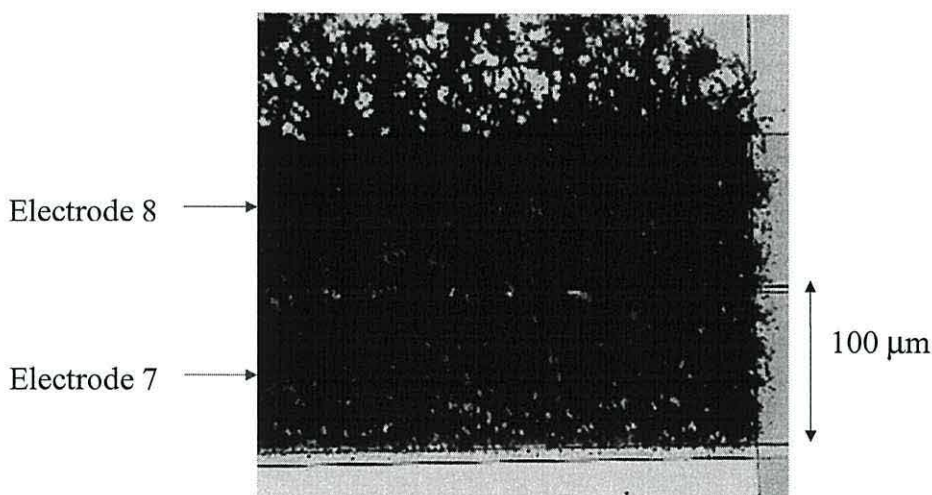


Figure 22. An image of the P3MT chemiresistor from an optical microscope.

The electrical connection was confirmed through voltammetry, as can be seen in Figure 23. The voltammetry is almost identical in each case, possessing identical charge, $Q_{ox} = 56 \pm 2 \mu\text{C}$. This would suggest that the P3MT-PF₆ film electrically connects the electrodes.

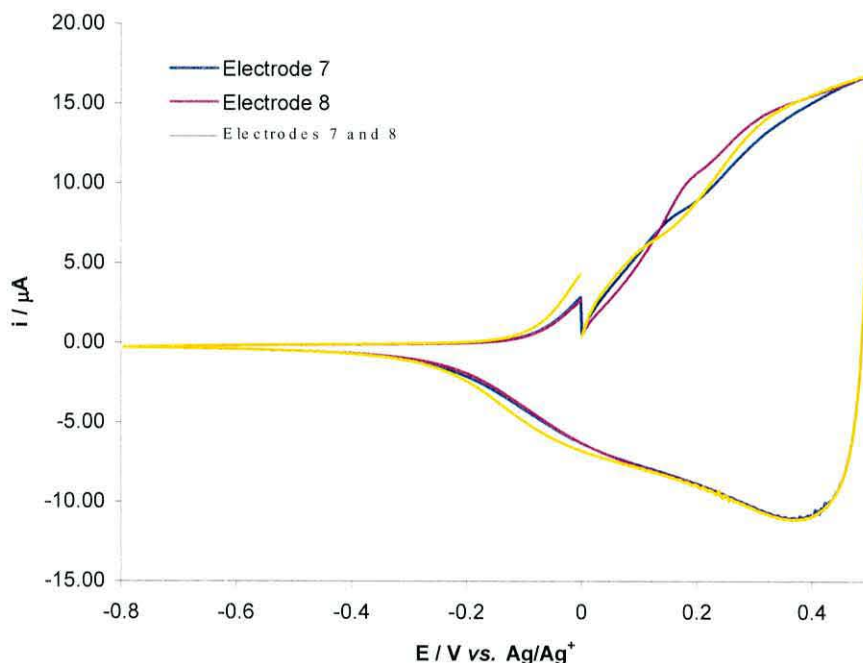


Figure 23. Voltammetry of the P3MT-HFP film formed onto the two platinum microband electrodes.

4.3.4.1 The Response of the P3MT chemiresistor

The baseline response of the P3MT sensor to a flow of nitrogen (50 ml/min, 0 % RH) was negligible, and is shown alongside the response of the chemiresistor towards 2,4-DNT (Figure 24). The response towards 2.78 ppm_v 2,4-DNT ($\Delta R_g = 0.60 \%$) was very small and observed as an increase in conductivity. This is similar in nature to the normalised response from the Pani chemiresistor, but of smaller magnitude, and supplies further evidence that the presence of 2,4-DNT acts to increase the conductivity of polymer films by interacting with the π -conjugated backbone. However, this response was still too small to be sufficient for the detection of nitroaromatic compounds, and therefore P3MT films were modified with the heteropolyanions.

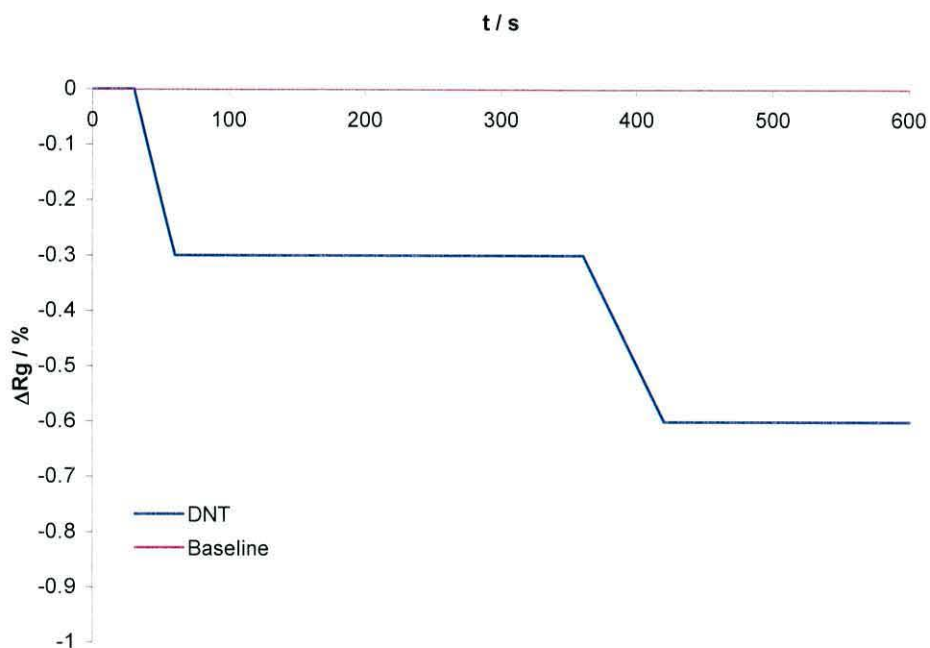


Figure 24. The response of a P3MT-PF₆ chemiresistor (+0.5 V vs. Ag/Ag⁺) towards nitrogen and nitrogen containing 2.78 ppm, 2,4-DNT, at a flow rate of 50 ml/min.

4.3.5 The P3MT-TS Chemiresistor

4.3.5.1 P3MT-TS

The silicotungstate anion, $[\text{SiW}_{12}\text{O}_{40}]^{4-}$, was the first HPA employed with the P3MT films. Once again, thick films of the P3MT-HPA were more difficult to deposit than the plain P3MT-PF₆. Figure 25 shows an optical microscope image of the P3MT-TS film.

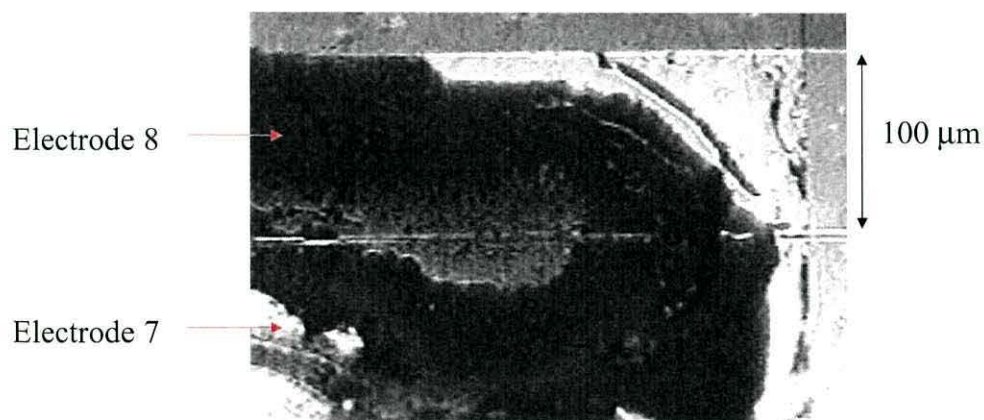


Figure 25. An image of the P3MT-TS chemiresistor from an optical microscope.

The morphology of the film can be seen to be very much more crystalline in nature than the fibular P3MT-PF₆ films. In fact, as the films dried they tended to contract and crack. This often resulted in the film becoming detached from the electrode surface, resulting in the loss of electrical connection between the electrodes.

As with the Pani-HPA films, polymer deposition sufficient to render an electrical connection between the electrodes required the arrays to be in the acidic solutions for fairly long periods of time, which consequently resulted in the degradation of the array. Therefore, the electrical connection between the electrodes was not determined using voltammetry, but again through measurement of conductivity. The resistance of the polymer (+0.6 mV vs. Ag/Ag⁺) across the 5 μ m gap was measured to confirm the electrical connection of the electrodes and found to be 102 Ω .

A typical voltammogram of a P3MT-TS film grown on the platinum microelectrodes can be seen in Figure 26. The figure shows the redox characteristics of the P3MT, but the redox chemistry of the TS anion cannot be observed.

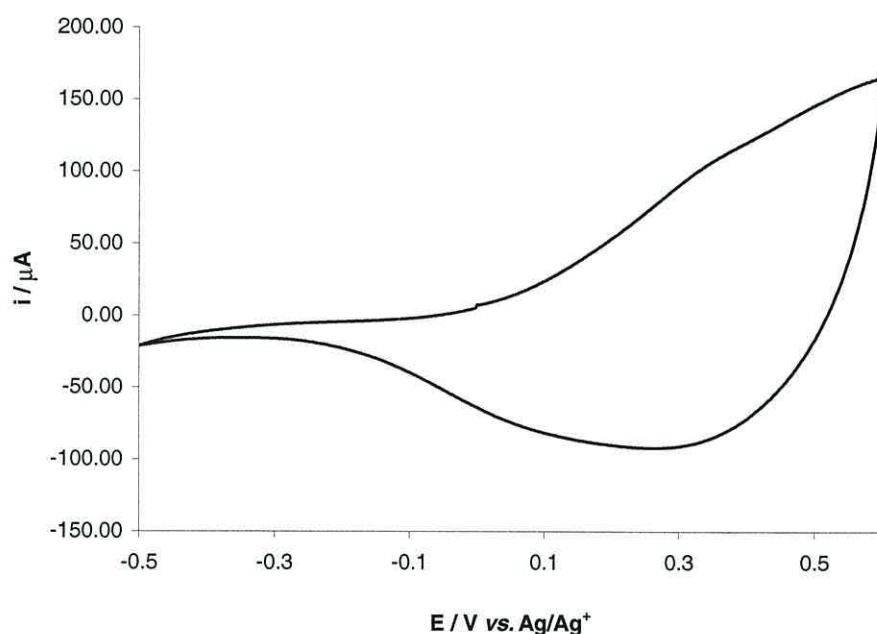


Figure 26. Voltammetry of the P3MT-TS film formed onto the two platinum microband electrodes. Notice the absence of the HPA redox couples.

4.3.5.2 The effect of film thickness on the HPA anion incorporation

The absence of the silicotungstate anion (TS) redox chemistry in the voltammetry of the P3MT-TS film prompted the suspicion that the anion may be escaping from the film or, as the polymer layer is relatively thick in order to bridge the gap, the HPA may not counter the entire charge associated with the film. Therefore, the effect of film thickness was investigated on a glassy carbon electrode. Glassy carbon was chosen as the working electrode material because in aqueous solutions the hydrogen evolution reaction at a platinum surface seriously masks the redox couple of the tungsten atoms in the HPA, which was used to estimate the amount of HPA present.

The voltammetry of P3MT-TS films of different thickness can be seen in Figure 27. It can be seen that as the charge associated with P3MT increased, the corresponding charge associated with the TS anion also increased. But what becomes apparent is that the ratio of polymer to anion charge was not constant as the film thickness increased (Table 3), varying from 2 to 18 as the number of cycles increased from 3 to 12. This suggests that as the polymer gets thicker, the amount of anion incorporated into the film to compensate for the doping charge decreases. This may reflect the relative difficulty observed in preparing thick films. However, it has previously been suggested that during deposition of thin polymer-HPA films, HPAs form a layer directly on the electrode surface from which the polymer then grows. The HPA is able to counter the doping charge of the thin polymer layer above it. This was termed the sea anemone effect [29]. It is possible that as the films become thicker this HPA layer is unable to maintain charge neutrality for the entire polymer film, and hence additional HPAs migrate into the film and become trapped in the polymer matrix. These additional HPAs may be less tightly bound than those at the electrode surface, and during characterisation in the HClO_4 solution, a degree of anion exchange occurs.

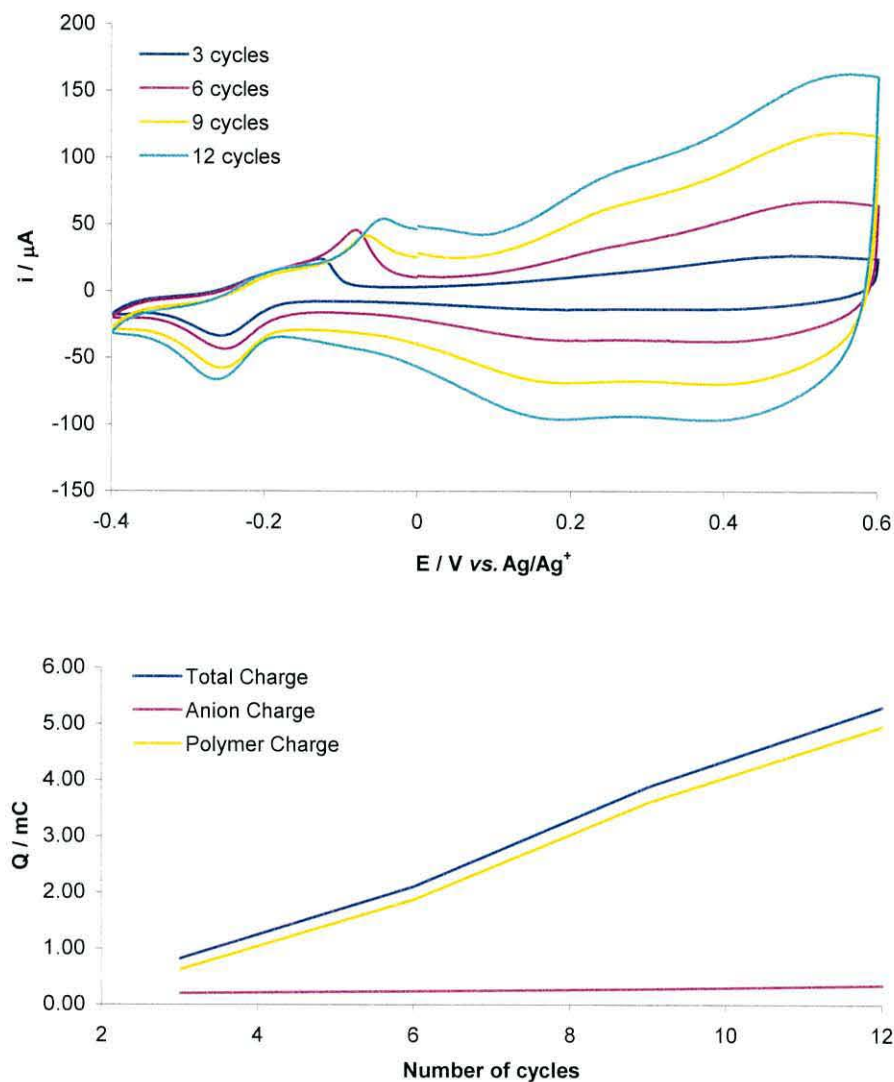


Figure 27. The effect of film thickness on the extent of anion doping by the HPA. Voltammograms were recorded using a glassy carbon electrode (0.07cm^2) in acetonitrile containing 0.1 M HClO_4 . Notice how the ratio of anion to polymer decreases with increasing film thickness.

No of Cycles	Total +ve Charge / C	Anion charge / C	Polymer charge / C	Ratio polymer/anion
3	8.78×10^{-4}	2.92×10^{-4}	5.86×10^{-4}	2.00
6	2.14×10^{-3}	4.64×10^{-4}	16.76×10^{-4}	3.61
9	3.53×10^{-3}	4.09×10^{-4}	31.21×10^{-4}	7.63
12	4.69×10^{-3}	2.40×10^{-4}	44.5×10^{-4}	18.54

Table 3. The effect of film thickness on the ratio of polymer to heteropolyanion for a P3MT-TS film.

The HPAs do not appear to be able to compensate for the entire charge of thicker polymer films. With electrochemical deposition, the polymer films are required to be thick in order to bridge the gap between the electrodes. However, in order to keep a high ratio of HPA to polymer, it would appear to be advantageous to keep the film thickness as low as possible. This could be achieved by using smaller gaps between the electrodes or by chemically growing the film and applying the polymer by another method, such as spin casting.

4.3.5.3 The baseline response of the P3MT-TS chemiresistor

The baseline response of the P3MT-TS chemiresistor was quite different from that of the plain P3MT-PF₆ chemiresistor. The response (Figure 28) was observed as an increase in the resistance of the film (10 %), a similar value to that observed by the Pani chemiresistor.

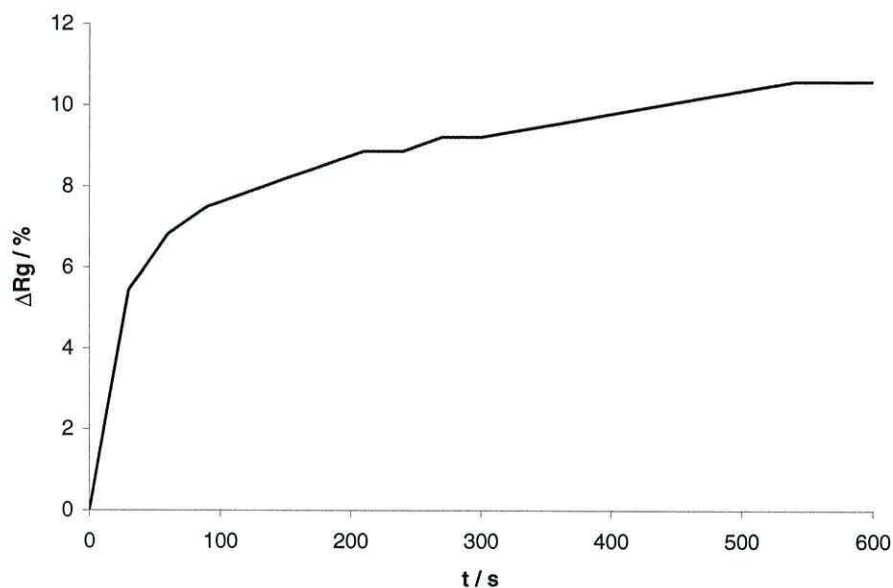


Figure 28. The baseline response of P3MT-TS (+0.6 V vs. Ag/Ag⁺) towards nitrogen at a flow rate of 50 ml/min.

The positive baseline response is believed to be due to the drying effect of the nitrogen gas flow. This can be observed in Figure 29 where the introduction of relative humidity (RH) into the nitrogen stream causes a progressive reduction of the response. It should be noted that the response in a nitrogen stream at 0 % RH, was

lower than that of the baseline response, however these experiments were conducted with different polymer films. It is also interesting to see that there was still a slight response to even 75 % RH, when the RH of the laboratory air was 47 %, which should therefore be the value expected to demonstrate a zero response. P3MT-PF₆ exhibited no response to humidity and this enhanced response, similar to the enhancement observed with polyaniline, would suggest that it is the presence of the HPA that is responsible, not film thickness.

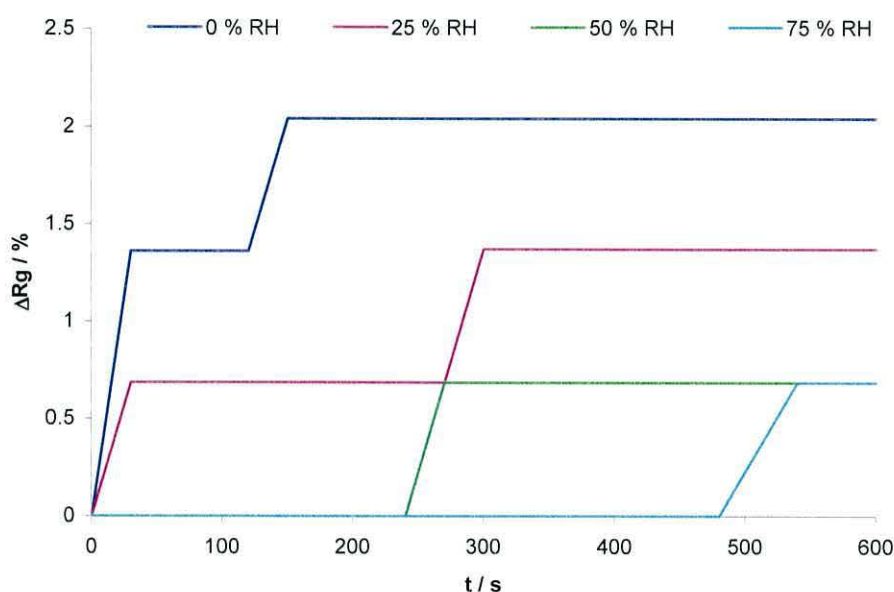


Figure 29. The effect of relative humidity on the baseline response of a P3MT-TS film (+0.6 V vs. Ag/Ag⁺) in nitrogen, at a flow rate of 50 ml/min.

4.3.5.4 The response of the P3MT-TS chemiresistor towards 2,4-DNT

The response of the P3MT-TS chemiresistor towards 2,4-DNT was observed as a reduction of the baseline response, indicating an increase of the films conductivity upon exposure to 2,4-DNT (Figure 30). The magnitude of the response ($\Delta R_g = 6.7\%$) is much larger than that observed for the plain P3MT-PF₆ chemiresistor. This suggests that the HPA was able to interact with both the P3MT and the nitroaromatic, with charge transfer from one to the other.

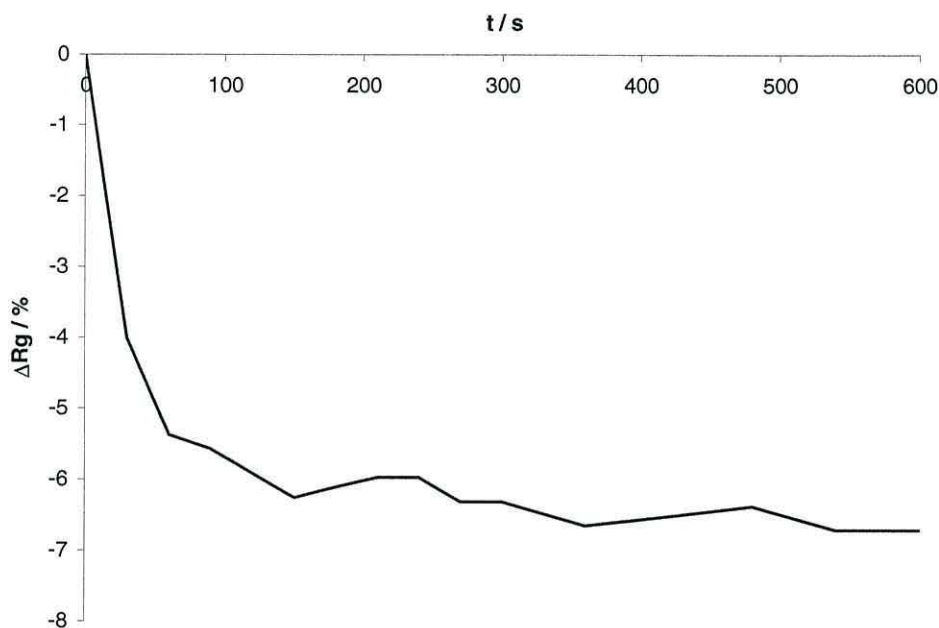


Figure 30. The response of the P3MT-TS chemiresistor (+0.6 V vs. Ag/Ag⁺) towards 2,4-DNT vapours in nitrogen, at a flow rate of 50 ml/min.

It should be noted that when the P3MT-HPA films were set at lower oxidation potentials, the film resistance was too high to measure with the digital voltmeter. Therefore, no measurements could be made for the response of different P3MT-HPA films to 2,4-DNT, at different oxidation levels.

4.3.6 The P3MT-PT chemiresistor

Through the replacement of the heteroatom, the catalytic characteristics of the HPA can be modified [32]. The effect of exchanging the silicon atom in the HPA for a phosphorus atom was observed using the phosphotungstate anion (PT), [PW₁₂O₄₀]³⁻. The optical microscope images of the polymer chemiresistors are shown in Figure 31.

Once more, in order to avoid unnecessary degradation of the array, the P3MT-PT film was not characterised in HClO₄, but the voltammetry of a similar film is shown in Figure 32. However, the resistance of the dried film was measured to be 441 Ω. The Voltammetry of the film showed typical behaviour for P3MT, but once again the redox characteristics from the tungsten in the HPA, were masked by the relatively large polymer signal.

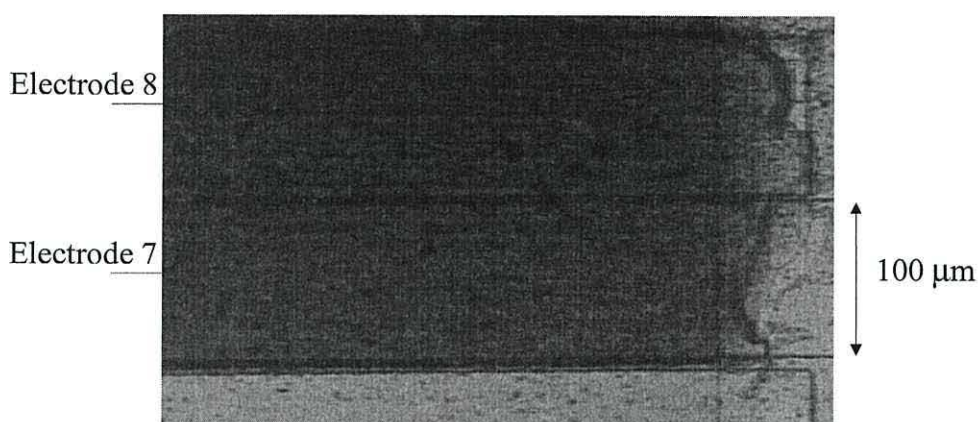


Figure 31. An image of a P3MT-PT chemiresistor from an optical microscope.

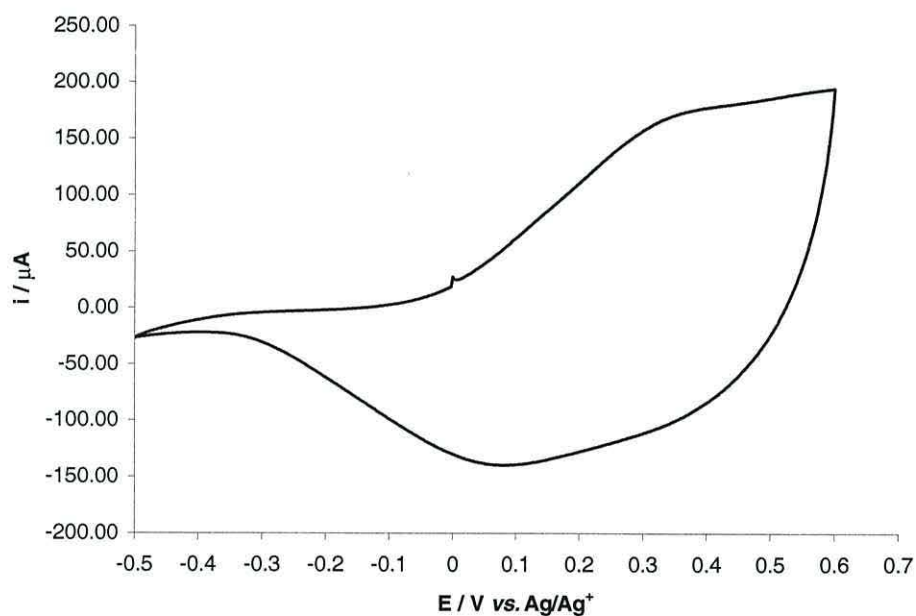


Figure 32. Voltammetry of the P3MT-PT film formed onto the two platinum microband electrodes. Notice the absence of the HPA redox couples.

4.3.6.1 The baseline response of the P3MT-PT chemiresistor

The baseline response of the P3MT-PT chemiresistor towards a 50 ml/min flow of purified nitrogen can be seen in Figure 33. The response displays typical P3MT-HPA behaviour, increasing in resistance upon exposure to the nitrogen flow, however the magnitude of the response, $\Delta R_g = 90\%$, is far greater than that observed for the

P3MT-PF₆ and P3MT-TS films. This suggests that the PT anion is able to interact more closely with the P3MT film.

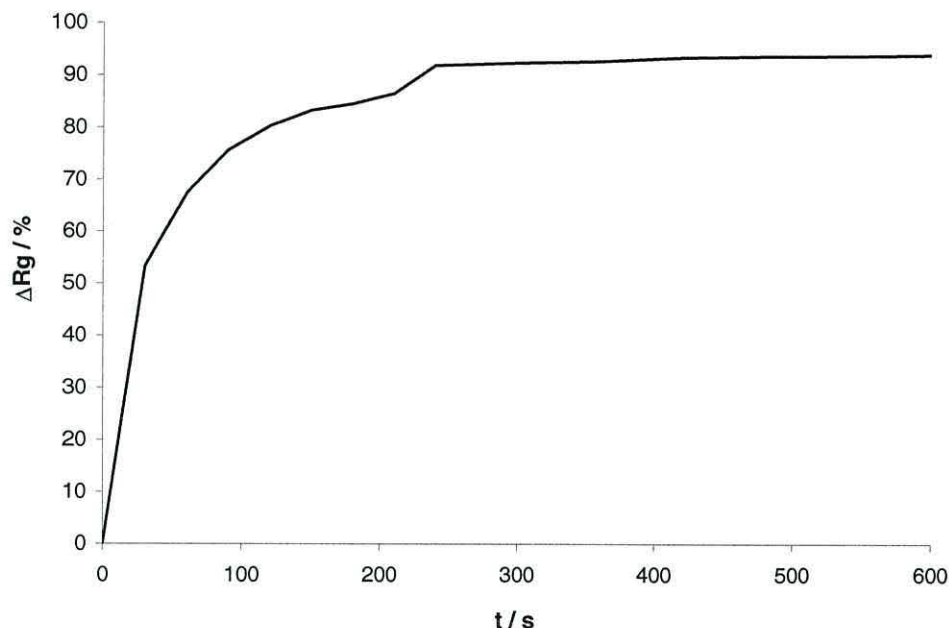


Figure 33. The baseline response of P3MT-PT (+0.6 V vs. Ag/Ag⁺) in nitrogen, at a flow rate of 50 ml/min.

4.3.6.2 The response of the P3MT-PT chemiresistor towards 2,4-DNT

Upon exposure to a vapour stream containing 2.78 ppm_v 2,4-DNT, the response of the P3MT-PT chemiresistor was observed to be much lower than the baseline response in nitrogen. This response is shown in Figure 34, normalised against the baseline response. The reduction in the resistance of the film would indicate that the 2,4-DNT causes the doping level in the polymer to be modified. The magnitude of the response ($\Delta R_g = 37.97\%$) is also larger than both P3MT-PF₆ ($\Delta R_g = 0.60\%$) and P3MT-TS ($\Delta R_g = 6.71\%$).

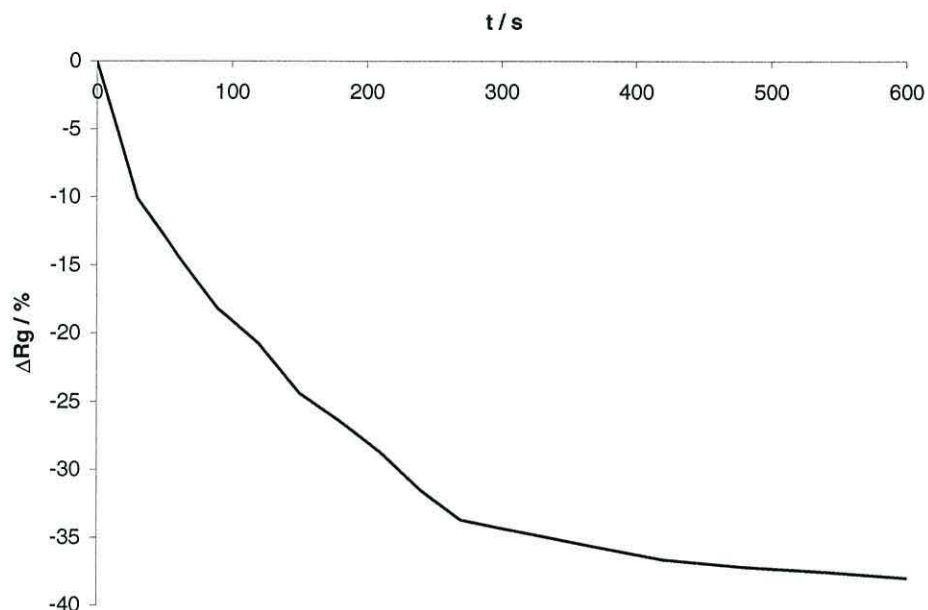


Figure 34. The response of P3MT-PT (+0.6 V vs. Ag/Ag⁺) towards 2.78 ppm_v 2,4-DNT, in nitrogen carrier gas at a flow rate of 50 ml/min.

4.3.7 The P3MT-PM chemiresistor

The phosphomolybdic anion (PM) was also employed with the P3MT films. An optical microscope image can be seen in Figure 35. The picture shows that the film produced had contracted whilst drying, causing the film to crack and split like dried mud. However, this did not result in a broken electrical connection nor was the conductivity hindered, and the resistance measured across the 5 μm gap was 208 Ω (+0.6 V vs. Ag/Ag⁺).

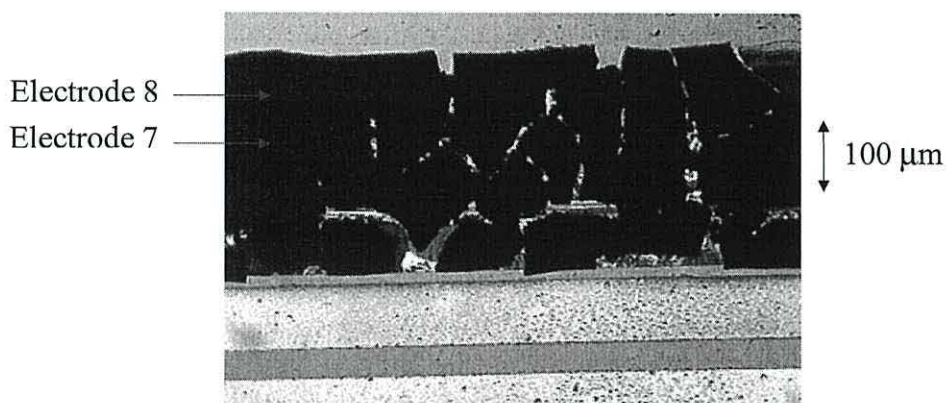


Figure 35. An image of the P3MT-PM chemiresistor from an optical microscope.

Analysis of an equivalent P3MT-PM film, grown onto Pt microband electrodes, Figure 36, shows the voltammetric characteristics of both the Poly(3-methylthiophene) and the molybophosphate anion. This was somewhat surprising considering that the voltammetry of thick polymer-HPA chemiresistor films did not display the characteristics of the HPA. However, it should be noted that the charge associated with the voltammogram is quite low, indicating a thin film or suggesting that only part of the film was being addressed, while the film in Figure 35 appears to be quite thick.

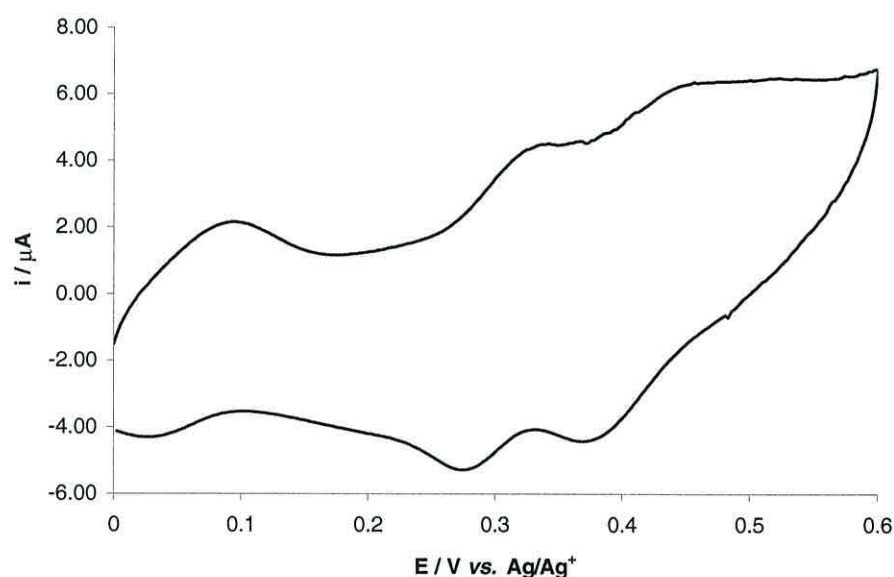


Figure 36. Voltammetric analysis of a P3MT-PM layer showing both the characteristics of P3MT and the molybdophosphate anion.

4.3.7.1 The baseline response of the P3MT-PM chemiresistor

The response of the P3MT-PM chemiresistor was observed in the nitrogen carrier gas, at 50 ml/min. It can be seen from Figure 37 that the response was not similar to those observed previously for any of the Pani or P3MT films. Initially, the resistance of the film decreased, $\Delta R_g = 4\%$, but then increased steadily beyond the base value in air, to a constant value. These results were consistent, reproducible and similar to those observed for metal oxides, such as $\text{BaSn}_{0.9}\text{Zr}_{0.1}\text{O}_3$, towards varying concentrations of a given analyte, such as hydrogen sulphide [65].

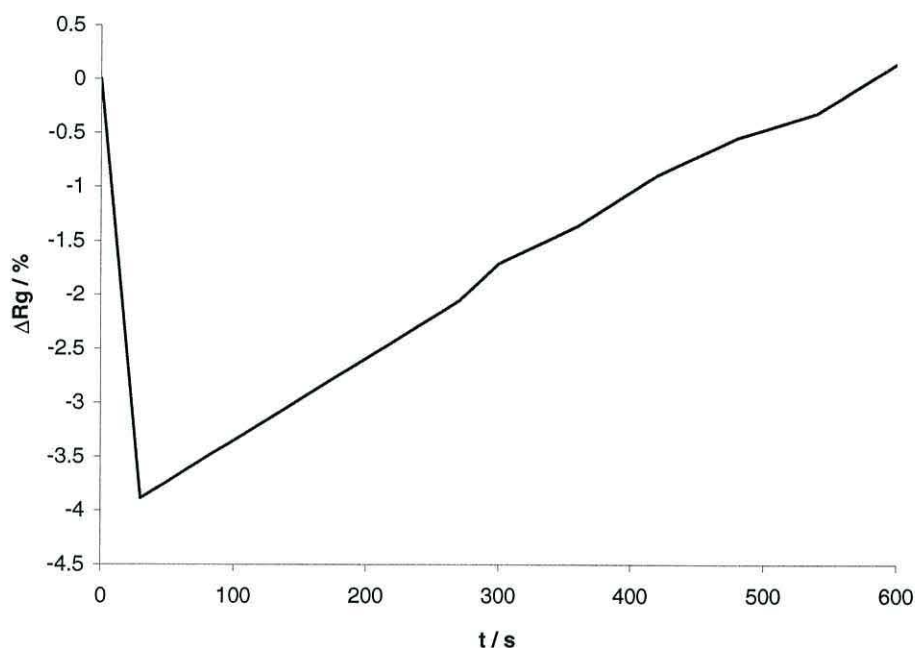


Figure 37. The baseline response of the P3MT-PM chemiresistor (+0.6 V vs. Ag/Ag⁺) in nitrogen, at a flow rate of 50 ml/min.

The reason for the observed response of the P3MT-PM chemiresistor is unknown, but it is suggested that the initial decrease of the film resistance may be due to polymer swelling. Because the films cracked whilst drying, any polymer swelling would be likely to result in the boundaries of these cracks being pushed together, which might lower the film resistance and increase the conductivity. The decrease in the film conductivity that follows would then be caused by the drying effect of the nitrogen carrier gas. If this is the case, the effects of polymer swelling must be much larger than the effects of drying in this film, but saturation must occur more rapidly as the drying effect takes over in the later stages.

4.3.7.2 The response of the P3MT-PT chemiresistor towards 2,4-DNT

The response of the P3MT-PM chemiresistor towards 2.78 ppm_v 2,4-DNT was observed as a reduction of the baseline response, as has been observed with the previous polymer chemiresistors.

Figure 38 shows the response, normalised against the baseline response. The initially observed increase in the resistance of the film, upon exposure to 2,4-DNT, indicates that the effect of polymer swelling has been reduced.

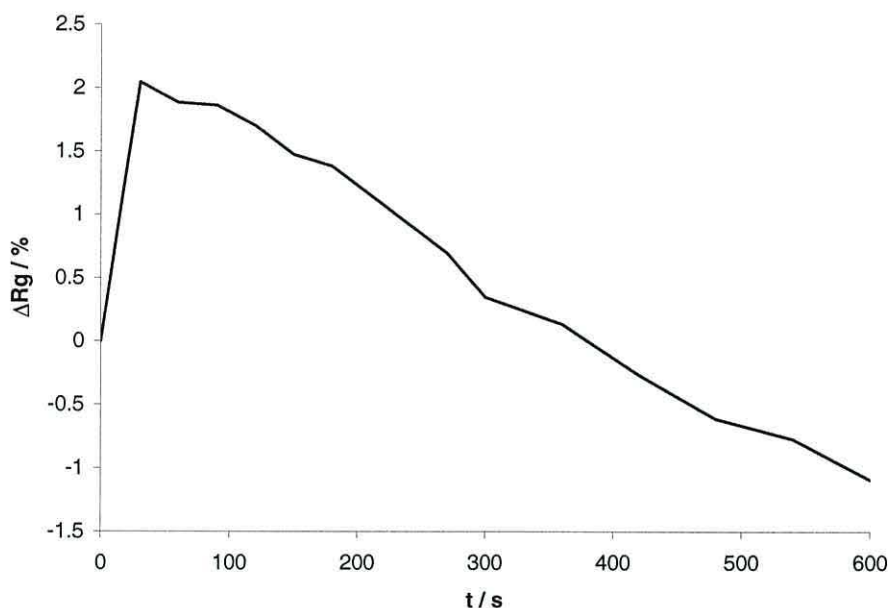


Figure 38. The response of P3MT-PM (+0.6 V vs. Ag/Ag⁺) towards 2.78ppm_v 2,4-DNT, in nitrogen at a flow rate of 50 ml/min.

The subsequent decrease in the film resistance would then be due to the interaction of the 2,4-DNT with the HPA and polymer, which would be similar in nature to those observed for the other P3MT-HPA films. Upon removal of the P3MT-PM chemiresistor from the 2,4-DNT vapour stream, the resistance of the film increased to a value above its initial base value. The resistance returned to its initial value slowly over a period of a few minutes. This again would indicate that two processes are at work. The initial fast response caused by polymer swelling, which relaxes quickly after removal from the vapour stream, may be due to the pressure of the vapour stream. The slightly slower drying-effect caused by the carrier gas is slowly restored by the RH of the laboratory air. The effects due to the interaction of 2,4-DNT with the polymer-HPA appear to be rapid and reversible.

4.4 Conclusions

Gas sensitive resistors were constructed from conducting polymer films grown on platinum microband electrodes. The polymer films resulted in the electrical connection of the electrodes, and the resistance of the films acted as the transduction mechanism. Generally, with the exception of the P3MT-PM films, the baseline response of the polymers was observed as an increase in the film resistance. This was attributed to the drying effect of the nitrogen carrier gas, since the films were kept in laboratory air at approximately 47 % RH, and was confirmed by the addition of water vapour. The addition of HPAs into the polymer film led to the enhancement of the chemiresistor response to humidity. The polymer films all exhibited a reduction of the baseline response when 2,4-DNT was present in the vapour stream. The presence of the HPA enhanced this response over the plain polymer films. This suggests that 2,4-DNT caused an increase in the conductivity of the film, which may be due to a modification of the doping level within the film, and was affected by the charge transfer between the DNT and the HPA, and then the HPA and the polymer.

The level of doping by the HPA was found to decrease with increasing film thickness, which may be due to the formation of a HPA layer at the electrode surface and the anion-exchange in the polymer bulk. Thinner polymer-HPA films would be desirable to enhance the response of the chemiresistors towards 2,4-DNT.

The best response ($\Delta R_g = 79\%$) obtained from the Pani films was with the TS anion, when the potential had been set at $-0.8\text{ V vs. Ag/Ag}^+$ (0.01 M). It is suggested that at this potential the polymer is in the neutral state whilst the HPA is in the reduced state. DNT is able to interact with the HPA, which in turn extracts electrons from the polymer, modifying the doping level. The best response ($\Delta R_g = 37.97\%$) obtained from the P3MT films was with the phosphotungstate anion.

4.5 Future Work

Preliminary studies always leave a great deal of work to be done. Here we have shown that modifying polymer films with heteropolyanions enhances their response

towards nitrogen vapour streams containing 2,4-DNT. However, this only constitutes a fraction of the work required to complete a study on this topic.

Experimentally, the chemiresistors could be improved dramatically by finding a satisfactory method for the electrochemical deposition of polymer films doped with the heteropolyanions. Currently, the thick films produced by voltammetry contain only small amounts of the HPA, certainly not enough to completely counter the charge of the doped polymer. It would also be a great advantage to be able to produce thinner films, which would limit the amount of polymer that is not countered by the HPA. This might also improve the response of the chemiresistor, as it would allow the DNT to diffuse through the entire polymer more quickly, speeding up the response. This might be achieved through the use of electrode arrays with smaller gaps, which would reduce the amount of polymer required to bridge the gap. These requirements could also be achieved, by producing the polymer chemically and then depositing the films by spin casting.

From the point of view of stability, the electrode arrays could be modified to include a more resistant epoxy resin to cover the connections between the electrodes and the pcb connecting board. The original resin was susceptible to attack from the organic solvents and acidic solutions. This often resulted in the degradation of the epoxy, which caused it to lift from the silicon, breaking the connection between the electrodes and the pcb connecting board. If a more resistant resin could be found, it could even be applied over the existing epoxy. This would also allow complete characterisation of the polymer-HPA based chemiresistors without fear of device failure.

The morphology of the polymer-HPA films appeared to be more crystalline in nature, when compared to the plain polymer films, and as a result, the films often cracked whilst drying. An advantageous method for the prevention of cracking might be through the addition of a suitable plasticiser into the monomer solution. Plasticisers are retained within the polymer structure, even when dried *in vacuo*, and help to improve the durability of the film. N-methylpyrrolidone is one such plasticiser that could be used with Pani.

The P3MT-HPA chemiresistors gave rise to an increased response towards the nitrogen carrier gas. It appeared that this response was a consequence of the drying effect of the carrier gas. Therefore, it would be appropriate to establish the precise nature of this response, in order to see how the HPA interacts with water vapour. This could be achieved using infra-red spectroscopy. Attempts could then be made to modify the polymer-HPA chemiresistors to eliminate this humidity interaction, while retaining the DNT interaction.

The polymer-HPA films also exhibited an increased response towards 2,4-DNT over the plain polymers. It is suggested that these responses are due to the interaction of the HPA with 2,4-DNT and the polymer, resulting in the modification of doping level in the polymer backbone. If this suggestion is confirmed, then the extent of polymer oxidation could be studied for thin polymer-HPA films grown onto ITO glass electrodes, using UV-Vis spectrophotometry.

Although the response of the polymer-based chemiresistors was studied for 2.78 ppm_v 2,4-DNT, the response was not studied at other concentrations. This is an obvious requirement for a sensor, so these tests should be conducted for a range of 2,4-DNT concentrations. It would also be useful to test the response of these polymer-based chemiresistors towards different nitroaromatics.

The P3MT-PM chemiresistor exhibited a different response to both the nitrogen carrier gas, and the 2,4-DNT. The reason for these observations is still unclear and further research is required.

4.6 References

1. C. K. Chiang, Y. W. Park, A. J. Heeger, H. Shirakawa, E. J. Louis, and A. G. MacDiarmid, *J. Chem. Phys.* **69** (1978) 5098-.
2. H. Shirakawa, E. J. Louis, A. G. MacDiarmid, C. K. Chiang, and A. J. Heeger, *J. Chem. Commun.* **1977** (1978) 578.
3. D. MacInnes Jr, M. A. Druy, P. J. Nigrey, D. P. Nairns, A. G. MacDiarmid, and A. J. Heeger, *Journal of chemical Society - Chemical Communications*. (1981) 317.
4. P. J. Nigrey, A. G. MacDiarmid, and A. J. Heeger, *J. Chem. Soc., Chem. Commun.* . (1979) 598.

5. G. P. Evans, *The electrochemistry of conducting polymers*. Advances in Electrochemical Science and Engineering, ed. H. Gerischer and C. W. Tobias. Vol. 1. VCH Publishers Inc., New York, (1990).
6. J. T. Lewis, *Faraday Discuss.* **88** (1989) 189-201.
7. F. Devreux, F. Genoud, M. Nechtschein, and B. Villeret. *On Polaron and Bipolaron formation in conducting polymers*. in *Proceedings of an International Winter School, Kirchberg, Tirol, March 14-21, 1987*. 1987. Kirchberg: Springer-Verlag.
8. J.-L. Bredas and G. B. Street, *Acc. Chem. Res.* **18** (1985) 309.
9. D. T. McQuade, A. E. Pullen, and T. M. Swager, *Chem. Rev.* **100** (2000) 2537-2574.
10. A. G. MacDiarmid, C. K. Chiang, A. F. Richter, N. L. D. Somasiri, and A. J. Epstein. *Polyaniline: Synthesis and characterisation of the Emeraldine oxidation state by elemental analysis*. in *Conducting Polymers Special Applications*. 1986. Sintra, Portugal: D.Reidel Publishing company.
11. T. M. Swager, *Acc. Chem. Res.* **31** (1998) 201-207.
12. S. Dogan, U. Akbulut, T. Yalcin, and S. Suzer, *Synth. Met.* **60** (1993) 27-30.
13. J. J. Miasik, A. Hooper, and B. C. Tofield, *J. Chem. Soc., Faraday Trans.* **82** (1986) 1117-1126.
14. M. G. H. Meijerink, D. J. Strike, N. F. de Rooij, and M. Koudelka-Hep, *Sens. Actuators, B.* **68** (2000) 331-334.
15. C. K. Tan and D. J. Blackwood, *Sens. Actuators, B.* **71** (2000) 184-191.
16. T. Hanawa, H. Yoneyama, S. Huwabata, and H. Hashimoto, *Synth. Met.* **30** (1989) 173-181.
17. P. Schottland, M. Bouguettaya, and C. Chevrot, *Synth. Met.* **102** (1999) 1325.
18. T. Hanawa and H. Yoneyama, *Chem. Soc. Jap.* **62** (1989) 1710-1714.
19. J. Feng and A. G. MacDiarmid, *Synth. Met.* **102** (1999) 1304-1305.
20. A. C. Partridge, M. L. Jansen, and W. M. Arnold, *Mater. Sci. Eng., C* **12** (2000) 37-42.
21. J. Langmaier and J. Janata, *Anal. Chem.* **64** (1992) 523-527.
22. F. Tanaka, S. Kojima, and K. Yoshino, *Synth. Met.* **102** (1999) 1358-1359.
23. N. T. Kemp, G. U. Flanagan, A. B. Kaiser, H. J. Trodahl, C. B., A. C. Partridge, and R. G. Buckley, *Synth. Met.* **101** (1999) 434-435.
24. D. Hodgins, *Sens. Actuators, B.* **26-27** (1995) 255-258.
25. A. Guiseppi-Elie, G. G. Wallace, and T. Matsue, *Chemical and Biological Sensors Based on Electrically Conducting Polymers*, in *Handbook of conducting polymers*, T. A. Skotheim, R. L. Elsenbaumer, and J. R. Reynolds, Editors. 1998, M Dekker: New York. p. 963.
26. S. K. Dhawan, D. Kumar, M. K. Ram, S. Chandra, and D. C. Trivedi, *Sens. Actuators, B.* **40** (1997) 99-103.
27. B. P. J. de Lacy Costello, G. P. Evans, N. Guernion, N. M. Ratcliffe, P. S. Sivanand, and G. C. Teare, *Synth. Met.* **114** (2000) 181-188.
28. A. G. MacDiarmid, *Synth. Met.* **84** (1997) 27-34.
29. V. W. Jones, *Conducting Polymers for use in Electrochromic Devices*. PhD Thesis (1995), University of Wales.
30. F. Cavani, *Catal. Today* **41** (1998) 73-86.
31. M. Fournier, R. Thouvenot, and C. Rocchiccioli-Deltcheff, *J. Chem. Soc., Faraday Trans.* **87** (1991) 349-356.
32. M. Sadakane and E. Steckhan, *Chem. Rev.* **98** (1998) 219-237.

33. M. Barth, M. Lapkowski, and S. Lefrant, *Electrochim. Acta*. **44** (1999) 2117-2123.
34. P. Wang and Y. Li, *J. Electroanal. Chem.* **408** (1996) 77-81.
35. W. Sun, H. Liu, J. Kong, G. Xie, and J. Deng, *J. Electroanal. Chem.* **437** (1997) 67-76.
36. B. Keita, F. Girard, L. Nadj, R. Content, R. Belghiche, and M. Abbessi, *J. Electroanal. Chem.* **508** (2001) 70-80.
37. B. Fabre and G. Bidan, *Electrochim. Acta*. **42** (1997) 2587-2590.
38. B. Fabre, G. Bidan, and M. Lapkowski, *J. Chem. Soc., Chem. Commun.* . (1994) 1509-1511.
39. B. Fabre and G. Bidan, *J. Chem. Soc., Faraday Trans.* . **93** (1997) 591-601.
40. F. Ragaini, M. Macchi, and S. Cenini, *J. Mol. Catal.* . **127** (1997) 33-42.
41. M. V. Joshi, S. Vaidya, R. Pandey, and D. Mukesh, *J. Catal.* . **183** (1999) 102-106.
42. M. V. Joshi and D. Mukesh, *J. Catal.* . **168** (1997) 273-277.
43. A. Bielanski, R. Dziembaj, A. Malecka-Lubanska, J. Pozniczek, M. Hasik, and M. Drozdek, *J. Catal.* . **185** (1999) 363-370.
44. D. G. Shchukin and D. V. Sviridov, *Electrochem. Commun.* **4** (2002) 402-405.
45. L. M. Abrantes, C. M. Cordas, and E. Vieil, *Electrochim. Acta*. **47** (2002) 1481-1487.
46. B. Fabre, S. Burlet, R. Cespuglio, and G. Bidan, *J. Electroanal. Chem.* **426** (1997) 75-83.
47. A. Mahmoud, B. Keita, L. Nadj, O. Oung, R. Contant, S. Brown, and Y. de Kouchkovski, *J. Electroanal. Chem.* **463** (1999) 129-145.
48. M. Hasik, A. Pron, J. Pozniczek, A. Bielanski, Z. Piwowarska, K. Kruczala, and R. Dziembaj, *J. Chem. Soc., Faraday Trans.* . **90** (1994) 2099-2106.
49. H. Sung, H. So, and W. Paik, *Electrochim. Acta*. **39** (1994) 645-650.
50. M. Lapkowski, G. Bidan, and M. Fournier, *Synth. Met.* **41-43** (1991) 407-410.
51. G. Bidan, M. Lapkowski, and J. P. Travers, *Synth. Met.* **28** (1989) C113-C120.
52. G. Bidan, E. M. Genies, and M. Lapkowski, *J. Chem. Soc., Chem. Commun.* . (1988) 533-535.
53. V. W. Jones, M. Kalaji, G. Walker, C. Barbero, and R. Kotz, *J. Chem. Soc., Faraday Trans.* . **90** (1994) 2061-1064.
54. Z. Jin, Y. Su, and Y. Duan, *Sens. Actuators, B.* **71** (2000) 118-122.
55. V. G. Kulkarni, W. R. Mathew, B. Wessling, H. Merkle, and S. Blaettner, *Synth. Met.* **41** (1991) 1009-1012.
56. T. Hagiwara, M. Yamaura, and K. Iwata, *Synth. Met.* **25** (1988) 243-252.
57. P. N. Bartlett, P. B. M. Archer, and S. K. Ling-Chung, *Sens. Actuators*. **19** (1989) 125-140.
58. G. P. Kittlesen, H. S. White, and M. S. Wrighton, *J. Am. Chem. Soc.* **106** (1984) 7389-7396.
59. E. W. Paul, A. J. Ricco, and M. S. Wrighton, *J. Phys. Chem.* **89** (1985) 1441-1447.
60. R. Wheldon-Williams, *Electrochemical Detection of Organics*. PhD Thesis (2002), University of Wales.
61. B. Fabre and G. Bidan, *Adv. Mater.* . **5** (1993) 646-650.
62. B. Ong, Y. Wu, L. Jiang, P. Liu, and K. Murti, *Synth. Met.* **Article in Press** (2003)
63. H. Masuda, D. K. Asano, and K. Kaeriyama, *Synth. Met.* **84** (1997) 209-210.

64. N. C. Billingham, P. D. Calvert, P. J. S. Foot, and F. Mohammad, *Polym. Degrad. Stab.* , **19** (1987) 323-341.
65. P. T. Moseley, *Sens. Actuators, B.* **6** (1992) 149-156.

REDOX SWITCHING OF POLYANILINE

5.1 Introduction

It has been demonstrated that gas-sensitive resistors (chemiresistors) can be produced through the deposition of a polymer film across a pair of adjacent microband electrodes. In its conducting state, the polymer establishes an electrical connection between the electrodes, with the conductance of the film acting as the transduction mechanism of the sensor.

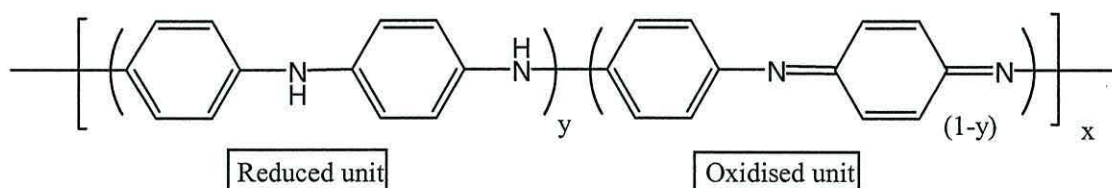
In order to ascertain whether or not the polymer films had successfully bridged the electrode gap, they were characterised by voltammetry, using each of the individual electrodes in turn, and then both electrodes operated together as a pair. If the polymer film had successfully bridged the gap, each electrode would be able to address (i.e. oxidise/reduce) the entire film. Therefore, as the film is finite, the corresponding charge associated with these processes should be identical for each electrode configuration, and it might be assumed that the corresponding voltammetry and chronoamperometry would be identical [1]. The following study, using polyaniline as the example of the conducting polymer, illustrates the effect of electrode contact area and position within an array on the electrochemical redox switching characteristics of the film.

5.1.1 Polyaniline (Pani)

Polyaniline was first reported in a paper by Letheby [2] in 1862. However, it has been suggested that its occurrence dates back to 1834 [3]. Pani is formed by the oxidative polymerisation of aniline in aqueous acidic media (typically HCl, HClO₄, or H₂SO₄). Polymerisation can be induced chemically or electrochemically using a range of conditions. Chemical synthesis is usually carried out in aqueous media using oxidising agents such as ammonium persulphate or ammonium peroxydisulphate, although other oxidising agents have been reported, as have other solvents [3]. Electrochemical synthesis is often the preferred polymerisation technique, as it enables films to be grown directly onto an electrode surface, and the electrode can then be used directly in

combination with other techniques including spectroelectrochemistry [4], microscopy [5] and ellipsometry [6]. Electrochemical polymerisation of Pani requires the application of an anodic potential sufficient to oxidise the monomer at the electrode surface, typically 0.99 V *vs.* SCE on platinum. However, after the formation of the initial polymer layer, the oxidation potential may be reduced (0.6 V *vs.* SCE) due to the autocatalytic behaviour of the polymer itself. It has been proposed that polymerisation proceeds *via* a mechanism whereby neutral aniline is incorporated into the chain by electrophilic attack of the nitrenium cation [7] (the nitrenium cation is formed *via* deprotonation of the iminium cation that is formed by the single two electron oxidation of the oligomer).

Polyaniline does not have a well-defined structure, but is composed of a complex series of different repeat units, dependent on the oxidation and doping levels. MacDiarmid *et al.* [8] described the structure of the polymer by the following general formula, where $1 \geq (1-y) \geq 0$.



The oxidation state of the polymer can then be defined by the value of $(1-y)$. For the totally reduced form of polyaniline (leucoemeraldine) $(1-y) = 0$, for the semi-oxidised polymer (emeraldine) $(1-y) = 0.5$ and for the totally oxidised polymer (pernigraniline) $(1-y) = 1$. The structure of polyaniline has been extensively studied [9-13] and the general consensus is that Pani exists in five forms, represented by repeat units, dependent on oxidation and protonation levels, as shown in Figure 1.

The morphology of Pani has also been well studied [14-22]. There are several factors that influence the film morphology, including preparation methods [9, 23, 24], types of anion employed [25] and the sweep rate [26].

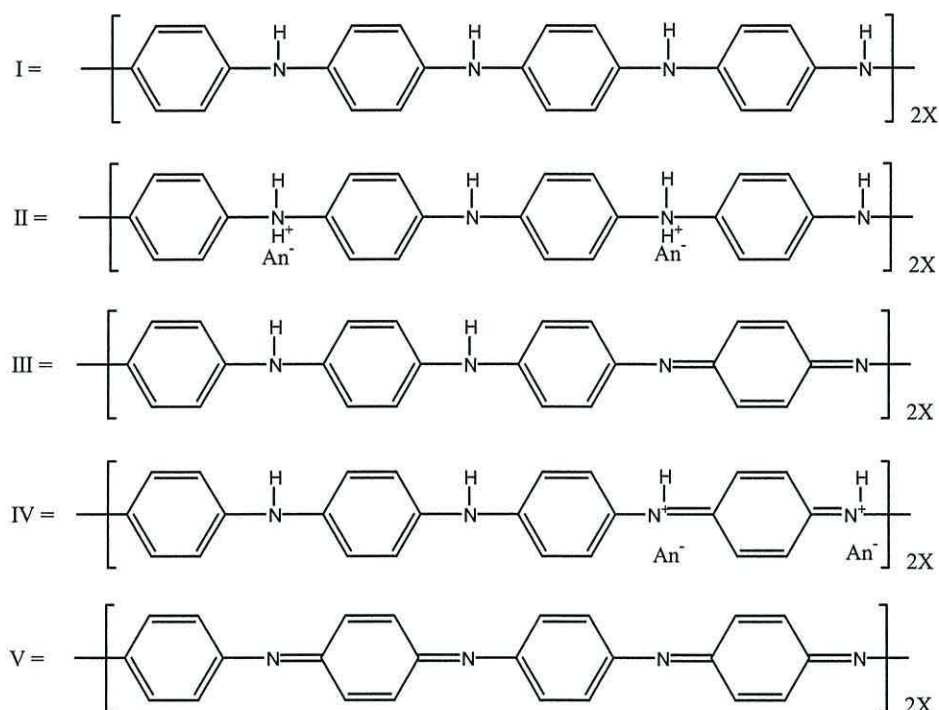


Figure 1. The five forms of Pani. I = leucoemeraldine base, II = leucoemeraldine salt, III = emeraldine base, IV = emeraldine salt, and V = pernigraniline [13].

Polyaniline can be oxidised and reduced between its different forms by chemical or electrochemical techniques. The first redox reaction occurs without modification or degradation of the film by a reversible amine-imine type transformation. However, further oxidation to the pernigraniline state is an irreversible process that modifies the polymer, rupturing the chain with subsequent hydrolysis yielding a quinonic structure [3]. During oxidation, the induced positive charge is compensated through the insertion of anions into the film. This maintenance of charge neutrality, has been verified using EQCM (electrochemical quartz crystal microbalance) measurements [27, 28]. Probe beam deflection has also shown the movement of protons to/from the film during redox processes [29], and this process is believed to precede anion insertion during the first oxidation with the reverse occurring on reduction. The following redox mechanism, shown in Figure 2, has been proposed for polyaniline [13].

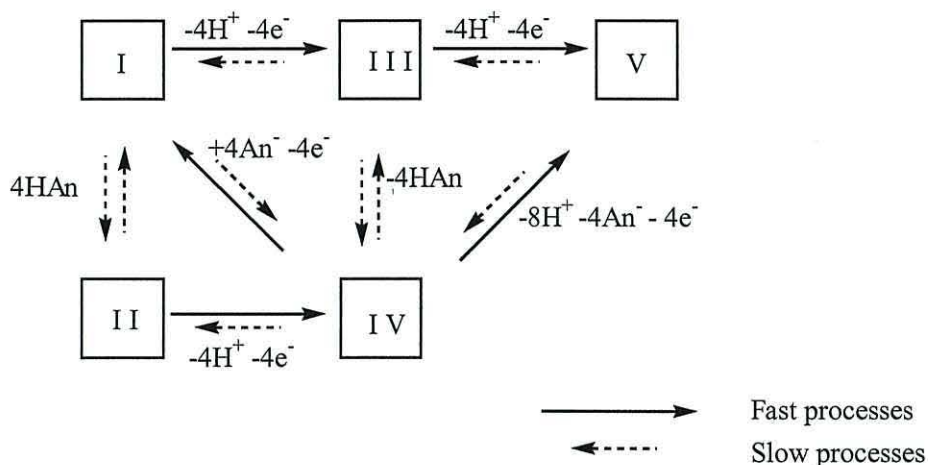


Figure 2. A proposed scheme for the redox processes in Pani [13]. I, II, III, IV and V relate to the Pani forms from Figure 1.

The conductivity range for polyaniline has been shown to span several orders of magnitude (10^{-10} to 10 Scm^{-1} [8]), reaching near metallic conduction levels. This fact alone has driven much of the research concerning the use of Pani in microelectronic devices [1, 30]. Conduction is highly dependent upon both the oxidation and protonation state of the polymer, with only the protonated emeraldine salt form exhibiting high conductivity. Initially, conduction proceeds *via* the formation of doubly charged spinless polarons (also known as bipolarons), but at higher doping levels segregation of the charge yields a conducting polaron lattice [31], which has been observed using electron spin resonance [32, 33] and optical spectroscopy [34, 35].

5.1.2 Redox switching of polyaniline

Redox switching of Pani between its insulating and conducting forms has received a great deal of attention over the past two decades. The switching reaction corresponds to the oxidation/reduction of the π -system of the protonated aniline units in the polymer, which are converted from the benzoid to the quinoid-type structures [36] and vice versa. The switching rate has been shown to be very fast in thin films [37] and several hypotheses have been offered to explain the rate-determining process.

It has been suggested that the rate of oxidation is controlled by the RC time constant associated with the series combination of the electrolyte resistance and film capacitance [38] and also the kinetics of anion insertion/removal [39]. The rate-limiting RC time constant can be overcome through the use of microelectrodes [13, 37, 40] and it has since been shown that proton/anion transfer processes are not rate-determining, rather that the process is kinetically controlled [37, 41, 42]. The oxidation step is analogous to electrocrystallisation of surface phases on mercury [37, 40]. The study of oxidative chronoamperometric responses of Pani thin-films led to the suggestion that in the initial stages of oxidation emeraldine “cylinders” are nucleated at the electrode surface, which is followed by the peripheral expansion of such cylinders, with ion incorporation and proton egress being sufficiently rapid to maintain charge neutrality [40]. A theory of propagation has been put forward by Tezuka and Aoki [41, 43] for the oxidative switching of conducting polymer free-standing films, which proposes that upon the application of an oxidising potential, only the neutral polymer that is very close to the electrode surface is oxidised, becoming locally conductive. The new conductive polymer now acts as the electrode, oxidising the neutral polymer immediately next to it and converting it to a new conductive domain. By iteration of this process the conductive zone is propagated to the top of the polymer film. The propagation of the conducting front has been visualised using photographic techniques [41], spectroscopic measurements using a diode array detector [44], and potentiometric measurements of adjacent electrodes [43]. The rate of propagation is kinetically controlled by the rate of charge transfer across the conducting/insulating boundary, which is dependent on the applied potential. Typical rates have been quoted at 1 mms^{-1} for polypyrrole (0.8 V vs. SCE) [44] and 0.1 mms^{-1} for polyaniline (0.5 V vs. SCE) [45].

It is now generally accepted that reductive switching occurs through a different mechanism to that of oxidative switching [46, 47]. This might be expected because if reduction occurred at the polymer/electrode interface a layer of insulating material adjacent to the electrode surface would disconnect the electrode from the oxidised polymer. Several suggestions have been made as to how the conversion process switches the conducting form to the insulating form of the polymer, including the progressive

contraction of the polymer strands from the polymer solution interface [40] and fractal formation [47]. Aoki and co-workers used percolation theory [47, 48] to model the reduction of conducting polymers, where the initial conversion of a polymer from conducting to insulating form occurs very rapidly and simultaneously throughout the film, but then stops at the percolation threshold of the molar fraction of the conducting species, as conduction in the film is broken. This is then followed by a slow relaxation process, which is reported as the competition between diffusional retrieval of electric pathways from the local conducting zones to the electrode and the electrochemical cut-off of the electric paths. This theory also helps to explain another significant feature of redox switching in conducting polymers, hysteresis [49]. Hysteresis, also known as the memory effect [50] or the first cycle effect [37], results in a discontinuity between the voltammetric characteristics of the first and subsequent cycles (oxidation), including variations of oxidation potential, peak current and peak charge.

The redox characteristics of a polymer film can be influenced by a number of factors. The oxidation peak potential has been observed to shift to more positive values with increasing pH [13, 36], anion size [13], reduction time [42, 49, 50], sweep rate [42, 49], decreasing film thickness and large films [45] and increasing temperature [51]. While the current maximum and redox charge decrease with decreasing temperature [40], reduction time [42] and charge will also decrease with increasing pH and anion size [13]. The study presented here aims to demonstrate that the redox characteristics of a single Pani film can also be manipulated by changing the size and position (within an array) of the working electrode.

5.2 Experimental

5.2.1 Electrodes

The platinum working electrodes formed part of an eight-electrode array (Windsor Scientific Ltd). In the first part of this study, the electrode dimensions were approximately $1000 \times 100 \mu\text{m}$, and the electrodes were separated by gaps of

approximately 5, 10, 25, 50, 50, 100, and 200 μm (Figure 3A). In the second part of this study, the electrode dimensions were $1000 \times 10 \mu\text{m}$, separated by gaps of 10 μm (Figure 3B). The electrode arrays were fixed to a printed circuit connecting board (pcb), which expanded the contacts to allow connection to the individual electrodes (Figure 3C). In both cases the secondary electrode was a Pt foil electrode, and all measurements were made relative to the saturated calomel electrode (SCE).

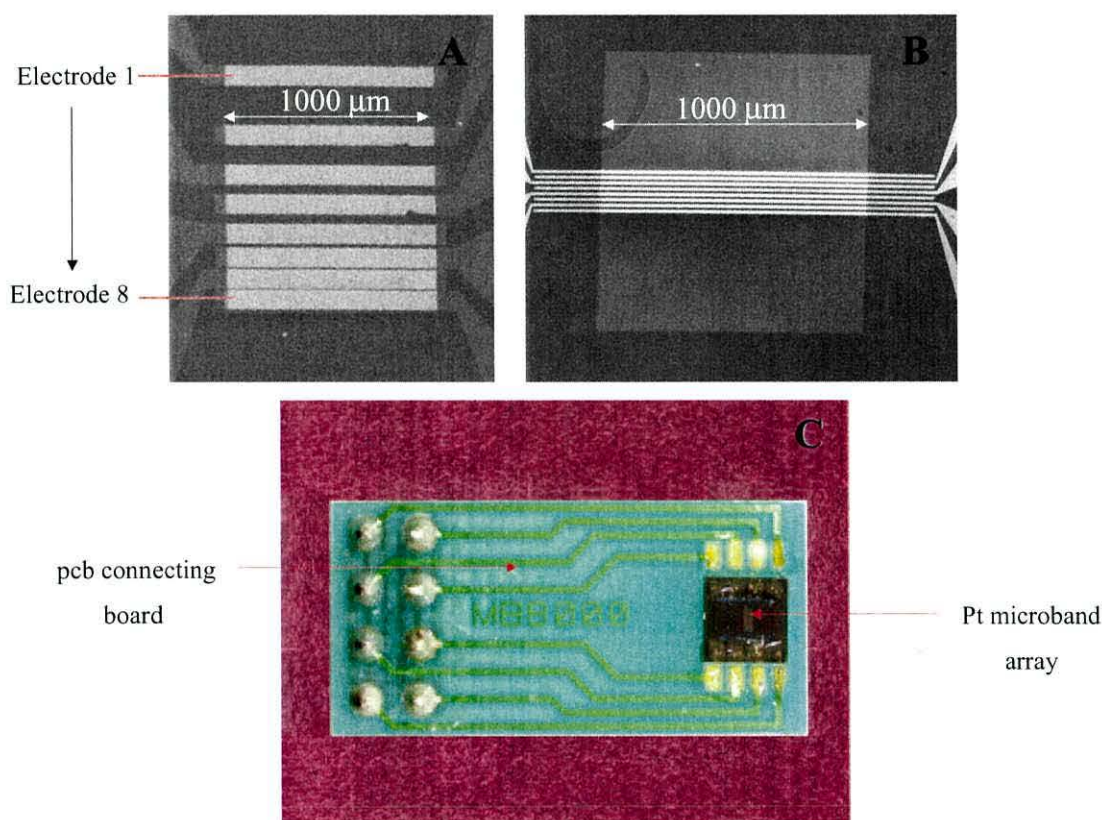


Figure 3. Typical platinum electrode arrays used during this study. The array (A) consisted of eight electrodes ($1000 \times 100 \mu\text{m}$) with separations varying from 5 – 200 μm . The array (B) consisted of eight electrodes ($1000 \times 10 \mu\text{m}$) with separations of 10 μm . An array is also shown mounted on a pcb connecting board (C).

5.2.2 Polymer deposition

Pani films were prepared potentiodynamically by cycling the potential between -0.2 V and $+0.75$ V, at 100 mVs^{-1} . The monomer solutions were prepared from 1 M aniline (used as supplied, 99.9+ %, Aldrich) in 1 M HCl. After the appropriate amount of charge had been passed the film was removed from the aniline solution and rinsed thoroughly with 1 M HCl and deionised water.

5.2.3 Voltammetry

Pani films were characterised in a monomer free 1 M HCl solution between -0.2 V and $+0.5$ V. The sweep rate was either 10 mV s^{-1} or 50 mV s^{-1} and this will be shown in the appropriate section. Prior to measurements, new Pani films were cycled several times to ensure the removal of any residual monomer trapped within the polymer layer.

5.2.4 Chronoamperometry

Characterisation by chronoamperometry was performed in 1 M HCl solutions. The potential of the working electrode was stepped from -0.2 V to a second potential limit (E_2), which will be shown in the appropriate section (usually $+0.5$ V). All experiments were conducted inside a Faradaic cage.

5.2.5 Potentiometric monitoring

Chronoamperometric and voltammetric measurements were conducted as described above. However, the potential of the electrodes situated adjacent to the working electrode were monitored during these measurements using homemade circuitry (Figure 4). The electronics were able to measure the potential of the monitoring electrodes through the application of 1 V across a large resistor ($100 \text{ M}\Omega$), which acted to keep any currents that flowed through the film low as possible. The potential was measured relative to that of the working electrode, so that when the polymer film between the working electrode and the monitoring electrode was reduced and insulating, the potential of the monitoring electrode followed the potential of the working electrode, offset by 1 V.

However, when the polymer film was oxidised and conducting, a short circuit was established between the working and monitoring electrode and the potential of the monitoring electrode was then dependent on the resistance characteristics of the film. Therefore, by observing the behaviour of the monitoring electrode potential, relative to the potential of the working electrode, oxidation could be monitored at different points across the film.

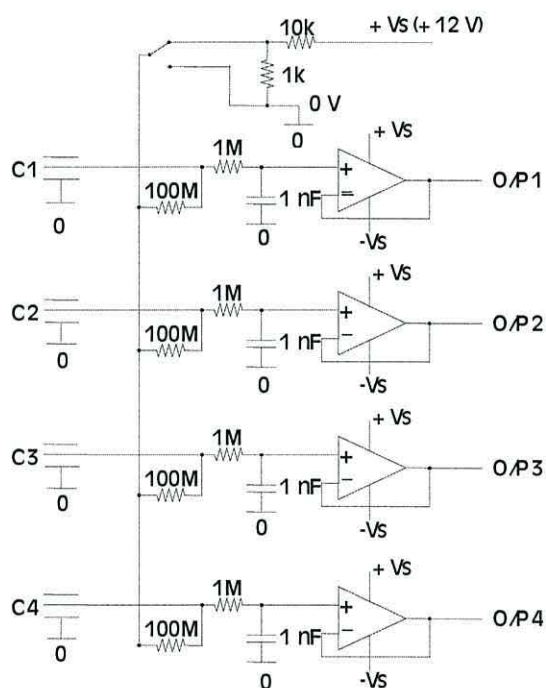


Figure 4. The electronics used to measure the potential of the monitoring electrodes, where C1-C4 corresponds to the electrode connections, and O/P 1-4 correspond to the output potentials.

5.2.6 Film thickness

The thickness of each polymer film was determined from a previously calculated charge/thickness ratio obtained from ellipsometry [6], and confirmed by SEM.

Prior to all voltammetric and chronoamperometric measurements the solutions were purged with nitrogen and the potential of the working electrodes was held at -0.2 V for a period of 10 minutes to ensure complete reduction of the Pani film.

5.3 Results and Discussion

5.3.1 The influence of electrode contact area

In order to study the effect of the electrode contact area on the redox characteristics of Pani, a film was deposited onto two adjacent platinum microband electrodes. These electrodes could then be used to address the redox chemistry of the polymer layer. In theory, each electrode should be able to address the entire film, and therefore the electrodes can be operated individually or together. The electrode contact area was varied by using either a single electrode or the electrode-pair as the working electrode.

5.3.1.1 Case A

The first method (Case A) relied on the use of the platinum electrode array shown in Figure 3A. Each electrode was $100 \times 1000 \mu\text{m}$, giving a contact area of $1 \times 10^{-3} \text{ cm}^2$. Pani was deposited over two adjacent Pt microband electrodes (electrodes 7 and 8) separated by a $5 \mu\text{m}$ gap, as can be seen in Figure 5.

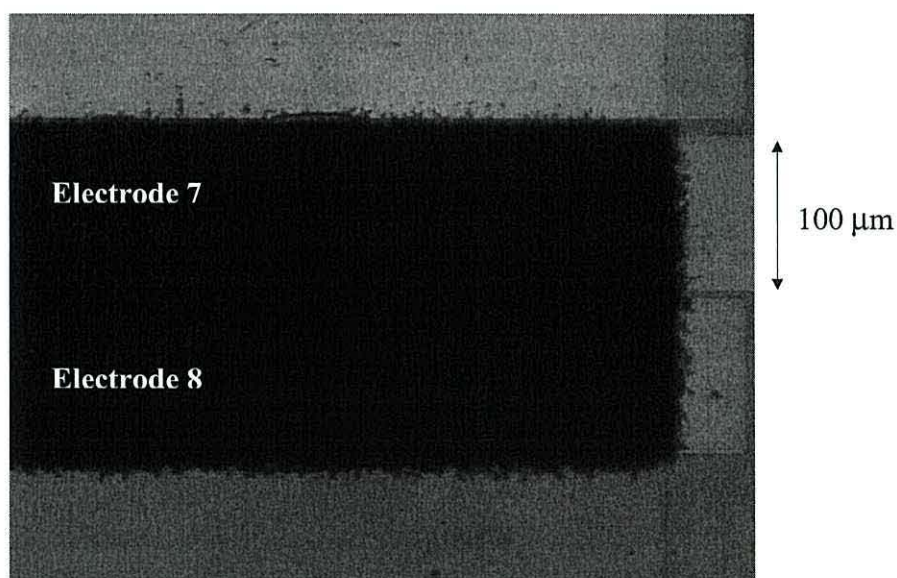


Figure 5. A Pani layer connecting two Pt micro-band electrodes (Case A).

When electrode 7 or electrode 8 were used individually to address the film, the contact area of the working electrode was $1.0 \times 10^{-3} \text{ cm}^2$. However, when both electrodes were operated together (from here on known as the “electrode-pair”) to address the film, the contact area of the working electrode was $2.0 \times 10^{-3} \text{ cm}^2$.

5.3.1.2 Case B

The situation above can be extended further to give rise to polymer films that are in contact with two electrodes of different contact areas. In the second method, Case B, the platinum electrode array shown in Figure 3A was also used, but in this case Pani was deposited onto a single Pt microband working electrode (electrode 8). Another platinum microband electrode (electrode 6) was used as the counter electrode and the film grew in the direction of the field across the $5 \mu\text{m}$ gap to a neutral microband electrode (electrode 7), situated between electrodes 6 and 8 (Figure 6). This resulted in two different contact areas, one equal to the area of the working electrode ($1.0 \times 10^{-3} \text{ cm}^2$), and another significantly smaller (approximately $1.0 \times 10^{-4} \text{ cm}^2$) on the neutral electrode. The contact area of the neutral electrode was estimated from SEM.

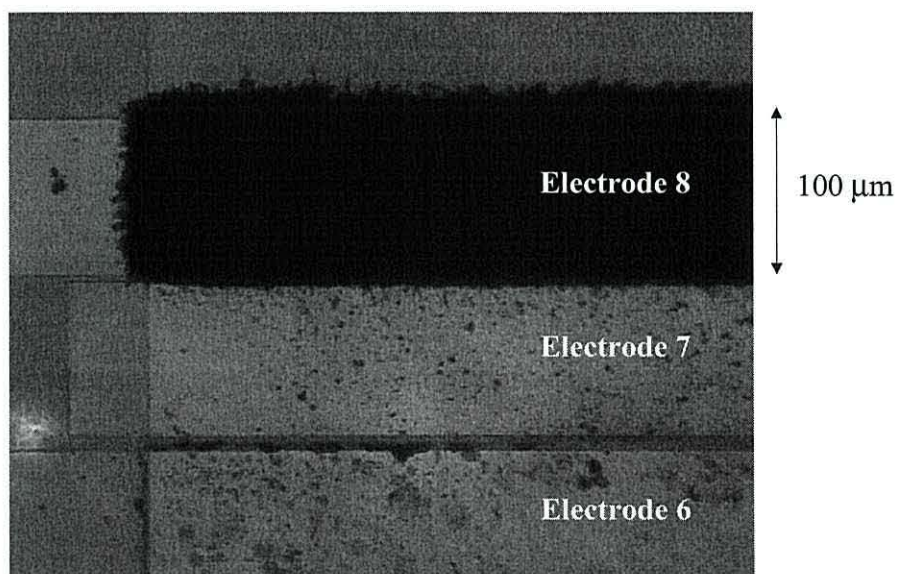


Figure 6. A Pani layer connecting two Pt micro-band electrodes (Case B).

5.3.1.3 Voltammetry – Case A

In order to ascertain that the polymer film had bridged the gap successfully and established electrical contact between the working and neutral electrodes, the voltammetry of the polymer film was characterised using electrode 7, electrode 8, and the electrode-pair in turn as the working electrode. It should be noted that if the film failed to bridge the gap, it was returned to the monomer solution and further Pani was deposited until electrical connection was established. These voltammograms are shown in Figure 7 and possess the typical features associated with the redox switching of Pani. The current-potential plots were all obtained under identical conditions and yield identical charges for the first oxidation ($Q = 338 \mu\text{C}$), thus confirming that each electrode was able to address the entire film. However, it can be seen from Figure 7 that the voltammograms are not identical for every electrode configuration.

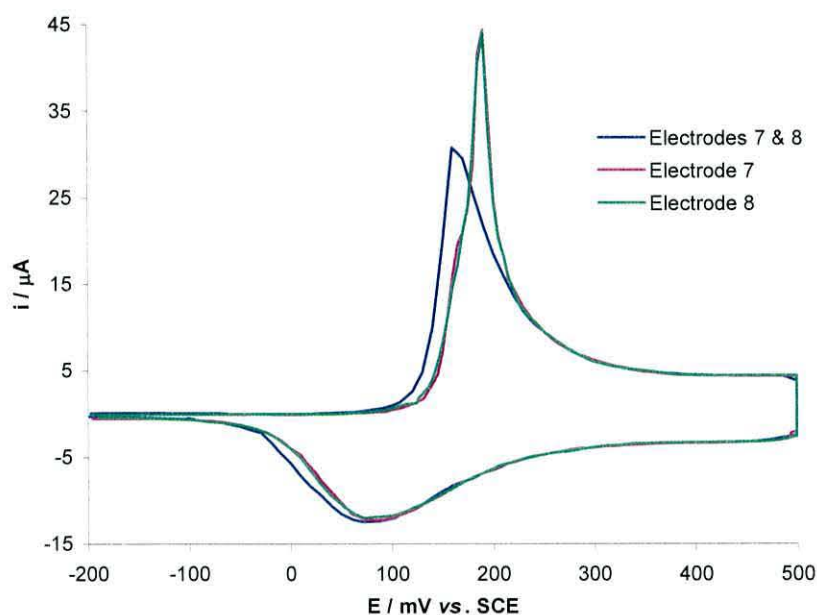


Figure 7. Cyclic voltammograms (1st cycle) obtained for a Pani film ($340 \mu\text{C}$, Case A), using electrode 7 (pink line), electrode 8 (green line), and the electrode-pair (blue line) as the working electrode.

The voltammogram obtained using the electrode-pair as the working electrode exhibits an anodic peak at $E_{p(ox)} = 170$ mV vs. SCE, with a current maximum of $I_{p(ox)} = 32$ μ A. Whereas, the voltammograms obtained using the individual electrodes exhibit anodic peaks at $E_{p(ox)} = 190$ mV vs. SCE and are sharper with $I_{p(ox)} = 44$ μ A, as can be seen in Table 1 in terms of the peak width at half current maximum (FWHM). The shift in peak potential suggests that a larger potential is required to switch the film when it is addressed through a single electrode. However, once oxidation starts, it would appear that it proceeds at a faster rate than when the electrode-pair is used.

Electrode	Contact Area / cm^2	FWHM / mV
Pair	2×10^{-3}	65
7	1×10^{-3}	30
8	1×10^{-3}	30

Table 1. FWHM values for the oxidation of a Pani film (340 μ C, Case A), obtained using different electrode contact areas.

The oxidation charge can be plotted as a function of potential, as is shown in Figure 8. The plot was obtained by integrating the voltammogram at 50 mV intervals and shows that below 150 mV no significant oxidation had occurred. Between 150 and 250 mV the charge associated with the electrode-pair is much larger than that associated with the individual electrodes, suggesting that when the electrode-pair was used to address the film, oxidation proceeded at a faster rate at lower potentials or the onset of oxidation occurred at lower potentials.

A Tafel-type plot can be constructed from the voltammogram (Figure 9). It must be emphasised that voltammetry is a dynamic process and that the sweep rate used was rather fast (10 mV s^{-1}), hence no values for fundamental parameters such as the exchange current density or the anodic transfer coefficient have been calculated.

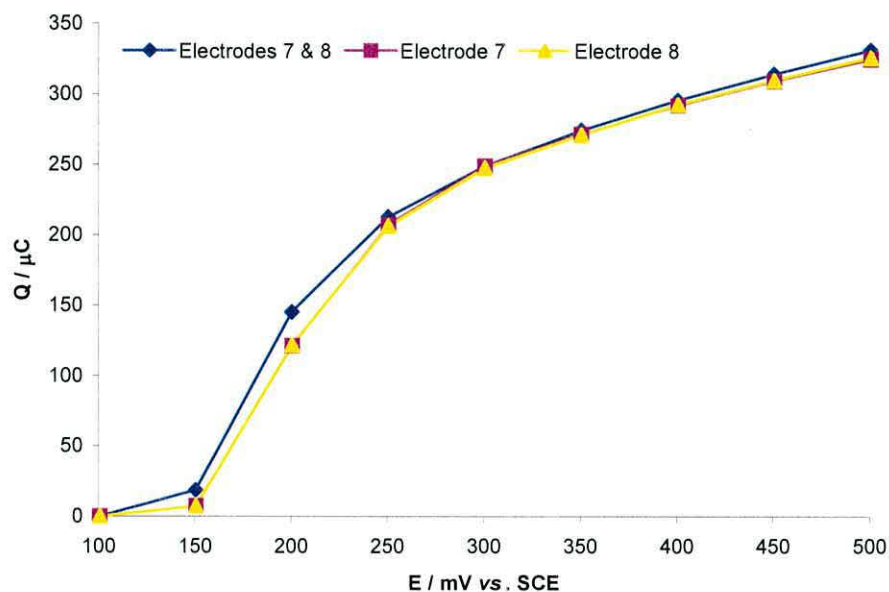


Figure 8. A plot of charge versus potential during the voltammetry of a polyaniline film (340 μC , Case A) addressed through the electrode-pair (blue line), electrode 7 (pink line) and electrode 8 (orange line).

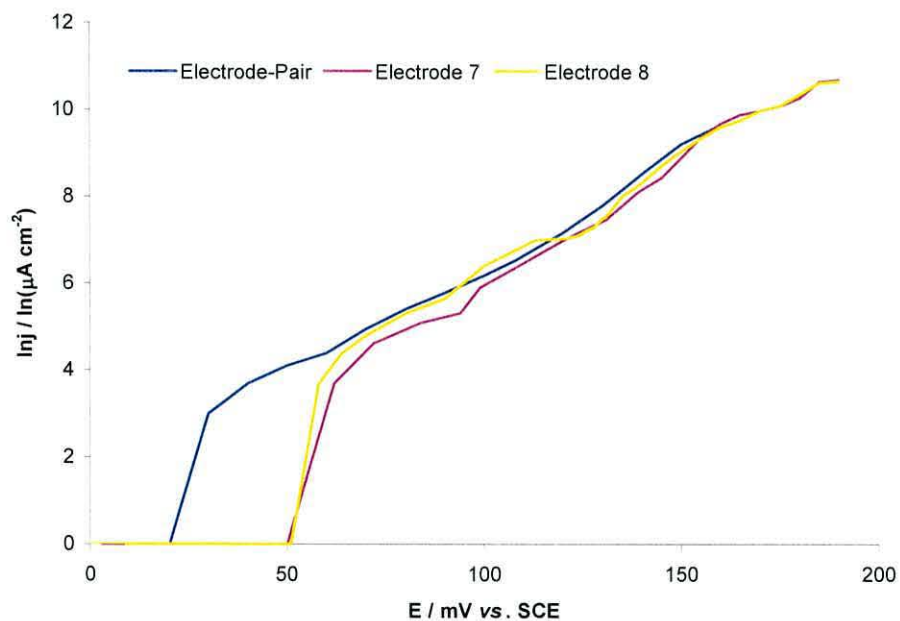


Figure 9. Tafel-type plots for the 1st oxidation of a Pani film (340 μC , Case A), addressed through the electrode-pair (blue line), electrode 7 (pink line) and electrode 8 (orange line).

Aoki and Tezuka [41, 44] also constructed Tafel-type plots using the logarithm of the propagation speed of the conducting insulating interface *versus* the second potential limit, after a series of potential steps. The plots, albeit obtained under different parameters, were very similar in nature to those obtained here. However, in Figure 9 it is interesting to note that the onset of current density did not occur at the same potential when different electrode contact areas were used to address the film. The onset of current density associated with the electrode-pair occurred at a lower potential than when the individual electrodes were used as the working electrode. The plots obtained using the individual electrodes were very similar. This suggests that oxidation is not feasible at lower potentials when smaller electrode contact areas are employed to address the film.

The reduction peak (Figure 7) associated with the electrode-pair, exhibits a maximum current, $I_{p(\text{red})} = 12 \mu\text{A}$, at a peak potential of $E_{p(\text{red})} = 85 \text{ mV vs. SCE}$, with a charge of $Q_{(\text{red})} = 348 \mu\text{C}$. The reduction peaks associated with the individual electrodes possess very similar peak potentials ($E_{p(\text{red})} = 84 \text{ mV vs. SCE}$) and current maxima ($I_{p(\text{red})} = 12.0 \mu\text{A}$), but the charge associated with the reduction peak is slightly smaller ($Q_{(\text{red})} = 340 \mu\text{C}$). This suggests that when smaller electrode contact areas are employed to reduce the film, electrical connection between the oxidised phase and the electrode surface is broken with a higher proportion of conducting (oxidised) islands remaining in the insulating (reduced) matrix. These points will be explained further during the voltammetry discussion later in the chapter.

5.3.1.4 Voltammetry - Case B

For Case B, the voltammetry observed using the different electrode configurations is shown in Figure 10. As with Case A, the voltammograms for the first oxidation were all obtained under identical conditions and exhibit identical charges ($Q_{(\text{ox})} = 310 \mu\text{C}$). The voltammograms obtained using the electrode-pair and electrode 8 have very similar contact areas and are comparable, with anodic peak potentials at $E_{p(\text{ox})} = 170 \text{ mV vs. SCE}$, and current maxima of $I_{p(\text{ox})} = 25 \mu\text{A}$ and $I_{p(\text{ox})} = 23 \mu\text{A}$, respectively. However, the voltammogram obtained using electrode 7, which possessed a significantly smaller

electrode contact area, exhibited a peak potential at $E_{p(ox)} = 210 \text{ mV vs. SCE}$, and a current maximum of $I_{p(ox)} = 40 \mu\text{A}$.

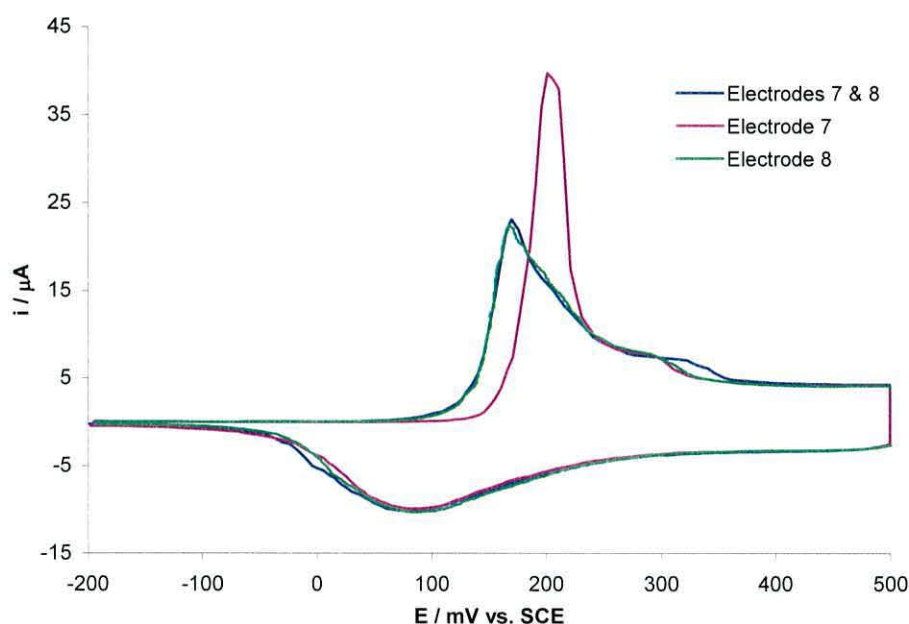


Figure 10. Cyclic voltammograms (1st cycle) for a Pani film (310 μC , Case B), using electrode 7 (pink line), electrode 8 (green line) and electrode-pair (blue line) as the working electrode.

The anodic peaks obtained using electrode 7 gave rise to a much sharper peak. The peak width at half current maximum (FWHM) value for electrode 7 can be seen in Table 2 and is much smaller than those obtained from electrode 8 and the electrode-pair. Again, this suggests that a higher potential is required to oxidise the film when an electrode of smaller contact area is used. However, once the oxidation process has initiated, it proceeds at a faster rate.

Electrode	Contact Area / cm ²	FWHM / mV
Pair	1.05×10^{-3}	80
7	0.05×10^{-3}	35
8	1×10^{-3}	80

Table 2. FWHM values for the oxidation of a Pani film (310 μC , Case B), obtained using different electrode contact areas.

Figure 11 shows the charge associated with the oxidation of the polyaniline film plotted as a function of potential.

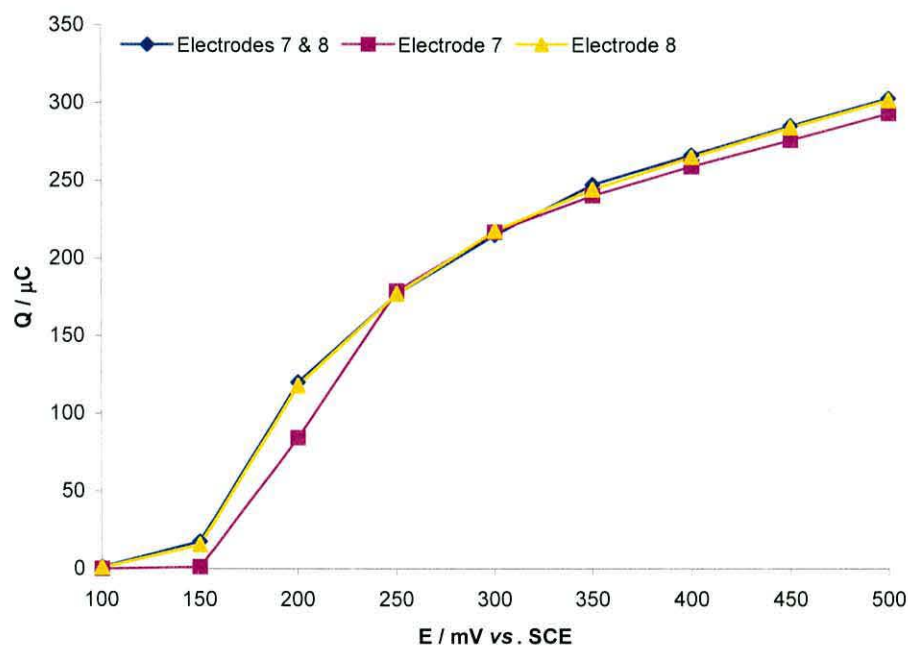


Figure 11. A plot of charge versus potential during the voltammetry of a polyaniline film (310 μC , Case B), addressed through the electrode-pair (blue line), electrode 7 (pink line) and electrode 8 (orange line).

Below 150 mV no oxidation of the film occurred. At 150 mV there was significant charge associated with electrode 8 and the electrode-pair, but no charge associated with electrode 7, suggesting that higher potentials are required to drive the oxidation of the film when the smaller electrode contact area was employed. Between 250 and 300 mV

the total charge observed was similar for each electrode configuration, but by 500 mV the overall charge associated with electrode 7 was slightly less than for electrode 8 and the electrode-pair. This may indicate that electrodes with smaller contact areas are unable to drive the oxidation process to completion, or may signify a diminished capacitive contribution.

Tafel-type plots constructed from the data obtained during the voltammetric oxidation of the Pani film are shown in Figure 12. In this case, the onset of current density associated with the electrode-pair occurred at a slightly lower potential than that associated with electrode 8, but the current density associated with electrode occurred at a much higher potential. This indicates once again, that smaller electrode contact areas require higher potential in order to drive the oxidation process.

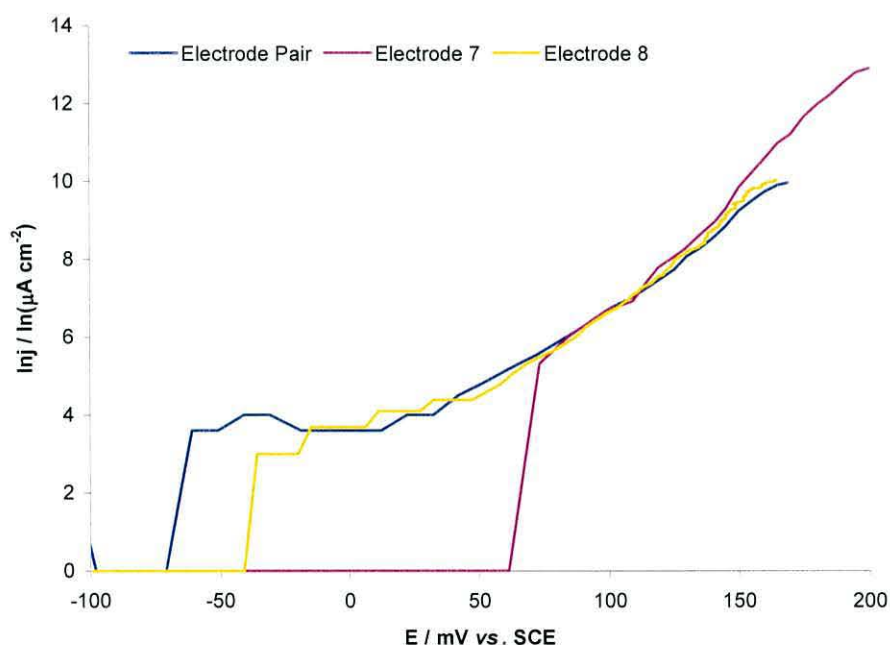


Figure 12. Tafel-type plots for the 1st oxidation of a Pani film (310 μC , Case B), addressed through the electrode-pair (blue line), electrode 7 (pink line) and electrode 8 (orange line).

It must be noted that the oxidation peak potentials for the electrode-pair, essentially contacting the entire polymer, were not always identical for case A and Case B polymer

films. This was to be expected since they were different films produced on different occasions from different monomer solutions. Although films were deposited with similar charge they were not all of equivalent thickness. These factors were likely to account for the differences in $E_{p(ox)}$ between the films and hence no direct comparison was made between them.

The reduction peaks (Figure 10) obtained from electrode 8 and the electrode-pair were also different from that obtained from electrode 7. Peak potentials for electrode 8 and the electrode-pair occurred at $E_{p(red)} = 90$ mV vs. SCE, the peak current was also very similar, $I_{p(red)} = 10.3$ μ A, and the charge associated with the reduction was $Q_{(red)} = 310$ μ C. The peak potential for electrode 7 was similar to those of electrode 8 and the pair, and the peak current was only slightly lower at $I_{p(red)} = 9.9$ μ A, but the charge associated with electrode 7 was much smaller at $Q_{(red)} = 274$ μ C indicating a substantial enhancement of the memory effect.

5.3.1.5 Voltammetry discussion

From the data shown above, it is obvious that the area of the working electrode in contact with a polymer film influences its redox characteristics. Two of the more interesting observations are the shift in the oxidation peak potential and the decrease of the charge associated with the reduction process.

Several factors are known to affect the oxidation peak potential. The first cycle effect, also known as the memory effect [37, 49, 50], causes a shift in the oxidation potential between the first and subsequent cycles due to incompleteness of the reduction process. The percolation theory put forward by Aoki and Tezuka [48] states that reduction occurs rapidly to begin with, but requires a long time to complete (logarithmic relaxation). As a result of this logarithmic relaxation, the length of time that the polymer film is subjected to a reducing potential has a marked effect on the potential required to drive the following oxidation [42]. The longer the reduction period prior to the oxidation, the higher the resulting oxidation peak potential, until complete reduction is attained. Film

thickness has also been shown to have a marked influence on the effect of reduction time on the oxidation peak potential [42], as does the sweep rate [52].

In order to compensate for the effects of slow relaxation, it is essential to ensure that the polymer film is completely reduced prior to all measurements. In the present study this was achieved by holding the potential of the film at -200 mV for exactly 10 minutes. This resulted in first-cycle oxidation peaks with identical charges to each other and to that of the chemically reduced film, irrespective of electrode contact area. Additionally, if the film were to retain any conducting material it would act to reduce the oxidation potential, as seen on the second cycle, in a similar way to the memory effect. Lower reduction charges were observed when smaller electrode contact areas were employed, and therefore it would be expected that a higher fraction of oxidised material should remain in the film. Consequently, smaller electrode contact areas should give rise to lower oxidation potentials, which is contrary to what was observed here. The incomplete reduction would also give rise to a diminished memory effect between first and subsequent cycles, which was not observed. The sweep rate was always kept at a constant value, and thus would not affect the results. Film thickness was kept constant as the voltammetry was conducted on single films and different films were not directly compared.

The anodic peak potential for the first oxidation was found to be dependent on the electrode contact area used to address the film. The reason for this appears to be two-fold. Firstly, reducing the contact area of the working electrode gives rise to a greater proportion of the polymer that is not in direct contact with the working electrode. This effectively increases the distance that the conducting-insulating interface must travel in order to complete the oxidation process. This is depicted in Figure 13, where the length of the arrows represents the distance that the conducting front must propagate for the entire polymer layer to be oxidised. As the potential is being altered with time, a longer propagation time would result in the process completing at a higher potential.

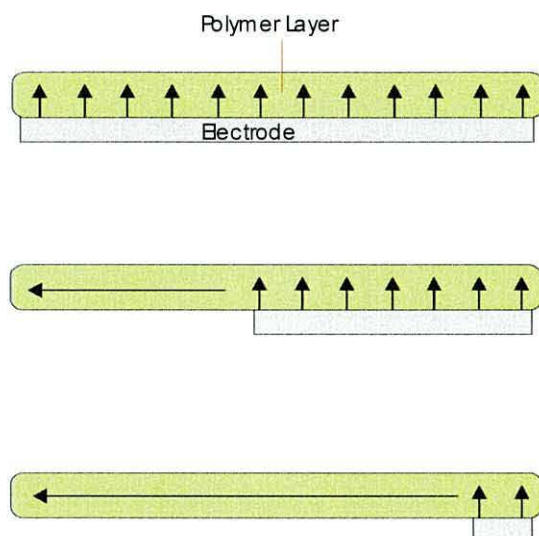


Figure 13. A representation of Pani oxidation depicting the effect of reducing the electrode contact area on the length of propagation. The length of the arrow represents the distance that the conducting front must travel in order to completely oxidise the film.

Secondly, there appears to be a shift in the percolation threshold potential. The percolation threshold potential has been defined as the potential at which the conducting zone begins to grow in a dopant-rich solution when the conducting polymer is electrochemically switched from the insulating to the conducting state [48]. This potential is an electrochemical measure of the percolation threshold of the molar fraction of the conducting species. Therefore, it is suggested that the propagation of the conducting-insulating front, which is a fairly rapid process, can only begin once this percolation threshold is attained. Small electrode contact areas give rise to fewer sites for the nucleation of the oxidised emeraldine phase, and hence higher potentials are required to reach the necessary fraction of oxidised polymer. This in turn, affects the oxidation peak potential. Only when the percolation threshold has been reached the conducting-insulating interface can propagate across the film (Figure 14). Hence, at the point onset of propagation the potential of the working electrode is higher when small electrode contact areas are employed to address the film, and therefore the propagation rate is likely to be faster, which results in a larger current maximum.

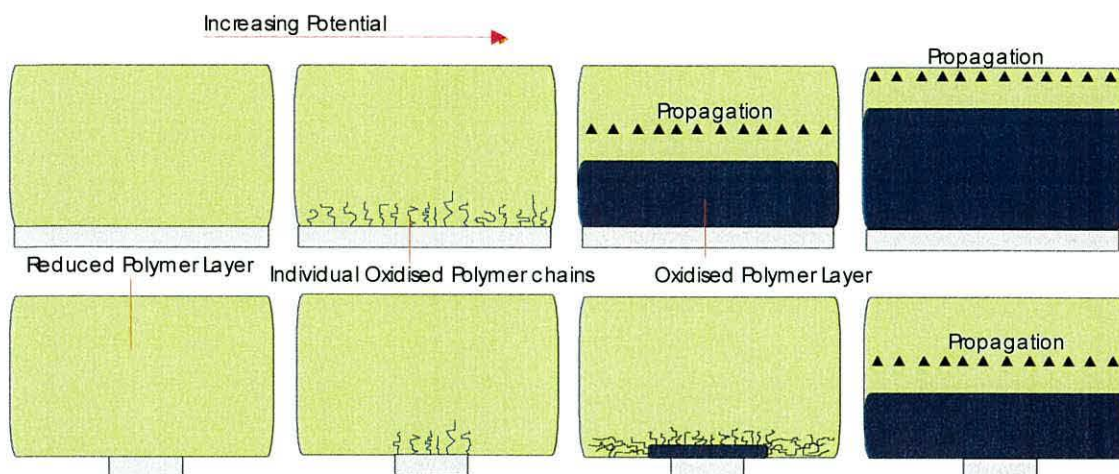


Figure 14. A schematic diagram showing the effect of electrode contact area on the percolation threshold potential, and the subsequent propagation of the conducting-insulating interface during the oxidation of a Pani film.

The reduction of conducting polymers can be described using the percolation theory, according to which the conversion occurs rapidly at first, but then stops at the percolation threshold of the molar fraction of the conducting species, i.e. when electrical connection between the conducting phase and the electrode surface has been broken. It is then followed by a slow relaxation process, which has been described as the competition between the retrieval of electric pathways from the local conducting domains to the electrode, and the electrochemical cut-off of the electric paths [48]. The lower reduction charge observed with smaller electrode contact areas indicates that a greater number of isolated “conducting islands” remain in the film when the percolation threshold is reached. This is because smaller electrode contact areas possess fewer electric pathways to the electrode surface, and hence electrical connection is likely to be broken more quickly. Therefore, it is evident that reducing the electrode contact area increases the percolation threshold, which consequently gives rise to a more substantial memory effect. This has been simply represented by Figure 15.

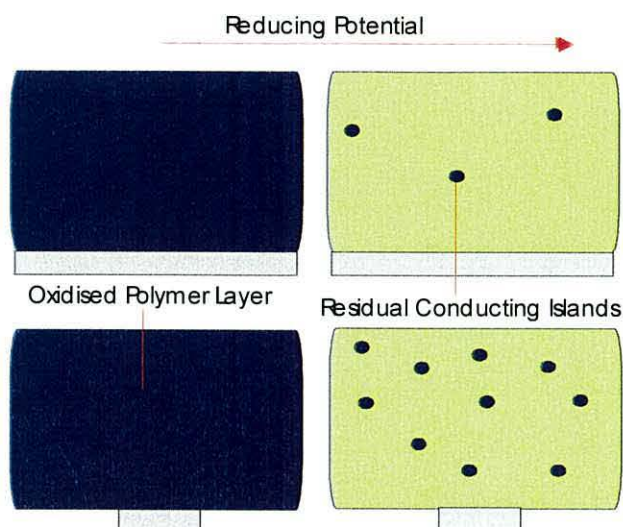


Figure 15. A schematic diagram showing the effect of electrode contact area on the reduction of a polymer film. The diagram highlights the increased percolation threshold, which alters the number of residual conducting islands.

5.3.1.6 Chronoamperometry – Case A

The effect of the electrode contact area on the redox behaviour of Pani was also examined using chronoamperometry. Potential step measurements were made using optimum iR compensation. The current transients for the first oxidation of a Pani film ($340\ \mu\text{C}$, Case A), obtained by stepping the potential of the working electrode between $-0.2\ \text{V}$ to $+0.5\ \text{V vs. SCE}$, can be seen in Figure 16. Each transient for the 1st oxidation possessed similar charge, $Q_{(\text{ox})} = 342\ \mu\text{C}$, which corresponded to the charge obtained from the voltammetric analysis indicating that each electrode was able to drive the oxidation process to completion. The effect of electrode contact area is quite clear. The transient obtained when the electrode-pair was used to address the film is sharper ($I_{p(\text{ox})} = 34.6\ \text{mA}$ and $t_{(\text{ox})} = 51.5\ \text{ms}$) than those obtained when the individual electrodes were employed ($I_{p(\text{ox})} = 11.9\ \text{mA}$ and $t_{(\text{ox})} = 107.6\ \text{ms}$). $I_{p(\text{ox})}$ corresponds to the peak current and $t_{(\text{ox})}$ is the time required for completion of the oxidation process. The larger electrode contact area gives rise to a greater number of nucleation sites for oxidation at the electrode surface, which means that there is a larger interfacial region between the conducting and insulating polymer. A greater amount of charge transfer can occur across this interface at any given time. The propagation distance is shorter when larger contact

areas are employed, as was depicted in Figure 13, which in turn allows the oxidation process to complete over a shorter time scale.

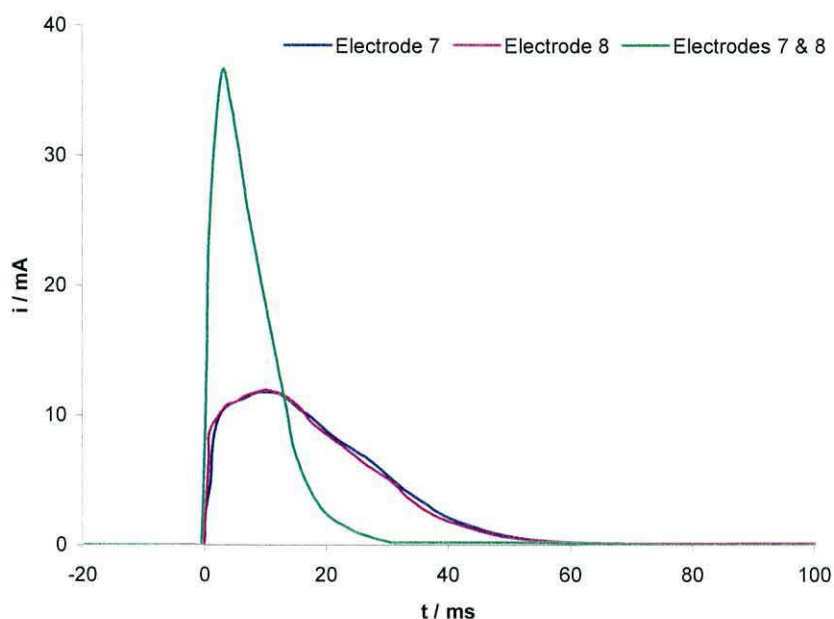


Figure 16. Current transients obtained after a potential step (-0.2 V to $+0.5$ V vs. SCE) for a Pani film ($340 \mu\text{C}$, Case A), using $8 \text{ k}\Omega$ of iR compensation, and the electrode-pair (green line), electrode 7 (blue line) and electrode 8 (pink line) as the working electrode.

The reduction transients (Figure 17) that immediately followed the oxidation (i.e. double potential step) also exhibited a sharper peak associated with the electrode-pair, which was integrated to give a significantly larger charge, $Q_{(\text{red})} = 324 \mu\text{C}$, than those associated with the individual electrodes, $Q_{(\text{red})} = 299 \mu\text{C}$. This again points to the fact that the electrode contact area has a major influence on the percolation threshold, resulting in what appears to be an enhanced memory effect.

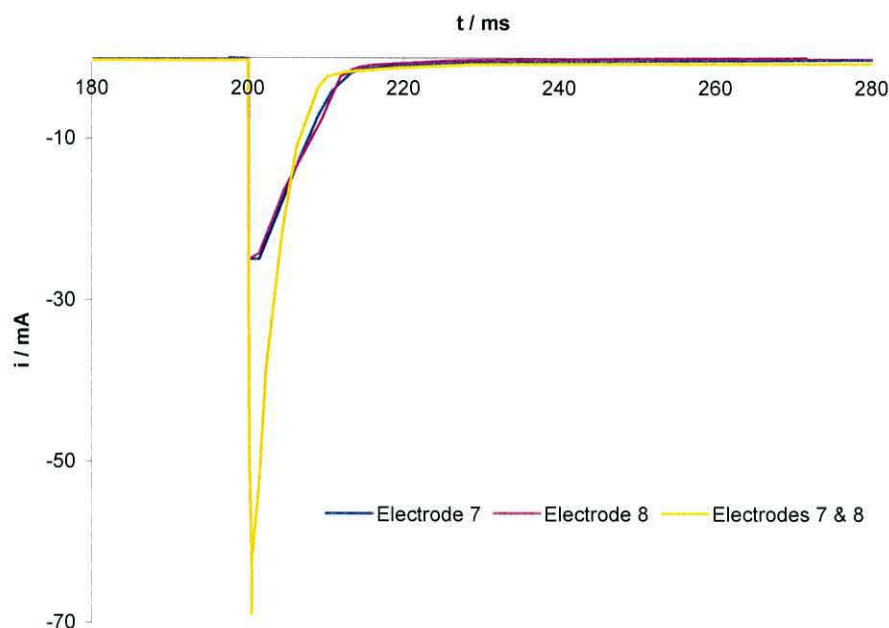


Figure 17. Current transients obtained after a potential step (+0.5 V to -0.2V) for the reduction of a Pani film, (340 μC , Case A), using 8 $\text{k}\Omega$ of iR compensation and the electrode-pair (orange line), electrode 7 (blue line) and electrode 8 (pink line) as the working electrode. The transients were obtained following an oxidation potential step.

Figure 18 shows the effect of the second potential limit (E_2), i.e. the potential to which the working electrode was stepped, on the current transients obtained. It must be noted that these transients were obtained without iR compensation. The figure shows that decreasing the second potential limit, E_2 , resulted in a decrease in the current maximum and increases the time required for the process to complete. In fact, it can be seen that for the timescale of the experiment the oxidation process did not go to completion for the low values of E_2 , as there was still a substantial current after 200 ms. However, the major difference between the transients obtained for the individual electrodes and that for the electrode-pair is the magnitude of current. The larger electrode contact area gave rise to higher currents, which consequently made the peaks sharper. The charge associated with the transient obtained for the electrode pair (349 μC following a -0.2 V to +0.5 V step) was also slightly higher than those obtained from the individual electrodes (338 μC following a -0.2 V to +0.5 V step). Of particular interest is the shape of the transients

associated with the individual electrodes. The transients appear to possess two peaks that overlap and merge together. At high potential limits these peaks overlap enough to resemble a single peak. However, at lower values of E_2 the transients possess two humps, indicative of two regions of polymer. The first region is likely to be the fraction of polymer that is in direct contact with the working electrode, with the second being the rest of the film overhanging the edge of the working electrode.

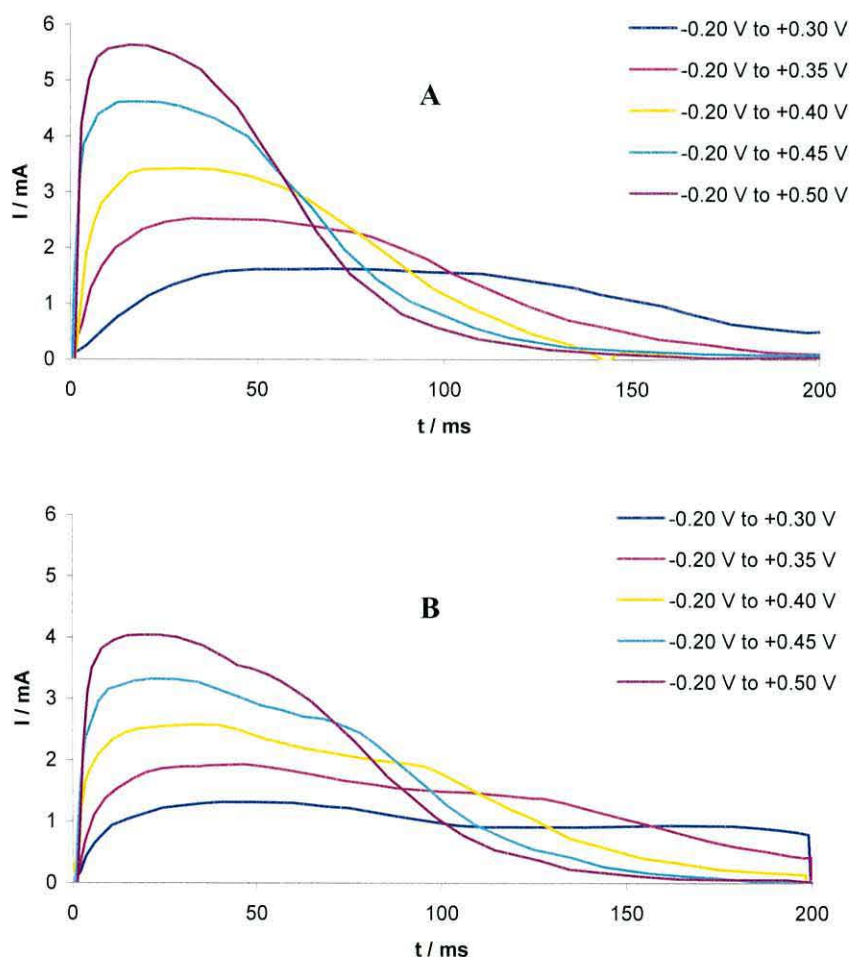


Figure 18. Current transients obtained in response to potential steps from -0.20 V to $+0.30$, 0.35 , 0.40 , 0.45 , 0.50 V vs. SCE), for the oxidation of a Pani film ($340 \mu\text{C}$, case A), using the electrode pair (A) and an individual electrode (B).

If the logarithm of the current maximum in Figure 18 is plotted against the second potential limit a Tafel-type plot is obtained. Figure 19 shows that the logarithm of the current density changes linearly with the potential limit, i.e. Tafel-type behaviour, which is an indication that the rate is kinetically controlled.

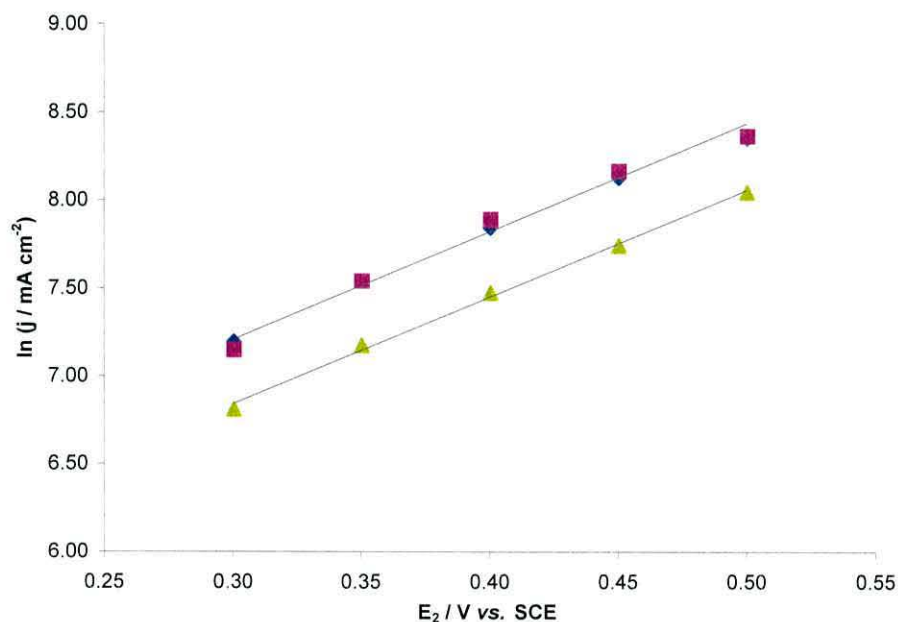


Figure 19. A plot of $\ln j$ vs. E_2 for the oxidation of a Pani film ($340 \mu\text{C}$, Case A), where the working electrode was electrode 7 (blue points), electrode 8 (pink points) and the electrode-pair (green points). The values of j were calculated from the current maxima derived from the current transients in Figure 18.

Since the observed current is a measure of the rate of charge transfer across the conducting-insulating interface it is also likely to be proportional to the propagation rate. Hence, these results agree with a similar analysis by Tezuka and Aoki, where the logarithm of the propagation rate was found to be directly proportional to overpotential, as can be seen in equation 1 [44, 48].

$$\ln v = \ln k_s + \{(\beta n F / R T) * (E - E^0)\} \quad (1)$$

Where, v is the propagation rate, k_s is the rate constant for the conversion of the insulating to conducting phase, β is the anodic transfer coefficient, n is the number of electrons involved in the oxidation, F is the Faraday constant, R is the gas constant, T is the temperature and $E - E^0$ represents the overpotential. The plots are linear and have similar gradients. However, there is a clear separation between the plots constructed for the individual electrodes and that of the electrode-pair, which occurs at a lower current density. This suggests that varying the electrode contact area alters the equivalent value of k_s . Below 0.3 V the current has been shown to drop rapidly (near 0.2 V) where the oxidation becomes thermodynamically unfeasible [41].

5.3.1.7 Chronoamperometry - Case B

For Case B, the effects of the electrolyte resistance were also observed and optimum iR compensation was applied. The effect of reducing the electrode contact area can also be seen. From the first oxidation transients in Figure 20, the charge associated with the electrode-pair was calculated and was comparable to that associated with electrode 8, at $Q_{(ox)} = 313 \mu C$. These values were also comparable to those obtained from the voltammetric measurements indicating that these electrode configurations were able to address the entire film. Although the transients possess similar charges, the electrode-pair exhibits a slightly larger current maximum, $I_p(ox) = 17.9 \text{ mA}$, with $t(ox) \approx 42.4 \text{ ms}$, compared with electrode 8, where $I_p(ox) = 13.9 \text{ mA}$ and $t(ox) \approx 60.6 \text{ ms}$. This is most likely to be due to the slight difference in contact area. However, the transient obtained using electrode 7, which possessed a significantly smaller contact area, exhibited a much smaller current maximum, $I_p(ox) = 4.9 \text{ mA}$ and gave rise to a smaller associated charge, $Q_{(ox)} = 274 \mu C$.

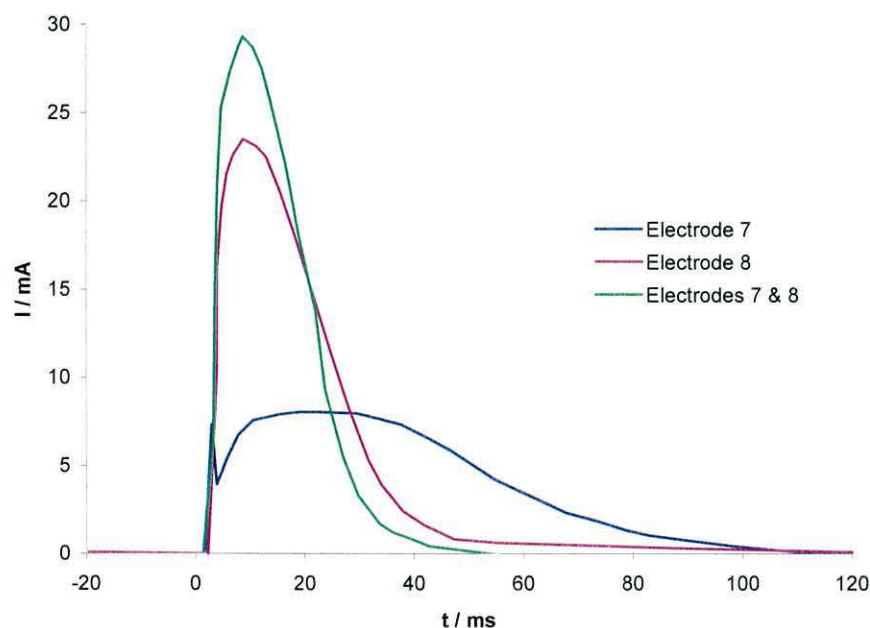


Figure 20. Current transients obtained in response to a potential step from -0.2 V to $+0.5$ V vs. SCE for a Pani film ($310 \mu\text{C}$, Case B), with $8 \text{ k}\Omega$ of iR compensation and the electrode-pair (green line), electrode 7 (blue line) and electrode 8 (pink line) as the working electrode.

The reduction transient for electrode 7 is also quite different from those of electrode 8 and the electrode-pair, possessing a much smaller charge, $Q_{(\text{red})} = 148 \mu\text{C}$, compared with $270 \mu\text{C}$ obtained for electrode 8 and the pair (Figure 21). This in turn affects the charge associated with the 2nd oxidation transient, which again suggests that the electrode contact area influences the percolation threshold.

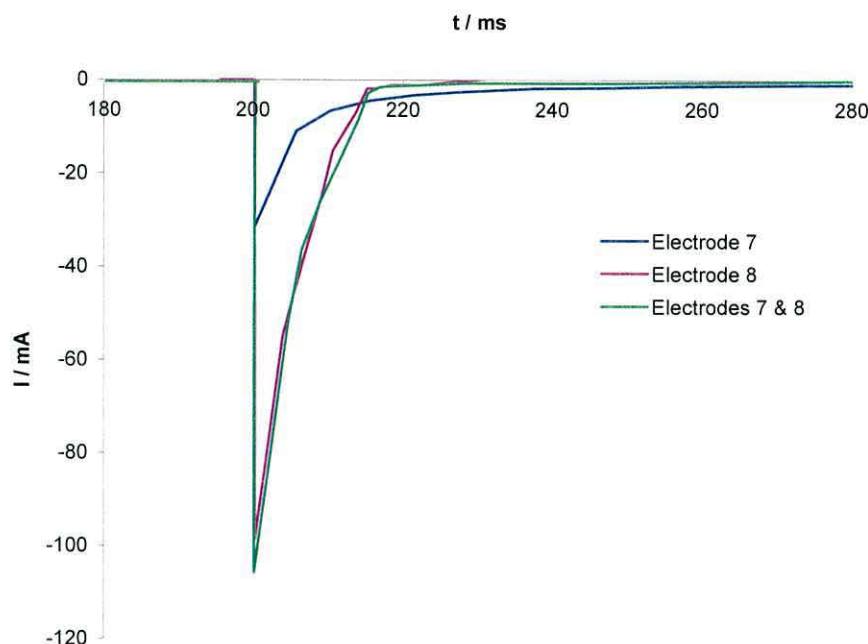


Figure 21. Current transients obtained following a potential step (+0.5 V to -0.2 V vs. SCE) for the reduction of a Pani film, (310 μC , Case B), with 8 $\text{k}\Omega$ of iR compensation and using the electrode-pair (green line), electrode 7 (blue line) and electrode 8 (pink line) as the working electrode. The transients were obtained following an oxidation potential step.

The effect of the second potential limit (E_2) on the potential step transients is shown in Figure 22. These transients were obtained without iR compensation, which accounts for the relatively low currents observed. The figure shows that for the first oxidation the magnitude of E_2 had a clear influence on the current maxima, the potential at which these maxima occurred, and the time required for the process to complete. The oxidation process did not proceed to completion within the timescale of the experiment for lower values of E_2 , which was indicated by the current at 200 ms as the experiment ended. The charge associated with the oxidation when the electrode-pair or electrode 8 was employed as the working electrode (193 μC for a potential step from -0.2 V to +0.5 V), was much greater than when electrode 7 was employed (170 μC for a potential step from -0.2 V to +0.5 V) and this was reflected by the charge associated with subsequent reduction and second oxidation processes. This indicates that the oxidation process was much slower when smaller contact areas were employed.

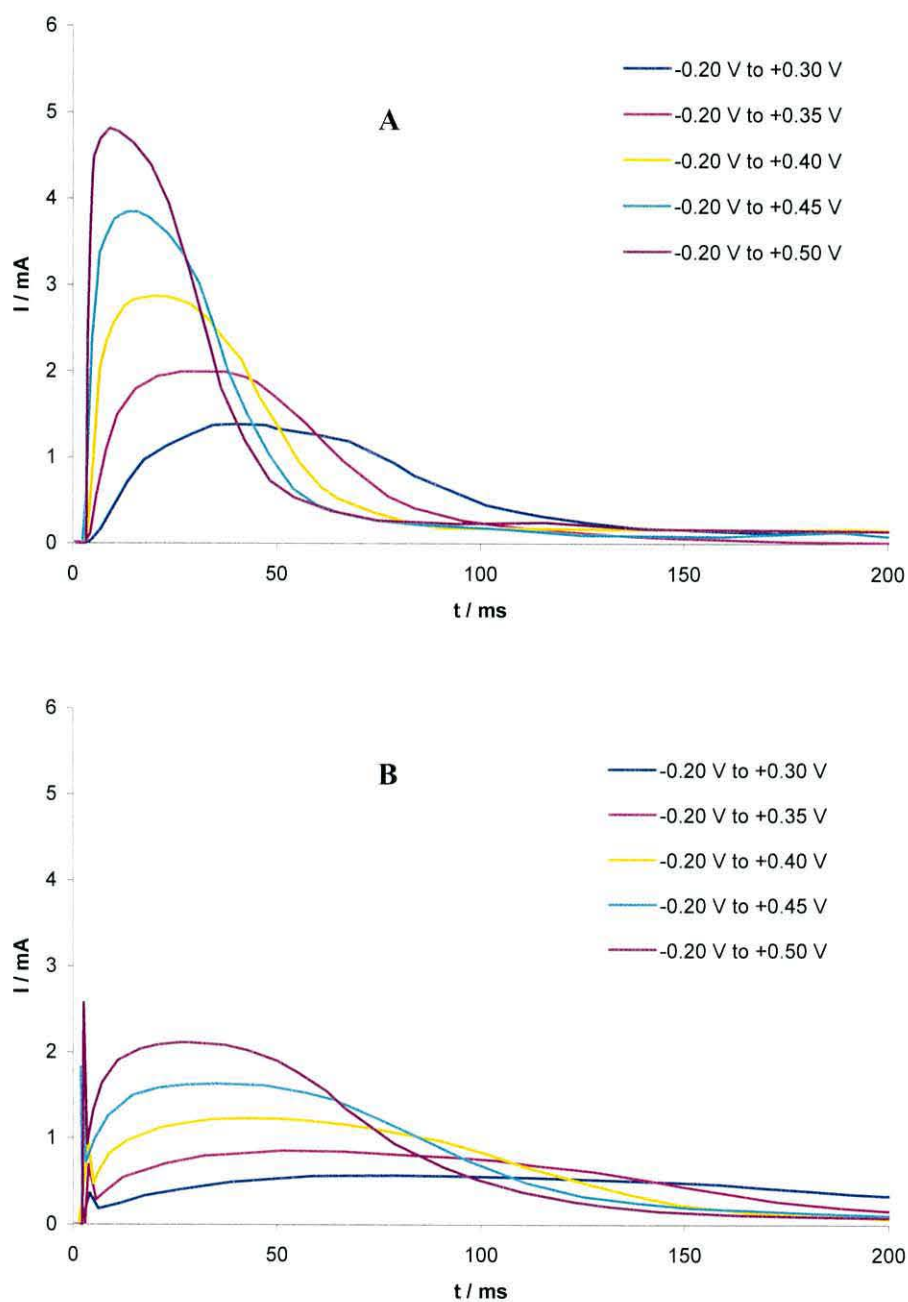


Figure 22. Current transients obtained following a potential step from -0.2 V to $+0.30$, $+0.35$, $+0.40$, $+0.45$, $+0.50$ V vs. SCE, for the oxidation of a Pani film ($190\ \mu\text{C}$, case B), using the electrode 8 (A), electrode 7 (B) as the working electrode.

Plots of $\ln j$ vs. E_2 were constructed from the potential step current maxima (Figure 23), and once again showed Tafel-type behaviour. The difference in current density between the different electrode contact areas was also apparent. The much smaller electrode contact area of electrode 7 gave rise to a much larger current density.

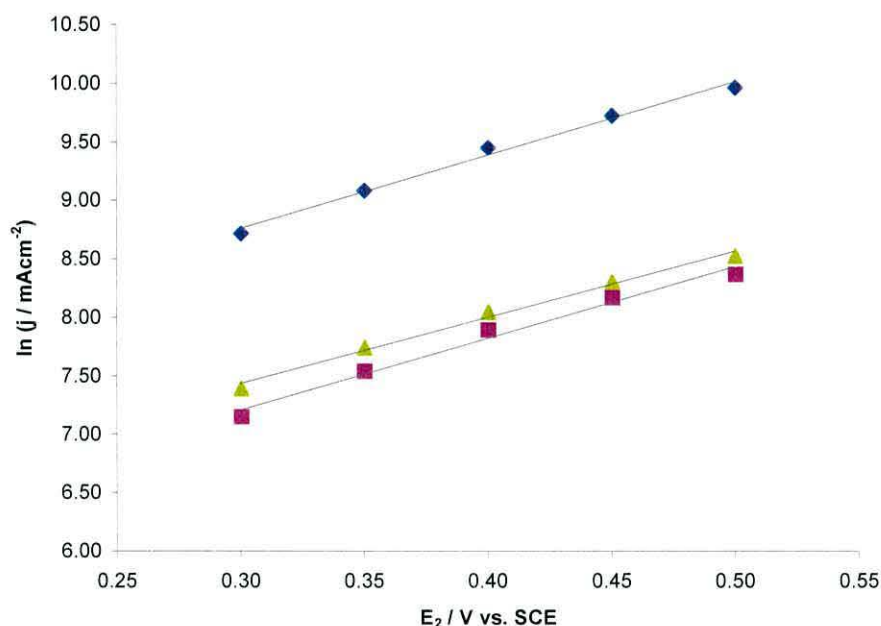


Figure 23. A plot of $\ln j$ vs. E_2 for the oxidation of a Pani film (310 μC , Case B), where the electrode adopted as the working electrode was electrode 7 (blue points), electrode 8 (pink points) and the electrode-pair (green points). The values of j were calculated from the current maxima derived from the current transients in Figure 22.

Normalisation of the current transients (I / I_{\max} vs. t / t_{\max}) allows the comparison of the oxidation process with other processes (Figure 24). The normalised oxidation plots for Pani bear a close resemblance to those observed for the two-dimensional electrocrystallisation of structures such as calomel on mercury, as has been noted previously by Kalaji *et al.* [37]. This resemblance helps to confirm the prediction that the oxidation process is kinetically controlled and governed by the nucleation of emeraldine centres and the expansion of a phase boundary. The normalised transients obtained here more closely resemble the reduced variable representation for instantaneous nucleation.

This is in contrast to those observed by Vuki *et al.* [40], which resemble the progressive nucleation representation. This may be a consequence of the larger resistance of the relatively thick films (10 μm) used in this study, as the films used by Vuki were much thinner (45 nm).

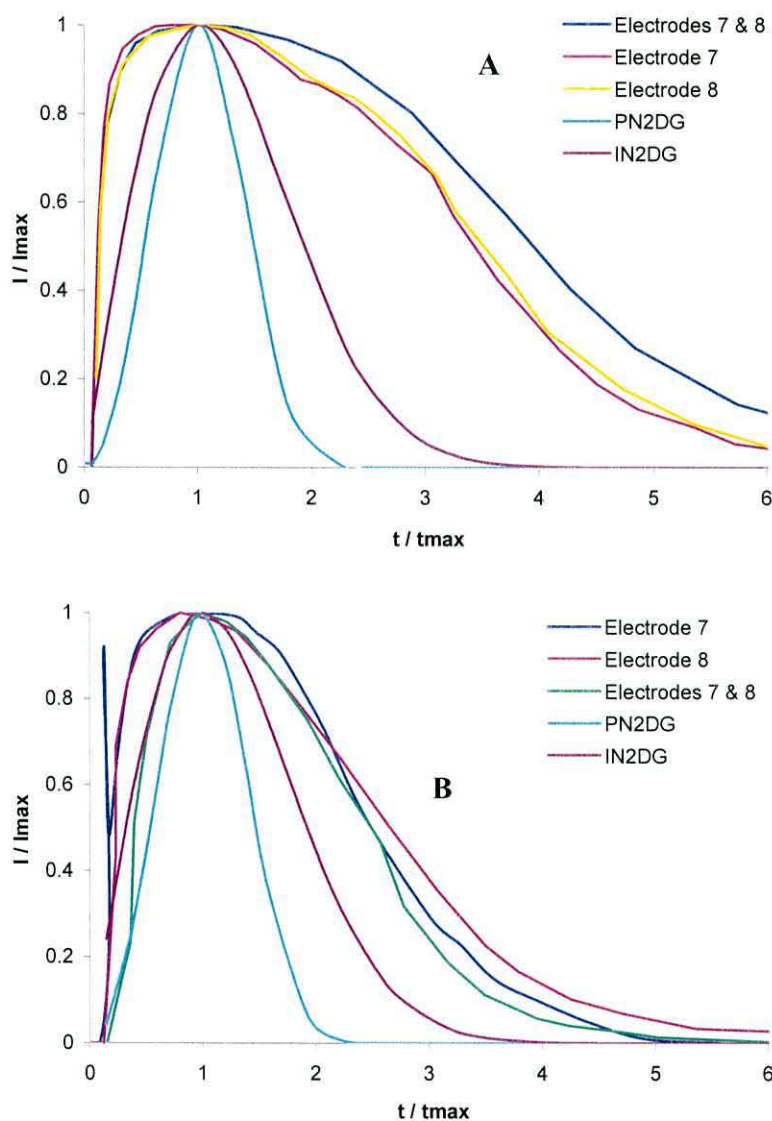


Figure 24. Normalised current transients following a potential step from -0.2 V to $+0.5$ V, for a Pani film (340 μC Case A, (A) and 310 μC Case B (B)), along with theoretical plots for 2D electrocrystallisation (progressive nucleation with 2D growth, PN2DG, and instantaneous nucleation with 2D growth, IN2DG).

5.3.1.8 Discussion of chronoamperometric results

The redox switching processes of polyaniline films have been studied using chronoamperometry. During oxidation, the potential was stepped from a reducing potential to a potential sufficient to oxidise the polymer film. The normalised oxidation transients indicate that emeraldine growth centres were formed at the electrode surface followed by peripheral expansion in a similar manner to two-dimensional electrocrystallisation (Figure 24). Once these centres had expanded across the electrode it is likely that oxidation continues *via* propagation of the conducting-insulating interface. The resultant current transients showed that the current maxima, the peak potential and the time required for the process to go to completion were dependent on the second potential limit (E_2), as seen in Figure 18 and Figure 22. This indicates that the rate of the oxidation process is kinetically controlled by the propagation of the conducting-insulating interface, which is in agreement with the literature [41, 43], with the diffusion of counter ions being sufficiently rapid not to influence the rate [53]. Reducing the electrode contact area resulted in smaller current maxima, longer oxidation timescales and smaller associated charges. These observations are best explained using propagation theory. As the oxidation process is kinetically controlled, the current maximum is likely to occur when the interface between the conducting and insulating material is at its largest. For relatively large electrode contact areas this is likely to be at the start of the process during the oxidation of the polymer that is in direct contact with the electrode. For smaller electrode contact areas the maximum area between the conducting and insulating phases is likely to be during the propagation of the conducting-insulating interface. This in turn is likely to delay the onset of the current maximum. Small electrode contact areas can also act to delay the propagation of the conducting front until the molar fraction of the conducting material reaches the threshold value. Reducing the electrode contact area also increases the distance that the front has to propagate, as can be seen in Figure 13, which increases the time required for the process to complete provided that propagation proceeds at a constant speed.

The reduction transients indicate that the reduction process is very rapid. The most significant observation was that the electrode contact area seemed to govern the extent of the reduction process, as was observed during the voltammetric measurements.

5.3.2 The influence of electrode position within the array

The working electrode contact area has been shown to influence the electrochemical redox switching characteristics of Pani films. The rate of polymer oxidation appeared to be dependent upon the kinetically controlled charge transfer reaction across the conducting-insulating boundary, and hence the propagation speed [41, 43]. Therefore, it is possible that the oxidation rate of any given film can be manipulated by altering the distance that the conducting insulating interface has to propagate in order to complete the oxidation process.

Experiments were conducted where the polymer was addressed using electrodes of identical contact area, from different positions across the film. This was achieved by depositing a polymer film onto an array of equivalent microband electrodes. When all the electrodes were used together to address the film (Figure 25, A), the distance that the conducting-insulating interface needed to travel in order to complete the oxidation was small. However, when only one individual electrode was used as the working electrode, the conducting-insulating boundary was required to travel further to complete the oxidation process. This was further extended by altering the position at which the working electrode makes contact with the polymer, by selecting an electrode from the centre (Figure 25, B) or the outside (Figure 25, C) of the array.

The platinum electrode array used during this part of the study was the array shown in Figure 3, B. The microband electrodes were $1000 \times 10 \mu\text{m}$, and were separated by gaps of $10 \mu\text{m}$. Pani was simultaneously grown potentiodynamically on to each of the eight electrodes, until sufficient polymer had been deposited to electrically connect them.

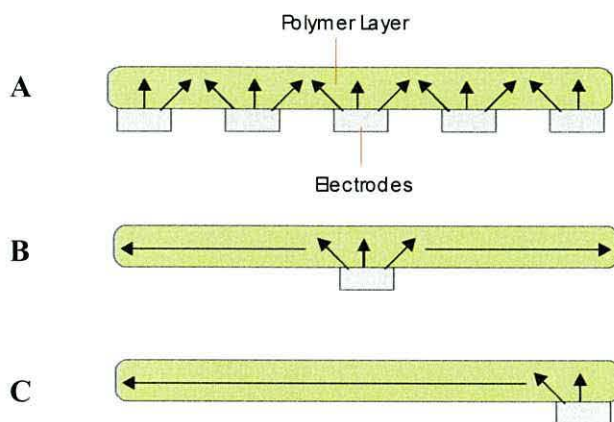


Figure 25. A schematic representation of a polymer film grown over an array of equivalent microelectrodes. The diagram depicts variations in the propagation distance induced by selecting the position of the working electrode within the array, i.e. when either all the electrodes (A), a single working electrode positioned in the centre of the film (B) or a single working electrode positioned at the edge of the film (C) were used to address the film.

Figure 26 shows a polyaniline film deposited onto the electrode array, and a pin has been pulled through the polymer to expose the electrodes beneath. In order to establish electrical contact between the electrodes, the films had to be relatively thick.

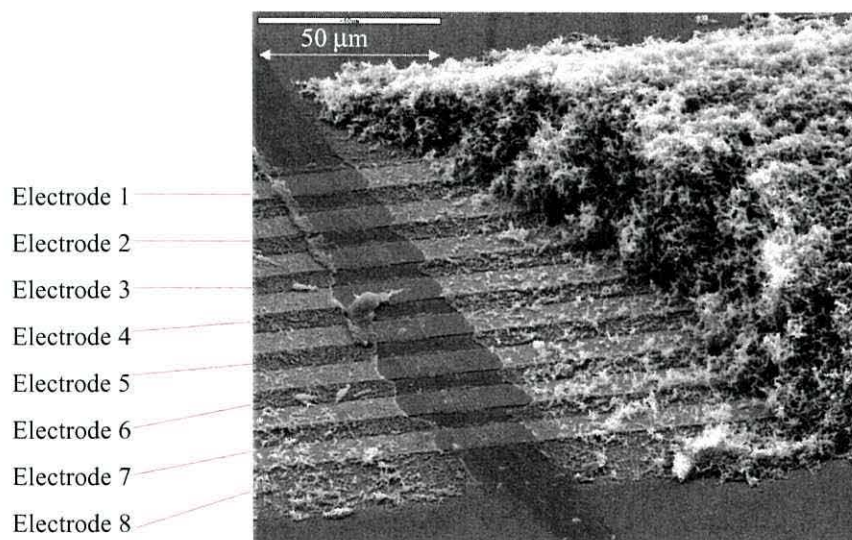


Figure 26. A Pani film ($Q_{(ox)} = 420 \mu C$) deposited onto an eight-electrode microband array.

It should be noted that the film shown in Figure 26 was not used in the following study. The film was grown for the SEM images and is much thicker ($420\ \mu\text{C}$, film thickness = $40\ \mu\text{m}$) than those used for the following experiments.

5.3.2.1 Voltammetry of Pani on the eight-electrode array

The voltammetric response showed that the each electrode gave rise to an oxidation peak of equivalent charge ($16\ \mu\text{C}$), indicating that each electrode was able to address the entire film. This charge translated to an estimated film thickness of $1.5\ \mu\text{m}$. Figure 27 shows the voltammograms from four of the eight micro-band electrodes, electrodes 1, 2, 3, 4, and all eight electrodes operated together. Electrodes 8, 7, 6, and 5 gave identical voltammetry to electrodes 1, 2, 3, and 4, respectively, and hence are not shown.

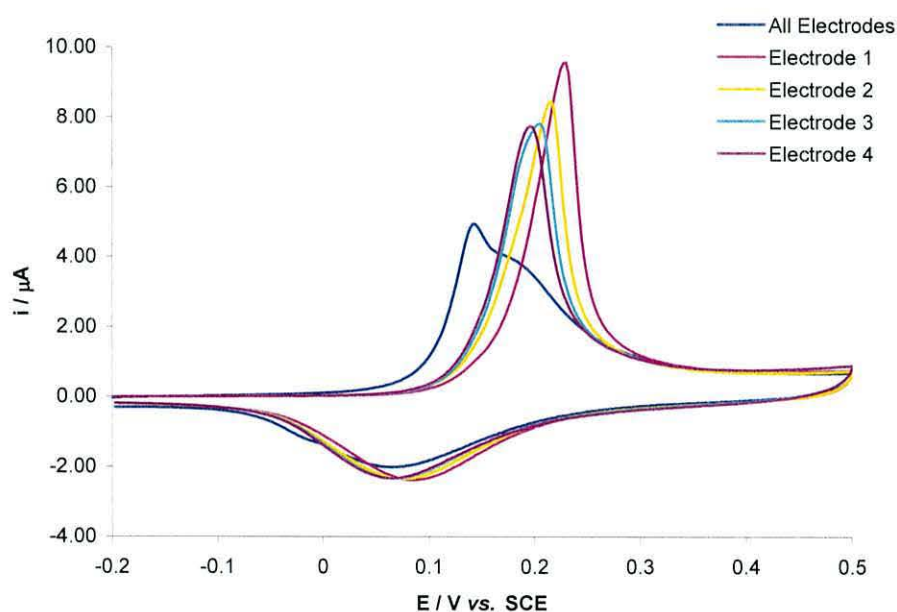


Figure 27. First cycle voltammetric responses of a Pani film ($16\ \mu\text{C}$) when electrode 1 (pink line), electrode 2 (orange line), electrode 3 (light blue line), electrode 4 (purple line), and all the electrodes operated together (blue line) were used as the working electrode. Electrode 1 is at the edge of the film, electrode 4 at the centre of the array.

The most noticeable feature in the voltammograms, is that the oxidation peak shifts towards more positive potentials as the electrode used to drive the oxidation is situated closer to the edge of the film. The oxidation peak obtained when all the electrodes were operated altogether appears at a much lower potential than that of the individual electrodes. This could be predicted from the first part of this study, and is due to the larger electrode contact area. The variation of anodic peak potentials was also observed on the second cycle, suggesting that this feature is independent of the memory effect. It is also important to note that the optimum iR compensation was applied; hence these features are not associated with the iR drop across the film.

The FWHM values for the anodic peaks (Table 3) show that the width of the peak at half the current maximum when all the electrodes operated together is much larger than those of the individual electrodes, which are approximately the same, except that associated with electrode 1 which is slightly lower. This broader spread of current and the shift of peak potential indicates that the electrode contact area is able to influence the potential at which oxidation of the polymer can commence.

Electrode	Contact area / cm^2	FWHM / mV
All	8×10^{-4}	100
1	1×10^{-4}	46
2	1×10^{-4}	51
3	1×10^{-4}	56
4	1×10^{-4}	54

Table 3. FWHM values for the oxidation of a Pani film, obtained using different electrode contact areas.

The charge associated with the oxidation of the Pani film can be plotted against potential in order to ascertain whether or not the oxidation process is limited at lower potentials by the working electrode contact area. The plots (Figure 28) show that when all the electrodes are operated together the associated charge was much larger at lower potentials (100 - 200 mV) than that associated with the individual electrodes. This might be

expected from the difference in electrode contact area. However, the plots situated closer to the edge of the film possessed lower charges than those of the individual electrodes situated towards the centre of the array, despite having equivalent working electrode contact areas.

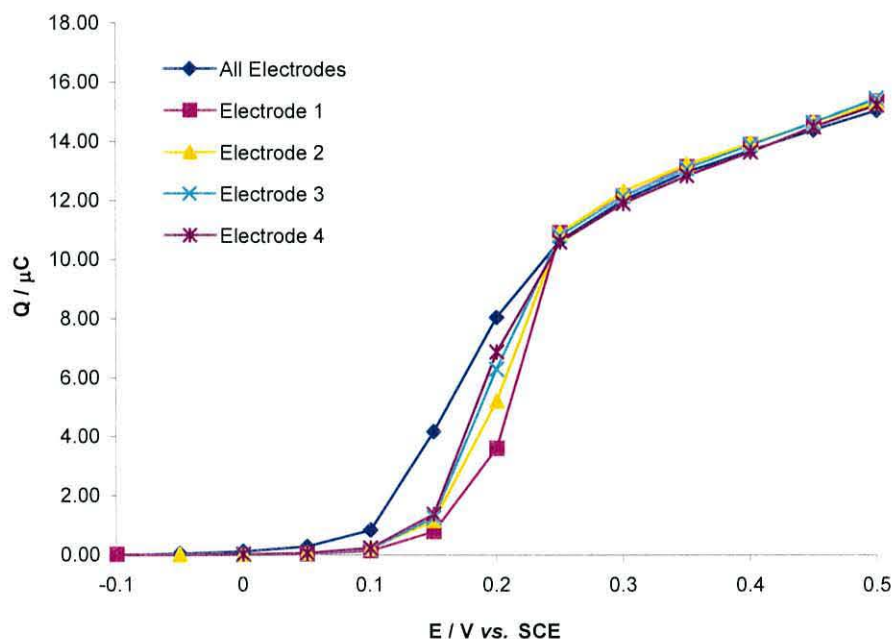


Figure 28. A plot of charge vs. potential for the oxidation of a Pani film (16 μC) when electrode 1 (pink line), electrode 2 (orange line), electrode 3 (light blue line), electrode 4 (purple line), and all electrodes (blue line) were used as the working electrode.

Tafel-type plots constructed from the voltammograms (Figure 29) show once again that the onset of oxidation occurs at significantly different potentials for different electrode configurations. When all the electrodes were operated together, the onset of oxidation occurred at a significantly lower potential compared the individual electrodes, and the onset of oxidation associated with the electrodes at the edge of the array occurred at higher potentials than the electrodes situated towards the centre of the array.

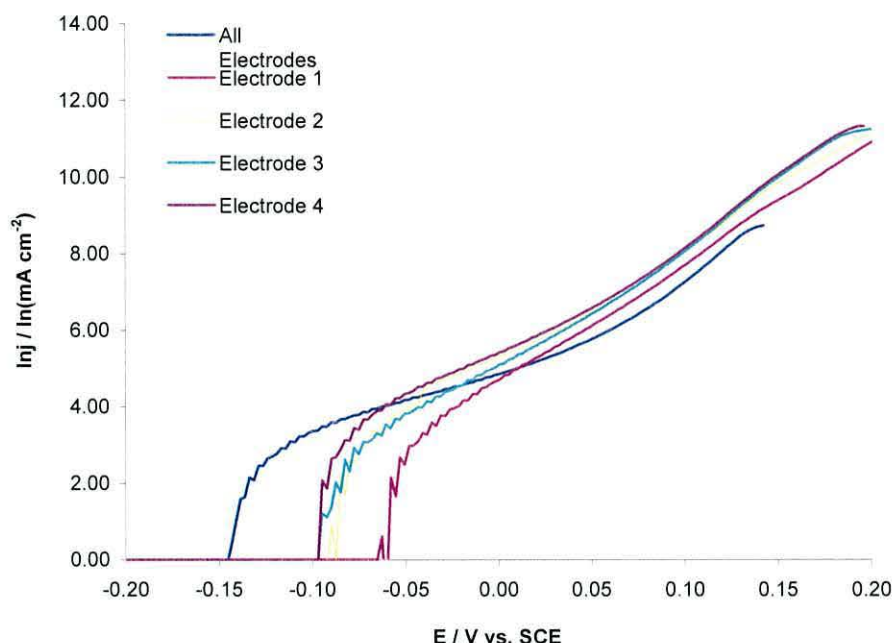


Figure 29. Tafel-type plots for the oxidation of a Pani film ($16 \mu\text{C}$) obtained using electrode 1 (pink line), electrode 2 (orange line), electrode 3 (light blue line), electrode 4 (purple line) and all electrodes (blue line) as the working electrode.

The data confirm that the voltammetric characteristics of a Pani film are not only influenced by the electrode contact area, but also by the electrode position within the array. When all electrodes are employed to address the film the working electrode contact area is large. Therefore, the number of sites available to nucleate emeraldine growth centres is also large and the molar fraction of conducting material required to propagate the conducting-insulating interface is easily and quickly attained. The propagation distance is also short, as the front has only to propagate the thickness of the film. When the individual electrodes are used to address the film, the number of sites available to nucleate emeraldine growth centres is much smaller, and therefore reaching the percolation threshold is more difficult, which delays the propagation of the conducting-insulating interface. Electrode 1 is situated at the edge of the film. At the initial stages of the oxidation process the polymer can only be oxidised in one lateral direction. This means that the interface between the oxidised and reduced polymer is smaller than if the working electrode were situated at the centre of the array. Therefore,

it can be concluded that the percolation threshold is more difficult to attain using an electrode at the very edge of the film (electrode 1), as the size of the interface between the oxidised polymer and the reduced polymer is small. The difference between the other individual electrodes (electrodes 2, 3, and 4) is attributed to differences in the propagation distance, which decreases as the electrode moves towards the centre of the array.

The voltammetric reduction peaks (Figure 27) are somewhat different to those observed during the electrode contact area study, in that the peaks exhibit a slight shift in peak potential and a variation of current maxima between the “individual electrodes” and “all electrodes” operated altogether. The electrodes situated closer to the edge of the film exhibit peaks at slightly more positive potentials. If this shift was simply caused by an increase in film resistance, it would be expected that the reduction peak would shift towards more negative potentials. It should be noted that the shift in oxidation peak potential is much larger than the shift for the reduction potential, as can be seen in Table 4.

Electrode	$E_{p(ox)} / \text{mV}$	$E_{p(red)} / \text{mV}$	$\Delta E_p / \text{mV}$
All 8	145	65	80
1	230	85	145
2	215	75	140
3	205	70	135
4	195	65	130

Table 4. A table of peak separations for the redox processes of a Pani film (16 μC).

Another feature of the voltammetry associated with Pani films deposited onto the eight electrode arrays, is that the observed capacitive charge is substantially smaller than has been observed for Pani films grown onto single electrodes possessing larger electrode contact area, or even that observed in the first part of this study when two electrodes were employed.

The capacitive and Faradaic components of the total charge were calculated by splitting the voltammogram into three parts using linear baselines as shown in Figure 30. The ratios of capacitive to Faradaic charge were obtained by dividing the capacitive charge by the charge associated with the oxidation or reduction processes.

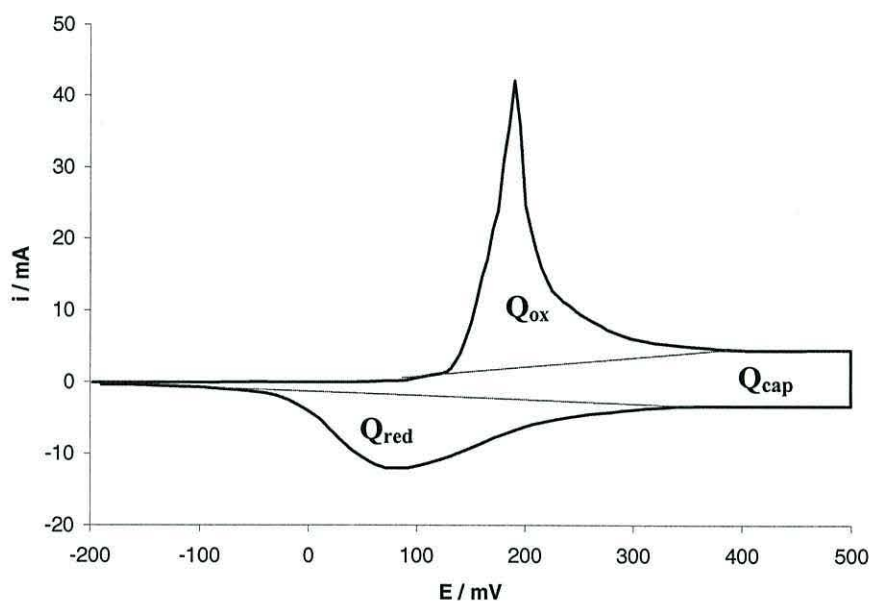


Figure 30. Linear baselines used during the calculation of the capacitive charge ratios.

Table 5 shows the ratio of the capacitive charge against anodic, cathodic and total charge for a series of Pani films formed upon platinum electrode arrays. The table highlights the effect of electrode configuration, i.e. the number of electrodes in contact with the film, on the capacitive/Faradaic charge ratios, and it can be seen that as the number of electrodes in contact with the film increased, the capacitance ratios decreased. The highest ratios were observed for Pani films deposited onto single Pt electrodes ($1 \times 10^{-3} \text{ cm}^2$), where no polymer extended beyond the edge of the electrode, while the smallest ratios were observed with the eight-electrode array.

From the results in Table 5, it can be seen that Pani films deposited onto the eight-electrode array gave rise to small capacitive charges, and that by using just one of the

individual electrodes as the working electrode the capacitive charge ratio was reduced further. When Pani is deposited onto the eight-electrode microband array, only 53 % of the polymer surface area is in contact with the electrode surface area due to the gaps between the electrodes. If a single electrode is employed, this value falls to only 6.7 %, and therefore it might be assumed that only the polymer that was close to the working electrode surface contributes to the capacitive charge.

The number of electrodes	Electrode contact Area / (cm ²)	Approximate Film Thickness (μm)	Q _{cap} / Q _{tot}	Q _{cap} / Q _{ox}	Q _{cap} / Q _{red}
1	1.00×10^{-3}	6.5	0.351	0.981	1.203
2	1.00×10^{-3}	6.5	0.318	0.857	1.026
2	2.00×10^{-3}	6.5	0.321	0.879	1.027
2	1.05×10^{-3}	6.5	0.341	0.937	1.155
2	1.00×10^{-3}	6.5	0.341	0.960	1.119
2	5.00×10^{-5}	6.5	0.346	0.923	1.243
8	8.00×10^{-4}	1.4	0.311	0.711	1.236
8	1.00×10^{-4}	1.4	0.273	0.653	0.867

Table 5. Capacitance ratios for a series of Pani films. The number of electrodes column shows the number of electrodes that the film was deposited onto, while the electrode contact area column shows the area of working electrode used to drive the oxidation. Subscript cap = capacitive, ox = oxidation, and red = reduction.

If only polymer that is situated close to the electrode surface contributes to the capacitive charge, then the same should be true for polymers formed onto individual electrodes. In order to test this hypothesis, films of different thickness were grown onto a single Pt microband electrode and the capacitive ratios calculated. The ratios of capacitive charge to total charge, oxidation charge, and reduction charge for these films can be seen in Table 6, and clearly show that the capacitive charge ratio decreases with increasing film thickness.

$Q_{ox} / \mu C$	Q_{cap} / Q_{tot}	Q_{cap} / Q_{ox}	Q_{cap} / Q_{red}
28.826	0.499	1.876	2.120
62.244	0.407	1.205	1.589
241.836	0.351	0.981	1.203
382.656	0.307	0.819	0.965
548.976	0.307	0.823	0.961

Table 6. The effect of film thickness (represented as the charge associated with oxidation) on the capacitive ratios.

The film thickness appears to have an influence over the capacity of the film to store charge. However, the ratios do seem to approach a limit, which are still higher than those observed for the eight-electrode microband array. Therefore, it is suggested that only the polymer with direct connection (i.e. is situated close) to the electrode surface contributes to the capacitive charge. Polymer beyond a certain distance, including the polymer formed in the gaps between adjacent electrodes, contribute only to the Faradaic charge, and not to the capacitive. Polymer formed in the gaps could be considered as additional film thickness. This idea can be further supported when thicker films are grown onto the eight-electrode microband array. These capacitive ratios are shown in Table 7.

Electrode area / μm^2	$Q_{ox} / \mu C$	Q_{cap} / Q_{tot}	Q_{cap} / Q_{ox}	Q_{cap} / Q_{red}
80,000	54.60	0.311	0.711	1.236
80,000	400.30	0.231	0.569	0.633

Table 7. The effect of film thickness (represented as charge associated with the oxidation of the film) on the capacitive ratios of an eight-electrode micro-band array.

The tables above show that thicker Pani films formed onto the eight-electrode array gave rise to smaller capacitive-to-redox charge ratios. The exact reason for these observations is not fully understood, but these results would be of interest when considering conducting polymers as materials for super capacitors. Increasing the thickness of the

polymer, or using larger amounts of the polymer, albeit giving rise to larger capacities, is likely to lead to less efficient capacitors. Efficient super capacitors are more likely to be found through the use of high surface area electrodes with very thin films, i.e. polymer-coated nano-particles.

5.3.2.2 Chronoamperometry

The switching process of Pani was studied using chronoamperometry, as a function of electrode position. Figure 31 shows the current transients obtained by stepping the potential from -0.2 V to $+0.5$ V vs. SCE using different electrodes within the array. All the transients were integrated to yield identical charges, $Q_{(ox)} = 23 \mu\text{C}$ ($2 \mu\text{m}$), indicating that each electrode is able to address the entire film.

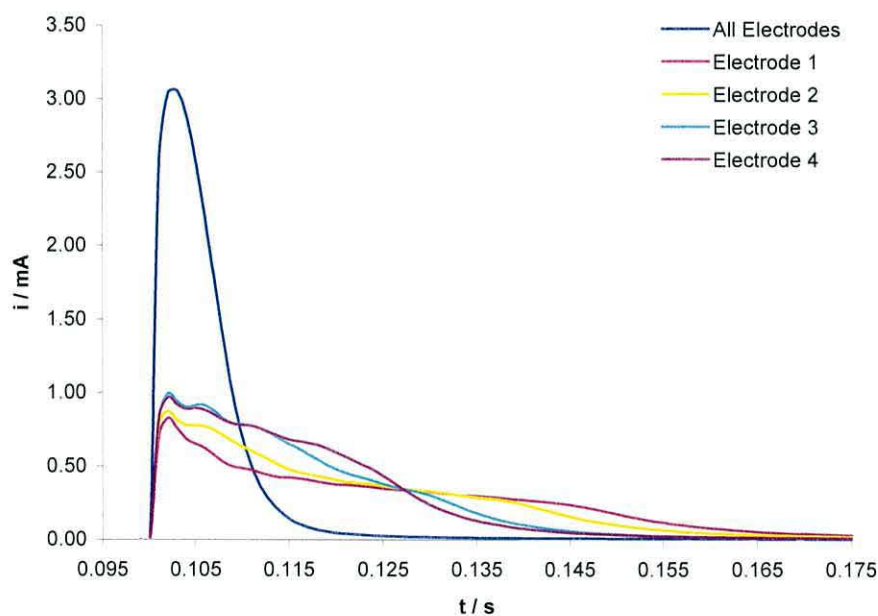


Figure 31. Current transients following a potential step from -0.2 V to $+0.5$ V for a polymer film, using electrode 1 (pink line), electrode 2 (orange line), electrode 3 (light blue line), electrode 4 (purple line) and all-electrodes (blue line) as the working electrode.

It is obvious from Figure 31 that the film can be switched more quickly when all the electrodes are operated together as the working electrode, rather than by using the

individual electrodes. This is due to the larger electrode contact area, which gives rise to a larger interface between the insulating and conducting material, and therefore a shorter propagation distance, as was represented in Figure 25, A.

The transients for the individual electrodes also display a slight trend, in that the electrodes positioned closer to the centre of the film give rise to slightly higher peak currents ($I_{p(ox)} = 0.97$ mA at the centre and $I_{p(ox)} = 0.83$ mA at the edge). This could be due to the area of the interfacial region between the conducting and insulating zones that is formed during the initial stages of oxidation. This has been depicted in Figure 32. As the current is a measure of the rate of charge transfer across the conducting-insulating interface, increasing the area of the interface will give rise to a larger current maximum. In fact, the peak current associated with electrode 3 and electrode 4, which are both situated towards the centre of the film is very similar and it is only the time required for the process to complete that varies significantly

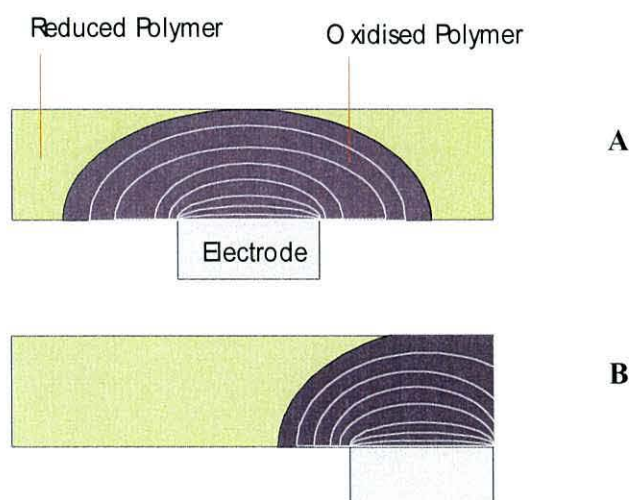


Figure 32. A simple representation of the oxidation of a Pani film, using electrode 4 in the centre of the array (A) and electrode 1 at the edge of the array (B) to address the film. The contour lines show the difference in interfacial area as oxidation proceeds.

Figure 31 also shows that the time required for the oxidation process to complete is shortened when the working electrode is situated at the centre of the film ($t_{\text{ox}} = 0.058$ s at the centre, $t_{\text{ox}} = 0.098$ s at the edge), which is due to the difference in the propagation distance to the edge of the film. When the working electrode is positioned at the centre of the array, the propagation distance to the edge of the film is half of when the working electrode is positioned at the opposite edge of the film. As the conducting-insulating interface propagates away from the working electrode at the centre of the film, the two equal fronts give rise to a larger overall interfacial area, and hence a slightly larger current is observed.

The reduction transients shown in Figure 33 occurred over a shorter timescale than the oxidation process, as has been previously reported in the literature [54]. This reflects the difference between the two processes, but it should be noted that reduction is incomplete over these timescales.

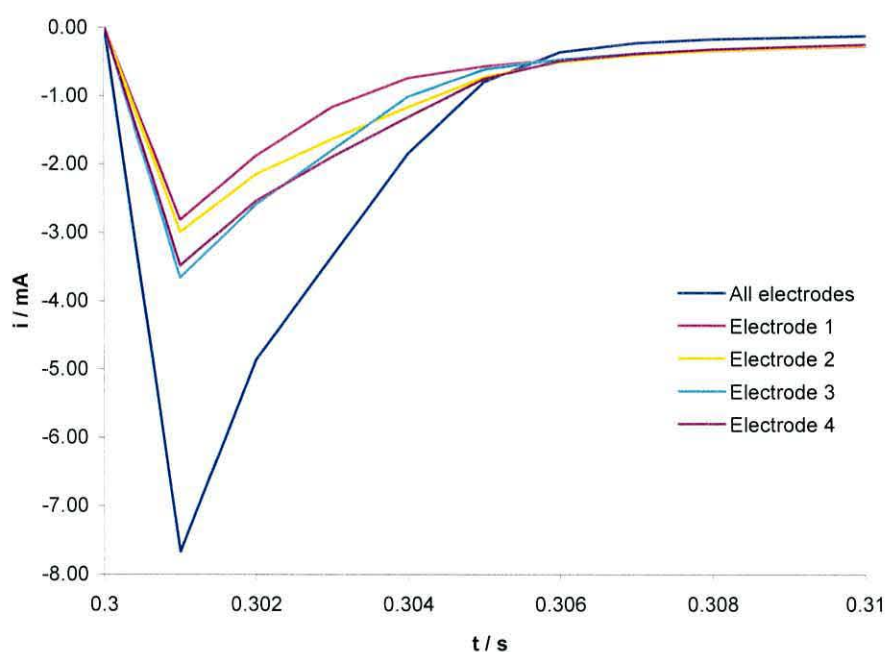


Figure 33. Potential step transients for the reduction of a polymer film, using electrode 1 (pink line), electrode 2 (orange line), electrode 3 (light blue line), electrode 4 (purple line) and all-electrodes (blue line) as the working electrode.

What is of great significance is that the reduction process proceeds further towards completion, within the timescale of the experiment, when all the electrodes are used to address the film. This is indicated by the difference in charge ($\Delta Q_{(\text{red})} = 6 \mu\text{C}$) between the transients obtained for the individual electrodes and the electrodes operated together. It has been suggested by Aoki [48] that reduction proceeds until the percolation threshold, which is the molar fraction of conducting material required for electron transfer through the film, after which reduction proceeds *via* slow relaxation [42]. Therefore, it is once again suggested that the electrode contact area is able to govern the percolation threshold of the polymer layer.

The reduction current maxima, although clearly influenced by electrode contact area, are also influenced by the electrode position. Peak currents associated with electrodes at the edge of the film, $I_{p(\text{red})} = 2.8 \text{ mA}$, are smaller than those at the centre, $I_{p(\text{red})} = 3.5 \text{ mA}$. When the working electrode is positioned at the edge of the film, the distance to the opposite edge is greater and there are fewer electric pathways to the electrode surface. The electrode positioned at the centre of the array has a shorter distance to either edge of the film, but more electric pathways to the electrode surface. This may account for the slightly higher current maximum observed.

5.3.2.3 Potentiometry

The data obtained so far indicates that propagation of the conducting-insulating interface influences the overall rate of the oxidation process. The next set of experiments was designed to monitor the propagation of the conducting front during voltammetry and chronoamperometry, in order to ascertain exactly how propagation influenced the switching process.

The propagation of the conducting front was monitored potentiometrically at electrodes adjacent to the working electrode, as shown in Figure 34. The electronics, are shown in Figure 4 on page 166.

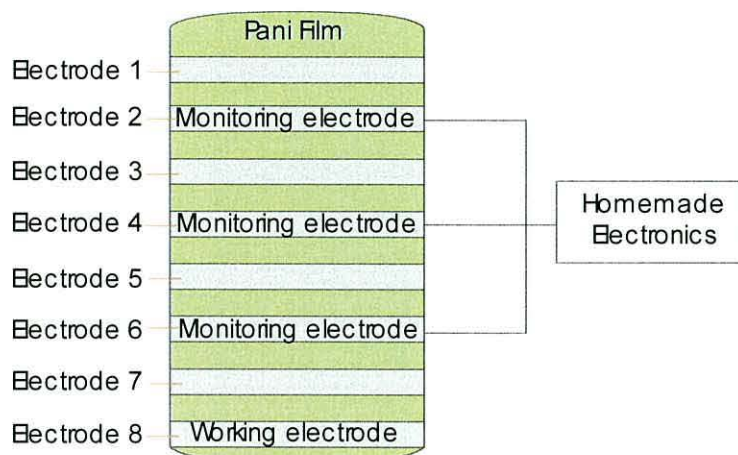


Figure 34. A schematic diagram depicting the potentiometric monitoring electrodes, where electrode 8 was used as the working electrode.

The electronics operated through the application of a 1 V potential difference between the monitoring electrodes and the working electrode, through a 100 M Ω resistor, which kept currents that were able to flow through the film relatively small ($< 0.1 \mu\text{A}$). The potential of each monitoring electrode was measured relative to the working electrode through a buffered amplifier. At sufficiently negative potentials when the Pani film was reduced and no current was able to flow between the working electrode and the monitoring electrodes, the potential of the monitoring electrodes imitated the potential of the working electrode, but offset by 1 V. But when the film was in the oxidised state and conducting, a short circuit was established between the working electrode and the monitoring electrodes and the potential of the monitoring electrodes became dependent on the resistance characteristics of the film. As the oxidation process is believed to proceed *via* the propagation of the conducting-insulating interface, the monitoring electrodes close to the working electrodes should short circuit before those situated further away. The propagation of the conducting-insulating interface can therefore be monitored as a function of time (or the potential of the working electrode) by determining the point at which the short circuit was established at each monitoring electrode. Reduction of the film can be observed as the point where breakdown of the electrical connection between the working and monitoring electrodes occurs, causing the potential of the monitoring electrodes to once more imitate that of the working electrode.

5.3.2.3.1 Potentiometric measurements during voltammetry

The potential of the monitoring electrodes was measured during cyclic voltammetry when electrode 8 was used as the working electrode. These plots can be seen in Figure 35 and have been offset for clarity. Zero seconds represents the start of the potential sweep, as the potential of the working electrode was swept linearly from -0.2 V to $+0.5$ V and then back to -0.2 V vs. SCE, and this is represented in Figure 35 in terms of time, between 0 and 28 s, i.e. at a sweep rate of 50 mV s^{-1} .

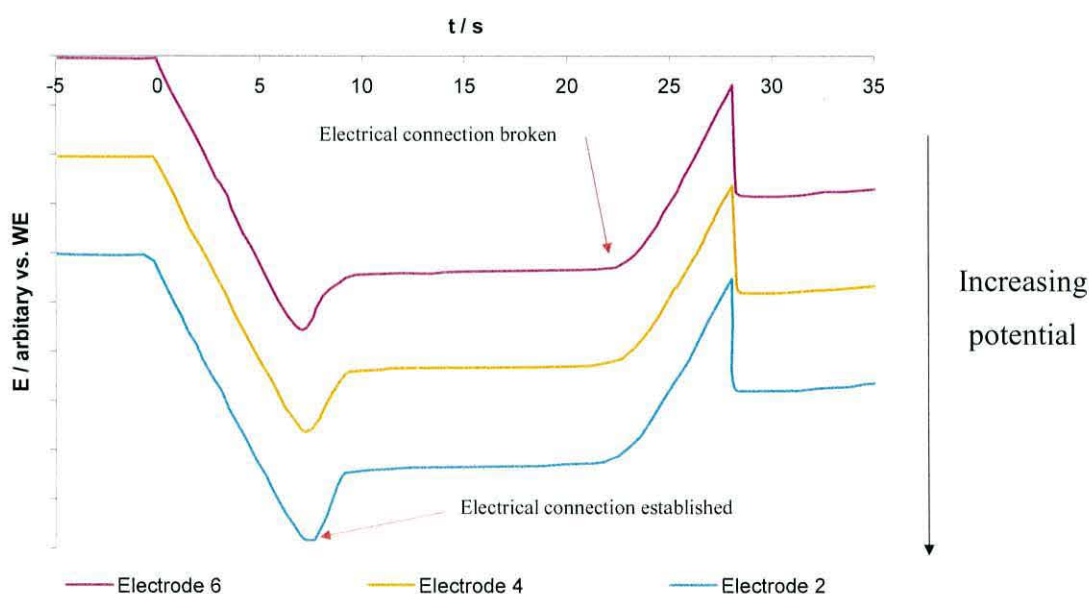


Figure 35. Potential plots for monitoring electrode 6 (pink line), electrode 4 (orange line) and electrode 2 (light blue line) when the WE was electrode 8, during cyclic voltammetry (-0.2 V to $+0.5$ V), at 50 mVs^{-1} .

During the anodic sweep (0 to 14 s) the potential of the monitoring electrodes initially increased with time, proportionally to the potential of the working electrode. At the point when electrical connection was established between the monitoring electrode and the working electrode (~ 7 -8 s), the potential of the monitoring electrode became dependent on the resistance characteristics of the film, which was observed as the sudden decrease of the monitoring electrode potential. When the potential of the working electrode was reversed the reduction of the film resulted in the loss of electrical connection between the

monitoring and working electrodes (~ 22 s), and this was observed in the potentiometric plot when the potential of the monitoring electrode began to fall proportionally to the potential of the working electrode.

It is difficult to see from Figure 35, but during oxidation establishment of the electrical connection between the monitoring electrodes and the working electrode did not occur at the same point. However, when this region is examined more closely (Figure 36) it can be seen that as the monitoring electrodes were situated further away from the working electrode, the time required for electrical connection to be established increased ($t_{\text{electrode 6}} = 7.1$ s, $t_{\text{electrode 4}} = 7.3$ s, $t_{\text{electrode 2}} = 7.5$ s). This confirms that during voltammetry oxidation does not occur instantaneously throughout the film, but is dependent on the propagation of the conducting-insulating interface.

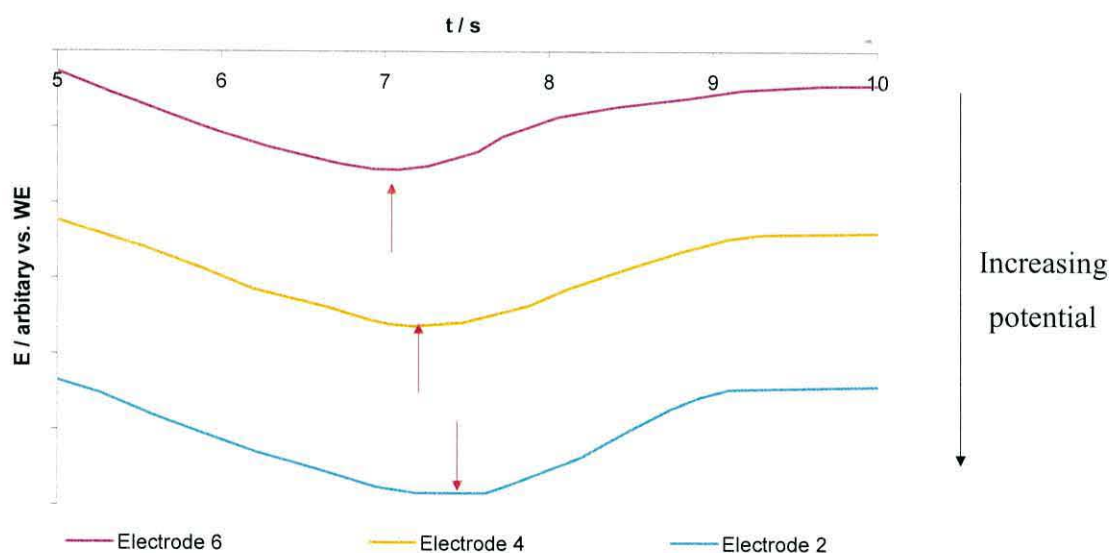


Figure 36. Potential plots for electrode 6 (pink line), electrode 4 (orange line), and electrode 2 (light blue line) adjacent to the WE (electrode 8), during cyclic voltammetry (-0.2 V to $+0.5$ V), at 50 mVs^{-1} . The arrows indicate the point at which electrical connection was established between the working and monitoring electrodes.

It is also worth noting that these small differences in time relate to significant differences in potential, with 0.2 s corresponding to 10 mV, at a sweep rate of 50 mV s^{-1} . This supports the idea that the shift in voltammetric peak potential observed for different working electrode positions (Figure 27) is caused by differences in the propagation distances. However, the point at which the electrical connections were broken during reduction occurred simultaneously; again highlighting the difference between the oxidation and reduction processes.

The effect of sweep rate on the propagation of the conducting front was studied during voltammetry and can be seen in Figure 37 and Figure 38. Increasing the sweep rate effectively acted to shift, to more positive potentials, the point at which electrical connection between the monitoring and working electrodes was established. The electrical connection between the monitoring electrodes and the working electrode occurred at higher potentials when faster sweep rates were used. It is likely that this is because there is less time available for propagation at faster sweep rates. At slower sweep rates there was more time at each given potential so the conducting front had more time to propagate, hence the electrical connection was established at a lower potential. In Figure 38 the sweep rate is proportional to the potential at which electrical connection occurs between the monitoring electrode and the working electrode, which is consistent with the behaviour of surface-bound processes.

It should be noted that the data in Figure 37 was collected as time vs. potential. Faster sweep rates resulted in the scan completing over a shorter time scale, and therefore the data was converted in order to obtain a potential vs. potential plot. The difference in y-scale magnitude for the individual plots is due to the conversion factor.

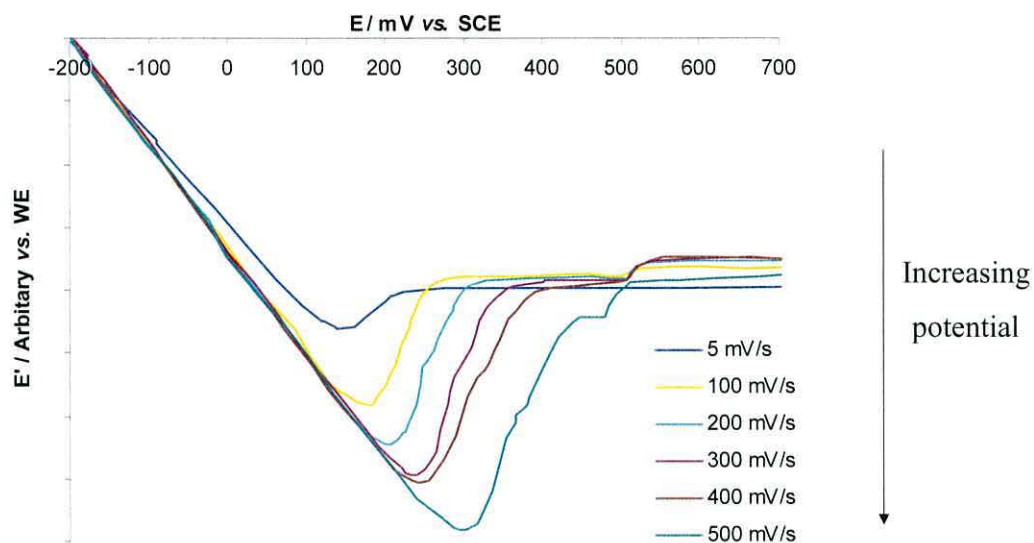


Figure 37. Potential plots for monitoring electrode 2 (WE = electrode 8) during a linear sweep from -200 mV to $+500$ mV, at sweep rates of 5, 100, 200, 300, 400 and 500 mV s^{-1} .

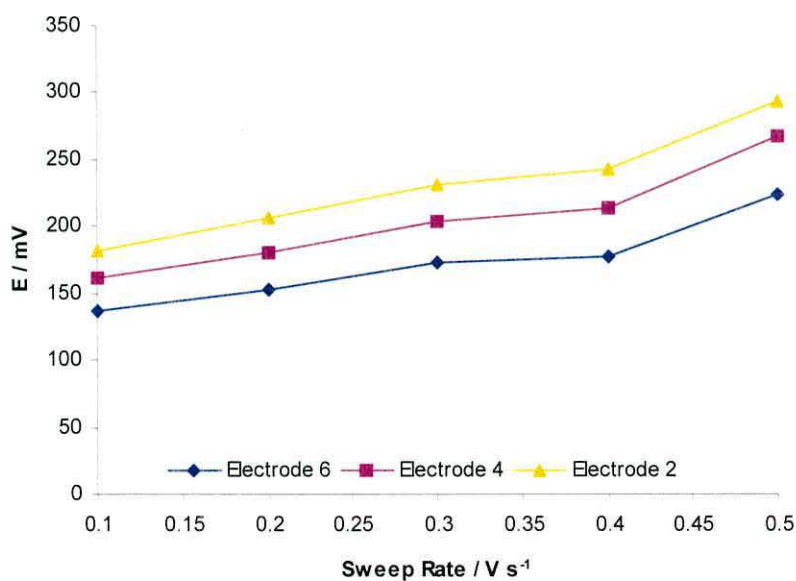


Figure 38. A graph to show the influence of sweep rate on the propagation of the conducting-insulating interface as measured potentiometrically at monitoring electrode 6 (blue line), electrode 4 (pink line) and electrode 2 (orange line) adjacent to the working electrode (electrode 8), where E is the observed voltammetric peak potential.

5.3.2.3.2 Potentiometric measurements following a potential step

The potential of the monitoring electrodes was also measured after a potential step and the data can be seen in Figure 39.

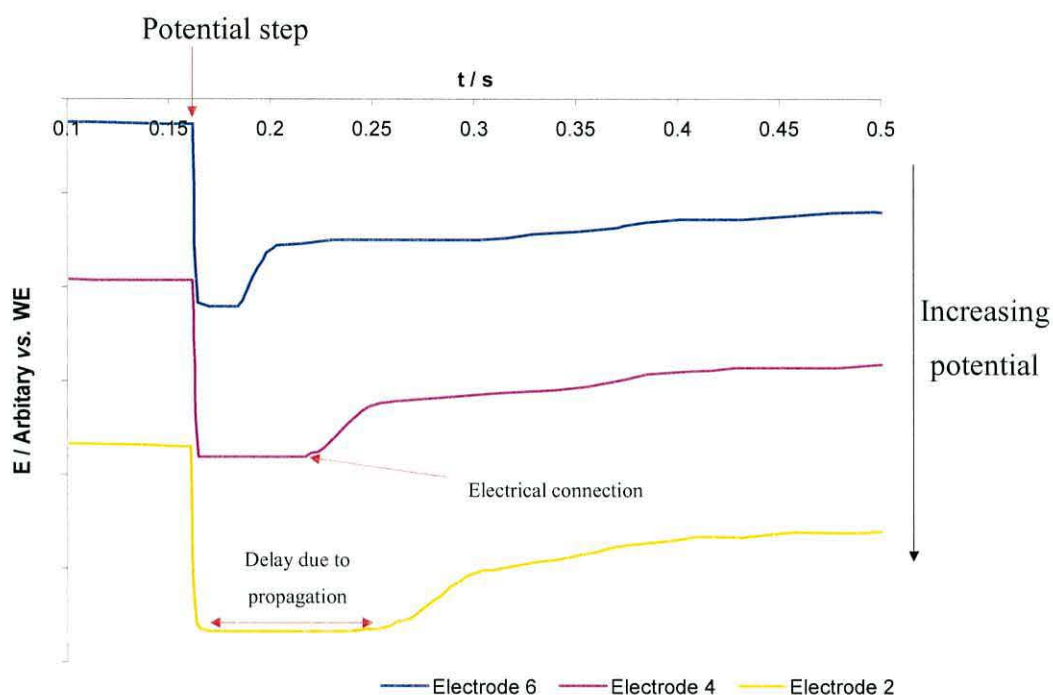


Figure 39. Potential transients for monitoring electrode 6 (blue line), electrode 4 (pink line) and electrode 2 (orange line) adjacent to the WE (electrode 8), following a potential Step from -0.2 V to $+0.5$ V.

The sudden rise in the potential of the monitoring electrodes (at $t = 0.16$ s) indicates the potential step (-0.2 V to $+0.5$ V vs. SCE). The potential of the monitoring electrodes was then observed to be constant for a short period of time during the propagation of the conducting-insulating interface, before suddenly decreasing when the electrical connection between the monitoring and working electrode was established. The difference in this delay can be plotted against the distance of the monitoring electrode from the working electrode, to give the propagation rate of the conducting front across the film (Figure 40).

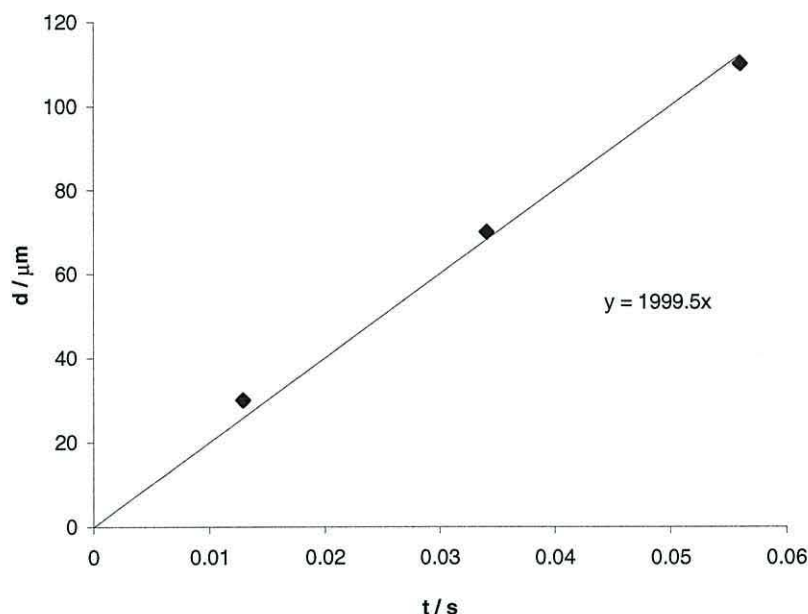


Figure 40. The propagation rate of the conducting front in a Pani film ($64 \mu\text{C}$), following a potential step (-0.2 V to $+0.5 \text{ V}$).

The propagation rate was calculated to be $2000 \mu\text{m s}^{-1}$. The propagation rate of the conducting-insulating interface decreased slightly as the front moved away from the working electrode. This might have been expected, since there may be a slight potential drop across the film (iR drop), which accounts for the higher propagation rate observed here in comparison to those calculated for the much larger films used by Aoki ($1000 \mu\text{ms}^{-1}$) using optical methods [45].

In the first part of this study, the oxidation process was shown to go to completion over a shorter timescale as the second potential limit was increased from $+0.3 \text{ V}$ to $+0.5 \text{ V}$. Therefore, it might be expected that the rate of propagation of the conducting-insulating interface would be proportional to the magnitude of the potential step. The magnitude of the potential step was indeed found to influence the rate of propagation (Figure 41), as has been observed previously [43, 48, 53], and Figure 42 shows that the propagation rate of the conducting-insulating interface decreased as the magnitude of potential step decreased.

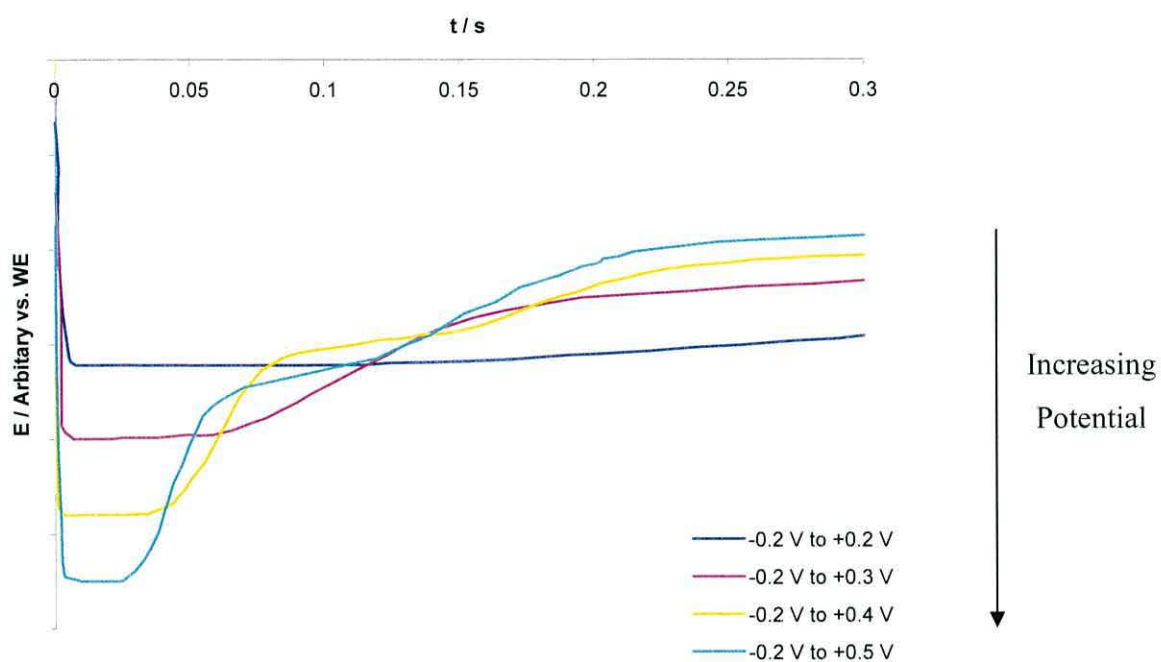


Figure 41. Potential transients for monitoring electrode 4, adjacent to the WE (electrode 8), following a potential step from -0.2 V to $+0.2$, $+0.3$, $+0.4$, and $+0.5$ V, respectively.

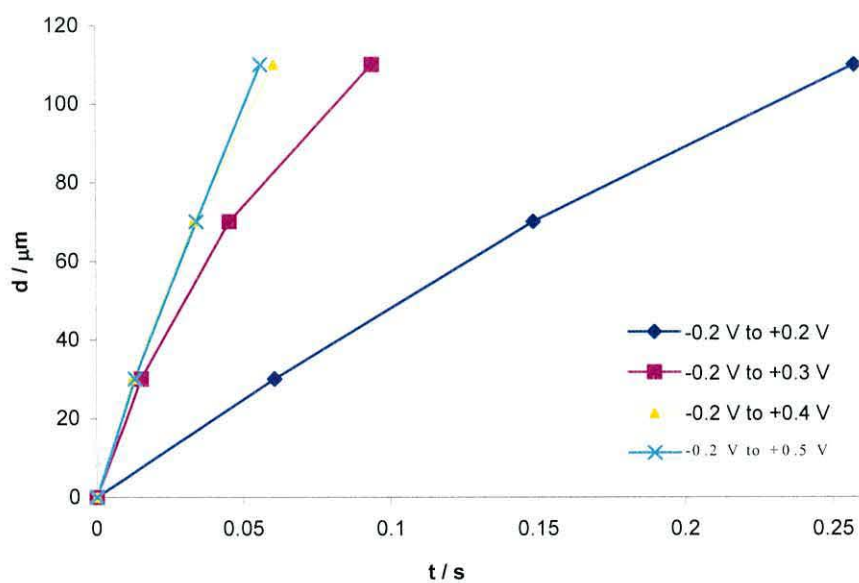


Figure 42. Propagation rates of the conducting front after a potential step from -0.2 V to $+0.2$, $+0.3$, $+0.4$ and $+0.5$ V, respectively, applied to the working electrode at the edge of the film.

Since the propagation rate is a function of the current, a Tafel-type plot can be drawn for the logarithm of the propagation speed vs. the second potential limit, E_2 [41, 44], as can be seen in Figure 43. The plot of the logarithm of the propagation speed should be proportional to the second potential limit, indicating kinetic control of the propagation. However, the plot is not linear and curves away. This might be due to a significant iR -drop across the film, or the blockage of growth due to incomplete percolation [48]. However, iR compensation was applied to the system to eliminate the ohmic drop and so this is unlikely. Propagation of the conducting-insulating interface may be limited by mass transport, such as diffusion of counter ions into the thick polymer films; however further evidence is required to support this.

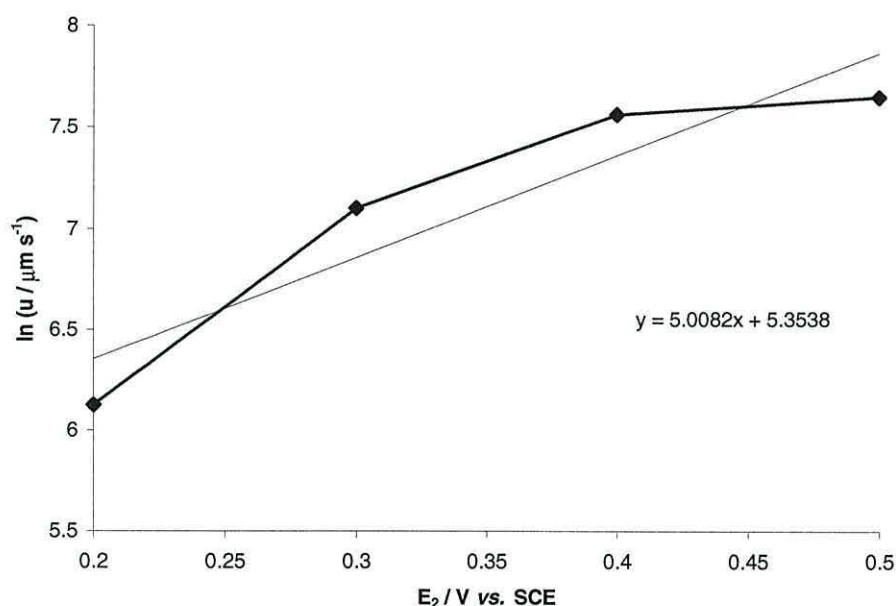


Figure 43. Logarithmic plot of propagation speed, u , against the second potential limit, E_2 .

The reduction transients obtained following a potential step, can be seen in Figure 44. The potential step corresponds to the sharp decrease in the potential of the monitoring electrodes as the electrical connection between the monitoring and working electrodes was broken. The reduction is incomplete at this stage and the potential slightly increases as percolation allows the film to become homogeneous. It then decreases again with

slow relaxation over a period of eight to ten minutes. The plots for monitoring electrodes 2, 4, and 6 are very similar, which suggests that the reduction process occurs simultaneously throughout the film. This is in agreement with the percolation theory [48].

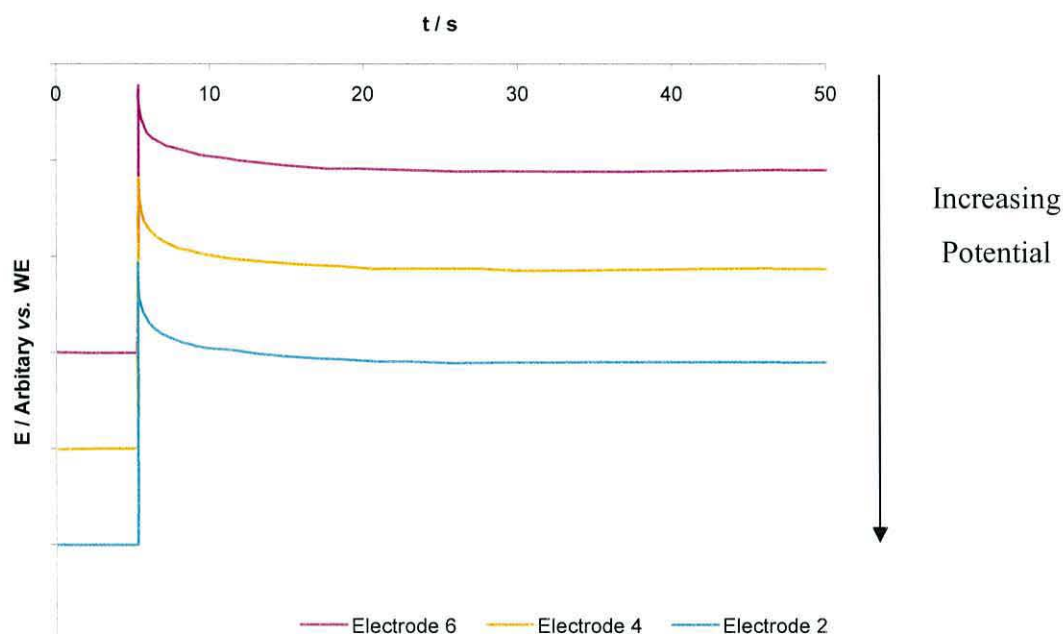


Figure 44. Potential transients for monitoring electrodes adjacent to the WE (electrode 8) following a Potential Step from +0.5 V to -0.2 V vs. SCE.

It has been suggested earlier in this chapter that when the working electrode is situated at the centre of the array, oxidation proceeds with the propagation of two conducting fronts in opposite directions. This suggestion was confirmed by monitoring the potential of the electrodes situated either side of the working electrode after a potential step.

The working electrode (electrode 5) was positioned at the centre of the array, and two monitoring electrodes were chosen so that they would be equidistant either side of the working electrode (electrodes 2 and 8). Another monitoring electrode was also used, situated closer to the working electrode, allowing the propagation to be monitored and confirmed. This set-up is depicted in Figure 45.

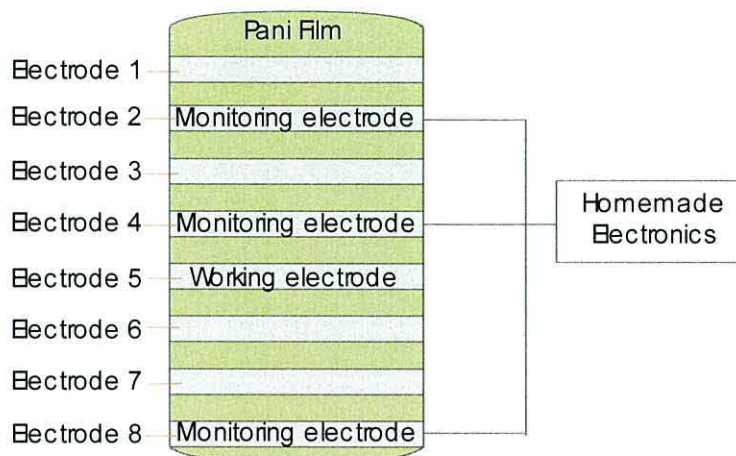


Figure 45. A schematic diagram depicting the potentiometric monitoring electrodes, where electrode 5 was used as the working electrode to address a Pani film.

The potentiometric plots can be seen in Figure 46. The sudden rise in potential again represents the potential step. The potential of the monitoring electrodes was then observed to be constant for a period as the conducting-insulating interface propagated from the working electrode. When the conducting front reached the monitoring electrode and caused a short circuit, the potential dropped and became dependent on the resistance characteristics of the film.

It is clear to see that the short circuit occurred at monitoring electrode 4 more quickly ($t_{\text{electrode 4}} = 0.006 \text{ s}$) than at electrodes 2 and 8 ($t_{\text{electrodes 2 \& 8}} = 0.03 \text{ s}$), which were situated further away from the working electrode, which indicates propagation of the conducting front. It is also interesting to note that electrical connection of monitoring electrodes 2 and 8, which are equidistant from the working electrode, occurred at the same point. This confirms the hypothesis that two conducting fronts propagate from the working electrode in opposite directions at equal speeds. The time required for the conducting front to reach electrodes 2 and 8, is half that required to propagate the conducting front across the entire film (0.06 s). It appears that by changing the position of the working electrode from the edge to the centre of the array, the film can be switched approximately twice as quickly.

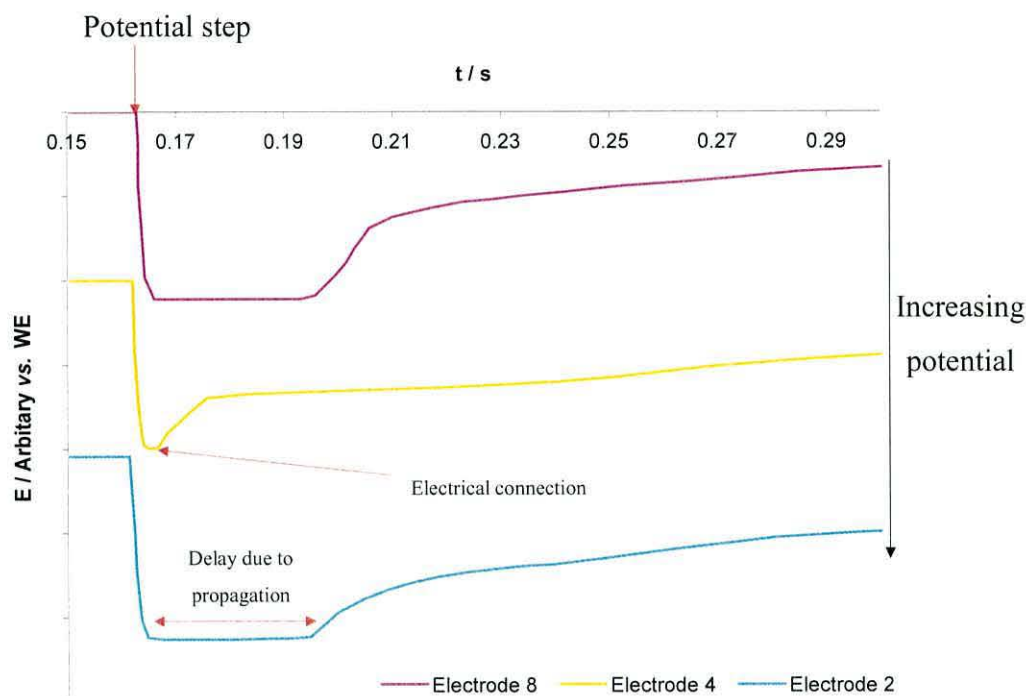


Figure 46. Potential transients for monitoring electrodes adjacent to the WE (electrode 5), after a Potential Step from -0.2 V to $+0.5$ V vs. SCE.

The potentiometric measurements, following a potential step from an oxidising potential to a reducing potential, were very similar to those obtained for the reduction of the film when electrode 8 was used as the working electrode (), and hence are not shown.

5.4 Conclusions

The redox switching characteristics of polyaniline have been studied using voltammetric and chronoamperometric methods, in conjunction with potentiometric monitoring of the electrodes adjacent to the working electrode. Oxidation of the polymer in direct contact with the electrode surface is believed to occur *via* the nucleation and propagation of the conducting-insulating interface in a direction perpendicular to the electrode surface. Polymer that is not in direct contact with the working electrode surface, i.e. overhanging the edge of the electrode, is oxidised by propagation of the conducting front away from but in the same plane as the electrode surface.

The electrode contact area was seen to influence the redox switching characteristics of polyaniline films. Voltammetric anodic peak potentials shifted to more positive potentials when the contact area was reduced, leading to the conclusion that reducing the size of the electrode contact area increases the percolation threshold potential, thus “blocking” the oxidation process at low potentials. This was reflected in the charge vs. potential plots, and Tafel-type plots constructed from the voltammetric results. Once the percolation threshold potential was reached, propagation of the conducting front proceeded rapidly. When the potential was instantaneously stepped to an oxidising potential the overall rate of the oxidation process appeared to be governed by the movement of the propagating front, which in turn was dependent on the applied potential, indicating a kinetically controlled process. Chronoamperometric transients indicated that the time required for completion of the oxidation process was also dependent on the electrode contact area. It is suggested that this is due to the increased propagation distance that arises as a result of decreasing the electrode contact area.

It is believed that reduction proceeds through a different mechanism to oxidation (i.e. not *via* propagation), and appears to be governed by the RC time constant until the percolation threshold is reached. Smaller electrode contact areas gave rise to lower charges associated with the reduction process. This maybe due to a modification of the percolation threshold, a direct result of fewer conducting pathways to the electrode surface, which gave rise to a larger number of “conducting islands” being disconnected from the electrode, and hence a smaller associated charge. This can be regarded as an “exaggeration” of the memory effect.

The position of the working electrode within the array was also shown to influence the redox switching characteristics of the polymer film. During oxidation, voltammetric studies indicated that an electrode situated at the periphery of the film gave rise to more positive anodic peak potentials than those situated near the centre of the array. This is due to a smaller interface between the conducting and insulating material, which increases the potential at which the percolation threshold is reached. The distance that the conducting-insulating interface is required to propagate is also much larger; hence

voltammetric peak potentials are shifted in an anodic (positive) direction relative to electrodes covering the entire film and electrodes at the centre of the film.

Potentiometric measurements of electrodes situated adjacent to the WE monitored the propagation of the conducting front, and the speed of propagation was found to be $2000 \mu\text{m s}^{-1}$ after a potential step where $E_2 = 0.5 \text{ V}$. Electrodes situated at the centre of the film required shorter periods (approximately half) for completion of the process. This is because two conducting-insulating interfaces propagate in opposite directions, and hence the propagation distance was effectively halved.

5.5 Future Work

It has been observed that the redox switching characteristics of Pani films can be influenced by the manipulation of the size and position of the working electrode. This brings about many possibilities and potential applications. But there is also a great deal of work that can still be done in order to ascertain the cause of particular observations and the effects of changing other conditions. It would be interesting to observe the influence of the film thickness on the switching characteristics of polymer films. It might be expected that very thin films would emphasise the effects on the redox switching of the film observed during this work. The effect of the electrode configuration could be further investigated in order to ascertain the reasons for the observed reduced capacitance of films deposited onto the eight-electrode array. Impedance studies would be most useful in this instance and may prove useful in helping to establish the poor stability of current polymer-based supercapacitors. It would be of interest to observe the effects of using more than one working electrode to drive the redox processes from different areas of the film. It may also be possible to maintain different areas of the film under different redox conditions by holding the film under potential control at different electrodes within an array. Of course, it would be intuitive to think about the possible applications applicable to the variation of the redox switching characteristics of polymers. Obvious examples would include variable microelectronic switches and self-contained sensor arrays. By controlling the potential of pairs of electrodes within an array, an array of chemiresistors

could be produced from a single film, all possessing different degrees of oxidised material.

5.6 References

1. E. W. Paul, A. J. Ricco, and M. S. Wrighton, *J. Phys. Chem.* **89** (1985) 1441-1447.
2. H. Letheby, *J. Chem. Soc., Faraday Trans.* **15** (1862) 161.
3. E. M. Genies, A. Boyle, M. Lapkowski, and C. Tsintavis, *Synth. Met.* **36** (1990) 139-182.
4. A. Zimmermann, U. Kunzelmann, and L. Dunsch, *Synth. Met.* **93** (1998) 17-25.
5. S. J. Sutton and A. S. Vaughan, *Polymer.* **36** (1995) 1849-1857.
6. R. Greef, M. Kalaji, and L. M. Peter, *Faraday Discuss.* **88** (1989) 277.
7. E. M. Genies and M. Lapkowski, *J. Electroanal. Chem.* **236** (1987) 199-208.
8. A. G. MacDiarmid and A. J. Epstein, *Faraday Discuss.* **88** (1989) 317-332.
9. H. Okamoto and T. Kotaka, *Polymer.* **39** (1998) 4349-4358.
10. H. Okamoto, M. Okamoto, and T. Kotaka, *Polymer.* **39** (1998) 4359-4367.
11. P. V. Prabhakaran, S. Venkatachalam, S. Sakthivel, B. Chandar Shekar, D. Mangalaraj, and S. K. Narayandass, *Eur. Polym. J.* **33** (1997) 1747-1752.
12. K. L. Tan, B. T. G. Tan, S. H. Khor, K. G. Neoh, and E. T. Kang, *J. Phys. Chem. Solids.* **52** (1991) 673-680.
13. M. Kalaji, L. Nyholm, and L. M. Peter, *J. Electroanal. Chem.* (1991)
14. G. T. Andrade, M. Jesus Aguirre, and S. R. Biaggio, *Electrochim. Acta.* **44** (1998) 633-642.
15. T. L. Porter, *Surf. Sci.* **293** (1993) 81-85.
16. L. Duic and S. Grigic, *Electrochim. Acta.* **46** (2001) 2795-2803.
17. M.-C. Su and J.-L. Hong, *Polymer.* **42** (2001) 3297-3300.
18. Q. Wu, Z. Xue, Z. Qi, and F. Wang, *Synth. Met.* **108** (2000) 107-110.
19. M. V. Giotto, T. J. Bonagamba, H. Panepucci, G. R. Valenciano, and L. H. C. Mattoso, *Synth. Met.* **101** (1999) 756-757.
20. J. Stejskal, M. Spirkova, A. Riede, M. Helmstedt, P. Mokreva, and J. Prokes, *Polymer.* **40** (1999) 2487-2492.
21. V. D. Jovic, T. Trisovic, B. M. Jovic, and M. Vojnovic, *J. Electroanal. Chem.* **408** (1996) 149-155.
22. T. Kugler, J. R. Rasmusson, W. R. Salaneck, J.-E. Osterholm, and A. P. Monkman, *Synth. Met.* **76** (1996) 181-185.
23. E. Sabatini, A. Redondo, J. Rishpon, A. Rudge, I. Rubinstein, and S. Gottesfeld, *J. Chem. Soc., Faraday Trans.* **89** (1993) 287.
24. M. J. Giz, S. L. de Albuquerque Maranhao, and R. M. Torresi, *Electrochem. Commun.* **2** (2000) 377-381.
25. B. Wang, J. Tang, and F. Wang, *Synth. Met.* **13** (1986) 329-334.
26. A. J. Bard and H. Yang, *J. Electroanal. Chem.* **339** (1992) 423.
27. G. Inzelt, *Electrochim. Acta.* **45** (2000) 3865-3876.
28. H. Daifuku, T. Kawagoe, T. Matsunaga, N. Yamamoto, T. Ohsaka, and N. Oyama, *Synth. Met.* **43** (1991) 2897-2900.

29. C. Barbero, M. C. Miras, O. Haas, and R. Kotz, *J. Electrochem. Soc.* **138** (1991) 669-672.
30. C.-T. Kuo and W.-H. Chiou, *Synth. Met.* **88** (1997) 23-30.
31. A. J. Epstein, J. M. Ginder, F. Zuo, R. W. Bigelow, H. S. Woo, D. B. Tanner, A. F. Richter, W. S. Huang, and A. G. MacDiarmid, *Synth. Met.* **18** (1987) 303.
32. V. Luthra, R. Singh, S. K. Gupta, and A. Mansingh, *Curr. Appl. Phys.* **3** (2003) 219-222.
33. L. Zhuang, Q. Zhou, and J. Lu, *J. Electroanal. Chem.* **493** (2000) 135-140.
34. S. Stafstrom, J. L. Bredas, A. J. Epstein, H. S. Woo, D. B. Tanner, W. S. Huang, and A. G. MacDiarmid, *Phys. Rev. Lett.* **59** (1987) 1464.
35. S. Stafstrom and J. L. Bredas, *J. Mol. Struct.* **188** (1989) 393-427.
36. J.-C. LaCroix and A. F. Diaz, *J. Electrochem. Soc.* **135** (1988) 1457-1463.
37. M. Kalaji, L. M. Peter, L. M. Abrantes, and J. C. Mesquita. (1989)
38. J.-C. LaCroix, K. k., and A. F. Diaz, *J. Electrochem. Soc.* **136** (1989) 1308.
39. E. M. Genies, G. Bidan, and A. F. Diaz, *J. Electroanal. Chem.* **149** (1983) 101-113.
40. M. Vuki, M. Kalaji, L. Nyholm, and L. M. Peter, *J. Electroanal. Chem.* **332** (1992) 315-323.
41. K. Aoki, T. Aramoto, and Y. Hoshino, *J. Electroanal. Chem.* **340** (1992) 127-135.
42. K. Aoki, J. Cao, and Y. Hoshino, *Electrochim. Acta.* **39** (1994) 2291-2297.
43. Y. Tezuka and K. Aoki, *J. Electroanal. Chem.* **273** (1989) 161-168.
44. Y. Tezuka, S. Ohyama, T. Ishii, and K. Aoki, *Chem. Soc. Jap.* **64** (1991) 2045-2051.
45. K. Aoki and Y. Teragishi, *J. Electroanal. Chem.* **441** (1998) 25-31.
46. M. Kalaji, L. Nyholm, and L. M. Peter, *J. Electroanal. Chem.* **325** (1992) 269-284.
47. K. Aoki, *J. Electroanal. Chem.* **300** (1991) 13-22.
48. K. Aoki and M. Kawase, *J. Electroanal. Chem.* **377** (1994) 125-129.
49. C. Odin, M. Nechtschein, and P. Hapiot, *Synth. Met.* **47** (1992) 329-350.
50. C. Barbero, R. Kotz, M. Kalaji, L. Nyholm, and L. M. Peter, *Synth. Met.* **55-57** (1993) 1545-1551.
51. K. Aoki and L. Jianquan, *J. Electroanal. Chem.* **441** (1998) 161-166.
52. Y. Tezuka, K. Aoki, H. Yajima, and T. Ishii, *J. Electroanal. Chem.* **425** (1997) 167-172.
53. Y. Tezuka, K. Aoki, and T. Ishii, *Electrochim. Acta.* **44** (1999) 1871-1877.
54. M. Kalaji, L. M. Peter, L. M. Abrantes, and J. C. Mesquita, *J. Electroanal. Chem.* **274** (1989) 289-295.

GENERAL CONCLUSIONS

This work has shown that gas-sensitive resistors constructed from metal oxides and conducting polymers, are suitable for the detection of nitroaromatic vapours. These sensing elements could be used as part of an array for the detection of explosives.

In the first part of this work, a vapour generator was designed and built in order to generate a calibrated vapour stream of 2,4-dinitrotoluene. The vapour generator was based on a flow of nitrogen that passed through a column that was packed with 2,4-DNT-coated glass beads. The nitrogen gas stream became saturated with vapours of the nitroaromatic within the column, which were then transported to the sensor. The vapour generator was calibrated using gas chromatography and was able to produce a vapour stream with a concentration between 0.47 ppm_v and 2.78 ppm_v 2,4-DNT, at column temperatures between -10 °C and 115 °C. 2,4-DNT was observed to condense on the glass walls of the generator between the exit of the column and the sensor port, despite silanisation of the glassware. A heater unit was designed to raise the temperature of this glassware to reduce this effect. If this proves to be successful, a larger concentration range may be obtainable.

The responses of chromium titanium oxide and tungsten oxide chemiresistors were observed in the presence of 2,4-DNT. The resistance of chromium titanium oxide chemiresistors increased upon exposure to the nitrogen carrier gas, which is believed to be due to a combination of the removal of adsorbed oxygen and water species. The presence of 2,4-DNT acted to further increase the resistance of the chemiresistor. This response was reversible, and was shown to be proportional to the square root of the concentration of 2,4-DNT in the vapour stream. The optimum operation temperature for maximum sensitivity towards 2,4-DNT was found to lie between 300 °C and 330 °C. It is suggested that the interaction of 2,4-DNT vapours with the CTO surface resulted in the decomposition of the nitroaromatic, which subsequently interacted with the adsorbed oxygen species, resulting in a higher electron density in the oxide layer, although further

experiments are required to confirm this. The response of the chromium titanium oxide chemiresistor was substantially affected by the presence of relative humidity in the vapour stream.

The resistance of tungsten oxide chemiresistors decreased upon exposure to the nitrogen carrier gas, and it is proposed that this is due to the removal of adsorbed oxygen species from the surface of the oxide, and this response was independent of relative humidity. The presence of 2,4-DNT in the vapour stream resulted in a slight increase of the film resistance, which was found to be independent of concentration. The response varied with operating temperature, and the optimum temperature was 500 °C. At this temperature, 2,4-DNT is likely to decompose (2,4-DNT decomposes at 300 °C). The presence of oxygen in the carrier gas severely diminished the chemiresistors response towards 2,4-DNT, and it is proposed that 2,4-DNT undergoes a competitive reaction with oxygen to replace the vacant oxygen adsorption sites.

Gas sensitive resistors were also constructed from conducting polymer films grown on to platinum microband electrodes. Generally, polymer films exhibited a slight decrease of the film resistance upon exposure to 2,4-DNT. The entrapment of HPAs into the polymer film led to the enhancement of the response towards 2,4-DNT. It is suggested that the interaction of the polymer and 2,4-DNT resulted in the modification of the doping level within the film, which was enhanced by charge transfer between 2,4-DNT and the HPA, and then the HPA and the polymer, however further work is required to confirm this.

The best response ($\Delta R_g = 79\%$) obtained from the Pani films was with the TS anion, when the potential had been set at -0.8 V. It is thought that this potential renders the polymer is in the neutral state and the HPA is in the reduced state, maximising charge transfer from the HPA to the nitroaromatic. The subsequent removal of charge from the polymer, in its neutral state, leads to a large modification of the film resistance.

The level of HPA incorporation was found to decrease with increasing film thickness. Therefore, it is suggested that the use of thin films would help to maximise the response

towards nitroaromatics. However, this work represents only a preliminary study, and the complete characterisation of the chemiresistors response towards 2,4-DNT is required before it could be used as a sensor for nitroaromatics.

In a second part of this work, the redox switching characteristics of polyaniline were studied using voltammetry and chronoamperometry, in conjunction with potentiometric monitoring of the electrodes adjacent to the working electrode. Reduction of the electrode contact area resulted in a shift of the oxidation peak to more positive potentials, during voltammetry. It is suggested that reducing the size of the electrode contact area leads to a lower number of sites available for nucleation and growth of oxidised polymer. This acted to increase the percolation threshold potential, effectively delaying the propagation of the conducting-insulating front at low potentials. When the potential was instantaneously stepped to an oxidising potential, the overall rate of the oxidation process appeared to be governed by the movement of the propagating front, which was a kinetically controlled process dependent on the applied potential. Chronoamperometric transients showed that as the electrode contact area was reduced, and hence the number of site available for oxidation was reduced, the current maxima decreased. The time required for completion of the oxidation process increased, which is due to the increased propagation distance that arising as a result of decreasing the electrode area.

It is believed that reduction proceeds through a different process to oxidation, and appears to be governed by the RC time constant, until the percolation threshold. Smaller electrode contact areas gave rise to lower charges associated with the reduction process. It is suggested that this is due to a modification of the percolation threshold, a direct result of fewer conducting pathways to the electrode surface, which gives rise to a greater number of "conducting islands" being disconnected from the electrode, and hence a smaller associated charge. This can be regarded as an "exaggeration" of the memory effect.

The position of the working electrode within the array was also shown to influence the redox switching characteristics of the polymer film. During oxidation, voltammetric

studies indicated that as the working electrode was moved from the centre of the film to the edge of the film, the oxidation peak potential shifted in a positive direction. The reason for this is two-fold. Firstly, the electrodes at the edge of the film give rise to a smaller interfacial region between the conducting and insulating polymer, which hinders propagation. Secondly, the distance that the conducting-insulating interface is required to propagate is also much larger for electrodes at the edge of the film. Chronoamperometry and potentiometric measurements of electrodes situated adjacent to the working electrode, were employed to calculate the speed of the propagation, which was found to be $2000 \mu\text{m s}^{-1}$ after a potential step from -0.2 to 0.5 V vs. SCE. The time required for the oxidation process to complete was shorter, approximately half, when the working electrode was situated at the centre of the film. This is because two conducting-insulating interfaces propagate in opposite directions, and hence the propagation distance was effectively halved.

The films deposited onto the eight-electrode microband array exhibit lower capacitive charges compared with films on single electrodes or electrode-pairs. It is thought that this may be a consequence of the amount of polymer that is not directly in contact with the electrode surface, i.e. the polymer that overhangs the electrode, and this was supported by studying films of different thickness. However, the reasons for these observations are not fully understood and further work is required.